A Hydrodynamic Perspective on the Formation of Asphaltene Deposits

Schutte, Koen

Important note
To cite this publication, please use the final published version (if applicable).
Please check the document version above.

A Hydrodynamic Perspective on the Formation of Asphaltene Deposits

A Hydrodynamic Perspective on the Formation of Asphaltene Deposits

PROEFSCHRIFT

ter verkrijging van de graad van doctor
aan de Technische Universiteit Delft,
op gezag van de Rector Magnificus prof. ir. K. C. A. M. Luyben;
voorzitter van het College voor Promoties,
in het openbaar te verdedigen op
woensdag 22 juni 2016 om 10:00 uur

door

Koen Christian Johannes SCHUTTE

natuurkundig ingenieur
Technische Universiteit Delft
geboren te Amsterdam

Dit proefschrift is goedgekeurd door de

promotor: Prof. dr. ir. R. A. W. M. Henkes en
copromotor: Dr. A. Twerda

Samenstelling promotiecommissie:

Rector Magnificus	voorzitter
Prof. dr. ir. R. A. W. M. Henkes	Technische Universiteit Delft
Dr. A. Twerda	Technische Universiteit Delft

onafhankelijke leden:

Prof. dr. ir. B. G. M. van Wachem	Imperial College London
Prof. dr. J. G. M. Kuerten	Technische Universiteit Eindhoven
Prof. dr. P. L. J. Zitha	Technische Universiteit Delft
Prof. dr. ir. B. J. Boersma	Technische Universiteit Delft
Prof. dr. R. F. Mudde	Technische Universiteit Delft

Dr. eng. L. M. Portela heeft in belangrijke mate aan de totstandkoming van dit proefschrift bijgedragen.

Abstract

Deposition of asphaltenes is a serious problem that may be encountered during the production of crude oil from subsurface reservoirs. Asphaltenes are a part of the crude oil itself that, depending on the operating conditions, such as the pressure and temperature, can separate from the oil. Eventually they may form deposits at the boundaries of the flow domain. This will increase the pressure loss in the production system and reduce the oil production rate, which leads to a significant loss of revenue of the well.

To optimise the strategy by which asphaltene deposition is handled in the field, engineering models that can reliably predict when and where deposition will occur are highly sought after. Such models can only be devised if the physical phenomena underlying asphaltene deposition are properly understood. This study fully focuses on the hydrodynamics of asphaltene agglomerates. The kinetics of the formation of particles during the separation from the crude oil and the chemical properties of asphaltenes are not explicitly studied. Very limited literature on the hydrodynamic aspects is available, and this work is intended to fill that gap.

To this end, we have developed and implemented an Eulerian-Lagrangian model for the transport, formation, break-up, deposition and re-entrainment of asphaltene agglomerates, as it occurs in the turbulent flows that are commonplace in wellbores and production pipelines. The complex structure of the agglomerates is explicitly taken into account; in this respect our model is the first of its kind. In principle, the model can also be used to study agglomeration and deposition phenomena in other systems, such as in atmospheric pollution transport or inside human veins or arteries.

Simulations for agglomeration and break-up in the *absence* of deposition and re-entrainment were carried out to investigate how the properties of the agglomerates change with the Reynolds number of the turbulent flow, the strength of the bonds inside the agglomerates, and the mechanism by which the agglomerates are broken. This was done for both channel- and pipe flows. Our results show that the properties of the agglomerates are rather insensitive to the mechanisms that cause their break-up as well as to the Reynolds number, provided the flow is turbulent. A noteworthy result is that the mean mass of the agglomerates scales exponentially with the strength of the internal bonds. The agglomerates have a very open and porous structure, and a fractal dimension of 1.8–2.3. The collision rate of the agglomerates is underpredicted by the

collision kernels that are typically used as closure relations in existing engineering models. Likewise, agglomerates typically do not break into two fragments of equal size, contrary to common assumptions made in the literature.

Further simulations were performed in which deposition and re-entrainment are *included* in the Eulerian-Lagrangian model. Three different regimes are found based on the strength of the adhesive forces between the dispersed phase and the walls of the flow domain. At small values of the adhesion strength, the deposit layer continuously moves over the wall. At intermediate adhesion strengths, the movement of the deposit layer becomes intermittent, which goes along with a strong tendency of deposited agglomerates to undergo further, mutual agglomeration. If the adhesion strength between the dispersed phase and the walls is large, stable deposit layers can be formed. In this regime, the strength of the internal bonds of the agglomerates becomes the limiting factor for the thickness of the deposit layer. The wall-normal velocity of the agglomerates during deposition, which is also used as a closure for engineering models, is underpredicted by empirical relations proposed in the literature.

The presence of the dispersed phase reduces the turbulence intensity. The associated reduction of the eddy viscosity outweighs the increase of the apparent viscosity that results from the presence of the dispersed phase. Therefore, at a fixed pressure drop an increase in the liquid flow rate occurs due to agglomeration and break-up of the dispersed phase if there is no deposition and re-entrainment. Conversely, the occurrence of deposition and re-entrainment increases the pressure gradient when the flow rate is fixed. The relative increase depends both on the internal strength of the agglomerates and on the strength of the particle-wall interaction.

Experimental data on the agglomeration and deposition of asphaltenes that have been obtained under well-defined flow conditions are reported only sporadically in the literature. Therefore, it is currently not possible to provide a thorough validation of the Eulerian-Lagrangian model. Instead, we have proposed alternative validation experiments that could be conducted in the future and we have also identified the type of modifications that can be made to the model to ensure that a proper validation will be more easily achievable.

Finally, we have extended an existing one-dimensional engineering model that can be applied on a field-relevant scale. This model was validated against literature data and field production measurements, and shows reasonably accurate predictions for both cases. Improvements of the closure relations that are used in the one-dimensional model have been derived from the Eulerian-Lagrangian simulation results. In future research, it will be necessary to find means to approximate the values of the empirical closure coefficients in engineering models *without* fitting the model predictions to measured data. After this additional step, the insights that have been obtained in this work can be used to achieve better predictions in models that can be applied on a field-relevant scale.

Samenvatting

Depositie van asfaltenen is een ernstig probleem dat kan optreden tijdens de productie van ruwe olie uit ondergrondse reservoirs. Asfaltenen zijn een deel van de ruwe olie zelf, dat zich, afhankelijk van omstandigheden zoals druk en temperatuur, afscheidt van de olie. Uiteindelijk kunnen ze afzettingen vormen aan de randen van het stromingsdomein. Aangezien hierdoor de drukverliezen in het productiesysteem toenemen en de olieproductie vermindert, leidt dit tot een aanzienlijk verlies van de opbrengsten van de bron.

Om de strategie waarmee asfalteendepositie in het veld wordt aangepakt te optimaliseren is het zeer wenselijk om te beschikken over praktisch toepasbare modellen die betrouwbaar kunnen voorspellen waar en wanneer depositie zal optreden. Zulke modellen kunnen alleen worden opgesteld als de fysische mechanismen die ten grondslag liggen aan de depositie goed begrepen zijn. Dit onderzoek richt zich op de hydrodynamica van asfalteenagglomeraten. De kinetiek van de vorming van deeltjes tijdens de faseafscheiding uit de ruwe olie en de chemische eigenschappen van de asfaltenen werden niet expliciet bestudeerd. Er is zeer weinig literatuur over de hydrodynamische aspecten beschikbaar, en dit werk is bedoeld om deze lacune op te vullen.

Hiertoe hebben we een Euleriaans-Lagrangiaans model voor het transport, de vorming, breking, depositie en het opnieuw meevoeren van asfalteenagglomeraten ontwikkeld en geïmplementeerd, zoals dat gebeurt in de turbulente stromingen die gewoonlijk optreden in de put en in productiepijpleidingen. De complexe structuur van de agglomeraten wordt expliciet in acht genomen; in dit opzicht is ons model het eerste in zijn soort. In principe kan het model ook worden gebruikt om agglomeratie en depositie in andere systemen te bestuderen, zoals tijdens het transport van atmosferische vervuiling of in menselijke (slag)aderen.

Simulaties waarin vorming en breking van agglomeraten optreedt in *afwezigheid* van depositie en meevoering zijn uitgevoerd om te onderzoeken hoe de eigenschappen van de agglomeraten veranderen als functie van het Reynoldsgetal van de turbulente stroming, de sterkte van de bindingen binnen de agglomeraten, en het mechanisme waardoor de agglomeraten worden gebroken. Dit is gedaan voor zowel kanaal- als pijpstromingen. Onze resultaten laten zien dat de eigenschappen van de agglomeraten grotendeels niet gevoelig zijn voor het breekmechanisme, en ook niet voor het Reynoldsgetal, zolang de stroming maar turbulent is. Een interessant resultaat is dat de gemiddelde massa van de agglomeraten exponentieel schaalt met de sterkte van de verbindingen in de agglomeraten. De agglomeraten hebben een zeer open en poreuze

structuur, en een fractale dimensie van 1.8–2.3. De botsingsfrequentie van de agglomeraten wordt onderschat door botsingskernels die gebruikt worden als sluitingsrelaties in bestaande praktisch toepasbare modellen. Eveneens vinden we dat agglomeraten doorgaans niet breken in twee even grote fragmenten, in tegenstelling tot aannames die over het algemeen gemaakt worden in de literatuur.

We hebben ook simulaties uitgevoerd waarin depositie en meevoering wél zijn meegenomen in het Euleriaanse-Lagrangiaanse model. Afhankelijk van de adhesiesterkte tussen de gedispergeerde fase en de randen van het stromingsdomein zijn er drie verschillende regimes te onderscheiden. Bij kleine waarden van de adhesiesterkte beweegt de depositielaag voortdurend over de wand. Bij middelgrote adhesiesterkte wordt de beweging van de depositielaag hortend en stotend, zodat er een sterke tendens naar verdere onderlinge botsingen tussen de afgezette agglomeraten bestaat. Als de adhesiesterkte tussen de gedispergeerde fase en de wand groot wordt, worden stabiele depositielagen gevormd. In dit regime wordt de sterkte van de interne verbindingen in de agglomeraten de beperkende factor voor de dikte van de depositielaag. De snelheidscomponent van de agglomeraten in de richting van de wand op het moment dat depositie plaatsvindt, die ook wordt gebruikt als sluitingsrelatie in praktisch toepasbare modellen, wordt onderschat door empirische modellen die in de literatuur zijn voorgesteld.

De aanwezigheid van de gedispergeerde fase vermindert de intensiteit van de turbulentie. De daarmee samengaande vermindering van de turbulente viscositeit overstemt de toename in de effectieve viscositeit die voortvloeit uit de aanwezigheid van de gedispergeerde fase zelf. Bij gelijkblijvende drukval treedt hierdoor een toename van het vloeistofdebiet op als er geen depositie en herinvoering plaatsvindt. Anderzijds veroorzaken de depositie en herinvoering een toename in de drukval bij een gelijkblijvend vloeistofdebiet. De relatieve toename hangt zowel af van de interne sterkte van de agglomeraten als van de sterkte van de adhesie tussen de deeltjes en de wand.

Experimentele data van agglomeratie en depositie van asfaltenen onder goed gedefinieerde stromingscondities zijn slechts sporadisch beschikbaar in de literatuur. Daarom is het op dit moment niet mogelijk tot een sluitende validatie van het Euleriaanse-Lagrangiaanse model te komen. Wel zijn er in plaats daarvan alternatieve validatie-experimenten voorgesteld die mogelijk in de toekomst uitgevoerd kunnen worden. Ook hebben we besproken welke aanpassingen er aan het model gemaakt kunnen worden om een goede validatie te vergemakkelijken.

Tot slot hebben we een bestaand ééndimensionaal model dat op de veldschaal kan worden toegepast verbeterd. Dit model is gevalideerd met zowel literatuur- als productiedata uit het veld, en we vonden dat het beide met redelijke nauwkeurigheid kan beschrijven. Op basis van de resultaten van de Euleriaanse-Lagrangiaanse simulaties zijn verbeteringen van de sluitingsrelaties voor ééndimensionale modellen afgeleid. In toekomstig onderzoek zal het noodzakelijk zijn om tot methoden te komen waarmee de waarden van de sluitingscoëfficiënten in zulke praktisch toepasbare modellen met redelijke nauwkeurigheid kunnen worden bepaald *zonder* de modelvoorspellingen aan gemeten data te fitten. Met deze extra stap kunnen de inzichten die met behulp van het Euleriaanse-Lagrangiaanse model zijn verkregen worden gebruikt om tot betere voorspellingen te komen in modellen die op een veld-relevante schaal kunnen worden toegepast.

Contents

Chapter 1

Introduction

The increasing awareness of the harmful environmental effects that are associated with the production of fossil energy stimulates the exploration and exploitation of renewable energy sources. The exhaustibility of natural resources also contributes to the motivation for this energy transition. The growth of the mondial population and the increasing welfare levels in developing countries make, however, that the human energy consumption is still increasing year by year. It is generally agreed upon that it will take at least several decades before the global energy demand can largely be covered by renewable energy. During this transition period, it therefore remains very important to produce conventional sources of energy as efficiently as possible.

At the time of writing this thesis, the majority of the global energy supply stems from the production of fossil fuels. Crude oil and natural gas are contained in subsurface reservoirs that may be located both on- or off-shore. Figure 1.1 shows a schematic representation of the typical components of the production system that is required to produce crude oil from an on-shore oil field. To avoid damage to the production system and to assure that operations can proceed in a safe manner, one of the most important aspects of the production of oil and gas is to ensure that stable operating conditions are achieved. This is known as *flow assurance*, and there are several aspects to this.

1.1 Flow assurance

The first aspect is that the production of oil and gas from a reservoir involves multiphase flows. Inside a gas reservoir, liquid water may be present that is co-produced by the gas, or a liquid phase may be formed due to condensation of water vapour or hydrocarbons from the gas when the pressure and temperature are decreasing when the gas is produced from the reservoir. As the reservoir pressure decreases over time, the gas velocity in the well tubing may become insufficient to produce the liquid from the reservoir to the surface, which ultimately results in a phenomenon called *liquid loading*. Liquids accumulate at the bottom of the well, thereby completely shutting in the gas in the reservoir and bringing the gas production to a halt.

For oil reservoirs, often some water is co-produced with the oil, whereas the lower pressure and temperature in the well tubing with respect to the reservoir gives rise to the formation of associated gas, caused by the evaporation of the lightest hydrocarbons in the oil. The resulting multiphase gas/liquid flow is relatively well understood, and commercially available simulation tools that solve for the velocity of both phases, the pressure and the temperature are used in the oil industry. PipeSim, from Schlumberger, and Prosper, from Petroleum Experts, are examples of such models to compute steady-state results, whereas Schlumberger's OLGA and Kongsberg's Ledaflow can obtain transient solutions for the flow inside the production string.

Unfortunately, the gas/liquid multiphase flow that occurs during the production of crude oil is not the only flow assurance aspect that needs to be considered during the design and operation of a well. Also, solids, like sand or small rock fragments, may be co-produced with the crude oil. Furthermore, certain fractions of the crude oil or of the other liquids that are produced from the reservoir may precipitate to form additional solids as the production is proceeding. Subsequently these might form deposits that restrict the flow domain. This can happen in any location that comes in contact with the oil: from inside the reservoir itself, to the wellbore, the production flowlines, or in other production equipment and processing facilities, that are used for instance at the downstream platform or refinery. As the thickness of the deposit layer increases, the pressure loss in the system will increase. This reduces the oil production rate, which can pose a significant loss of revenue.

The typical solids that are responsible for the formation of deposit layers during
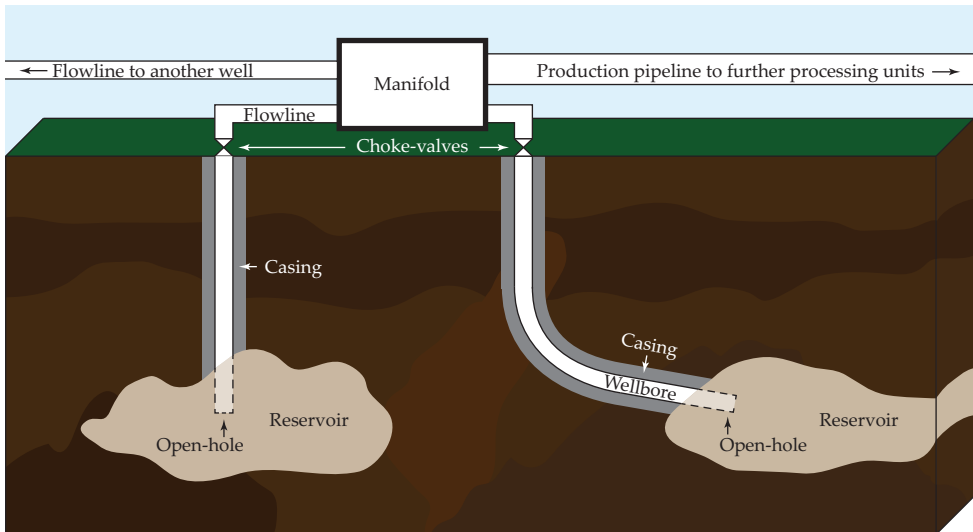
Figure 1.1: Schematic representation of the typical components of the production systems that are installed in an oil field, showing one vertical and one deviated production well.

the production of crude oil are *hydrates*, *wax*, *scale* and *asphaltenes*. In the current state of the art in the oil industry, the results of the multiphase flow solvers that were described earlier are used as input to dedicated models that are used to predict when these solids are formed and how their deposit layers are growing. The present knowledge of the aforementioned substances is such, however, that whereas the formation of hydrates is relatively well understood and thus well predictable, highly empirical models are used to predict what is happening to the poorly comprehended asphaltenes. Obtaining a better understanding of asphaltene deposition is the topic of this research.

1.2 A general introduction to asphaltenes

The term *asphaltenes* was first introduced in 1837 by the French chemist Jean-Baptiste Boussingault. Asphaltenes are the most polar and aromatic fraction of the heavy components of crude oil. In terms of flow assurance, asphaltenes may be problematic already before forming deposit layers. The presence of asphaltenes significantly increases the viscosity of crude oil, thus decreasing the oil production rate at a given reservoir pressure. Experiments have shown that the viscosity of crude oils may reduce by over 90% if the asphaltenes contained in the oil are removed (Luo and Gu, 2007).

Definition

A common method for characterising the composition of crude oils uses solubility criteria to separate the crude oil into four fractions: *Saturates*, *Aromatics*, *Resins* and *Asphaltenes* (see, e.g., Lundanes and Greibrokk (1994)). Saturates are non-polar molecules and consist of normal- and iso-alkanes (C_nH_{2n+2}) and cyclo-alkanes, while aromatics consist of double-bonded hydrocarbon ring structures similar to benzene. Resins and asphaltenes form a continuum of molecules with increasing molecular weight, aromaticity and hetero-atom (viz. non-carbon and non-hydrogen) content. The complementary fraction to asphaltenes in crude oil is often denoted short-hand as *maltenes*. The most commonly accepted definition of the asphaltene fraction is that asphaltenes are soluble in toluene (C_7H_8), and insoluble in normal heptane (C_7H_{16}). Some other definitions also exist, however, for instance by using other normal alkanes as the insoluble delimiter of the asphaltene fraction (e.g. pentane, C_5H_{12}) (Speight et al., 1984).

Crude oil consists of mixtures of very large numbers of chemical components. As a consequence of the solubility-based definition of asphaltenes, the asphaltene fraction of a crude oil can therefore not be explicitly described by a tractable number of chemical compounds. Asphaltenes are chemically ill-defined, and, by definition, polydisperse. Nevertheless, it is generally agreed upon that most asphaltene molecules share some common features. They have a backbone that is formed by one or more poly-aromatic hydrocarbon cores, that have peripheral hydrocarbon side-chains and hetero-atoms attached to them; common types of the non-hydrogen and non-carbon

atoms that are found in asphaltenes are nitrogen, sulfur and oxygen, as well as several metallic atoms, such as vanadium, nickel, and iron (Hammami and Ratulowski, 2007).

Stability of asphaltenes in crude oil

While asphaltenes are present in any crude oil, it is not the concentration that determines the stability of the crude-oil/asphaltene dispersion. Crude oils with high asphaltene content are not per se more prone to suffering from asphaltene deposition then crude oils that only contain seemingly insignificant concentrations of asphaltene. The overall oil composition, the pressure, and, to lesser extent, also the temperature are much more important factors for determining asphaltene stability. It is generally accepted that during primary oil production, the pressure is the most critical parameter (Wang and Civan, 2005).

Large changes in pressure are encountered when the oil is taken from the reservoir (where the pressure typically can be as high as a few hundred bars), and is brought to atmospheric conditions. When the pressure is depleted, the light-end components of the crude oil expand at a higher rate than the heavier components, thereby changing the volumetric composition of the oil. Since asphaltenes are, by definition, insoluble in the light components of the crude, pressure depletion thus decreases the stability of the asphaltenes in the oil. This decrease in stability proceeds up to the point where the pressure reaches the *bubble point*. At the bubble point, the light end components of the crude oil start to evaporate. Further decrease of the pressure shifts the composition of the crude oil towards increasing fractions of asphaltene-compatible components. Therefore, the asphaltene stability in general is lowest at or near the bubble point.

When an oil field ages, the reservoir pressure decreases as the reservoir gets partially depleted of oil. As a result, after some years of production, the pressure is insufficient to overcome the pressure drop and the hydrostatic pressure of the oil production system, and the production will come to a halt. Typically, a very significant percentage of the crude oil still remains in the reservoir at this point. If further production from the oil field is to occur, the pressure in the reservoir has to be artificially boosted to restart the oil production, by, for example, injecting water or gas into the reservoir using injection wells. Alternatively, the viscosity of the crude oil inside the reservoir can be reduced, for instance by injecting steam, surfactants, or carbon dioxide. These strategies are known to significantly increase the propensity of asphaltene-oil dispersion destabilisation, however, thereby increasing the risks of suffering from asphaltene deposition: asphaltene-related problems therefore most commonly are encountered towards the end of the life of an oil field.

How the industry currently deals with asphaltene deposition

It is of great interest to the oil industry to be able to predict, preferably before starting the exploitation of a new oil field, or before drilling a new oil wells, to what extent asphaltene deposition will pose a problem during the lifetime of the field. On the one hand, knowing whether asphaltene deposition is expected to occur can influence

the outcome of the assessment whether producing oil from a particular field is at all economically feasible. On the other hand, early anticipation of the occurrence of asphaltene deposition will allow for preventive measures, such as the installation of injection points for chemical asphaltene deposition inhibitors, to be included early on in the design of the well.

Unfortunately, even when asphaltene deposition is properly anticipated and an injection system for deposition inhibitors is included in the well design, injecting deposition inhibitors is not a no-brain solution to prevent the deposition of asphaltenes. On the one hand, deposition inhibitors are proprietary chemicals that are developed by service companies, which makes them expensive. Moreover, the inhibitor chemicals have to be tailored to the crude oil that is produced by the well. It has been reported for instance by Vargas et al. (2010) that inhibitors that are perfectly functional to prevent deposition of asphaltenes in one crude oil, can actually promote additional deposition in other crude oils.

If asphaltene deposition is actually encountered during oil production, several measures can be taken to remove the deposits. The best technique depends on the location where the asphaltene deposits are formed. For deposits that are formed inside the production pipeline downstream of the well-head choke, mechanical scraping of the deposit layer using a device called a *pig* is the most commonly applied remediation technique. For removing deposits that are formed inside the porous rock of the reservoir, or inside the wellbore or production tubing, where mechanical access is not possible, chemicals are used to remove the deposition layer. This can either be done by applying a *solvent job*, in which an asphaltene solvent is injected, or by an *acid job*, in which acid is injected into the reservoir to actually dissolve part of the porous rock, thereby opening up new flow paths.

The intervention costs associated with removing asphaltene deposits are considerable, starting at approximately five hundred thousand dollars for on-shore wells, to three million dollars or more for deep-water off-shore wells that require cleaning inside the wellbore (Creek, 2005). These figures are notwithstanding the value of the deferred production associated with the clean-up operation, which can easily exceed a million dollars per day. Since all of the remedial techniques sketched above require a shut-in of the well, one ought to maximise the time interval between interventions. Also, it is highly beneficial to be able to predict the deposition of asphaltenes beforehand, as this allows for a planning to be made in which the optimal timing of the clean-up operations is determined, considering the availability of the equipment that is needed to clean a well. This poses another motivation for arriving at predictive models for asphaltene deposition at a production scale.

1.3   From phase separation to deposit formation

Considering the current state of the art as described in the literature, the most striking observation that can be made is that it has been frequently overlooked that asphaltene phase separation is a necessary, though *insufficient*, condition for the formation of asphaltene deposits. It is well known in other fields of science and engineering that

different stages can be distinguished in the evolution that a dispersed phase goes through after its formation; this distinction, however, is typically not made in the asphaltene research community.

Starting at the point where a mixture becomes super-saturated, initiating the formation of a dispersed phase, at least six stages can be distinguished in the evolution of the dispersed phase. These stages are: nucleation, growth, agglomeration, break-up, deposition and re-entrainment. Depending on their source and chemical properties, and on the prevailing conditions in their environment, dispersed asphaltenes may either have a solid character (particles), or be liquid-like (droplets) (Pan and Firoozabadi, 2000); for convenience and short-hand notation, we will refer to either of these states as particles from here on.

During nucleation, new dispersed particles are formed at locations where no dispersed phase was present earlier. These particles can grow as a result of further condensation onto their surface. When two or more particles collide, they may merge or form a bond between them, resulting in the formation of agglomerates. Non-uniformity of the forces that are acting on an agglomerate can result in the break-up of this agglomerate. When agglomerates reach to the boundaries of the flow domain, finally, the interaction between the walls and the dispersed phase will determine whether deposition and/or re-entrainment will occur.

It is frequently reported that asphaltene agglomerates have a fractal character, with a very open structure. Figure 1.2 shows microscopic images of the evolution of asphaltenes after phase separation in the absence of flow, that have been obtained by

10 minutes	1 hour
20 minutes	3 hours
35 minutes	30 hours
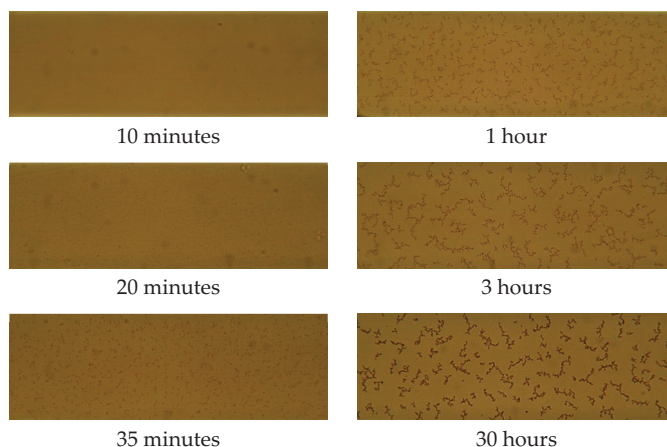
Figure 1.2: Formation fractal asphaltene agglomerates after phase separation. The smallest dimension of the micro-channels is 200 micrometres. Adapted with permission from (J. S. Buckley, Asphaltene deposition, *Energy & Fuels*, 26:4086–4090). Copyright (2012) American Chemical Society.

Buckley (2012). In this figure, the formation of such a fractal structure can be clearly monitored.

On the one hand, the relative rate at which the agglomeration, break-up, deposition and re-entrainment processes occur are strongly dependent on the interaction forces that occur between the individual asphaltene particles that emerge from the phase separation process, and the interaction force between the asphaltenes and the walls. On the other hand, the flow of the medium from which the asphaltenes are separating is also very important for the evolution of the dispersed asphaltene phase. Along with the thermal motion for the smallest dispersed particles, the flow provides an important contribution to the transport of the dispersed phase. The relative strength of the forces that are induced onto the dispersed phase by the flow when compared to the aforementioned interaction forces determines at what rate the agglomeration, break-up, deposition and re-entrainment proceed. Obtaining a better understanding of how the flow affects the formation of asphaltene agglomerates and deposits is therefore of key importance to better understand asphaltene deposition in general.

1.4   Objectives and approach

In this work, we consider the formation of asphaltene deposits inside a wellbore or in a production pipeline. It is our main objective to improve the level of understanding of the influence of the turbulent flow on the deposition process, including the re-entrainment of asphaltenes and the formation and break-up of asphaltene agglomerates that precedes the deposition. By using a dedicated physical-numerical model, we will significantly improve the accuracy with which these processes are resolved when compared to the models that have been proposed earlier in the literature for asphaltene deposition under turbulent flow conditions. Because the flow inside the reservoir has a completely different character than the flow in the wellbore and in the production pipelines, we will not consider the deposition of asphaltenes inside the reservoir in this work.

Our approach is as follows:

- We develop an Eulerian-Lagrangian model, in which we take into account the formation, break-up, deposition and re-entrainment of agglomerates, by tracking of the motion of individual primary particles that are dispersed in a turbulent flow. This model explicitly includes the structure of the agglomerates. Break-up of the agglomerates is taken into account using a comprehensive analysis of the stresses that are induced inside the agglomerates as a result of the distribution of hydrodynamic forces. This model is based on an existing, particle-laden flow solver: the Direct Eulerian-Lagrangian Flow Turbulence (DELFT) code.

- Numerical simulations of both channel and pipe flows are conducted with this model, to study:

- – How the Reynolds number of the flow, the break-up mechanism, and the strength of the bonds inside the agglomerates influence the properties of the agglomerates formed by the competition of collisions and break-up, both for flows in channel and pipe geometries.

  – How the flow rate and intensity of the turbulence are affected by the presence of this dispersed phase.

  – How the rate of deposition and re-entrainment, as well as the characteristics of the deposit layers that are formed at the boundaries of the flow domain, depend on the adhesion strength between the dispersed phase and the walls.

  – How the pressure drop in the domain increases under the influence of the deposition and re-entrainment.

- An existing one-dimensional engineering model for asphaltene deposition in gas/liquid multiphase flows is improved and extended by:

  – Integrating the agglomeration and break-up routines with routines describing deposition and re-entrainment.

  – Taking into account the decrease in diameter of the flow domain that results from the deposition in the multiphase flow solver.

- The insights that are obtained using the detailed Eulerian-Lagrangian model are used to formulate improved sub-models and closure-relations for the one-dimensional engineering model.

The Reynolds number of the turbulent flow and the strength of the bonds between the primary particles are varied in the simulations that are conducted using the Eulerian-Lagrangian model. Such variations will also be found between different wellbores and pipelines as well as over time, and between asphaltenes that originate from different crude oils.

Constructing the Eulerian-Lagrangian model requires a functional picture of how the actual asphaltene phase separation proceeds. Finding an accurate description of this process, which includes the conditions under which the phase separation is initiated, is outside the scope of this work.

In absence of well-established models for the phase separation process (see Chapter 2), we will assume simple relations to describe the amount of asphaltenes that separate from the crude oil under given conditions. In accordance with the assumptions that were made by previous researchers that proposed models for the evolution of asphaltenes after phase separation (Maqbool et al., 2009, 2011[†],[‡]), we will assume that immediately after the phase separation, spherical primary particles are formed that can stick to each other upon collision. Each of these primary particles represent a very large number of asphaltene molecules. Figure 1.3 shows a sketch that summarises our vision of the evolution of asphaltenes under the influence of flow.
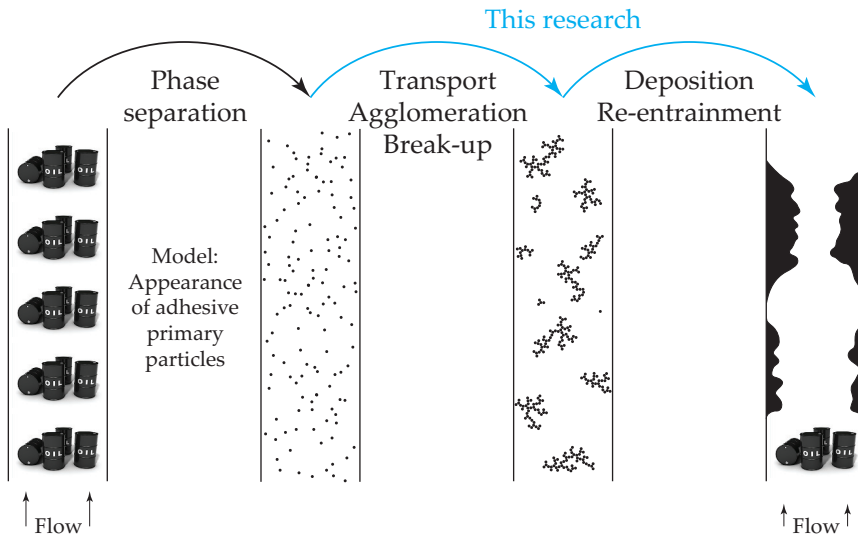
Figure 1.3: Sketch of the assumed asphaltene evolution under the influence of flow. Directly after separating from the liquid phase, we assume that the asphaltene forms spherical primary particles (which each consist of a very large number of asphaltene molecules) that stick to each other upon collision. Due to transport by the flow, collisions occur and agglomerates are formed and broken. These agglomerates can subsequently deposit at the walls of the flow domain, and possibly re-entrain, thereby reducing the cross-sectional area of the wellbore or production pipeline that is open to the flow, which reduces the oil production rate.

1.5 Outline

In Chapter 2, we give a concise overview of the existing experiments and models that have been used to describe the different aspects of the asphaltene deposit formation. Chapters 3 and 4 contain descriptions of the Eulerian-Lagrangian model and the one-dimensional gas/liquid multiphase engineering model, respectively.

In Chapters 5 (channel geometry) and 6 (pipe geometry), we study the formation and break-up of agglomerates using the Eulerian-Lagrangian model, in the absence of deposition and re-entrainment. We find that the properties of the agglomerates in both flow geometries are similar, and that the differences between them can be related to differences in the turbulent flow structure. The collision rate of the agglomerates is underpredicted by existing collision kernels that are used as closure relations for one-dimensional engineering models. Furthermore, we find that agglomerates preferentially break-up in asymmetric fragments. At a prescribed pressure drop, the presence of the agglomerates is found to increase the flow rate in both geometries, as a result of the decreasing turbulence intensity and the associated reduction of the eddy viscosity, which is larger than the increase in viscosity caused by the presence of

the agglomerates itself.

In Chapter 7, the deposition and re-entrainment of agglomerates are considered, along with their influence on the pressure drop over the domain. As expected, the pressure drop is found to increase at constant flow rates when deposition occurs, and the magnitude of this increase is found to depend both on the internal strength of the agglomerates, as well as on the strength by which the agglomerates adhere to the boundaries of the flow domain.

In Chapter 8, we will give a critical review on the ability of the proposed Eulerian-Lagrangian model to accurately describe the evolution of actual asphaltenes after phase separation. Also, the verification and validation of both models will be discussed, and we will explain to what extent the insights that have been obtained using the Eulerian-Lagrangian model can be used for the improvement of the closure relations in one-dimensional engineering models. That chapter also contains some predictions for optimal oil production strategies as obtained using the one-dimensional drift-flux model that was considered in this work.

In Chapter 9, conclusions will be drawn and possibilities for future applications and improvements of the Eulerian-Lagrangian will be discussed. We will also give our vision on how asphaltene-related research should proceed in the future.

Chapter 2

Overview of existing experiments and models

In this chapter, a concise overview of relevant experimental data on the different stages of the formation of asphaltene deposits that have been reported in the literature are given. Also, we outline what type of models have been proposed to predict the conditions under which asphaltene phase separation occurs, the evolution stages asphaltenes go through after the phase separation, and the asphaltene deposition and re-entrainment. Furthermore, models for agglomeration, break-up, deposition and re-entrainment that have been proposed in other fields of science and engineering are discussed as far as they are relevant for the purpose of the present thesis.

2.1 Stability of asphaltenes in crude oil

Although consensus has been reached in the literature on the most dominant mechanisms causing asphaltene phase separation during the production of crude oil, the microscopic mechanisms that provide the stability and drive the phase separation of asphaltenes are not incontestably established. The more recent literature tends to agree on the view that even in a well-dispersed state, asphaltenes form supra-molecular structures that are often called *nano-aggregates*, with dimensions of a few nanometres (Porte et al., 2003; Mullins, 2011). Some literature indicates that resins play a vital role in the stabilisation of asphaltenes, by shielding these aggregates from approaching each other and further growing in size, while other researchers provide experimental results that suggest that the nano-aggregates are stabilised by the peripheral side-chains of the asphaltene molecules themselves wrapping around the aggregate.

From a pragmatic perspective, the exact mechanism that provides asphaltene stability is irrelevant to our work. Asphaltenes separate from a crude oil when the crude oil and the asphaltenes become, what we will call, *incompatible*. Thermodynamically it then becomes favourable for the asphaltenes to form a separate phase, and from this point on, the formation of such a phase will be initiated. The ability of a particular

solvent phase (a crude oil, or a chemical mixture that is used as a model for crude oil in the laboratory) to keeping asphaltenes in a stable solution will be referred to as the *solvent quality*.

Another aspect of asphaltene phase separation that historically has been heavily debated in the literature is the question whether the phase separation is reversible or not. Modern literature indicates that the process is indeed at least partially reversible, although the re-dissolution kinetics may be much slower than those of the phase separation. This finding is supported by results that were obtained by Hammami et al. (2000) and Joshi et al. (2001) for pressure depletion and re-pressurisation of live crude oil samples. Rassamdana et al. (1996) showed that asphaltenes that are separated from a crude oil by adding light alkanes to it can be re-dissolved by subsequently stripping the alkanes, or adding more crude oil to a sample. In this work, re-dissolution of asphaltenes will not be taken into account.

Experimental techniques to assess asphaltene phase stability

The standard test for studying the asphaltene phase stability is the titration test, in which an asphaltene anti-solvent, such as heptane, is progressively added to an asphaltene containing oil sample. Effectively, the addition of the anti-solvent deteriorates the solvent quality of the oil sample with respect to the asphaltenes, and therefore, asphaltenes will start to separate from the sample when sufficient anti-solvent has been added. The required relative amount of anti-solvent to provoke asphaltene precipitation is a measure of the stability of the asphaltenes in the studied (model)[*] oil sample. In titration experiments, typically only the *onset* of asphaltene phase separation is determined. The onset marks the minimum solvent quality that is required to keep the asphaltenes stably dispersed. It is also possible to measure the total asphaltene content of a crude oil using this method. This is done by continuing the titration until an excess amount of anti-solvent has been added to the sample, and by subsequently separating the precipitated asphaltenes from the sample with for instance a sieve or filter paper.

An important pitfall in titration experiments that are used to determine the onset of asphaltene phase separation is that the phase separation itself is a dynamic process. It will take some time before the first asphaltenes that have been destabilised form particles that are large enough to be detected. If this time scale is longer than the time interval over which anti-solvent is added during the titration experiment, the stability of the asphaltenes will be overestimated; this is because at the apparent onset point, more anti-solvent is present in the system than at the point of the actual start of the phase separation. Maqbool and co-authors (Maqbool et al., 2009, 2011[†],[‡]) studied this effect in detail. They observed that asphaltene particles larger than 500 nanometres were eventually formed also for heptane concentrations lower than the apparent onset that is found in short-term titration experiments, albeit after much longer time scales than those that are usually applied in asphaltene titration

---

[*]An overview of the different types of crude oil samples will be given in Section 2.5.

experiments. Hammami et al. (2000) found similar results in pressure depletion experiments on live crude oil samples: when the pressure was lowered step-wise, the onset pressure was determined to be tens of bars higher than when the pressure was lowered continuously, which indicates that true onset pressures can only be determined if the fluid is given sufficient time to equilibrate.

Cimino et al. (1995[‡]) conducted a systematic set of titration experiments in recombined model oils with different solvent/anti-solvent mixtures, and found that the onset of asphaltene phase separation only depends on the quality of the solvating medium and not on the asphaltene concentration. Buckley (1996) related the onset of phase separation to the mixture refractive index, and found that the onset occurs at a characteristic refractive index per anti-solvent used, irrespective of the dilution of the samples by non-polar asphaltene solvents.

Asphaltene phase stability models

The complexity of both the asphaltene and crude oil compositions calls for simplifications to be made when modelling the asphaltene phase stability. Due to the lack of a proper understanding of how the separation of asphaltenes proceeds at a molecular level, a wide variety of models to predict asphaltene phase stability have been proposed in the literature. A common approach is to describe the asphaltene fraction using either one, or multiple, pseudo-components (imaginary chemical species, with representative properties), or by describing its properties using continuous distribution functions. Similar approaches are used to represent the maltenes.

The most simple approach that can be used is to construct purely empirical, black-box models, that do not have an underlying physicochemical theory. This approach was for instance adopted by Rassamdana et al. (1996, 1999), who constructed scaling relations based on the results of titration experiments for a light stock-tank oil using heptane to decane.

Since the asphaltene nano-aggregates have typical dimensions of a few nanometres, their stable state in a crude oil or a model oil mixture can be described as a colloidal dispersion. Therefore, many of the models for asphaltene phase separation that have been proposed in the literature build upon knowledge previously obtained for colloidal dispersion stability. Under this paradigm, asphaltene colloids are either assumed to be lyophilic (e.g., Hirschberg et al. (1984), Kawanaka et al. (1991), Cimino et al. (1995[†]), Browarzik et al. (1999), Correra and Donaggio (2000) and Akbarzadeh et al. (2005)), or lyophobic (e.g. Leontaritis and Mansoori (1987), Victorov and Firoozabadi (1996) and Pan and Firoozabadi (2000)). In the first case, asphaltenes are assumed to be able to disperse themselves inside their surrounding medium, whereas in the latter case, external stabilisation mechanisms (e.g. adsorption of resin molecules) are required to maintain the stability of the dispersion. Park and Mansoori (1988) and Porte et al. (2003) proposed two-stage models, in which it is assumed that asphaltene phase separation is a process with both lyophobic and lyophilic aspects.

Based on the model by Hirschberg et al. (1984), de Boer et al. (1995) proposed a simple screening method for evaluating the risk of asphaltene phase separation occurring

during the production of crude oil, which is known in the industry as the «de Boer plot». It is an evaluation based on the difference in reservoir and bubble-point pressures, the density of the reservoir fluid and the asphaltene saturation at reservoir conditions. Generally, the de Boer plot tends to be too pessimistic, however, and therefore, it is best only to use it for identifying non-problematic oils (Hammami and Ratulowski, 2007).

A more advanced framework for describing the phase stability of complex mixtures is the Statistical Associating Fluid Theory. Within this framework, the basic building block of a molecule (a *monomer*) interacts with other monomers through repulsive and attractive forces. A single monomer can represent one atom, a functional group, or even a complete molecule. Due to their increased complexity, numerical methods are required for solving the phase equilibrium in these methods. Vargas et al. (2009) developed a method to determine the parameters needed to characterise all maltene fractions of crude oil within this framework. Ting (2003) and Buenrostro-Gonzalez et al. (2004) demonstrate that models that are based on Statistical Associating Fluid Theory can predict asphaltene phase stability over a range of normal alkane titrators after being calibrated just for heptane.

There is still much work to be done before asphaltene phase separation models with general applicability can be constructed (and we may question whether this is at all feasible), but contributing to the development of such a model falls outside the scope of this thesis. Instead, we focus on what happens to the asphaltenes in their journey from phase separation to the formation of actual deposits.

2.2   Asphaltene evolution after phase separation

The external forces, such as gravity, the forces that are induced by the carrier-phase flow, the inter-particle forces and the forces that act between the particles and the walls of the flow domain, determine the evolution of the asphaltenes after phase separation.

The experimental results by Maqbool and co-authors (Maqbool et al., 2009, 2011[†],[‡]) and by Khoshandam and Alamdari (2010) show that by using proper instrumentation, the size evolution of destabilised asphaltene particles can be monitored starting right when they are formed at the nanometre scale. If the mixture is not being agitated, it can take considerable time for these nanometre-size particles to grow further; Khoshandam and Alamdari (2010), for instance, show that it can take more than twenty minutes for all particles to grow larger than two-hundred nanometres. Asphaltene agglomerates with larger length-scales, which typically are formed after several hours without sample agitation, can form extended fractal structures. This for instance can be seen in the microscopic images shown in Figure 1.2 of Chapter 1, which show the evolution of phase-separated asphaltenes in the absence of flow, as obtained by Buckley (2012). Estimates of the mass-radius fractal dimensions of asphaltenes agglomerates range from 1.3 (Rahmani et al., 2005[†]) to 2.0 (Rahmani et al., 2005[‡]), and may be expected to vary strongly depending on the source of the asphaltenes.

Asphaltene evolution under flow conditions

Since in this thesis we focus on the influence of flow on the asphaltene evolution, experiments that are conducted under well-defined flow conditions are of special interest to our work. Such experiments have been reported in the literature much more scarcely than experiments in which samples are either kept stationary, or are being agitated using an ill-defined flow field (for instance induced by a magnetic stirring bar), but the work of some research groups stand out in this respect. In particular, Rahmani and co-workers (Rahmani et al., 2003, 2004) studied the agglomeration and break-up of asphaltenes in toluene-heptane model oil mixtures using a Taylor-Couette flow-cell that is operated under laminar flow conditions. Solaimany-Nazar and Rahimi (2008, 2009) performed Taylor-Couette flow-cell experiments similar to those by Rahmani and co-workers. Both groups of authors find that under these conditions, the asphaltene agglomerates grow to average diameters on the $\mathcal{O}(100)$ micrometres. In Chapter 8, we will further discuss these experiments for the purpose of validating the Eulerian-Lagrangian model that was developed and implemented in this work.

Models for asphaltene agglomeration and break-up

The evolution of dispersed asphaltenes after phase separation typically has not been studied on the level of individual agglomerates before, as is done in this work. Instead, multi-fluid (Eulerian-Eulerian) methods have frequently been used in the literature to describe this evolution. In an Eulerian-Eulerian method, the particles that make up the dispersed phase are not tracked individually; instead the dispersed phase is treated as quasi-continuous and only global properties, like the spatial variation of the concentration, the velocity and the particle size distribution are solved for. Almost all researchers that studied asphaltene agglomeration and break-up before used discretised population balance equations to describe the evolution of asphaltenes after phase separation. The use of population balance equations to describe the agglomeration and break-up of a dispersed phase is a well-established technique, that is also frequently applied in other fields of science and engineering.

Population Balance Equations. The basic form of the population balance equation was first proposed by von Smoluchowski in 1917. In essence, the equation describes how the number density of particles (or agglomerates) of a particular size evolves over time. Considering a closed control volume without in and outflow, and neglecting deposition and re-entrainment, this can be expressed as:

$$\frac{\partial \mathcal{N}(r,t)}{\partial t} = \text{Birth} - \text{Death} \tag{2.1}$$

where $\mathcal{N}(r,t)$ represents the number of agglomerates per unit volume with a characteristic dimension r at time t. Nucleation leads to the birth of primary particles, whereas inter-particle collisions, that result in the formation of agglomerates, cause both the birth of a larger agglomerate, and the death of two or more smaller ones.

15

Similarly, agglomerate break-up causes the birth of small agglomerates, at the expense of the death of a large agglomerate. Growth of agglomerates as a result of super-saturation, finally, also causes the number of small agglomerates to decrease, and the number of large agglomerates to increase. In mathematical terms, these processes can be described by:

$$\frac{\partial \mathcal{N}(r,t)}{\partial t} + \mathcal{G}_R \frac{\partial \mathcal{N}(r,t)}{\partial r} =$$
$$\frac{1}{2}\int_0^r \varsigma_u^{r-u}\Gamma_u^{r-u}\mathcal{N}(u,t)\mathcal{N}(r-u,t)\,du - \int_0^\infty \varsigma_u^r\Gamma_u^r\mathcal{N}(u,t)\mathcal{N}(r,t)\,du \qquad (2.2)$$
$$+ \int_r^\infty \beta_u\mathcal{D}_u\mathcal{B}_{u\to r}\mathcal{N}(u,t)\,du - \int_0^r \beta_r\mathcal{D}_r\mathcal{B}_{r\to u}\mathcal{N}(r,t)\,du + \mathcal{M}(r,t)$$

where $\mathcal{G}_r$ represents the growth rate of agglomerates with dimension r, Γ_u^{r-u} represents the collision kernel between agglomerates of size r and u, $\mathcal{D}_r$ represents the break-up kernel of agglomerates with dimension r, $\mathcal{B}_{r\to u}$ represents the yield of agglomerates of size u that results from the break-up of agglomerates with a dimension equal to r, and $\mathcal{M}(r,t)$ represents the appearance of agglomerates of size r due to nucleation. The values of ς and β represent collision and break-up efficiencies, respectively. The collision efficiency accounts for the fact that not all collisions between agglomerates will lead to the agglomerates bonding to each other.

For any system of practical interest, obtaining an analytical solution to equation (2.2) is not feasible. Instead, several techniques have been proposed in the literature to obtain approximate solutions. The most straight-forward method involves discretising the particle size distribution, leading to the following formulation of the population balance equation:

$$\frac{\partial \mathcal{N}_k}{\partial t} + \mathcal{G}_k \frac{\partial \mathcal{N}_k}{\partial r} = \frac{1}{2}\sum_{i=1}^{k-1}\varsigma_i^{k-i}\Gamma_i^{k-i}\mathcal{N}_i\mathcal{N}_{k-i} - \sum_{i=1}^{K}\varsigma_k^i\Gamma_k^i\mathcal{N}_k\mathcal{N}_i +$$
$$\sum_{i=k+1}^{K}\beta_i\mathcal{D}_i\mathcal{B}_{i\to k}\mathcal{N}_i - \sum_{i=1}^{k-1}\beta_k\mathcal{D}_k\mathcal{B}_{k\to i}\mathcal{N}_k + \mathcal{M}_k \qquad (2.3)$$

where $\mathcal{N}_k$ represents the number of agglomerates per unit volume that belong to the discretised population class k and K is the index that describes the largest particle class considered. Alternative techniques for solving equation (2.2) are based on Monte-Carlo techniques (Liffman, 1992), or involve solving for the moments of the distribution function of $\mathcal{N}(r,t)$. The latter technique has not been applied before in models describing the asphaltene evolution, however. Obtaining expressions for the collision and break-up rates constitutes the closure problem for solving equation (2.3).

Models describing the initial evolution stages. Maqbool et al. (2011[†]) and Khoshandam and Alamdari (2010) use a population balance equation to model the initial stage of the evolution of asphaltenes after phase separation. They consider asphaltene

nano-aggregates to appear as the primary particles during the phase-separation process, and monitor the subsequent growth of the agglomerates until they reach the size of a few micrometres. Maqbool et al. (2011[†]) assume that the phase separation occurs at a much shorter time scale than the formation of the agglomerates, such that all separated asphaltenes appear as primary particles at the start of the simulations. By contrast, Khoshandam and Alamdari (2010) also take the growth of previously separated agglomerates as a result of a prolonged period of super-saturation into account in their model.

Eskin and co-authors (Eskin et al., 2011, 2012) proposed a model for the evolution of asphaltenes after the phase separation, in which a population balance model is used to account for the agglomeration and break-up. Deposition and re-entrainment are taken into account using empirical correlations for the mean velocity and velocity fluctuations in turbulent flows. Like in the model by Maqbool and co-authors, the collision efficiency required to fit the model predictions of this model to experimental data is very small $\left(\mathcal{O}\left(10^{-5}\right)\right)$.

In this thesis, we will also apply a population balance equation to model the evolution of asphaltene agglomerates after phase separation. This population balance model is used in combination with a one-dimensional multiphase drift-flux flow solver for the liquid- and gas-phase motion, which is described in Chapter 4. In that chapter, we will give more details on the closure relations that are required for the model given in equation (2.3). The dispersed-phase solvers that are used in the model are based on the models by Eskin and co-authors.

Models describing the evolution at larger length-scales. Rahmani and co-authors (Rahmani et al., 2003, 2004) and Solaimany-Nazar and co-authors (Solaimany-Nazar and Rahimi, 2008, 2009; Rahimi and Nazar, 2010) use population balance equations to model the evolution of asphaltene agglomerates in a Taylor-Couette flow device. Faraji and Solaimany-Nazar (2010) used a Monte-Carlo approach to solve a similar set of equations. In these models, primary particles are assumed to have a diameter of several tens of micrometres, which is equal to the size of the smallest particles that could be detected in experiments that were conducted by the same authors. Although the models by Rahmani and co-authors and Solaimany-Nazar and co-authors can represent the temporal evolution of the average size of the agglomerates as observed in the experiments fairly well, a poor resemblance is found for the instantaneous particle size distributions that are reported by Rahmani et al. (2004).

2.3 Agglomeration/break-up in other fields of science and engineering

Even though the Eulerian-Eulerian models discussed above are very efficient and thus very useful for studying deposition and re-entrainment in full-scale systems, a proper understanding of the underlying physics of these processes is required for defining proper closure relations in such models. Therefore, it is also very instructive to study agglomeration, break-up, deposition and re-entrainment on the level of individual

particles and agglomerates (this is the so-called Lagrangian approach). To this end, in this thesis, we have developed and implemented an Eulerian-Lagrangian model, describing the agglomeration, break-up, deposition and re-entrainment of asphaltene particles, under influence of a turbulent flow, thereby resolving the actual shape and motion of individual agglomerates. To put this model in perspective, we will first give here an overview of similar models that have been previously described in the literature. It is important to note, however, that in the Eulerian-Lagrangian methods that have been proposed in the literature, agglomerates are typically represented by equivalent spherical entities, thereby not accounting for their internal structure.

Models that do take into account the full spatial structure of agglomerates throughout the agglomerate life-cycles are reported more rarely in the literature, but a few examples do exist. Richardson (1995) studied the formation of particle agglomerates in an astrophysical context, considering three possible outcomes for a collision event: agglomeration («coagulation», in the terminology of Richardson), restitution and fragmentation. When coagulating, the colliding primary particles are joined by a rigid bond, such that the formation of complete agglomerate structures can be monitored over time. In a later work, Perrine et al. (2011) applied an extended version of this model, which considers two mechanisms of agglomerate break-up: particles are either liberated from pre-formed agglomerates by the event of a high speed impact of another agglomerate, or when the relative accelerations of primary particles induce stresses that surpass the strength of the bonds that keep the particles attached to the agglomerate.

Mäkinen (2005) proposed a model for the agglomeration of icy particles in astrophysical systems. In this model, particle collisions are considered to result in agglomeration if the relative kinetic energy of the colliding particles is fully dissipated within the time that the individual particles are in contact with each other. Fragmentation of agglomerates is considered using an analysis of induced internal stresses in all inter-particle bonds. Bonds are broken if either of the internal stress components exceeds the maximum stress the bond can withstand; the strength of the bonds is modelled to be proportional to the area of overlap between the particles.

Chen and Doi (1999) studied the dissociation of aggregating colloids in strongly-sheared flows, at low Reynolds numbers. Their model considers that sticky particles can roll over each other without slipping at their contact point; also in this model, bonds between particles are considered to break when the induced stresses exceed the strength of those bonds.

Ernst et al. (2013), finally, used Lattice-Boltzmann simulations to fully resolve the flow primary particles that are settling in a quiescent fluid, as a first step towards the development of a numerical model that describes the transport and formation of agglomerates in a turbulent flow. Due to the very fine grid resolution that is required to resolve the flow around the particles, only a very limited number of primary particles can be used in such simulations: Ernst et al. used only 50 particles, and find that the largest agglomerate that is formed consists of 36 particles.

It will still take many years before the computational power is large enough to conduct such fully-resolved simulations for a large number of primary particles, and at large Reynolds numbers for the carrier-phase flow. In the Eulerian-Lagrangian model that is described in Chapter 3, we therefore do not resolve the flow around the agglomerates, but rather use the so-called point particle approach, in which it is assumed that the interactions between the particles and the flow can be described by considering only flow properties measured at the particle centre. The basic building blocks of the agglomeration and break-up modules of the Eulerian-Lagrangian model that is proposed in this work are similar to the models proposed by Richardson (1995), Chen and Doi (1999) and Mäkinen (2005). A major difference, however, is that we consider a turbulent flow (rather than gravitation or laminar flow) as the driving force for agglomeration and break-up.

2.4 Asphaltene deposition

Experimental data on asphaltene deposition

Although experimental data on asphaltene deposition are relatively scarce in the literature, deposition measurements have been reported in geometries with scales that vary over multiple orders of magnitude. At the smallest scales, Wang et al. (2008) and Boek and co-workers (Boek et al., 2008, 2010) conducted experiments in metal and glass capillaries, respectively, to mimic deposition in porous reservoir rock, whereas Papadimitriou et al. (2007) studied asphaltene deposition in actual porous rock samples.

Jamialahmadi et al. (2009) used thermal resistivity measurements to determine the deposition rate of asphaltenes from pentane-diluted crude oil samples in a turbulent flow-loop. This measurement technique relies on changes in the thermal resistivity across the pipe wall that occur when asphaltene deposit layers are formed. In this way, the spatial evolution of the deposit layer at a fixed location downstream of a heated wall segment was derived from measurements of the wall temperature. Bulk Reynolds numbers in the range from approximately 6000 to 30 000 were considered and it was found that the rate of asphaltene deposition increases linearly both with the flow rate inside the loop, as well as with the asphaltene concentration. The deposition rate was also found to depend on the surface temperature of the pipe, with a two-fold increase being found when the temperature is increased from 111°C to 125°C. The experiments lasted for 400 hours and the typical deposit layer thicknesses that were found after the experiments range from 50 to 200 micrometres.

An important aspect to keep in mind, however, is that pumps are required to circulate the crude oil in a flow-loop. These pumps are prone to act as a strong artificial source of agglomerate break-up, thereby reducing the accuracy of flow-loop experiments for studying asphaltene agglomeration and/or deposition.

At a length scale that is intermediate to the capillary and the flow-loop, Schlumberger developed a commercially available high-pressure Taylor-Couette flow-cell, which can be run both in batch and flow-through modes. One of the benefits of such a setup

is that there are no artificial sources of agglomerate break-up introduced, as the flow driven by the moving walls of the device. Results of some asphaltene deposition experiments conducted in the Schlumberger Taylor-Couette flow-cell are reported in the open literature.

Akbarzadeh and co-workers (Akbarzadeh et al., 2009, 2012), used the device to conduct both batch and flow-through experiments, with five different oil samples. The results of these experiments show that the amount of deposition

- decreases when the pressure is kept slightly below the onset pressure, instead of slightly above the bubble point
- increases when the residence time of the fluid is increased (viz. when the flow-through rate is lowered)
- decreases when the wall shear stress increases, at higher rotational rates (although this effect is not found for all crude oil samples)
- reaches a plateau in the batch experiments if the run-time of the experiments is increased.

Eskin et al. (2011) provide additional insight in the experiments performed using the Taylor-Couette flow-cell by Akbarzadeh and co-workers. They conducted experiments where the liquid collected from the outlet of a flow-through experiment was re-introduced in the experimental setup after being reconditioned at reservoir conditions for five days, allowing for the separated asphaltenes to be re-dissolved in the liquid. The deposit layer formed in the first experiment was disposed; yet the amount of deposition formed in the second experiment was slightly higher than in the first experiment. Even though the deposition reached a plateau in the first experiment, the liquid present in the experimental setup thus was not compositionally depleted of asphaltene molecules that are able to form a deposit layer. To explain this, the authors posed the hypothesis that during the course of the first experiment, asphaltene agglomerates have been formed that are too large to be deposited in the Taylor-Couette flow-cell (as these would be removed by the shear stress at the wall). This explanation gives rise to the concept of a critical agglomerate size, where only agglomerates that are smaller than this critical size are able to deposit at the walls.

By assuming that agglomerates are well dispersed inside the turbulent core flow in the Couette flow experiments, Eskin et al. (2011) showed that the deposition rate in the Taylor-Couette flow-cell is representative for the deposition rate that occurs for flow in a pipeline, provided that the wall-shear stress in both geometries is matched. At matched values of the wall-shear stress, however, the turbulent energy dissipation rate is significantly higher in the Taylor-Couette flow-cell than in the pipe. The collision and break-up frequencies, which affect the particle size distributions, are therefore not necessarily similar in both geometries.

In a work that contains perhaps one of the most valuable experimental data sets reported in the literature on asphaltene deposition, Haskett and Tartera (1965) studied

asphaltene deposition *in situ* in a number of wells in the Hassi-Messaoud field in Algeria. These authors measured the profile of deposits formed in the well tubing using gauge rings that were descended into the well, during systematic studies that lasted over several months. Their most important conclusion is that asphaltene deposition mainly occurs in the single-phase flow region of the well (viz. below the location where the bubble point occurs). Only rarely, deposits were observed in the two-phase flow region. The deposit layers are found to extend over a significant region in the streamwise direction, typically between 300 to 600 metres, although the region with the strongest diameter reduction is usually found to extend only over roughly one-tenth to one-fifth of the entire deposition range. The data that are reported by Haskett and Tartera will be used for the validation of the one-dimensional drift-flux model in Chapter 8.

Alkafeef et al. (2005) published asphaltene deposit layer profiles for one well in an oil field in Kuwait, albeit at a lower level of detail than Haskett and Tartera (1965). They found that the maximum decrease in the open cross-section of the wellbore is about 45%, and that the location of the deposit layer moves towards a deeper location in the well if the location of the phase separation onset and the bubble point pressure move down in the well due to a decrease in the reservoir pressure over time.

Eulerian-Eulerian models for asphaltene deposition

Most of the models that so far have been proposed for modelling asphaltene deposition are based on empirical correlations for the deposition of spherical particles from laminar or turbulent flows. One example of such a model was proposed by Escobedo and Mansoori (2010); these authors were early adopters of modelling the deposition of asphaltenes, as their first contributions date back to 1995. In their model the deposition rate of spherical particles from a turbulent flow is evaluated as a function of the particle diameter using Fick's law of diffusion, corrected for the particle inertia. Another simple deposition model based on empirical relations for mass transport in turbulent flows was constructed by Jamialahmadi et al. (2009); the parameters of this model were fitted to experimental data on the asphaltene deposit layer thickness obtained by thermal conductance measurements in the flow loop discussed earlier.

Ramirez-Jaramillo et al. (2006) proposed a model in which molecular diffusion is assumed to be the driving force for the deposition of asphaltene particles in oil production pipelines, balanced by re-entrainment of particles due to the shear stress exerted on the deposit layer by the fluid phase. Vargas et al. (2010) used a pseudo first-order reaction mechanism to account for the formation of deposits out of asphaltenes that are transported to the walls of the flow domain by a diffusion-driven process, while considering convection to dominate the asphaltene transport in the streamwise direction.

As an extension to the population balance model that describes the formation and break-up of asphaltene agglomerates, Eskin et al. (2011) take the contributions of Brownian motion and turbulent velocity fluctuations to the asphaltene deposition into account. The removal of deposited particles from the wall due to the wall shear

stress is modelled assuming a yield stress for the deposit layer. The free parameters of the model are the inter-particle collision efficiency, the particle-wall collision efficiency and the critical agglomerate size (viz. the size of the largest agglomerates that can be part of the deposit layer), complemented with a re-entrainment coefficient and a re-entrainment yield stress exponent. By assuming that the particles are transported by a plug-flow regime inside the pipe, the authors show that the deposition model that is tuned to the Taylor-Couette flow experiments predicts similar deposit layer thicknesses as reported in the literature by Alkafeef et al. (2005).

Eskin et al. (2012) extended the pipe deposition model derived by Eskin et al. (2011), by considering incremental time steps in the formation of the deposit layer, allowing to take into account the influence of the deposition rate on the flow. Also, the flowline deposition model was coupled to a model for the flow in the wellbore. This way, the increase in the bottomhole pressure that occurs when the flow rate decreases as a result of the deposition is captured and thereby, the shift of the locations where the onset and bubble point pressures occur in the depth of the well is also reproduced by the model.

Eulerian-Lagrangian models for asphaltene deposition

The work of Boek and co-authors (Boek et al., 2008, 2010) is, to our knowledge, the only prior example in which an Eulerian-Lagrangian method is used to consider the asphaltene-flow interactions from first principles. These authors used two-dimensional Stochastic Rotation Dynamics for the continuous fluid-phase, in combination with coarse-grained Molecular Dynamics for the dispersed-phase, to simulate the deposition of asphaltenes inside square capillary tubes. In these simulations, the van der Waals force is assumed to be the dominant interaction both between asphaltene particles, and between the asphaltene particles and the walls of the capillary. The primary particle size is set at three micrometres, and the interaction range between the particles is increased with respect to the physical interaction range to make simulations feasible for realistic time scales.

Firstly, assuming an infinitely deep potential well for the asphaltene-wall interaction, Boek et al. (2008) find that the flow rate decreases when the particle-particle interaction potential increases in magnitude (viz. when the asphaltene particles become more sticky). For small well-depths, a monolayer deposit is formed, whereas for increasingly strong interaction potentials, the capillary becomes transiently clogged, or even permanently blocked. In a second set of simulations, it is assumed that the particle-wall interaction is equally strong as the mutual particle interaction, which corresponds to a situation where asphaltene particles deposit onto a layer of asphaltenes that has been formed on the wall before. With this configuration, the simulations are capable of reproducing the experimental results for different flow rates, with the same value of the interaction potential.

Boek et al. (2010) extended the parameter space that was studied using the method by Boek et al. (2008), considering a larger variation of flow rates. They find that the

total amount of deposition increases if the flow rate increases, whereas the reduction in flow systematically increases as the interaction potentials get stronger.

The detailed simulations that have been conducted by Boek and co-authors, are, due to their small length scale, not representative for the length scales that are relevant for the asphaltene deposition in the wellbore and production pipeline. This is where our Eulerian-Lagrangian modelling approach that is described in Chapter 3 comes into play.

2.5 Why is knowledge on asphaltenes still so obscure?

As an epilogue to this chapter, we ask ourselves why, despite active research efforts over at least the past five decades, there is still relatively little known about asphaltenes. The general lack of knowledge is illustrated quite well by the fact that, at least until ten years ago, the range of estimated molar masses of asphaltene molecules reported in the literature varied over several orders of magnitude. Only recently, consensus on the molar mass has been reached. It is now generally agreed upon that the true molar mass of asphaltene molecules is of the $\mathcal{O}(1000)$ grams per mole (see, e.g., Mullins (2011)). It is likely that older, less sensitive measuring techniques measured the molar mass of the nano-aggregates that are formed even when asphaltenes were still dispersed in their environment, rather than of individual molecules. This can explain the very large apparent molecular masses (of up to 10^9 grams/mole) reported in earlier literature.

In our opinion, the main causes for the lack of proper understanding of asphaltenes are threefold. Firstly, the solubility-criterion definition of asphaltenes hinders acquiring a proper understanding. Secondly, the way crude oil samples are obtained and laboratory experiments on asphaltenes are conducted do not assure that the laboratory data are sufficiently representative of what actually is happening to asphaltenes in the field. Finally, there is a lack of knowledge exchange between the different stakeholders of the asphaltene deposition problem.

Asphaltene definition. Due to the inherently imprecise definition of asphaltenes, and the large variation of crude oil compositions between different oil fields, or even between different wells in one field, it can be expected that asphaltenes from different sources have significantly different properties. This expectation is supported by the fact that little consensus has been reached in the literature on even some of the most basic properties of asphaltene molecules, like the molecular mass illustrated above, the global molecular architecture, as well as the mechanism by which asphaltene phase separation proceeds. A very likely explanation for these apparent inconsistencies is that asphaltenes that originate from different crude oils simply *are* different. Heavy debates in the literature, for instance on whether asphaltene molecules consist of single poly-aromatic hydrocarbon cores with peripheral side chains (the «island» structure (Groenzig and Mullins, 2000)), or multiple inter-linked poly-aromatic cores (the «archipelago structure» (Strausz et al., 2008; Liao et al., 2009)), do not provide a constructive contribution to proceed in acquiring better knowledge on the asphaltene deposit formation process.

Obtaining crude oil samples. The complex nature of crude oil, and the extreme conditions that are typically prevailing inside oil reservoirs, make that getting a proper experimental characterisation of asphaltenes under reservoir conditions is a formidable task. To obtain the best possible representation of what happens to the asphaltenes during actual crude oil production, experiments ideally should be conducted on so-called *live* crude oil samples; these are samples that are obtained, and kept, at a pressure and temperature similar to the conditions inside the reservoir, to be lowered only during the experiment itself. This ensures that the composition of the oil does not change before the start of the experiment, and this thus will allow to examining the behaviour of the crude oil as if it still was inside the reservoir.

Due to the very high costs involved in collecting live crude oil samples, as well as in conducting experiments under conditions of high temperature, and, more importantly, high pressure, experiments on asphaltenes are not typically conducted using live oil samples. Frequently, *dead* crude oil samples («stock-tank oil») are used instead. Contrary to live crude oil, dead crude oil has been stored at a temperature and pressure lower than inside the reservoir (usually ambient temperature and pressure). Unfortunately, the composition of the crude oil changes if the pressure and temperature are altered: the volumetric fractions of the light and heavy components shift with respect to each other, and light fractions might even evaporate and be lost from the sample. Furthermore, asphaltene phase separation and deposition of asphaltenes might already have occurred upstream of the sample collection point if dead crude oil samples are used that have not been acquired down-hole, resulting in an incomplete picture of the range of asphaltenes that is present inside the reservoir. Indeed, results reproduced by Hammami and Ratulowski (2007) have shown that un-careful sample acquisition can change the pressure at which asphaltenes start to separate from a crude oil by as much as 150 bar.

Even though conducting experiments on dead crude oil samples is far easier than on samples of live crude oil, such experiments still by no means are straightforward: one of the major drawbacks is that crude oil usually is completely opaque, thus preventing any optical techniques to be used in the experiments. Most frequently, crude oil samples are therefore substituted by so-called *model oil* mixtures, in which asphaltenes, that have been separated from either live or dead crude oil samples, are dissolved in some asphaltene solvent, such as toluene, to which subsequently an asphaltene anti-solvent, such as heptane, is added to simulate the deterioration of the crude oil solvent quality as induced by changes in pressure and temperature during normal oil production. One has to keep in mind that the results obtained this way cannot be expected to be one-to-one transferable to the behaviour of the asphaltenes in the original crude oil under actual reservoir conditions; in our opinion, the literature has been too optimistic on this most of the time.

Lack of transparency and knowledge exchange. The final contribution to the lacking general knowledge on asphaltenes is given by the fact that there is no or little knowledge sharing amongst many of the stakeholders that are involved in research on asphaltenes. It is an open secret that at least some oil producing companies have a

lot more knowledge on asphaltenes than they share with the outside world, albeit that this knowledge is of a highly empirical rather than of fundamental nature. On the other hand, a mist of secrecy is surrounding the preventive measures that are currently applied in the field to prevent asphaltene deposition. Oilfield service companies for instance are highly protective regarding the composition of the asphaltene deposition inhibitors, whereas the composition of other fluids that are injected for flow assurance purposes (such as corrosion inhibitors) is more openly shared. This approach has to change before large steps in remediating production losses due to asphaltene issues can be taken.

2.6   Summary

Despite the vast body of literature that exists on the molecular and thermodynamic characterisation of asphaltenes, the microscopic mechanisms that provide stability and drive the phase separation of asphaltenes are still disputed in the literature. For this reason, a variety of models for the asphaltene stability have been proposed, often based on opposing assumptions. For the purpose of our work, the exact mechanism that provides stability to asphaltenes is not important, however. The phase separation proceeds when the asphaltenes and its surrounding medium become incompatible. Similar to the assumptions made by other researchers, we assume that upon separation from the crude oil, asphaltenes form spherical adhesive particles that each consist of many molecules. In our Eulerian-Lagrangian model, these particles are subsequently transported and they form agglomerates that can break, deposit and re-entrain, under the influence of a turbulent flow.

The evolution of asphaltenes after phase separation has been studied by several authors in the literature. The experimental results by Rahmani and co-authors and Solaimany-Nazar and Rahimi are obtained under well-defined flow conditions, and will be further considered for the purpose of model validation in Chapter 8. Akbarzadeh and co-authors studied the deposition of asphaltenes under the influence of pressure depletion, also under well-defined flow conditions, but unfortunately, they did not report any measurements on the properties of the deposit layer or rates of deposition and re-entrainment.

Eulerian-Eulerian population balance models are typically used in the literature to model the evolution of asphaltenes after the phase separation, in absence or presence of empirical relations for the deposition and re-entrainment. The same approach will be used in Chapter 4 of this thesis, in which we improve and extend a previous model implementation made by TNO on the basis of the work of Eskin et al. (2011). This model will be validated against literature data on asphaltene deposit profiles which have been measured in an Algerian oilfield by Haskett and Tartera (1965), as well as to field production data that were made available to us but not have been published in the literature.

In other fields of science and engineering, more advanced numerical models for agglomeration and break-up have been proposed, albeit not under the influence of flow, or at a level of detail that is too large to be currently applicable to study the

properties of a large number of agglomerates. The only previous model in which asphaltene-flow interactions have been investigated at a detailed level is the work of Boek and co-authors. These authors considered the problem on a capillary length scale, which is, however, not representative for the length-scales that are relevant for the asphaltene deposition in the wellbore and production pipeline. This gap will be bridged by the Eulerian-Lagrangian model approach adopted in our work, as will be described in Chapter 3. This model has similarities to the models by Richardson (1995), Chen and Doi (1999) and Mäkinen (2005). In contrast to these authors, we consider a turbulent flow as the driving force for agglomeration and break-up.

It is our strong belief that the general lack of knowledge on asphaltenes is the result of poor research strategies that have been adopted in the past. Far too little attention has been paid to the fact that due to the imprecise definition of asphaltenes, there is no point in trying to obtain one universal description of asphaltenes that is valid for different crude oils. Furthermore, differences between commonly applied experimental procedures with respect to the real mechanisms that drive asphaltene phase separation in the field have been underestimated, and much too frequently no clear distinction between the phase separation and the actual deposit formation processes is made. This has led to overlooking the influence of flow on the cascade of processes that follow after the phase separation, but precede the deposit formation. Finally, the secrecy-shrouded attitude of oil producers and oilfield service companies towards sharing knowledge in the literature certainly has hindered progress in this field.

Chapter 3

Development and implementation of an Eulerian-Lagrangian asphaltene flow model

In this chapter, we discuss the development and implementation of the Eulerian-Lagrangian model for the formation, break-up, deposition and re-entrainment of asphaltene agglomerates. This model was implemented as an extension of an existing, particle-laden flow code, called Direct Eulerian-Lagrangian Flow Turbulence (DELFT). A single-phase flow is considered as the carrier phase for the dispersed particles. To keep the complexity of the carrier-phase solver tractable, the multiphase flow of liquid and gas, which often occurs in actual oil production systems (namely at pressures that are below the bubble point), are not presently considered.

In essence, the solver of the dispersed-phase only interacts with the continuous-phase solver by virtue of velocity and force-field interpolations, making the implementation very portable. Therefore it requires limited effort to adapt the model for use with different flow solvers. This feature allows us to convert the model from its initial implementation in the channel geometry to a pipe geometry with relative ease, as will be demonstrated in Section 3.11.

3.1 Model basis: DELFT

The DELFT code was developed by a series of faculty members and previous PhD candidates and MSc students at Delft University of Technology, over the past two decades. The most notable developers of the single-phase flow solver were Eggels (1994), Pourquié (1994) and Boersma (1997), who constructed versions of the code in cylindrical coordinates, and van Haarlem (2000), who implemented the original version of the channel-geometry code.

In both geometries, the basis of the DELFT code is a Large-Eddy Simulation (LES) finite-volume turbulent flow solver. It uses a two-step predictor-corrector method to

solve the incompressible Navier-Stokes equations on a staggered computational grid. In the LES mode, the Smagorinsky model, together with van Driest damping of the eddy viscosity near the walls, is applied to account for the sub-grid turbulence scales. When the sub-grid models are disabled, the code can also be used for Direct Numerical Simulations (DNS). Figure 3.1 shows a representation of the naming conventions for the grid directions that are used in the channel and pipe geometries, respectively.

In Cartesian coordinates and using a finite-volume discretisation, the incompressible Navier-Stokes equations can be written as:

$$\rho_f \left(\frac{\mathbf{U}_f^{n+1} - \mathbf{U}_f^n}{\Delta t} \right) + \rho_f \mathbf{A}\left(\mathbf{U}_f\right) = -\nabla P^{n+1} + \mu_f \mathbf{D}\left(\mathbf{U}_f\right) + \mathcal{F}^n \tag{3.1}$$

$$\nabla \cdot \mathbf{U}_f^{n+1} = 0 \tag{3.2}$$

where ρ_f and μ_f represent the fluid density and viscosity, respectively, $\mathbf{A}$ represents the discretised advection operator, and $\mathbf{D}$ the discretised diffusion operator. In the actual implementation, a central differencing scheme is used for all spatial interpolations required for computing the advection and diffusion terms. $\mathcal{F}^n$ represents the external forces acting on the fluid.

The fluid velocity $\mathbf{U}_f$ at the new time step $n+1$ is solved using a two-step procedure: first, the velocity field is predicted using a constant pressure gradient in the streamwise direction, which is the driving force of the flow, whereas this velocity field is corrected by applying the continuity condition, viz.:

$$\rho_f \left(\frac{\mathbf{U}_f^* - \mathbf{U}_f^n}{\Delta t} \right) + \rho_f \mathbf{A}\left(\mathbf{U}_f\right) = -\nabla \overline{P} + \mu_f \mathbf{D}\left(\mathbf{U}_f\right) + \mathcal{F}^n \tag{3.3}$$

$$\rho_f \frac{\mathbf{U}_f^{n+1} - \mathbf{U}_f^*}{\Delta t} = -\nabla \mathcal{P}^{n+1} \tag{3.4}$$
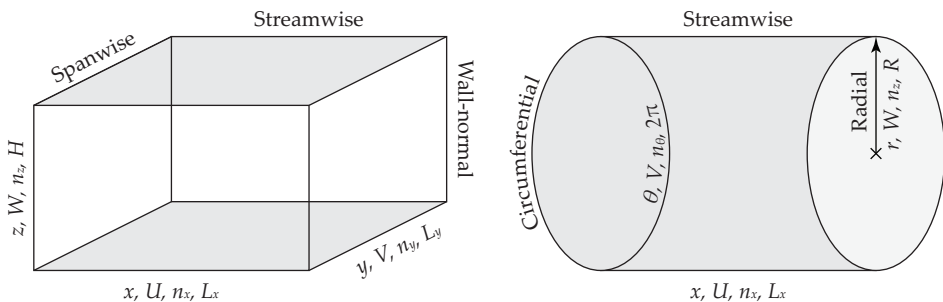
Figure 3.1: Naming conventions for the grid directions that are used in the channel and pipe geometries, complemented with the associated coordinate, the velocity component, the number of grid nodes, and the overall dimension.

where the total pressure P is given by $\overline{P} + \mathcal{P}$. The pressure correction $\mathcal{P}$ is found by applying the continuity condition (3.2) to expression (3.4), to arrive at:

$$\nabla \cdot \nabla \mathcal{P}^{n+1} = \frac{\rho_f}{\Delta t} \nabla \cdot \mathbf{U}_f^* \qquad (3.5)$$

which is solved using an algorithm based on Fast Fourier Transforms in the streamwise and spanwise directions in the channel (the streamwise and circumferential directions in the pipe), combined with Gauss-Jordan elimination in the wall-normal direction, in which the grid-spacing is non-uniform. Expanded into components at the left-hand-side, equation (3.5) reads:

$$\frac{\partial^2 \mathcal{P}^{n+1}}{\partial x^2} + \frac{\partial^2 \mathcal{P}^{n+1}}{\partial y^2} + \frac{\partial^2 \mathcal{P}^{n+1}}{\partial z^2} = \frac{\rho_f}{\Delta t} \nabla \cdot \mathbf{U}_f^* \qquad (3.6)$$

where x, y and z denote the streamwise, spanwise and wall-normal directions, respectively, as indicated in Figure 3.1. The right-hand-side of equation (3.6) can readily be computed from the predicted velocity field. After applying a forward FFT transform in the x and y directions, the latter expression can be reduced to:

$$\left(\lambda_x + \lambda_y + \frac{\partial^2}{\partial z^2} \right) \widehat{\mathcal{P}}^{n+1} = \frac{\rho_f}{\Delta t} \nabla \cdot \widehat{\mathbf{U}}_f^* \qquad (3.7)$$

where λ_x and λ_y are the eigenvalues of the FFT transforms in the stream- and spanwise directions, respectively, and $\widehat{\mathcal{P}}^{n+1}$ and $\nabla \cdot \widehat{\mathbf{U}}_f^*$ denote the (x,y)–Fourier transforms of $\mathcal{P}^{n+1}$ and $\nabla \cdot \mathbf{U}_f^*$. Equation (3.7) is then solved by a straight-forward matrix elimination in the partial Fourier space, after which the physical correction velocity field $\mathcal{P}^{n+1}$ is obtained using backward FFTs in the stream- and spanwise directions.

Non-dimensionalisation. The actual implementation of the continuous-phase solver used in the DELFT code has been non-dimensionalised using a characteristic length scale H (equal to either the full channel height, or the pipe diameter), the (average) pressure-gradient velocity u_∇ (defined in equation (3.12)) and the fluid density and viscosity. This non-dimensionalisation yields the so-called *outer units*, or star-units, which are defined as:

$$x^* = \frac{x}{H} \qquad \mathbf{U}^* = \frac{\mathbf{U}}{u_\nabla} \qquad t^* = \frac{t u_\nabla}{H} \qquad (3.8)$$

The actual implementation of the predictor and corrector equations is therefore given by:

$$\frac{\mathbf{U}_f^* - \mathbf{U}_f^n}{\Delta t} + \mathbf{A}\left(\mathbf{U}_f\right) = -\nabla \overline{P}^{n+1} + \frac{1}{Re_\nabla} \mathbf{D}\left(\mathbf{U}_f\right) + \mathcal{F}^n \qquad (3.9)$$

$$\frac{\mathbf{U}_f^{n+1} - \mathbf{U}_f^*}{\Delta t} = -\nabla \mathcal{P}^{n+1} \qquad (3.10)$$

where we have omitted the usual *-unit notation denoting the non-dimensionalisation to avoid confusion with the star denoting the predicted velocity field. Throughout this thesis, we will also use non-dimensional star-units to describe the results of the Eulerian-Lagrangian model unless noted otherwise. Most of the time, the * will be omitted for short-hand notation.

From equation (3.9) it is clear that a single-phase flow can be fully described by the Reynolds number. In outer units, the relevant Reynolds number is the pressure-gradient Reynolds number Re_∇, which is defined by:

$$Re_\nabla = \frac{\rho_f u_\nabla H}{\mu_f} \tag{3.11}$$

The (average) pressure-gradient velocity u_∇ is defined as:

$$u_\nabla = \sqrt{-\frac{1}{\mathbb{G}} \frac{\partial \overline{P}}{\partial x} \frac{H}{\rho_f}} \tag{3.12}$$

where $\mathbb{G}$ is equal to 2 in the channel and 4 in the pipe; $\partial \overline{P}/\partial x$ is the pressure gradient that is the driving force of the flow. The non-dimensional mean fluid velocity $\bar{U}_f$ (in outer-units) relates the pressure-gradient Reynolds number to the bulk Reynolds number:

$$Re_{\text{bulk}} = Re_\nabla \bar{U}_f \tag{3.13}$$

Wall-units. Another commonly used non-dimensionalisation involves the parameters that determine the flow close to a wall. Although we will use these wall- (or plus-) units only sporadically in this work, we give the definition here for later reference:

$$x^+ = \frac{x u_\nabla \rho_f}{\mu_f} \qquad \mathbf{U}^+ = \frac{\mathbf{U}}{u_\nabla} (= \mathbf{U}^*) \qquad t^+ = \frac{t u_\nabla^2 \rho_f}{\mu_f} \tag{3.14}$$

Channel geometry. The channel-geometry version of DELFT uses a second-order Adams-Bashfort time integration scheme. The maximum admissible non-dimensional time step for the continuous-phase solver is determined using a modified Courant-Friedrichs-Lewy (CFL) criterion, given by:

$$\Delta t = \min \left[\frac{\mathbb{C}}{\left| \frac{U_f}{dx} \right| + \left| \frac{V_f}{dy} \right| + \left| \frac{W_f}{dz} \right| + \frac{1}{Re_\nabla} \left(\frac{1}{dx^2} + \frac{1}{dy^2} + \frac{1}{dz^2} \right)} \right] \tag{3.15}$$

where U_f, V_f and W_f denote the fluid-velocity components in the x, y and z directions, respectively, (see Figure 3.1) and the minimum denotes a spatial minimum over all grid-cells in the computational domain. C represents the Courant number, that was kept at 0.25 in all channel-geometry simulations described in this thesis.

Pipe flow. In the DELFT code for the cylindrical geometry, explicit time integration is used for the integration of those terms of the Navier-Stokes equations that do

not involve derivatives in the circumferential direction. For the terms that contain circumferential derivatives, a first-order implicit time integration scheme is used to prevent the occurrence of severe time step constraints resulting from the very small linear dimensions of the grid-cells in this direction near the centre of the pipe. The maximum admissible time step also in this case is given by a modified CFL criterion, viz.:

$$\Delta t = \min \left[\frac{\mathbb{C}}{\left| \frac{U_f}{dx} \right| + \left| \frac{W_f}{dr} \right| + \frac{1}{Re_\nabla} \left(\frac{4}{dx^2} + \frac{4}{dr^2} \right)} \right] \tag{3.16}$$

Like for the channel geometry, we used a fixed Courant number of 0.25 in the pipe geometry throughout this work.

3.2 Modifications made to DELFT fluid-phase solvers

Although the main focus of the model development conducted in this work is on the solver for the dispersed phase, we have also introduced some modifications to the fluid phase solvers of the DELFT codes. For future reference, we will discuss these modifications briefly in this section.

Code modernisation. Both versions of the DELFT code historically have been implemented in Fortran. We re-structured the channel code, such that it now takes advantage of the new features that have been introduced in recent versions of this programming language. All subroutines, functions and global variables, are now contained in modules, thereby benefiting from implicit interfacing, which increases the chance that programming errors are detected by the compiler. The implementation of the pipe geometry solver was converted from FORTRAN 77 to Fortran 90, and re-factored such that the structure of the channel and pipe codes are now similar. This allowed us to incorporate both geometries into a single executable. To our best knowledge, this is the first effort to bring the DELFT solvers for both geometries together in one package, in which the actual geometry to be used can be selected at runtime.

Replacement of FFT library. In the original DELFT codes, the VFFT library by Sweet et al. (1990) was used to compute the FFTs needed for solving equation (3.7). Our experience, however, is that this FFT library does not deliver correct results for all arbitrary numbers of grid-points. For certain choices of n_x and n_y, velocity fields corrected using VFFT-based pressure correction fail to meet the zero-divergence criterion, resulting in non-physical results and ultimately compromising the numerical stability of the simulations. To remediate this issue, we have chosen to implement the FFTW library (Frigo and Johnson, 2005) for use in the corrector-step. According to benchmark results shown by these authors, FFTW is one of the fastest FFT libraries available today, and, it is available free of charge. Although for optimum performance, the number of grid-nodes can best be selected according to some specific guidelines (as it is the case in any FFT implementation), our experience shows that this library performs reliably for any number of grid-points. It thus is a «fool-proof» solution.

Two-way coupling between fluid and dispersed phases. Like Portela and Oliemans (2003), who used the DELFT code with two-way coupling for spherical, colliding particles, we model the force exerted by the dispersed phase on the continuous fluid phase by using Newton's third law, summing the contributions of all particles that are within one control volume for the fluid phase solver:

$$\mathcal{F}^n_{(x,y,z)} = -\sum_p \mathbf{F}_p \tag{3.17}$$

where $\mathbf{F}_p$ represents the force that the fluid exerts on the particle, as explained in Section 3.4, and the sum runs over all primary particles that have their centre located inside the fluid control volume of the particular velocity component. For particles that that have their centre located outside the actual fluid computational domain (within the context of our deposition model, some of the primary particles can, theoretically, be located inside the wall), the forces on the fluid phase are exerted in those control volumes that are closest to the particle, inside the flow domain.

Time integration in the pipe geometry. The explicit time integration scheme that was used in the original DELFT code for the pipe geometry is the leapfrog scheme. A known artefact of this time integration scheme in modelling non-linear fluid motion is the so-called «time-splitting», which exhibits itself as decoupling between subsequent velocity-field snapshots, resulting in temporal oscillations of the velocity field. A common way of controlling this phenomenon, that was also applied in the original version of the cylindrical pipe geometry DELFT code, is the use of a temporal Asselin filter, in which subsequent time steps are slightly intermixed to prevent de-coupling between them. This technique, however, reduces the truncation error of the leapfrog scheme from second to first order (Durran, 1991).

In the context of our model, we found that the intensity of the time-splitting is increased when two-way coupling between the dispersed phase and the continuous phase is considered, thereby posing another incentive to replace the leapfrog integration scheme. As a substitute, we implemented the second-order Adams-Bashfort time integration, that was also used for the channel geometry, for all those terms that are explicitly integrated in time in the pipe geometry. Using the resulting integration scheme, in which the time integration of the circumferential derivatives is still treated implicitly, no further issues related to time splitting were encountered.

In-/out-flow conditions in streamwise direction. Since we are interested in simulating the deposition of asphaltenes at the walls of the flow domain, and also want to study the influence that the formation of such a deposit layer has on the flow of the continuous phase, it is desirable to step away from the periodic boundary conditions in the streamwise direction that historically have been used in the DELFT code. More specifically, we have implemented in-/out-flow boundary conditions in our model. The inflow conditions are, at each time step, given by the instantaneous velocity profile of a fixed cross-section of a simultaneously running simulation with periodic boundary conditions. At the downstream boundary of the main domain, we use a uniform pressure boundary condition to model the fluid outlet. The latter condition

corresponds to a constant streamwise gradient boundary condition for the velocity fields.

The difficulty that now arises is that the FFT that was used to arrive at equation (3.7) is valid only for periodic boundary conditions in the streamwise and spanwise directions. In-/outflow boundary conditions require that the Poisson equation is solved with a Dirichlet (constant pressure) boundary condition at the downstream end of the computational domain, and a staggered von Neumann boundary condition at the upstream end of the computational domain (corresponding to a zero pressure gradient over the plane $x = 0$). Fortunately, Schumann and Sweet (1988) derived transforms similar to FFTs that can handle such boundary conditions in spectral space, as well as pre- and post-processing steps that can be used to generate these transforms using standard FFT libraries. Using these transforms the pressure correction equation can still be solved using the fast algorithm defined by equation (3.7), albeit using different values for the eigenvalues λ_x and λ_y.

Since the definition of the Fourier transform used by Schumann and Sweet (1988) differs slightly from the definition used in FFTW, we here quickly repeat the derivation of these steps for our particular problem for future reference. First, we consider the backward FFT transform calculated by the FFTW library (Fourier analysis). It is given by (Frigo and Johnson, 2005):

$$Q_k = \sum_{j=1}^{N} \mathcal{Q}_j e^{2\pi(j-1)(k-1)\sqrt{-1}/N} \qquad \text{for } k = 1, 2, \dots, N \tag{3.18}$$

where $\mathcal{Q}_j$ is the j$^{\text{th}}$ (complex) component of the Fourier transform of Q, and N represents the number of sampling points. Note that we use a different range of the indices when compared to Frigo and Johnson. For a real input vector Q, the first half of the Fourier spectrum $\mathcal{Q}$ is the complex conjugate of the remaining spectrum. Using this symmetry, and expanding the complex exponential, equation (3.18) can be rewritten as:

$$Q_k = \mathbb{R}\left(\mathcal{Q}_1\right) + 2\sum_{j=1}^{n}\left[\mathbb{R}\left(\mathcal{Q}_{j+1}\right)\cos\left[\frac{2\pi j(k-1)}{N}\right] - \mathbb{I}\left(\mathcal{Q}_{j+1}\right)\sin\left[\frac{2\pi j(k-1)}{N}\right]\right] \tag{3.19}$$

for uneven N, where $n = (N-1)/2$.

The (un-normalised) backward transform that corresponds to Dirichlet – von Neumann boundary conditions for the pressure correction equation is given by (Schumann and Sweet, 1988):

$$Q_k = \sum_{j=1}^{n} \mathcal{Q}_j \sin\left[\frac{(2j-1)k\pi}{N}\right] \tag{3.20}$$

Following the procedure by Schumann and Sweet, the transform given in equation (3.20) can be calculated using the FFTW library by combining two transforms ($\mathcal{X}$

and $\mathcal{Y}$) into one vector Q of length N, by multiplying X by $\sin(k\pi/N)$ and Y by $\cos(k\pi/N)$:

$$Q_k = \sum_{j=1}^{n} \left[\mathcal{X}_j \sin\left[\frac{(2j-1)\,k\pi}{N}\right] \sin\left[\frac{k\pi}{N}\right] + \right.$$
$$\left. \mathcal{Y}_j \sin\left[\frac{(2j-1)\,k\pi}{N}\right] \cos\left[\frac{k\pi}{N}\right] \right] \tag{3.21}$$

Re-arranging, and using $\sin a \sin b = [\cos(a-b) - \cos(a+b)]/2$ and $\sin a \cos b = [\sin(a-b) + \sin(a+b)]/2$, we obtain:

$$Q_k = \mathcal{X}_1 + \sum_{j=1}^{n-1} \left[(\mathcal{X}_{j+1} - \mathcal{X}_j)\cos\left[\frac{2jk\pi}{N}\right] + (\mathcal{Y}_{j+1} + \mathcal{Y}_j)\sin\left[\frac{2jk\pi}{N}\right] \right] -$$
$$\mathcal{X}_n \cos\left[\frac{2kn\pi}{N}\right] + \mathcal{Y}_n \sin\left[\frac{2kn\pi}{N}\right] \tag{3.22}$$

Using $\sin(a+b) = \sin a \cos b + \cos a \sin b$ and $\cos(a+b) = \cos a \cos b - \sin a \sin b$, this takes the form of the backward FFTW transform, given in equation (3.19), when we set:

$$\mathbb{R}\,(\mathcal{Q}_1) = \mathcal{X}_1$$
$$\mathbb{R}\,(\mathcal{Q}_{j+1}) = \frac{1}{2}\left[(\mathcal{X}_{j+1} - \mathcal{X}_j)\cos\frac{2\pi j}{N} + (\mathcal{Y}_{j+1} + \mathcal{Y}_j)\sin\frac{2\pi j}{N}\right]$$
$$\mathbb{I}\,(\mathcal{Q}_{j+1}) = \frac{1}{2}\left[(\mathcal{X}_{j+1} - \mathcal{X}_j)\sin\frac{2\pi j}{N} - (\mathcal{Y}_{j+1} + \mathcal{Y}_j)\cos\frac{2\pi j}{N}\right] \tag{3.23}$$
$$\mathbb{R}\,(\mathcal{Q}_{n+1}) = -\frac{1}{2}\left[\mathcal{X}_n \cos\frac{2\pi n}{N} - \mathcal{Y}_n \sin\frac{2\pi n}{N}\right]$$
$$\mathbb{I}\,(\mathcal{Q}_{n+1}) = -\frac{1}{2}\left[\mathcal{X}_n \sin\frac{2\pi n}{N} + \mathcal{Y}_n \cos\frac{2\pi n}{N}\right]$$

for $j = 1, \ldots, n - 1$. Hence, the transform (3.20) can be calculated simultaneously for two stripes in the streamwise direction by pre-processing $\mathcal{X}$ and $\mathcal{Y}$ using expression (3.23) to arrive at $\mathcal{Q}$ and using the FFTW to compute the transform Q. Subsequently, the values of X_k and Y_k can be found by post-processing:

$$X_k = (Q_k + Q_{N-k})/\left[2\sin\left(\frac{k\pi}{N}\right)\right]$$
$$Y_k = (Q_k - Q_{N-k})/\left[2\cos\left(\frac{k\pi}{N}\right)\right] \tag{3.24}$$

This completes the backward transform. The forward transform can be obtained by inverting the algorithm above: thus, we start by pre-processing X and Y to arrive at

Q. The resulting elements of Q are supplied to the forward FFTW transform, that is given by:

$$\mathcal{Q}_k = \sum_{j=1}^{N} Q_j e^{-2\pi(j-1)(k-1)\sqrt{-1}/N} \tag{3.25}$$

Finally, the inverse of the set of equations in (3.23) is used to determine the values of $\mathcal{X}_k$ and $\mathcal{Y}_k$:

$$\mathcal{X}_1 = \mathbb{R}\left(\mathcal{Q}_1\right) \qquad \text{and} \qquad \mathcal{Y}_n = \mathbb{R}\left(\mathcal{Q}_{n+1}\right)\sin\left[\frac{2\pi n}{N}\right] - \mathbb{I}\left(\mathcal{Q}_{n+1}\right)\cos\left[\frac{2\pi n}{N}\right]$$

$$\mathcal{X}_{j+1} = \mathcal{X}_j + 2\mathbb{R}\left(\mathcal{Q}_{j+1}\right)\cos\left[\frac{2\pi j}{N}\right] + 2\mathbb{I}\left(\mathcal{Q}_{j+1}\right)\sin\left[\frac{2\pi j}{N}\right]$$

$$\text{for } j = 1, 2, \ldots, n-1 \tag{3.26}$$

$$\mathcal{Y}_j = 2\mathbb{R}\left(\mathcal{Q}_{j+1}\right)\sin\left[\frac{2\pi j}{N}\right] - 2\mathbb{I}\left(\mathcal{Q}_{j+1}\right)\cos\left[\frac{2\pi j}{N}\right] - \mathcal{Y}_{j+1}$$

$$\text{for } j = n-1, n-2, \ldots, 1$$

The eigenvalues of the von Neumann–Dirichlet transforms, needed to solve equation (3.7), are given by:

$$\lambda_x = -4\sin^2\frac{(2x-1)\pi}{2N} \tag{3.27}$$

where $x = 1, \ldots, n$, whereas the normalisation factor for the transform pair is equal to:

$$\mathcal{N} = \frac{4}{N} \tag{3.28}$$

The solution procedure for the Dirichlet – von Neumann boundary conditions outlined above can be converted to the boundary conditions considered in our work (von Neumann – Dirichlet) by reverting the order of the elements of X and Y before conducting the Fourier analysis, and after the Fourier synthesis. Since this solution algorithm only requires pre- and post-processing of the Poisson equation in the streamwise direction, it can readily be integrated in the existing FFT solver implemented in the DELFT code.

3.3 Model for the dispersed phase

In contrast to the continuous-phase solvers, the models for the dispersed phase used in this work have been developed almost entirely from scratch. Several authors have extended the DELFT codes with solvers for dispersed-phase motion before. However, neither of these extensions have considered particles that were attaching to each other, forming structures with complex shapes. Having said that, some of the basic concepts of the dispersed-phase solvers introduced by the previous authors were of great benefit to us and have partially been reused. Most importantly, Woittiez

(2007) incorporated collision routines by Li et al. (2001) into the channel version of the DELFT code for non-interacting one- and two-way coupled dispersed phases used by Portela and Oliemans (2003); these collision routines have, in an adapted form, been incorporated in the present model as well.

As explained in Chapter 1, we consider asphaltene particles to act as a precursor to agglomerate and deposit formation. We model the asphaltene phase separation by the sudden appearance of primary particles; we consider these particles to be spherical, and we describe them as point particles, with a finite radius. In this so-called point-particle approach, the interaction between the continuous and dispersed phases is described by considering only flow properties at the location of the centre of the primary particles. The effects of the finite dimensions of the primary particles are neglected when determining the force exerted on the particles by the flow (and visa versa).

We assume that each collision between primary particles results in the formation of a bond between those particles: this corresponds to a collision efficiency equal to unity (the «hit-and-stick» approach). Physically, the probability of particles adhering during a collision event depends on the relative time scales involved in the adhesion process and the particle contact time. Since these time scales are much smaller than the macroscopic time scale over which we need to study the deposition process, it is computationally not feasible to model the inter-particle collisions in microscopic detail. As we only consider agglomeration in competition with break-up, the simplification of assuming a 100% collision efficiency from a pragmatic perspective is a fair approximation, as, at least to some extent, physically improper agglomeration events will quickly be undone by the break-up of the bonds.

Colliding particles can be either *unbounded*, or they can be part of an agglomerate that has been formed earlier; for colliding agglomerates, the pair of primary particles that collides is identified, thereby keeping track of the internal structure of all agglomerates formed. All collisions between particles and agglomerates are considered to be purely inelastic, conserving both linear and angular momentum. The inter-particle bonds formed during collisions are considered to have an infinite resistance to deformation, resulting in agglomerates that are rigid up to the point where the bonds between individual particles are broken; the relative position of primary particles inside an agglomerate does not change as long as the agglomerate stays structurally intact. We consider bonds inside the agglomerates to break when the stresses induced inside them exceed the strength of the bonds, as will be explained in Section 3.9. The assumption of infinite agglomerate rigidity seems to be a fair approximation of the reality for asphaltenes that have a solid-like character; of course this also means that our model will not be suitable for describing the evolution of asphaltenes that phase separate in a liquid-like state.

3.4   Equations of motion for the agglomerates

Since we consider agglomerates to be infinitely rigid, the primary particles that are part of one agglomerate move together and therefore they are no longer described

by individual equations of motion of single, spherical particles. The agglomerate motion is described by a superposition of the linear velocity of the centre of mass of the agglomerate, and the rotation of the agglomerate around its centre of mass. By definition, the vector $\mathbf{X}_{cm}$, describing the location of the centre of mass of an agglomerate, is given by:

$$\mathbf{X}_{cm} \equiv \frac{1}{m_a} \sum_p m_p \mathbf{X}_p \tag{3.29}$$

where the sum runs over all primary particles that are part of the agglomerate, the vector $\mathbf{X}_p$ denotes the location vector of the primary particle p, m_p represents the mass of this primary particle, and m_a is the agglomerate mass, given by $m_a \equiv \sum m_p$. The rate of change of the linear velocity of the centre of mass, $\mathbf{U}_{cm}$, is given by:

$$m_a \frac{d\mathbf{U}_{cm}}{dt} = \sum_p \breve{\mathbf{F}}_p \tag{3.30}$$

where $\breve{\mathbf{F}}_p$ denotes the hydrodynamic force that is acting on particle p, as given by equation (3.40). Similarly, the equation for the angular velocity of the agglomerates is given by:

$$\frac{d\left(\mathbf{I}^S \mathbf{\Omega}^S\right)}{dt} = \mathbf{T}^S = \sum_p \left(\mathbf{r}_p \times \breve{\mathbf{F}}_p\right) \tag{3.31}$$

where $\mathbf{r}_p$ denotes the position vector of the centre of the primary particle and with respect to the agglomerate centre of the mass, $\mathbf{T}^S$ denotes the total torque and $\mathbf{I}^S$ represents the moment of inertia tensor. For given values of $\mathbf{U}_{cm}$ and $\mathbf{\Omega}^S$, the instantaneous velocity of the individual primary particles inside an agglomerate follows from the linear and rotational velocities of the agglomerate using the relation:

$$\mathbf{U}_p = \mathbf{U}_{cm} + \mathbf{\Omega}^S \times \mathbf{r}_p \tag{3.32}$$

For an agglomerate that is build-up from interconnected spherical particles, the moment of inertia tensor $\mathbf{I}^S$ is given by:

$$\mathbf{I}^S = \sum_p m_p \begin{bmatrix} r_y^2 + r_z^2 + \frac{2}{5}R_p^2 & -(r_x r_y) & -(r_x r_z) \\ -(r_x r_y) & r_x^2 + r_z^2 + \frac{2}{5}R_p^2 & -(r_y r_z) \\ -(r_x r_z) & -(r_y r_z) & r_x^2 + r_y^2 + \frac{2}{5}R_p^2 \end{bmatrix} \tag{3.33}$$

where R_p is the primary particle radius, r_x, r_y and r_z represent the distance from the centre of the primary particle to the centre of the agglomerate along the x, y and z axes of the computational grid, respectively. Let $\mathbf{B_x}$, $\mathbf{B_y}$, and $\mathbf{B_z}$, and I_x^B, I_y^B and I_z^B represent the eigenvectors and eigenvalues of $\mathbf{I}^S$, respectively. $\mathbf{B_x}$, $\mathbf{B_y}$, and $\mathbf{B_z}$ form the basis of a non-inertial body-reference frame associated with the agglomerate. In this body-reference frame, the moment of inertia tensor is diagonal, and is given by:

$$\mathbf{I}^B = \begin{bmatrix} I_x^B & 0 & 0 \\ 0 & I_y^B & 0 \\ 0 & 0 & I_z^B \end{bmatrix} \tag{3.34}$$

The rotational motion of the agglomerate with respect to the stationary reference frame of the computational grid corresponds to a time evolution of the base vectors $\mathbf{B_x}$, $\mathbf{B_y}$, and $\mathbf{B_z}$ of the body-reference frame; this time evolution can be described using the Rodrigues' formula (see, e.g. Mason (2001)):

$$\mathbf{B}^{n+1} = \mathbf{B}^n \cos\varphi + \frac{\mathbf{\Omega}^S}{|\mathbf{\Omega}^S|} \left(\frac{\mathbf{\Omega}^S}{|\mathbf{\Omega}^S|} \cdot \mathbf{B}^n \right) (1 - \cos\varphi) + \left(\frac{\mathbf{\Omega}^S}{|\mathbf{\Omega}^S|} \times \mathbf{B}^n \right) \sin\varphi \qquad (3.35)$$

where the incremental rotation angle φ is given by $\varphi = |\mathbf{\Omega}^S| \, \Delta t$.

If required, matrices and vectors describing the agglomerate state can be transformed between the agglomerate body reference frame and the stationary reference frame of the computational grid using the transformation matrix $\mathcal{R}$:

$$\mathcal{R} = \begin{bmatrix} \mathbf{B}_{x|x} & \mathbf{B}_{y|x} & \mathbf{B}_{z|x} \\ \mathbf{B}_{x|y} & \mathbf{B}_{y|y} & \mathbf{B}_{z|y} \\ \mathbf{B}_{x|z} & \mathbf{B}_{y|z} & \mathbf{B}_{z|z} \end{bmatrix} \qquad (3.36)$$

where the columns of $\mathcal{R}$ are equal to the base vectors of the agglomerate body-reference frame. Using equation (3.36), we can for instance compute $\mathbf{I}^S = \mathcal{R}\mathbf{I}_B$, and if needed, the reverse can be computed as $\mathbf{I}^B = \mathcal{R}^{-1}\mathbf{I}^S$. Since $\mathcal{R}$ is orthogonal, its inverse is equal to its transpose, and therefore $\mathcal{R}^{-1}$ can easily be found without considering the actual matrix inversion.

For objects of arbitrary shape, the moment of inertia tensor is not rotation invariant in the stationary reference frame, and as a result, expression (3.31) cannot trivially be solved for $d\mathbf{\Omega}^S/dt$ in its present form. We employ a standard technique for solving the rotational velocity equation, which involves transforming it to the body-reference frame of the agglomerate, where it reduces to the Euler equations for the rotation of a rigid body:

$$\mathbf{I}^B \frac{d\mathbf{\Omega}^B}{dt} - \mathbf{\Omega}^B \times \left(\mathbf{I}^B \mathbf{\Omega}^B \right) = \mathbf{T}^B \qquad (3.37)$$

For a more in-depth explanation of this solution strategy, as well as the theory of solid-body dynamics in general, the reader is referred to a classical mechanics textbook, like Goldstein et al. (2002).

3.5 Hydrodynamic forces acting on dispersed phase

The linear acceleration of the agglomerate centre of mass and the angular acceleration of the agglomerate are induced by the balance of forces and torques that are acting on the agglomerate, respectively. Both quantities are the result of the forces that are acting on the individual primary particles that are part of the agglomerate, and hence, we first consider the force acting on a single spherical particle that is dispersed in a fluid flow.

The motion of a particle, that is dispersed inside an unsteady flow at small Reynolds numbers, is well described by the Basset-Boussinesq-Oseen equation, which,

neglecting the Faxen force (viz. flow non-uniformity), is given by (Crowe et al., 1997):

$$
\rho_p \frac{4\pi R_p^3}{3} \frac{d\mathbf{U}_p}{dt} = \underbrace{6\pi\mu_f R_p \left(\mathbf{U}_f - \mathbf{U}_p\right)}_{\text{drag}} + \underbrace{\frac{\rho_f}{2}\frac{4\pi R_p^3}{3}\left(\frac{D\mathbf{U}_f}{Dt} - \frac{d\mathbf{U}_p}{dt}\right)}_{\text{added mass}} -
$$

$$
\underbrace{\frac{4\pi R_p^3}{3}\left(\nabla P - \nabla \cdot \mathbb{T}\right)}_{\text{pressure gradient}} + \underbrace{6\sqrt{\pi\rho_f\mu_f}R_p^2 \int_{t_0}^{t}\frac{1}{\sqrt{t-\tau}}\left[\frac{d\mathbf{U}_f}{d\tau} - \frac{d\mathbf{U}_p}{d\tau}\right]d\tau}_{\text{history force}} + \mathbf{F}_{\text{other}} \quad (3.38)
$$

where ρ_p denotes the density of the dispersed phase, the carrier-phase velocity $\mathbf{U}_f$ is evaluated at the location of the particle centre, and $\mathbb{T}$ is the stress tensor in the fluid. The other forces, represented by $\mathbf{F}_{\text{other}}$, may include external forces, such as the gravitational force or an electromagnetic force, or other fluid forces, such as the lift force. In this work, we are interested in simulating upward vertical flows of systems that have density ratios between the dispersed and continuous phases close to one. As a result, gravity does not have a component in the wall-normal direction, and the streamwise gravity-induced slip velocity of the particles is negligible when compared to typical turbulent velocity fluctuations. Likewise, it is expected that the influence of the lift force is small, such that this force can also be neglected.

The only force acting on the dispersed phase considered in this work is the drag force, corrected for the added mass effect. The drag force is approximated using Stokes drag, without accounting for shielding effects for primary particles that are close to each other (the «free-draining» approximation). Due to the high local particle-concentration inside the agglomerates, shielding effects in reality are likely to have an substantial impact on the force exerted on the primary particles; this effect, however, is also very complex to model in detail.

In general, one may expect that the drag force on a particle that is directly exposed to the flow is slightly enhanced due to the presence of a sheltered particle downstream of it, whereas the drag force on the sheltered particle itself can significantly decrease (Schutte, 2010). For simplicity, these effects were neglected in the present model. The overall overestimation of the total drag force on the agglomerates introduced by this simplification is partly compensated by the fact that we use Stokes drag to compute the drag force on individual primary particles. The Stokes drag approximation strictly only holds for particle Reynolds numbers much smaller than unity, whereas typical values of the particle Reynolds number in our work are between 0 and 10). For particle Reynolds numbers above one, Stokes drag is known to underestimate the actual drag force. Another reason for omitting a correction to the Stokes drag formulation is that in this way the linearity of the drag force is preserved.

Considering only Stokes drag and the added mass force, equation (3.38) reduces to:

$$
\rho_p \frac{4\pi R_p^3}{3}\frac{d\mathbf{U}_p}{dt} = \mathbf{F}_p = 6\pi\mu_f R_p\left(\mathbf{U}_f - \mathbf{U}_p\right) + \frac{\rho_f}{2}\frac{4\pi R_p^3}{3}\left(\frac{D\mathbf{U}_f}{Dt} - \frac{d\mathbf{U}_p}{dt}\right) \quad (3.39)
$$

Approximating the material derivative of the fluid velocity in the added mass term by just the time derivative, equation (3.39) reduces to:

$$\breve{\rho}_p \frac{4\pi R_p^3}{3} \frac{d\mathbf{U}_p}{dt} \equiv \breve{\mathbf{F}}_p = 6\pi \mu_f R_p (\mathbf{U}_f - \mathbf{U}_p) \quad \text{with} \quad \breve{\rho}_p = \left(\rho_p + \frac{\rho_f}{2}\right) \tag{3.40}$$

where $\breve{\rho}_p$ can be seen as the effective density of the dispersed phase corrected for the added mass effect. We have verified that the properties of the steady-state agglomerate population formed in absence of deposition and re-entrainment does not change when the lift force and the full formulation of the added mass are in fact included in the model, showing that the simplifications made above are reasonable. In Chapter 8, we will further address the reasonability of the hydrodynamic force model used in this work, by comparing its predictions to fully resolved simulations of the flow around an agglomerate.

The expression for $\breve{\mathbf{F}}_p$ given in equation (3.40) is used to describe the hydrodynamic force acting on any single primary particle (both unbounded particles, and particles that are part of agglomerates), and $\breve{\rho}_p$ substitutes ρ_p when calculating the mass of primary particles and/or agglomerates. Rewriting this last equation, one can arrive at an expression for the particle relaxation time τ_p:

$$\frac{d\mathbf{U}_p}{dt} = \frac{1}{\tau_p} (\mathbf{U}_f - \mathbf{U}_p) \quad \text{where:} \quad \tau_p \equiv \frac{2\breve{\rho}_p R_p^2}{9\mu_f} \tag{3.41}$$

which is a measure for how quickly particles can adapt to changes in the fluid velocity.

3.6 Algorithm of dispersed-phase solver and time integration

Within one time step of the solver of the dispersed phase, the following sequence of actions is taken:

> **procedure** TIME STEP OF DISPERSED-PHASE MODEL
>> Inject additional primary particles (if applicable)
>> Update of linear and angular acceleration of agglomerates $\quad\quad$ ▷ Section 3.4
>> Checking for and execution of agglomerate break-up $\quad\quad$ ▷ Section 3.9
>> Detection of collisions between primary particles, and with walls ▷ Section 3.7
>> **while** <More collisions are to be executed> **do**
>>> **if** <Inter-particle collision> **then**
>>>> Execute actual agglomeration $\quad\quad$ ▷ Section 3.8
>>> **else** <Particle-wall collision>
>>>> Execute particle-wall collision $\quad\quad$ ▷ Section 3.10
>>> **end if**
>> **end while**
>> Time advancing of all agglomerates to the end of the time step $\quad\quad$ ▷ This section
>> Collecting of agglomerate statistics
>> Dispersed-phase model time step done $\quad\quad$ ▷ Go back to main program.
> **end procedure**

The equations of motion of the agglomerates are integrated using an explicit time-integration scheme. The linear and rotational centre-of-mass acceleration of all agglomerates is determined using equations (3.30) and (3.37); unless an agglomerate experiences a collision, these accelerations are assumed to be constant throughout the time step. For agglomerates that collide during the time step Δt, either amongst each other or with the walls, collisions are resolved with sub-time-step temporal accuracy. By splitting the time step, these agglomerates are advanced prior to the collision such that the momentum exchange takes place at the instant the primary particles are touching. This is done to ensure that no artificial overlap of primary particles builds up over time.

A synchronised time step is used between the continuous- and dispersed-phase solvers. To ensure stability, the time step is chosen such that it is equal to or smaller than the minimum of: (i) the time step dictated by the continuous-flow solver, (ii) half of the relaxation time of a single primary particle, as defined in equation (3.41), and (iii) the largest value of Δt for which any particle present in the domain travels more than half a fluid grid-cell per time step, in any given direction. No numerical stability issues were encountered using this set-up.

3.7 Collision detection

Because primary particles are part of agglomerates, which obey the laws of solid body motion, the future trajectory of the individual primary particles is determined by the rotation of the agglomerate body reference frame base vectors, given in expression (3.35). Although we assume that the linear and rotational acceleration of the agglomerates is constant during on time step, the acceleration of the individual primary particles will, due to the solid body motion, not be constant during this period. As a result, the procedure for predicting when particles collide becomes significantly more complex compared to the case where the particle velocities are assumed to be constant throughout one time step. In fact, a closed expression for the collision time interval can no longer be obtained. A first approximation to the collision time interval can be found by assuming that the change in the linear acceleration of the primary particles is small enough so that it can be neglected throughout the time step. The distance $\mathbb{D}$ between the centres of the particles m and s is then given by:

$$\mathbb{D}\left(t\right) = \left|\left(\mathbf{X}_m + \mathbf{U}_m t + \mathbf{A}_m t^2\right) - \left(\mathbf{X}_s + \mathbf{U}_s t + \mathbf{A}_s t^2\right)\right| \qquad (3.42)$$

where $\mathbf{A}$ represents the acceleration of the respective primary particle, resulting from a time-differentiation of equation (3.32). Since particles collide when their outer shells collide, that is, when $\mathbb{D} = R_m + R_s$, we may as well solve equation (3.42) for $\mathbb{D}\left(t\right) \cdot \mathbb{D}\left(t\right) = (R_m + R_s)^2$. In order to proceed efficiently, we discard all higher order terms in t in the approximation for the squared norm of $\mathbb{D}$, and approximate the collision time interval using a second order expansion of expression (3.42). Collisions with the walls are detected using a similar algorithm, that only takes into account the motion of one particle in the wall-normal direction.

In case that a collision is detected within a time interval Δt, or even slightly after it, the colliding particles are fictitiously advanced in time to the instant of the predicted collision using the full equations of solid body motion. Starting from this state, a new estimate of the collision time interval is made to refine the precision of our approximation. Our results show that collisions are only very rarely overlooked this way. There still is, however, a finite probability that a collision is not detected. If such situations arise, pairs of primary particles will, at the end of the time step, have a finite overlap, even though they are not part of the same agglomerate. This can easily be detected and is corrected by the collision detection algorithm at the start of the next time step, by joining the agglomerates as if they collided exactly at the time instant that the overlap is detected. A similar approach is used in case that collisions between particles and the walls of the flow domain were not detected.

3.8 Particle attachment: agglomeration

As explained before, we assume that each collision between primary particles results in the formation of a bond between these particles. This corresponds to assuming that all collisions between particles and agglomerates are purely inelastic, conserving both linear and angular momentum. By analogy with the definition of the location of the centre of mass, given in expression (3.29), the velocity of the centre of mass of the newly formed agglomerate that corresponds to the conservation of linear momentum is by definition equal to:

$$\mathbf{U}_{\text{cm}} \equiv \frac{1}{m_a} \sum_p m_p \mathbf{U}_p \tag{3.43}$$

In case that two agglomerates m and s collide, equation (3.29) can be calculated more efficiently using:

$$\mathbf{U}_{\text{cm}}^n = \frac{1}{m_a^n} \left(m_a^m \mathbf{U}_{\text{cm}}^m + m_a^s \mathbf{U}_{\text{cm}}^s \right) \tag{3.44}$$

where n denotes the new agglomerate that is formed. Let $\mathbf{I}_n^S$ denote the moment of inertia tensor of the newly formed agglomerate, as given by equation (3.33). The rotational velocity of the agglomerate after the collision can then readily be found by equating the total angular momentum before and after the collision:

$$\mathbf{I}_n^S \mathbf{\Omega}_n^S = \mathbf{I}_m^S \mathbf{\Omega}_m^S + m_a^m \left(\mathbf{X}_{\text{cm}}^m - \mathbf{X}_{\text{cm}}^n \right) \times \left(\mathbf{U}_{\text{cm}}^m - \mathbf{U}_{\text{cm}}^n \right) + \tag{3.45}$$

$$\mathbf{I}_s^S \mathbf{\Omega}_s^S + m_a^s \left(\mathbf{X}_{\text{cm}}^s - \mathbf{X}_{\text{cm}}^n \right) \times \left(\mathbf{U}_{\text{cm}}^s - \mathbf{U}_{\text{cm}}^n \right) \tag{3.46}$$

since all quantities at the right-hand-side of this equation are known prior to the collision. As a result, $\mathbf{\Omega}_n^S$ can be solved for using standard matrix inversion of the three-dimensional matrix-vector equation given in expression (3.46). Subsequently, the updated linear velocity of the individual primary particles is computed using expression (3.32).

3.9 Break-up

In general, in a rigid body, four principal modes of internal stress, which could result in the breakage of that body, can be distinguished: *straining*, *shearing*, *bending* and *twisting*. Straining is associated with the normal component of the force exerted on the body, and shearing with the tangential force component, whereas bending and twisting are associated with the normal and tangential components of the induced torque, respectively. A schematic representation is given in Figure 3.2. In our model, all of these break-up mechanisms are taken into account.
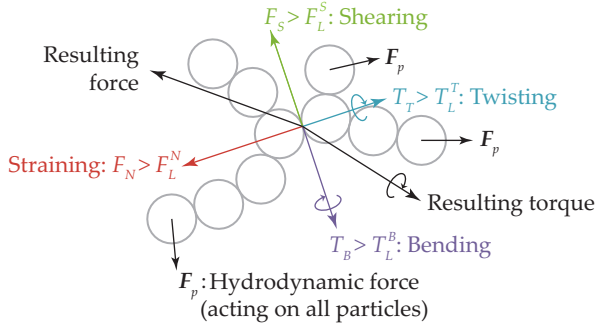
Figure 3.2: Decomposition of internal stresses induced in inter-particle bonds by hydrodynamic forces. F_L^N, F_L^S, T_L^B, T_L^T denote the maximum normal, shear, bending and twisting stresses that bonds can withstand, respectively.

The internal stresses in the bonds between the primary particles in the agglomerates are computed by equating the mass times the acceleration of the individual primary particles, resulting from the differentiation of equation (3.32), to the force balance over the respective particles themselves:

$$m_p \frac{d\mathbf{U}_p}{dt} = m_p \left(\frac{d\mathbf{U}_{cm}}{dt} + \frac{d\mathbf{\Omega}^S}{dt} \times \mathbf{r}_p + \mathbf{\Omega}^S \times \frac{d\mathbf{r}_p}{dt} \right) = \mathbf{F}_p + \sum_b \mathbf{F}_b \qquad (3.47)$$

where the sum runs over all bonds the particle p has with other primary particles («nearest-neighbours»), and the $\mathbf{F}_b$'s represent the forces in those bonds. It is for this reason that for each primary particle we have to keep track which other particles are its nearest neighbours. Similarly, the angular acceleration of each primary particle must result from a balance of torques acting on the primary particle:

$$\frac{d\left(\mathbf{I}_p^S \mathbf{\Omega}^S\right)}{dt} = \mathbf{T}_p^S + \sum_b \mathbf{T}_b^S \qquad (3.48)$$

where $\mathbf{I}_p^S$ is the specific moment of inertia of the primary particle with respect to the agglomerate centre of mass. Like equation (3.31), equation (3.48) is solved using a

transformation to the non-inertial reference frame attached to the agglomerate, viz.:

$$\mathbf{I}_p^B \frac{d\mathbf{\Omega}^B}{dt} - \mathbf{\Omega}^B \times \left(\mathbf{I}_p^B \mathbf{\Omega}^B\right) = \mathbf{T}_p^B + \sum_b \mathbf{T}_b^B \tag{3.49}$$

In the body-reference frame, the tensor $\mathbf{I}^p$ is diagonal, and its elements are given by:

$$\mathbf{I}_p^B = m_p \begin{bmatrix} \left(\hat{r}_y^2 + \hat{r}_z^2 + \frac{2}{5}R_p^2\right) & & \varnothing \\ & \left(\hat{r}_x^2 + \hat{r}_z^2 + \frac{2}{5}R_p^2\right) & \\ \varnothing & & \left(\hat{r}_x^2 + \hat{r}_y^2 + \frac{2}{5}R_p^2\right) \end{bmatrix} \tag{3.50}$$

where $\hat{r}_x$, $\hat{r}_y$ and $\hat{r}_z$ represent the distance from the centre of the primary particle p to the centre of mass of the agglomerate along the primary axes of the body reference frame ($\mathbf{R}_x$, $\mathbf{R}_y$ and $\mathbf{R}_z$), respectively.

Evaluating expressions (3.47) and (3.49) for all primary particles in an agglomerate results in two systems of n vector equations. Since we consider agglomerates to be rigid, and our model fully resolves agglomerate collisions in time, the probability that two agglomerates collide with more than one primary particle pair at the same time is infinitesimally small. As a result, any combination of primary particles that are part of one agglomerate are connected by one unique pathway only, and in an agglomerate that consists of n particles, exactly $n-1$ bonds between the particles are present. The number of unknown values of $\mathbf{F}_b$ and $\mathbf{T}_b$ is thus also equal to $n-1$. Hence, the systems of equations given by expressions (3.47) and (3.49) are always closed.

We exploit the fact that in absence of cyclic structures, agglomerates will always contain a non-zero number of primary particles that have only one nearest neighbour, and, consequently, only one unknown value of $\mathbf{F}_b$ and one unknown value of $\mathbf{T}_b$ in the balances of force and torque over them, respectively. Therefore equations (3.47) and (3.49) can readily be solved for these particles, thereby reducing the number of unknowns in the force and torque balances for the nearest neighbours of these particles. As a result, the number of unknowns in equations (3.47) and (3.49) for all particles that have two nearest neighbours will be reduced to one. By repetitively applying this solution scheme, the balances of force and torque over all primary particles in the agglomerate can be solved for in only a few sweeps. A subsequent geometric decomposition yields the straining (F_N), shearing (F_S), bending (T_B) and twisting (T_T) components of the stress in all the inter-particle bonds in the agglomerate.

Bonds are considered to be broken when any of the internal stress components exceed threshold values that are characteristic for the strength of the bonds, provided that the resulting fragments of the agglomerates, move apart afterwards. As such, our method cannot represent break-up due to excessive compressive* stresses in the bonds in the agglomerates, since in this case, the fragments of the agglomerates (almost) always would immediately re-collide after being broken apart. Although it may seem

---

*Compressive stresses correspond to negative values of the straining stress F_N.

counter-intuitive, the condition of agglomerate fragments moving apart is not a priori satisfied if the maximum resistance of the inter-particle bonds against either shearing, bending, or twisting is exceeded. Immediate re-attachment can still occur in this case, depending on the balance between the individual stress components, especially in the simultaneous presence of compressive stresses.

Any given bond inside an agglomerate connects two fragments, or *branches*, of that agglomerate; for the purpose of agglomerate break-up, we must be able to determine the structure of each of these branches. This information can be obtained from piece-by-piece unravelling the branch-structure from the information stored for the nearest-neighbour pairs for all primary particles. In order to determine whether breaking a particular inter-particle bond would result in a valid break-up event, we consider the relative acceleration of the resulting agglomerate fragments. This process is repeated either until a valid break-up point is found, or until we run out of bonds that are eligible for break-up based on the inter-particle stress distributions (in the latter case, the agglomerate will not be broken in the current time step). One agglomerate is broken in a maximum of two fragments during one time step.

For agglomerates that consist of a significant number of primary particles, unravelling the agglomerate branch structure from stored nearest-neighbour information, as well as solving for the inter-particle stresses using expressions (3.47) and (3.49), can be quite tedious from a computational perspective. Therefore, we do not check for break-up of each agglomerate during each time step. Only those agglomerates that were involved in either inter-particle, or particle-wall collisions in the previous time step are checked for break-up at the beginning of the next time step. Once in every 10 time steps, all agglomerates that consist of more than a cut-off number of N_c primary particles are checked for break-up. The value of N_c is dynamically determined from the cumulative distribution function of previously broken agglomerates, by selecting N_c such that less than 0.5% of those agglomerates contained under N_c primary particles.

Actual break-up of agglomerates. Having determined a proper location in which an agglomerate can be broken given the considerations outlined above, and having determined the branches of the agglomerate that are formed when this bond is broken, the actual break-up process is straightforward. The linear and angular velocity of the agglomerate branches after break-up is set such that the velocity of the primary particles does not change instantaneously during the breakage. As such, the location and linear velocity of the centre of mass of the agglomerate branches can be found using the definitions of $\mathbf{X}_{\text{cm}}$ and $\mathbf{U}_{\text{cm}}$, given in equations (3.29) and (3.43), respectively. The moment of inertia tensor of the branches subsequently can be found using equation (3.33). The angular velocity of the agglomerate branches that corresponds to conserving the angular momentum and the instantaneous primary particle velocity during the agglomerate break-up is given by:

$$\mathbf{\Omega}_m^S = \mathbf{\Omega}_s^S = \mathbf{\Omega}_o^S \tag{3.51}$$

where $\mathbf{\Omega}_o^S$ is the rotational velocity of the original, broken agglomerate in the stationary reference frame.

3.10 Interaction between particles and wall

Boundary conditions at walls of flow domain. At the walls of the flow domain, we consider two types of boundary conditions for the dispersed phase: reflective and attractive. When no deposition and re-entrainment of agglomerates is considered, collisions between agglomerates and the walls of the flow domain are resolved in time, and in each collision, the linear and angular velocity of the agglomerates are changed such that the wall-normal velocity component of the primary particle that has collided with the wall is reversed. In the limit of an agglomerate that consists only of one primary particles, this corresponds to a specular reflection. In the latter case, the velocity of the particle and agglomerate after the wall-collision can be written as:

$$W_p^n = W_{cm}^n = W_{\text{target}} \tag{3.52}$$

Here W denotes the wall-normal velocity component, the subscript p denotes the particle, cm the centre of mass, and the superscript n marks the state directly after the wall collision. For a perfect specular reflection, the target velocity W_{target} should be equal to $-W_p^o$, where the superscript o denotes the state just before the collision (as also used below). For reasons that will be explained shortly, we define W_{target} slightly differently, however, if W_p^o and dW_p^o/dt have opposing signs:

$$W_{\text{target}} = \begin{cases} -\frac{1}{2}\left(1+e\right)\frac{dW_p^o}{dt} & \text{if} \quad \left|W_p^o\right| < \frac{1}{2}\left(1+e\right)\left|\frac{dW_p^o}{dt}\right|\Delta t_{\text{rest}} \\ -W_p^o & \text{if} \quad \left|W_p^o\right| > \frac{1}{2}\left(1+e\right)\left|\frac{dW_p^o}{dt}\right|\Delta t_{\text{rest}} \end{cases} \tag{3.53}$$

where Δt_{rest} represents the remainder of the time step Δt after the particle-wall collision and e is a small number (we use $e = 10^{-6}$). The distinction on the basis of the magnitude of the wall-normal velocity before the collision is made to ensure that particles that have virtually no wall-normal velocity (and thus should be stationary with respect to the wall) do not «float» into the wall during the remainder of the time step Δt_{rest}. This is a simple fix to ensure that particles remain inside the computational domain (in fact, they will be lying almost exactly flush with the wall after the remaining time step), removing the need to take very small time steps for those particles that are really close to the wall.

If the agglomerate consists of more than one primary particle, the specular reflection results both in a linear and angular impulse acting on the agglomerate. To ensure that the new velocity of the primary particle of the agglomerate that has collided with the wall satisfies equation (3.53), this amounts to:

$$U_{\text{cm}}^n = U_{\text{cm}}^o \qquad\qquad V_{\text{cm}}^n = V_{\text{cm}}^o \qquad\qquad W_{\text{cm}}^n = W_{\text{cm}}^o + \frac{\mathbf{S}_z}{m_a}$$

$$\left.\mathbf{\Omega}_x^B\right|^n = \left.\mathbf{\Omega}_x^B\right|^o + \frac{\mathbf{\Delta L}_x^B}{I_x^B} \quad \left.\mathbf{\Omega}_y^B\right|^n = \left.\mathbf{\Omega}_y^B\right|^o + \frac{\mathbf{\Delta L}_y^B}{I_y^B} \quad \left.\mathbf{\Omega}_z^B\right|^n = \left.\mathbf{\Omega}_z^B\right|^o + \frac{\mathbf{\Delta L}_z^B}{I_z^B} \tag{3.54}$$

where the angular impulse $\mathbf{\Delta L}^B$ is given by:

$$\mathbf{\Delta L}^B = \mathcal{R}^{-1} \left(\mathbf{r} \times \mathbf{S}\right) \tag{3.55}$$

and $\mathbf{S} = [0, 0, \mathbf{S}_z]^T$ is the linear impulse exerted by the wall on the primary particle (defined in the stationary reference frame), given by:

$$\mathbf{S}_z = -\frac{\left(W_p^o - W_{\text{target}}\right) m_a}{1 + m_a \left[\left(\mathbf{r} \times \mathbf{B}_x\right)_z^2 / I_x^B + \left(\mathbf{r} \times \mathbf{B}_y\right)_z^2 / I_y^B + \left(\mathbf{r} \times \mathbf{B}_z\right)_z^2 / I_z^B\right]} \tag{3.56}$$

Deposition model. When adhesive walls are considered, resolving the actual deposition process from a microscopic perspective is not feasible in the context of our modelling approach, as, physically, the interaction range between the particles and the wall will be very small. Instead, a mesoscopic description of the attachment process is needed. To our best knowledge, no attempts have been made to take deposition into account in a Eulerian-Lagrangian model in which the structure of agglomerates is explicitly taken into account before.

In analogy to our inter-particle collision model, an obvious choice for modelling deposition would be to consider that primary particles form bonds with the walls of the flow domain when colliding into them, to assume that these bonds are rigid, and to attribute limiting stresses to the bonds in a similar way as for the inter-particle bonds. Initial investigations using such an approach revealed, however, that this model produces clearly non-physical results. The assumption that rigid bonds are formed between particles and walls of the flow domain prevents agglomerates to re-orientate themselves with respect to the walls. As particles are predominantly transported in the streamwise direction by the continuous carrier-phase, such an assumption causes the bonds inside deposited agglomerates to be mainly in a state of compressive internal stress. As a result, agglomerates can break neither from the wall, nor internally, considering the break-up formulation implemented in our model. Consequently there is a quick formation of upside-down «tree-shaped» structures, which are attached to (both) wall(s) of the flow domain at their side(s).

Theoretically, this problem could be solved by relaxing the assumption that particle-wall bonds are infinitely rigid. This would, however, significantly increase the complexity of the break-up algorithm, as multiple primary particles of one agglomerate will eventually come in contact with the walls, violating the assumption that pathways between primary particle pairs in agglomerates are always unique. A deposition model along these lines was therefore not further pursued.

Instead, the particle-wall attachment is treated by modelling the walls by interaction potentials rather than solving for the actual collisions of agglomerates with the walls of the flow domain; in this way, particles are not forced to stick instantly to the wall when reaching it. Again, making the interaction range very small would result in a very stiff problem, requiring very small time steps, which is undesirable. Instead, we relax the requirement that particles exactly adhere to the wall, by assuming a finite

interaction range between the wall and the particles. A damped harmonic oscillator, also known as a spring-dashpot system, acting in the wall-normal direction, is used to account for the attractive interaction between asphaltene particles and the walls of the flow domain:

$$\mathbf{F}_{\text{dho}}^{\text{wall}} = -\xi \left(cW_p \pm k\delta_s \right) \gamma F_L^N \hat{z} \tag{3.57}$$

where k and c are spring and damping constants, respectively, W_p represents the wall-normal component of the primary particle velocity and δ_s the normalwise distance from the wall to the face of the particle; $\hat{z}$ is the unit-normal in the direction of the positive wall-normal coordinate. The plus sign corresponds to the bottom wall of the channel domain, and the minus sign to the top wall. The parameter γ is a scaling factor that relates the particle-wall interaction force to the particle-particle interaction force, whereas ξ accounts for the finite interaction range between particles and the wall:

$$\xi = \begin{cases} 25 & \text{if the particle centre is inside the wall} \\ 1.0 - (\delta_s/\delta_c)^2 & \text{if the particle centre is inside the flow and } \delta_s < \delta_c \\ 0 & \text{if } \delta_s > \delta_c \end{cases} \tag{3.58}$$

where δ_c is the range of the particle-wall interaction. It is purely for reasons of numerical stability that the value of ξ does not approach infinity inside the wall. Physically, the repulsive force is compressive, and therefore, it is not limited by the maximum straining stress γF_L^N that bonds between the particles and the wall can withstand. As will be further discussed in Section 7.1, the value of $\xi = 25$ inside the wall is found to give a satisfactory balance between a sufficiently strong repulsive force inside the wall and numerical stability.

The parameters k and c in equation (3.57) are related by the so-called damping ratio, which is given by:

$$\zeta = \frac{c}{2\sqrt{m_p k}} \tag{3.59}$$

where m_p represents the mass of a single primary particle; $\zeta = 1$ corresponds to critical damping.

Deposited agglomerates will slide over the walls of the flow domain indefinitely if no constraining force is applied in the wall-parallel direction. In order to prevent this, the velocity of those particles for which δ_s is smaller than the particle radius is adapted such, that it relaxes towards a no-slip boundary condition with a characteristic time scale t_{rns}. This relaxation is achieved by the introduction of an additional force $\mathbf{F}_{\text{rns}}^{\text{wall}}$, that has the form:

$$\mathbf{F}_{\text{rns}}^{\text{wall}} = \psi_p \xi F_{\text{rns}}^{\text{wall}} \tag{3.60}$$

where ψ_p is a coefficient vector that scales with the predicted velocity deviation of the primary particle parallel to the wall after t_{rns} if $\mathbf{F}_{\text{rns}}^{\text{wall}}$ would not be applied. The unknown scalar variable $F_{\text{rns}}^{\text{wall}}$ in equation (3.60) is the same for all primary particles in the agglomerate; it is found by minimising the root-mean-square velocity deviation of the deposited particles after t_{rns}.

If the magnitude of either the wall-normal or wall-parallel component of the total particle-wall interaction force for any primary particle, given by $\mathbf{F}_{\text{dho}}^{\text{wall}} + \mathbf{F}_{\text{rns}}^{\text{wall}}$, exceeds the maximum magnitude (which is equal to γF_L^N in the wall-normal, and γF_L^S in the wall-parallel direction), the respective component is truncated. The minimisation process that underlies equation (3.60) is repeated until a consistent set of values for $\mathbf{F}_{\text{rns}}^{\text{wall}}$ is obtained for all particles.

3.11 Dispersed-phase solver in the cylindrical geometry

So far, we have only discussed the implementation of the dispersed-phase solver in the channel geometry. In this section, we will explain how this solver was adapted to simulate agglomerate formation, break-up, deposition and re-entrainment in the pipe geometry.

To limit the programming effort, we have chosen not to implement the dispersed-phase solver itself in cylindrical coordinates; instead, the equations for the dispersed phase motion, outlined earlier in this chapter, are solved in Cartesian coordinates also for the pipe. In essence, the only two modifications that need to be made are: (i) to translate the Cartesian coordinates of the primary particles to cylindrical coordinates, and (ii), to represent the cylindrical domain wall on the Cartesian grid.

The first adaptation is made simply by attributing an additional cylindrical coordinate to the particles, that is updated every time that the Cartesian coordinate is updated. The second adaptation is a slightly more involved, since it affects both the collision detection and the particle-wall interactions. Basically, it comes down to replacing all references to wall-normal distances and velocities to the respective quantities measured along the radial pipe coordinate. A similar replacement needs to be made for wall-parallel quantities, that in the pipe consist of streamwise and circumferential contributions. Thereafter, a translation back to the Cartesian coordinate reference system has to be made; in this way, the solution strategy explained in this chapter can be used without further modification.

The integration between the channel and pipe geometries is made such the actual geometry can be chosen using an input flag in the computer code. This means that maintenance of separate codes for both geometries is no longer needed.

3.12 Code efficiency

Since we want to maximise the number of primary particles that can be considered in our simulations, it is important to maintain a good code efficiency. In a typical simulation using our model, most of the computational time is spent in the solver for the dispersed phase. Since we implemented this solver essentially from scratch, a fair amount of effort was spent on optimising the structure of the solver such that the computational effort and overhead were minimised. We will give a brief outline of what measures have been taken to keep the computational efficiency up, and we will highlight some of the obvious pitfalls one could be faced with when constructing

such a code as the one considered in this work. Thereafter, we will share our thoughts on future possibilities for code parallelisation.

Bookkeeping of the agglomerate structure

Since, in contrast to most models for particulate agglomeration previously proposed in the literature, we are interested in resolving the structure of the agglomerates over time, a vast amount of additional bookkeeping is necessary when compared to a dispersed-phase solver in which only spherical particles are considered. Most of the additional parameters that have to be taken care of, such as the base vectors for the reference frames that are co-rotating with the agglomerates, the rotational velocity of the agglomerates, and the moment of inertia tensor, have to be updated for at most a few times per time step for each agglomerate. Therefore, computing these parameters does not put a large burden on the computational efficiency. From this perspective, particularly the bookkeeping of the agglomerate structure is an interesting challenge.

In principle, one could account for the agglomerate structure just by storing information about pairs of primary particle nearest-neighbours. Retrieving which primary particles together form one agglomerate from this information is a tedious process, however, and since this information is required frequently, this approach is both impractical, and very inefficient. In Figure 3.3 a simple structure for a more efficient primary particle bookkeeping system is sketched. This system uses one array `P` to store unique integers that identify all primary particles that are present in the flow domain, an array `L` to store the number of primary particles in each agglomerate, and another array `S` to store for each agglomerate the index in array `P` that corresponds to the first primary particle belonging to that agglomerate.

Upon collision, in this system, the array `P` has to be re-arranged such that the primary particles that belong to both agglomerates that have collided become adjoining, and the lines in arrays `L` and `S` referring to either of the agglomerates have to be removed. To this end, all lines of the arrays below the removed line have to be shifted up by one line, and so have the items of all arrays that are storing physical parameters associated with the agglomerates ($\mathbf{X}_{cm}, \mathbf{U}_{cm}, \mathbf{I}, \mathbf{\Omega}, \dots$). Especially when large numbers of agglomerates and/or when large collision and break-up rates are to be considered, the latter requirement can result in a significant decrease in performance due to excessive shifting of parameters in the computer memory.

To eliminate the need for continuously reorganising variables that carry agglomerate-specific information, we introduced an additional abstraction layer, which decouples the numbering of agglomerates to the ordering of entries in arrays describing agglomerate properties, thereby allowing the data in the latter variables to become non-consecutive. An additional array `N` is used to indicate which of the lines of the arrays `S` and `L` contain information on agglomerates that are actually present in the system. In this way, the number of required memory operations can significantly be reduced at the expense of using a slightly increased memory usage. The only variables that need to be re-arranged during each agglomeration and break-up event in this improved system are the arrays `N` and `P` (not `S`, `L`, as well as any arrays that

Before collision

S	L	P
1	4	1
5	1	827
6	2	45
8	27	355
35	4	2
39	1	3
40	10	89
50	3	4
53	35	47
88	8	65

Simple system

S	L	P
1	6	1
7	1	827
8	27	45
35	4	355
39	1	3
40	10	89
50	3	2
53	35	4
88	8	47
101	13	65

Improved system

N	S	L	P
1	1	6	1
2	7	1	827
4	-	-	45
5	8	27	355
6	35	4	3
7	39	1	89
8	40	10	2
9	50	3	4
10	53	35	47
11	88	8	65

Figure 3.3: Bookkeeping structure used to monitor which primary particles belong to which agglomerate. To the left, an initial condition before a collision event is sketched. In the centre, the collision event is accounted for using a simple scheme, whereas to the right, an improved scheme is used to minimise shifting of variables in the computer memory. The information that is contained in the arrays P, L, S, N is explained in the main text.

contain physical parameter) resulting in a much more efficient code with respect to memory management.

Collision detection

If done naively, $N_p^2/2$ particle pairs have to be checked for collision in each time step. For any significant number of primary particles N_p, such an approach would be extremely slow. As a starting point for making the collision detection algorithm more efficient, Woittiez (2007) incorporated the cell-index technique in a previous dispersed-phase solver in the DELFT code, meant for non-agglomerating particles. In this technique, an additional grid is overlaid on the computational domain, to make a rough selection of the particle pairs that can be excluded from further consideration, because they will most certainly not collide within a given time step Δt. To this end, the dimensions of the cells of the overlaid grid are chosen equal to or larger than the maximum distance that any particle can cover within this time interval. All potential collision partners for a given primary particle must then reside either in the same cell as the particle itself, or in any of the twenty-six nearest-neighbour cells surrounding that cell. Since, from the perspective of numerical accuracy, the distance that one particle can travel typically is much smaller than the linear dimensions of the computational grid-cells of the continuous fluid phase solver, the number of

cells of the cell-index grid will typically be larger than the number of fluid nodes, thereby significantly reducing the number of particle pairs that have to undergo a more detailed consideration of their future trajectory.

To maximise the efficiency of the cell-index technique, it is important to minimise the number of times that the cell index has to be rebuilt. For this reason, we construct the cell index only once during every time step, before any collision is actually executed, after which the time interval for all predicted collisions are stored in a short-list. Subsequently, a heap-sort algorithm is used to sort the collision short-list in order of ascending time interval to the collision. One by one, these collisions are then executed according to the methodology explained in sections 3.8 and 3.10. Since the velocity and acceleration of primary particles changes during a collision, each collision event might influence collisions that will be occurring in the future, thereby changing the short-list of upcoming collisions. However, these changes are, of course, limited, to those collisions in which primary particles are involved that are part of the agglomerate(s) that have been involved in other collisions that have taken place after the cell index was built. As a result, the collision short-list only has to be reconsidered for a limited number of primary particles per collision event, thereby significantly reducing the computational effort.

3.13 Possibilities for code parallelisation

Although time did not allow us to implement a parallel version of our model in the context of the present project, we have considered doing so and we will therefore present some of our considerations.

One of the most important aspects of constructing efficient parallel codes is minimising the communication required between CPU's: if this is not possible, the bottleneck in the simulations will be the communication itself, and, since this communication typically is orders of magnitude slower that the communication within one CPU, poorly parallelised codes may even perform worse than their single-core counterparts. This makes that one should carefully consider whether parallelisation is actually worthwhile, before actually deciding to make the effort of doing it.

It would be highly beneficial if the number of primary particles that can be considered in one simulation can be increased significantly. In our single-core implementation, the dispersed-phase solver already consumes far more computational time than the continuous fluid phase solver if we consider 10^6 primary particles (and single simulations can take up to weeks of clock time on the fastest single-core processors available today). This means that if we would want to increase the particle number to, say, 10^9, the only option to do this would be to consider code parallelisation.

We first consider how this might work out when considering one-way coupling between the continuous- and dispersed-phase solvers. In this case, the evolution of the continuous phase becomes decoupled from the dispersed phase. Since the computational effort associated with the continuous phase is limited when compared to the dispersed phase, a simple yet reasonable approach would be to solve for the

velocity field of the continuous phase in the entire domain on a single CPU-core and in duplicate on all other CPU-cores as well. Starting from the same initial conditions, the results of the carrier-phase solver are deterministic and independent of the dispersed-phase motion. Therefore, we can be sure that an identical fluid velocity field would be known to each of the parallel processes, at each instant in time.

If the linear dimensions of the agglomerates are significantly smaller than the dimensions of the computational domain, the dispersed phase-solver has a reasonably local character: agglomeration and/or break-up of an agglomerate on the one side of the domain will not affect the formation and/or break-up of agglomerates far away from this first agglomerate; the same goes for deposition and re-entrainment. For this reason, local domain decomposition seems to be a feasible option for parallelising the dispersed-phase solver. If some overlap is used between the parts of the domain that are solved on different CPU's, such that the motion of agglomerates that are close to the domain boundaries are solved simultaneously on multiple CPU cores, communication can be limited to every once in so many time steps: the exact time interval required will depend on the time it takes for an agglomerate to cover a distance equal to the overlap in the domains.

Generalising the considerations above to two-way coupling and larger agglomerate sizes, the following observations can be made. When we consider two-way coupling, the flow field in the entire computational domain becomes dependent on the dispersed phase, through the force distribution given in equation (3.17), combined with the spatially global character of the pressure correction. Therefore, communication between all CPUs would be necessary at every time step (since the force distribution needs to be gathered and distributed), when the fluid velocity field is solved in its entireness on each CPU core individually. This would diminish the overall efficiency of the parallelisation, thereby making this approach very unattractive. Provided it is applied to both the fluid- and dispersed-phase solvers, however, local domain decomposition remains a feasible option for code parallelisation, as long as agglomerates do not become too large with respect to the overall dimensions of the computational domain (which, typically, they indeed will not do).

3.14   Summary

In this chapter, the development and implementation of the Eulerian-Lagrangian model for the agglomeration, break-up, deposition and re-entrainment of asphaltene particles was described. This model was implemented as an extension of an existing, particle-laden flow code (DELFT), considering both channel and pipe geometries. A single-phase flow is considered as the carrier phase to the dispersed particles, to keep the complexity of the carrier-phase solver tractable. The model was adapted such that both periodic boundary conditions can be used in the streamwise direction, as well as in- and outflow boundary conditions.

For the dispersed phase, spherical primary point particles are considered that have a finite radius. They are assumed to adhere to each other upon collision, and the structure of the agglomerates formed this way is explicitly taken into account in the

model. The motion of the agglomerates is given by the laws of solid body motion, and break-up of the agglomerates occurs according to the four principal mechanisms of break-up (straining, shearing, bending and twisting), following an analysis of the stresses that are induced inside the agglomerates by spatial variations of the hydrodynamic force acting on the agglomerates. We consider the total hydrodynamic force (which consists of the drag force and the added mass force) to scale linearly with the slip velocity of the primary particles with respect to the continuous carrier phase. No corrections are made for the shielding effects of nearby primary particles (the «free-draining» approximation).

Particle-wall interactions are either handled by specular-reflective collisions (in the absence of deposition and re-entrainment), or by using a novel damped-harmonic-oscillator-formulation for the particle-wall interaction force in the wall-normal direction, combined with a force that relaxes the wall-parallel component of the velocity of depositing agglomerates towards the velocity of the wall. This coarse-grained description of the microscopic adhesion that occurs in physical particle-wall contact ensures that deposition and re-entrainment can be taken into account in the model without experiencing numerical stability issues, or facing severe time-step constraints.

Special attention was paid to ensure that the numerical model is as efficient as possible. We employed efficient collision and break-up detection algorithms and we ensured that the bookkeeping of the agglomerate structure is handled as efficient as possible. We have also identified possibilities to parallelise the algorithm in the future, even though that was not implemented in the present work.

Chapter 4

One-dimensional engineering model

The Eulerian-Lagrangian model described in Chapter 3 cannot be applied as an engineering model for predicting asphaltene deposition in complex or extended geometries under realistic oil producing conditions. Using the model this way would require an enormous amount of computational power. In order to assess to what extent the fundamental insights that are obtained using the Eulerian-Lagrangian model can be used to improve closure relations in engineering models similar to those that have been proposed in the literature, we have also considered a one-dimensional model in this work.

The base implementation of the model described in this chapter was conducted at the TNO Heat Transfer and Fluid Dynamics group in Delft by Ruud van der Linden, Yuko Enquist and Aris Twerda. Originally, the model was implemented in `MATLAB`; to improve the computational efficiency, we have rewritten all routines in Fortran 90. We also improved and extended the model by considering two-way coupling between the fluid- and dispersed-phase solvers. In this way, the effects that the agglomeration and the deposition of asphaltenes have on the flow are included in the model. Parts of this extension of the model was achieved in collaboration with TNO staff members Tom Busking and Andries van Wijhe.

4.1 Two-phase carrier flow model

In the one-dimensional engineering model, a two-phase (oil/gas) flow is considered as the carrier for the dispersed phase. The components of the considered production system are an open-hole region inside the reservoir from which the oil flows into the wellbore, the wellbore itself and an adjustable choke valve, that connects to a flowline for which we assume a fixed pressure boundary condition. The geometry of the system is schematically shown in Figure 4.1.

A one-dimensional computational grid is used that spans both the open-hole region and the wellbore, which are divided into n_x equidistant cells in the streamwise direction. The boundary conditions for solving the flow in this region are the pressure
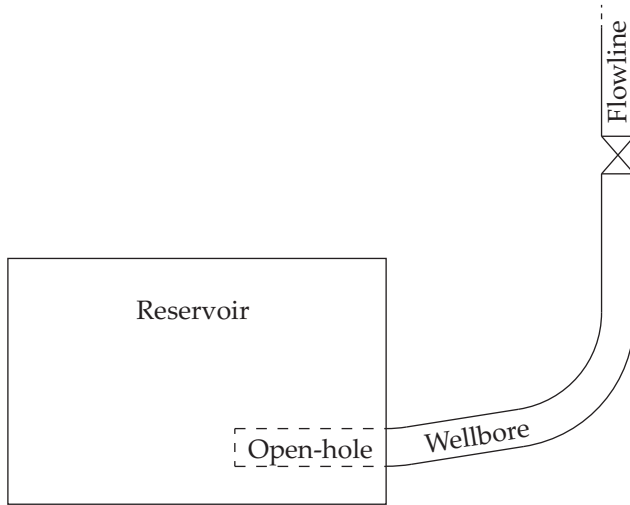
Figure 4.1: Schematic representation of well geometry considered in the one-dimensional model.

inside the reservoir and the flowline pressure, and the opening of the choke valve. Furthermore, the composition and thermodynamic properties of the reservoir fluid are specified, by using a PVT-table, that specifies the equilibrium density of the liquid and gas phases (ρ_l and ρ_g), the specific heat of the liquid and gas phases (C_l and C_g) and the equilibrium vapour quality χ as a function of the pressure and temperature. The value of χ represents the fraction of the total mass that is in the gas phase under equilibrium conditions.

The total pressure drop between the reservoir and the flowline, ΔP_t, is given by the sum of the pressure drops over the inflow region of the reservoir to the wellbore, ΔP_r, over the wellbore itself, ΔP_w, and over the choke valve ΔP_c:

$$\Delta P_t = \Delta P_r + \Delta P_w + \Delta P_c \tag{4.1}$$

Both ΔP_r, ΔP_w and ΔP_c are a function of the total mass flow rate $\dot{m}$ that is produced by the well, and the latter two pressure drops also depend on the hold-up (the fraction of the cross-sectional area that is occupied by the respective phase) of liquid and gas (α_l and α_g) inside the system. These variables thus have to be found as a function of the streamwise coordinate subject to the boundary conditions and the given fluid composition characterisation.

The solution procedure that is adopted iteratively determines the mass flow rate and corresponding phase hold-ups that yield the prescribed pressure drop. To this end, a specific mass flow rate $\dot{m}$ is assumed and the corresponding ΔP_t is determined. Sub-

sequently, the mass flow rate is adjusted such that the ΔP_t approaches the specified pressure drop to a set tolerance level.

Pressure drop over the wellbore. If we assume that the flow inside the wellbore is quasi-steady, the one-dimensional form of the Navier-Stokes equations for a gas/liquid flow, can be found as:

$$\frac{dP}{dx} = \mathcal{F} - \alpha_g \rho_g U_g \frac{dU_g}{dx} - \alpha_l \rho_l U_l \frac{dU_l}{dx} \tag{4.2}$$

where $\mathcal{F}$ represents the external forces acting on the fluids and U_l and U_g denote the velocities of the liquid and gas phases, respectively. It is reasonable to assume that the flow inside the wellbore is quasi-steady since changes in the total mass flow rate of the well will occur over time scales that are significantly longer than the longest time scales in the turbulent flow.

The external forces $\mathcal{F}$ in equation (4.2) that are considered are the gravity and the wall friction. The gravitational contribution is given by $f_g = g \sin(\varphi) \left(\alpha_g \rho_g + \alpha_l \rho_l \right)$, where φ is the local inclination angle from the horizon, whereas the frictional force is written as:

$$f_w = \frac{1}{2} \frac{c_f}{D} \left(\alpha_g \rho_g + \alpha_l \rho_l \right) |U_m| \, U_m \tag{4.3}$$

where c_f is the Fanning friction factor and U_m is the mixture velocity. By definition, the mixture velocity is given by the sum of the gas and liquid superficial velocities:

$$U_m = \alpha_g U_g + \alpha_l U_l \tag{4.4}$$

We use a simple Blasius relation to compute c_f as:

$$c_f = 0.316 Re_{\text{mix}}^{-1/4} \tag{4.5}$$

where Re_{mix} is the mixture Reynolds number:

$$Re_{\text{mix}} = \frac{\left(\alpha_l \rho_l + \alpha_g \rho_g \right) U_m D}{\mu_m} \tag{4.6}$$

where μ_m is the mixture viscosity, which we approximate by the viscosity of the liquid phase, and D is the local diameter of the wellbore.

Combining all aforementioned equations, the pressure drop over any segment of the wellbore can be written as:

$$\frac{dP}{dx} = \left(g \sin(\varphi) + \frac{0.316 Re_{\text{mix}}^{-1/4}}{2D} |U_m| \, U_m \right) \left(\alpha_g \rho_g + \alpha_l \rho_l \right)$$

$$- \alpha_g \rho_g U_g \frac{dU_g}{dx} - \alpha_l \rho_l U_l \frac{dU_l}{dx} \tag{4.7}$$

Integrating (4.7) over all cells of the computational domain, the total pressure drop over the wellbore ΔP_w can be computed. To proceed further, relations describing the

liquid and gas hold-ups, densities and velocities, as a function of the total mass flow rate $\dot{m}$, the pressure P and the temperature T are required.

The gas- and liquid-phase velocities (U_g and U_l) that appear in equation (4.7) are averaged over the part of the cross-section that covers the flow of the considered phase. In two-phase gas/liquid flows, U_g and U_l are not a priori equal: there might be a slip between the two phases. In vertical flows, for instance, the gas tends to concentrate in the centre of the pipe, and therefore, the average gas velocity tends to be higher than the average liquid velocity. The slip velocity between the gas and liquid is further increased by buoyancy effects, since the gas density is significantly lower than the liquid density. We use the drift-flux model, that was first proposed by Zuber and Findlay (1965), to account for these effects. In this model, the average gas velocity is expressed as:

$$U_g = C_0 U_m + U_d \qquad (4.8)$$

C_0 is the distribution parameter (which has a typical value slightly above one) that accounts for the increased gas velocity with respect to the mixture velocity, caused by the non-uniform gas distribution over the pipe cross section, and U_d is the drift velocity of the gas caused by the buoyancy effect.

The volumetric flow rates of the mixture, and the liquid and gas phases can be written as:

$$Q_m = Q_l + Q_g = U_m A \qquad Q_l = U_l \alpha_l A \qquad Q_g = U_g \alpha_g A \qquad (4.9)$$

where Q_g and Q_l denote the volumetric flow rates of the gas and liquid, respectively. Combining equations (4.8) and (4.9) gives an expression for the gas hold-up:

$$\alpha_g = \frac{Q_g}{C_0 \left(Q_g + Q_l \right) + U_d A} \qquad (4.10)$$

where A denotes the cross-sectional area of the wellbore.

Since the liquid and gas hold-ups are trivially related to each other ($\alpha_l = 1 - \alpha_g$), (4.10) relates the liquid and gas hold-ups to the volumetric flow rates of the respective phases provided closure relations can be found for the values of C_0 and U_d. Here, the closure relations proposed by Shi et al. (2005) are used.

The derivation of the drift velocity U_d that is used by Shi et al. assumes that U_d is equal to the rise velocity of gas bubbles in a stagnant liquid medium if the hold-up of the gas phase is small ($\alpha_g \leq \alpha_m$). For large α_g ($\alpha_g \geq \alpha_s$), the drift velocity is assumed to be such that the gas velocity is just able to support the upward motion of a thin annular liquid film formed at the walls of the pipe, preventing it from flowing downward. A linear interpolation is used between these two regimes for intermediate values of α_g. Shi et al. (2005) use α_m = 0.2 and α_s = 0.4, and the same values are used in this work. The resulting drift velocity has the following functional form:

$$U_d = \frac{(1 - \alpha_g C_0) \, C_0 \mathcal{K} U_c}{\alpha_g C_0 \left(1 - \sqrt{\frac{\rho_g}{\rho_l}} \right) + 1} \qquad (4.11)$$

where $\mathcal{K}$ is equal to $1.53/C_0$ if $\alpha_g \leq \alpha_m$, $\mathcal{K} = \mathrm{Ku}_c(\widehat{D})$ if $\alpha_g \geq \alpha_s$, and a linear interpolation between these values if $\alpha_m < \alpha_g < \alpha_s$.

The Kutateladze number represents a balance between inertia, buoyancy and surface tension. The critical Kutateladze number Ku_c marks the onset of flooding, in which the liquid film at the wall no longer can be dragged upwards by the gas velocity. An accurate parametrisation of the critical Kutateladze number that is reported by Shi et al. (2005) is given by:

$$\mathrm{Ku}_c = \begin{cases} 0.0 & \text{if } \widehat{D} < 2.0 \\ -0.977 + 1.375\Xi + 0.0871\Xi^2 - 0.0424\Xi^3 & \text{if } 2.0 \leq \widehat{D} \geq 50 \\ 3.2 & \text{if } \widehat{D} > 50 \end{cases} \qquad (4.12)$$

where $\Xi = \ln \widehat{D}$, and the dimensionless diameter $\widehat{D}$ is given by:

$$\widehat{D} = \sqrt{\frac{g\left(\rho_f - \rho_g\right)}{\sigma}} D \qquad (4.13)$$

where σ is the gas/liquid interfacial tension. In equation (4.11), U_c represents a characteristic velocity, that is given by:

$$U_c = \left[\frac{\sigma g\left(\rho_l - \rho_g\right)}{\rho_l^2}\right]^{1/4} \qquad (4.14)$$

The only remaining parameter that is required to close equations (4.8) and (4.11) is the distribution parameter C_0. The value of this parameter depends on the flow regime that is occurring inside the wellbore. In the bubble and slug flow regimes, the value of C_0 is largest, and a value of 1.2 has been used in several drift flux models proposed in the literature (Shi et al., 2005). In the annular flow regime, the value should be close to one. When the gas hold-up approaches unity, the value of C_0 should also go to one, as the mixture velocity should become equal to the gas velocity in that case. Furthermore, the product of α_g and C_0 should never exceed unity. The following expression for C_0, that satisfies these requirements, was proposed by Shi et al. (2005):

$$C_0 = \frac{\mathbb{S}_A\left(1 - \mathbb{S}_B\right)^2}{\left(1 - \mathbb{S}_B\right)^2 + \left(\mathbb{S}_A - 1\right)\left(\mathbb{B} - \mathbb{S}_B\right)^2} \qquad (4.15)$$

where the value of $\mathbb{B}$ is given by:

$$\beta = \max\left(\alpha_g, \mathbb{S}_F \frac{\alpha_g\left|U_m\right|}{U_{\mathrm{sgf}}}\right) \qquad (4.16)$$

The values of the coefficients $\mathbb{S}_A$, $\mathbb{S}_B$ and $\mathbb{S}_F$ are set equal to the original set of parameters considered by Shi et al., and are given by 1.2, 0.3 and 1.0, respectively. U_{sgf} is the critical gas velocity that marks the onset of flooding (viz. the lowest gas velocity for which the liquid film at the wall is just moving upward). Its value is related to the

critical Kutateladze number and the characteristic velocity U_c through the following relation:

$$U_{\text{sgf}} = \text{Ku}_c \sqrt{\frac{\rho_l}{\rho_g}} U_c \tag{4.17}$$

For given values of the volumetric flow rates of liquid and gas, equation (4.10) can now be used to compute the hold-up of gas (and thus also the hold-up of the liquid) in any location inside the wellbore. To compute the values of Q_g and Q_l, we assume that the liquid and gas phases are in thermodynamic equilibrium everywhere inside the wellbore. As such, the volumetric flow rates of both phases that correspond to a given total mass flow rate $\dot{m}$ can be determined from the PVT-table that describes the fluid composition as a function of pressure and temperature. The volumetric flow rates of gas and liquid are then given by:

$$Q_g = \dot{m} \frac{\chi(P,T)}{\rho_g(P,T)} \qquad Q_l = \frac{\dot{m} - Q_g \rho_g(P,T)}{\rho_l} \tag{4.18}$$

The procedure for solving the flow inside the wellbore now takes on the following form:

procedure SOLVING THE FLOW INSIDE THE WELLBORE FOR A FIXED VALUE OF $\dot{m}$
    Assume an initial pressure distribution inside the wellbore
    while <Pressure has not converged> **do**
        Compute the volumetric flow rates according to equation (4.18)
        Compute the hold-up of both phases according to equation (4.10)
        Compute the phase velocities using the inverse of equation (4.9)
        Compute the pressure drop and update the pressure using equation (4.7)
    end while
end procedure

Pressure drop induced by the choke. The pressure drop over the choke is modelled by taking into account the two-phase flow inside the choke, and accounting for the sudden expansion of the gas phase when the pressure is lowered. Like in the original model by TNO, we use the model by Al-Safran and Kelkar (2009). This model accounts for the slip between the liquid and gas phases and follows from the conservation of mass, momentum and energy, with the following assumptions:

- the flow in the valve is one-dimensional

- the acceleration is the dominant term contributing to the pressure drop

- there is no mass exchange between the liquid and gas phases inside the choke

- the liquid phase is incompressible

- the gas phase expands polytropically

Given these assumptions, the mass flow rate through the choke is expressed as:

$$\dot{m} = \sqrt{\frac{2C_D^2 A_t^2 P_u \left[\mathbb{O}\left(1-p\right) + \frac{\mathbb{N}}{\mathbb{N}-1}\left(1 - p^{\frac{\mathbb{N}-1}{\mathbb{N}}}\right)\right]}{\chi_g \rho_{g|u}^{-1}\left(p^{-1/\mathbb{N}} + \mathbb{O}\right)^2 \left[\chi + \frac{1-\chi}{\mathbb{U}}\right]}} \tag{4.19}$$

where C_D is the valve discharge coefficient, A_t is the valve cross-sectional area of the throat of the valve (viz. the smallest cross-section), P_u is the pressure upstream of the valve, p is a parameter that is related to the pressure difference over the valve, $\mathbb{N}$ is the polytropic-gas-expansion exponent, $\rho_{g|u}$ is the gas density downstream of the valve, and ($\mathbb{U} = U_g/U_l$) is the slip ratio inside the valve. For simplicity, and in contrast to Al-Safran and Kelkar (2009), we assume a constant value of $\mathbb{U}$ equal to one in the model that is described in this chapter.

The parameter $\mathbb{O}$ is given by:

$$\mathbb{O} = \frac{\mathbb{U}\left(1-\chi\right)\rho_{g|u}}{\chi \rho_l} \tag{4.20}$$

whereas the polytropic-gas-expansion exponent can be expressed as:

$$\mathbb{N} = \frac{\kappa \chi C_g + \left(1-\chi\right)C_l}{\chi C_g + \left(1-\chi\right)C_l} \tag{4.21}$$

where κ is the adiabatic index of the gas, C_g is the specific heat of the gas at constant volume and C_l is the specific heat of the liquid. The value of the gas specific heat ratio κ is determined by:

$$\kappa = \frac{\log\left(P_d/P_u\right)}{\log\left(\rho_{g|d}/\rho_{g|u}\right)} \tag{4.22}$$

where $\rho_{g|d}$ is the gas phase density downstream of the valve.

An important aspect in determining the flow through the valve is whether the flow inside the value is subcritical or critical. For subcritical flow, the mass flow rate through the valve explicitly depends on the pressure drop over the valve, and $p = P_u/P_t$, where P_t is the pressure at the throat of the choke. If the pressure difference over the valve reaches a critical value, however, the flow through the valve becomes critical, and a decrease in throat pressure will no longer cause the flow rate to increase. Following the model proposed by Al-Safran and Kelkar (2009), we model the critical pressure ratio p_c using the following equation:

$$p_c^{1-1/\mathbb{N}} = \frac{\mathbb{O}\left(1-p_c\right) + \frac{\mathbb{N}}{\mathbb{N}-1}}{\frac{\mathbb{N}}{\mathbb{N}-1} + \frac{\mathbb{N}}{2}\left(1 + \mathbb{O}p_c^{1/\mathbb{N}}\right)^2} \tag{4.23}$$

In the derivation of equations (4.19) and (4.23), it was assumed that the cross-sectional area of the choke of the valve is much smaller than the cross-sectional area of the

inflow section of the choke. The equations for arbitrary ratios of the cross-sectional area can be found in the appendix of the paper by Al-Safran and Kelkar (2009).

Since (4.23) is an implicit relation, an iterative procedure is required to solve for the value of p_c. As soon as its value is determined, the value of p is set according to:

$$p = \begin{cases} P_d/P_u & \text{if } P_d/P_u > p_c \\ p_c & \text{if } P_d/P_u < p_c \end{cases} \tag{4.24}$$

Al-Safran and Kelkar use an empirical relationship to calculate the pressure at the throat of the choke from the pressure downstream of the choke. This equation works well only at the critical flow boundary and furthermore is dependent on the geometry of the downstream part of the valve. For this reason, we neglect the pressure recovery downstream of the valve, and assume that the pressure in the throat is equal to the pressure downstream of the valve (viz. the pressure in the flowline).

The values of ρ_l and $\rho_{g|u}$ are determined by interpolation of the PVT-table at the pressure upstream of the valve. The values of χ, C_g and C_l are determined the same way, at the mean pressure in the valve. Similarly, the gas density downstream of the valve ($\rho_{g|d}$) is calculated using the pressure downstream of the valve.

Equation (4.19) expresses the mass flow rate through the choke valve as a function of the pressures upstream and downstream of the valve. In our algorithm, however, it is the mass flow rate through the valve that is fixed in each iteration of the flow solver, and thus the inverse of this relation is required. The pressure upstream of the valve is therefore also computed iteratively. For each guess of $\dot{m}$ that is made inside the wellbore, the pressure drop over the valve is computed by first assuming a certain pressure drop, calculating the corresponding mass flow rate through the valve, and adjusting the pressure drop over the valve until the required value of $\dot{m}$ is found through the valve.

Pressure drop in the inflow region of the reservoir. The pressure drop inside the reservoir ΔP_r is the result of frictional losses that occur when the crude oil flows through the porous rock that comprises the reservoir matrix. Since the dimensions of the pores of the reservoir rock are very small, the Reynolds number in the pores is very low, such that Stokes flow can be assumed in this region. If we assume that the accumulated cross-section of the permeable rock that is open to the flow does not change significantly over the time intervals we are interested in, the value of ΔP_r will thus scale linearly with the volumetric flow rate of the crude oil that is produced from the reservoir. The scaling coefficient that relates the volumetric flow rate to the pressure drop is the so-called Productivity Index (PI), which gives:

$$\Delta P_r = \dot{m}/(\text{PI}\rho_l) \tag{4.25}$$

As long as no asphaltene deposition occurs inside the reservoir, we assume that the value of the parameter PI is a constant, that will be specified as a input to the model.

Complete solution procedure. Once the three contributions to the total pressure drop over the system, ΔP_r, ΔP_w, and ΔP_c are computed for a given mass flow rate

$\dot{m}$, the total pressure drop is compared the difference in the reservoir and flowline pressures, and the mass flow rate is adjusted such that the pressure drop over the system matches the required value after a number of iterations. As soon as this procedure is finished, the complete flow in the wellbore is known for the given well geometry (viz. at a certain state of asphaltene deposition), and the dispersed phase models come into play to compute the evolution of the dispersed phase over the next incremental step.

4.2   Model for the dispersed phase

We use the population balance equation given in equation (2.3) to describe the evolution of the asphaltene particles after phase separation in the context of the one-dimensional engineering model. This equation is solved in each computational cell of the model inside the wellbore. We assume that particle nucleation is dominant over agglomerate growth, such that $\mathcal{G}_k$ is equal to zero for particles in all size classes $k = 1 \ldots K$. For convenience, we here repeat the resulting equation:

$$\frac{\partial \mathcal{N}_k}{\partial t} = \frac{1}{2} \sum_{i=1}^{k-1} \varsigma_i^{k-i} \Gamma_i^{k-i} \mathcal{N}_i \mathcal{N}_{k-i} - \sum_{i=1}^{K} \varsigma_k^i \Gamma_k^i \mathcal{N}_k \mathcal{N}_i +$$
$$\sum_{i=k+1}^{K} \beta_i \mathcal{D}_i \mathcal{B}_{i \to k} \mathcal{N}_i - \sum_{i=1}^{k-1} \beta_k \mathcal{D}_k \mathcal{B}_{k \to i} \mathcal{N}_k + \mathcal{M}_k \qquad (4.26)$$

The population balance that is presented in equation (4.26) only takes into account the rate of change in the number of agglomerates of a certain size that results from nucleation, agglomeration and break-up. Since we consider the agglomeration, break-up, deposition and re-entrainment of the asphaltene agglomerates to occur inside the wellbore, in which there is a flow occurring in the streamwise direction, the influence of agglomerate transport by the flow, and that of deposition and re-entrainment, also has to be taken into account:

$$\frac{\partial \mathcal{N}_k}{\partial t} = \frac{1}{2} \sum_{i=1}^{k-1} \varsigma_i^{k-i} \Gamma_i^{k-i} \mathcal{N}_i \mathcal{N}_{k-i} - \sum_{i=1}^{K} \varsigma_k^i \Gamma_k^i \mathcal{N}_k n_i +$$
$$\sum_{i=k+1}^{K} \beta_i \mathcal{D}_i \mathcal{B}_{i \to k} \mathcal{N}_i - \sum_{i=1}^{k-1} \beta_k \mathcal{D}_k \mathcal{B}_{k \to i} \mathcal{N}_k + \mathcal{M}_k + \qquad (4.27)$$
$$\left. \frac{\partial \mathcal{N}_k}{\partial t} \right|_{\text{transport}} - \left. \frac{\partial \mathcal{N}_k}{\partial t} \right|_{\text{deposition}} + \left. \frac{\partial \mathcal{N}_k}{\partial t} \right|_{\text{re-entrainment}}$$

For simplicity, we assume that all asphaltene agglomerates are dispersed in the liquid phase of the carrier flow. Since the agglomerates are small, they will almost act as tracers of the liquid phase velocity, such that slip between the dispersed phase and the liquid phase can be neglected. As such, the additional $\partial \mathcal{N}_k / \partial t$ caused by the

transport in the streamwise direction can be written as:

$$\frac{\partial \mathcal{N}_k}{\partial t}\bigg|_{\text{transport}} = \frac{\left[\pi D^2 \alpha_l U_l \mathcal{N}_k\right]_{i-1} - \left[\pi D^2 \alpha_l U_l \mathcal{N}_k\right]_i}{\alpha_l \pi D^2 \Delta x} \tag{4.28}$$

where the subscripts i and $i-1$ denote the local and upstream cells, respectively. Δx the grid-cell spacing, that is constant in our model. The contributions to $\partial \mathcal{N}_k / \partial t$ that result from the deposition and re-entrainment of agglomerates can straight-forwardly be related to the net deposition flux, that will be derived in equation (4.41).

We model the phase separation of asphaltenes by a continuous appearance of primary particles in the region inside the flow domain where the pressure is within the asphaltene phase separation window. We assume that the rate at which the phase separation proceeds is fastest in the middle of this pressure window, and smallest near the window boundaries. A normal distribution is used to capture this relation in mathematical form, in which we assume that the total width of the phase separation pressure window is equal to four standard deviations of the Gaussian distribution. As such, the rate of appearance of primary particles in each grid-cell, $\mathcal{M}_k$, in equation (4.26) can be written as:

$$\mathcal{M}_k = \begin{cases} \frac{1}{2}\frac{Q_l c_a \rho_a}{m_p} \left[\text{erf}\left(\frac{P(k+1)-P_{\text{mean}}}{\sqrt{2}P_\sigma}\right) - \text{erf}\left(\frac{P(k)-P_{\text{mean}}}{\sqrt{2}P_\sigma}\right)\right] & \text{if } k = 0 \\ 0 & \text{if } k \neq 0 \end{cases} \tag{4.29}$$

where c_a and ρ_a denote the concentration and density of the asphaltenes, respectively, and m_p is the mass of a primary particle. P_{mean} denotes the mid-point of the phase separation pressure window, and $P_\sigma = (P_{\text{max}} - P_{\text{min}})/4$, where P_{max} and P_{min} denote the maximum and minimum pressures for which asphaltene phase separation occurs.

Collision kernels. The collision kernels Γ and break-up kernels $\mathcal{D}$ in equation (4.26) need to be described by closure relations. For many mechanisms that cause agglomerate collision, the time averaged collision kernels have been derived in the literature. The collision kernel for particles that are moving due to thermal (or Brownian) motion is, for instance, given by (Friedlander, 2000):

$$\Gamma_i^k = \frac{2k_B T}{3\mu_l}\frac{(d_i + d_k)^2}{d_i d_k} \tag{4.30}$$

where k_B is the Boltzmann constant, μ_l is the liquid viscosity and d_i is the particle diameter of species i. Under laminar flow conditions, the collision kernel due to fluid shear is given by:

$$\Gamma_i^k = \frac{1}{6}G\left(d_i + d_k\right)^3 \tag{4.31}$$

where G is the shear rate. Saffman and Turner (1956) derived an expression for the collision kernel due to fluid shear for particles that are smaller than the Kolmogorov micro-scale eddies in turbulent flows:

$$\Gamma_i^k = \frac{1}{8}\sqrt{\frac{8\pi}{15}}\sqrt{\frac{\epsilon}{\nu}}\left(d_i + d_k\right)^3 \tag{4.32}$$

where ϵ represents the dissipation rate of turbulent kinetic energy and ν is the kinematic viscosity of the suspending fluid. Finally, for small particles that are sedimenting in a fluid under influence of gravity, the collision kernel is expressed as (Han and Lawler, 1991; Rahmani et al., 2004):

$$\Gamma_i^k = \frac{\pi g}{72 \mu_l} \left(d_i + d_k \right)^2 \left| \left(\rho_i - \rho_l \right) d_i^2 - \left(\rho_k - \rho_l \right) d_k^2 \right| \tag{4.33}$$

where it is assumed that the dispersion is dilute enough such that only two-particle collisions occur and three-particle collisions can be neglected.

Collision kernel used in this model. Since we follow the basic setup of the population balance model that is used by Eskin et al. (2011), our one-dimensional model considers, like these authors, that inter-particle collisions are predominantly caused by the effects of Brownian motion and turbulent velocity fluctuations. The total collision kernel is therefore given by the sum of expressions (4.30) and (4.32), viz.:

$$\Gamma_i^k = \frac{2 k_B T}{3 \mu_l} \frac{\left(d_i + d_k \right)^2}{d_i d_k} + \frac{1}{8} \sqrt{\frac{8 \pi}{15}} \sqrt{\frac{\epsilon}{\nu}} \left(d_i + d_k \right)^3 \tag{4.34}$$

where the energy dissipation rate ϵ is computed as:

$$\epsilon = \frac{4 \left[\frac{1}{8} c_f \rho_l U_l^2 \right] U_l}{\rho_l D} \tag{4.35}$$

where the term between the square brackets denotes the shear stress at the wall as induced by the liquid phase and c_f is the friction factor, given in equation (4.3). The collision cross-sections of the agglomerates that appear in expression (4.34) are computed by taking into account the fractal nature of the asphaltene agglomerates, using the following relation:

$$d_i = 2 R_p N_i^{1/D_f} \tag{4.36}$$

where R_p is the radius of the primary particles, N_i represents the number of primary particles per agglomerate of size class i and D_f is the fractal dimension.

Break-up kernels. As was explained in Chapter 3, break-up of aggregates is caused by stresses that are induced inside the agglomerates as a result of spatial variations of hydrodynamic forces. Modelling the agglomerate fragmentation process is therefore much more complex than predicting how frequent agglomerates collide with each other. Closure relations for the agglomerate break-up rate are typically empirical correlations, that relate the break-up rate to the particle diameter and to the shear stress in the fluid. Kusters (1991) for instance calculated the particle fragmentation rate by considering a balance between the energy needed to break an agglomerate and the available turbulent kinetic energy:

$$\mathcal{D}_i = \sqrt{\frac{4}{15 \pi}} \sqrt{\frac{\epsilon}{\nu}} \exp\left(\frac{-\epsilon_{c|i}}{\epsilon} \right) \tag{4.37}$$

where $\epsilon_{c|i}$ represents the typical energy needed to break an agglomerate. This critical energy was related to the agglomerate size and the fluid shear rate by Flesch et al. (1999):

$$\epsilon_{c|i} = \varrho \left(\frac{\epsilon}{\nu}\right)^{\upsilon/2} \frac{1}{d_i} \tag{4.38}$$

where ϱ and υ represent empirical constants.* The model due to Flesch et al. was used by Eskin et al. (2011), with $\varrho = 7 \cdot 10^{-4} \text{ m}^3/\text{s}^{1.4}$ and $\upsilon = 1.6$.

Pandya and Spielman (1983), proposed an expression of the following form for the break-up rate of agglomerates:

$$\mathcal{D}_i = \varrho G^\upsilon d_i \tag{4.39}$$

where G is equal to the average fluid shear rate ($G = \sqrt{\epsilon/\nu}$ in a turbulent flow). The symbols ϱ and υ in equation (4.39) represent different quantities than they do in equation (4.38). Here, ϱ is a proportionality constant and υ is constant related to the aggregate strength.* Barthelmes et al. (2003) modified equation (4.39) for agglomerates that have a fractal structure, and Faraji and Solaimany-Nazar (2010) used the resulting expression to calculate the break-up rate of asphaltene agglomerates in the context of a population balance model:

$$\mathcal{D}_i = \varrho G^\upsilon V_p^{1/3} \left(\frac{d_i}{d_p}\right)^{1/D_f} \tag{4.40}$$

where V_p represents the volume the primary particles.

In addition to the break-up rate, also closure relations are needed to model the size distribution of the agglomerate fragments that result from one break-up event. In the literature, only binary breakage has been considered in models that describe asphaltene evolution using population balance equations; that is, all break-up events are assumed to lead to formation of two identical, new agglomerates, which both contain half of the primary particles that were present in the agglomerate that is broken. When considering the results of our one-dimensional model simulations in Chapter 8, we will consider different distributions between the agglomerate sizes to investigate to what extent this is of influence on the model results.

Break-up kernel used in this model. In our model, we used the expression for the agglomerate break-up rate that was also used by Faraji and Solaimany-Nazar (2010), given in expression (4.40). In this respect we deviate from the model by Eskin et al. (2011), because we found that for the conditions that occur inside the wellbore, the critical break-up energy that is computed in equation (4.38) using the parameters reported by Eskin et al. is so much larger than the turbulent dissipation rate, that the break-up rate predicted by equation (4.37) is always equal to zero. The values for the closure parameters ϱ and υ are: $\varrho = 3.88 \cdot 10^{-3}$ s/m and $\upsilon = 2.0$, the same values that were used by Faraji and Solaimany-Nazar (2010).

---

*The symbol υ should not be confused with the symbol for the dynamic viscosity, ν.

Deposition and re-entrainment. To account for deposition and re-entrainment of agglomerates, the same approach as used by Eskin and co-workers is applied. They consider particles to deposit at the walls of the flow domain due to Brownian motion and due to transport by turbulent velocity fluctuations. Re-entrainment of particles due to shear removal of the deposit layer is also taken into account in the model. The net deposition mass flux per unit of wall area is given by:

$$\mathbb{Q} = \frac{\phi}{2} \sum_{i=1}^{K} [m_i \mathcal{N}_i (\mathcal{V}_{B_i} + \mathcal{V}_{T_i})] \left[1 - \vartheta \left(\frac{\tau_w}{\tau_w^0} - 1 \right)^q \right] \tag{4.41}$$

where ϕ is the deposition efficiency, m_i the mass of an agglomerate of type i, and $\mathcal{N}_i$ the number of agglomerates of size class i per unit volume, and $\mathcal{V}_B$ and $\mathcal{V}_T$ represent the deposition velocities due to Brownian motion and turbulent velocity fluctuations, respectively. The final term in equation (4.41) represents the re-entrainment of particles; ϑ and q are empirical parameters, whereas τ_w is the wall shear-stress and τ_w^0 the critical yield stress for shear removal.

By analogy to the distribution function of the molecular speed distribution in idealised gasses, Eskin et al. (2011) assume that the velocity distribution of the asphaltene agglomerates, that have typical dimensions of one to tens of nanometres, follow a Maxwell-Boltzmann distribution. The mean velocity is then given by:

$$\mathcal{V}_{M_i} = \sqrt{\frac{8k_B T}{\pi m_i}} \tag{4.42}$$

where k_B is the Boltzmann constant, T is the temperature. Since only half of the asphaltene agglomerates is moving towards the wall, the deposition velocity due to Brownian motion that is adopted by Eskin et al. is equal to half of $\mathcal{V}_{M_i}$:

$$\mathcal{V}_{B_i} = \sqrt{\frac{2k_B T}{\pi m_i}} \tag{4.43}$$

Using similar considerations, and by assuming that the agglomerates act as perfect tracers to the fluid phase velocities, the deposition velocity due to turbulent velocity fluctuations is evaluated as:

$$\mathcal{V}_{T_i} = \sqrt{\frac{2\overline{w_i'^2}}{\pi}} \tag{4.44}$$

where $\overline{w_i'^2}$ is the average-wall normal velocity fluctuation, evaluated at the location of the centre of a particle that is just touching the wall (viz. at a distance $z_i = d_i/2$ from the wall). The values of $\overline{w_i'^2}$ are computed from empirical correlations for wall-bounded flows. We use the same relation as Eskin et al., who used a relation reported by Guha (2008):

$$\sqrt{\overline{w_i'^2}} = \frac{5 \cdot 10^{-3} \left(\delta_i^+ \right)^2}{1 + 2.923 \cdot 10^{-3} \left(\delta_i^+ \right)^{2.128}} u_\tau \tag{4.45}$$

where u_τ is the friction velocity ($u_\tau = \sqrt{\tau_w/\rho_l}$) and δ^+ is the dimensionless wall-normal coordinate, given by $\delta_i^+ = \delta_i u_\tau \rho_l / \mu_l$.

For computing the collision, break-up and deposition rates of the agglomerates, we always assume that the asphaltene particles are dispersed in the liquid phase and not in the gas phase. For this reason, only liquid-phase parameters appear in the closure relations that have been sketched in the previous paragraphs.

4.3 Coupling between model components

Now that all of the terms of the population balance equation given in expression (4.27) have been closed, the evolution of the dispersed phase that proceeds under given flow conditions can be determined. In our model, two-way coupling between the multiphase flow and the dispersed-phase has been realised, by changing the diameter of the wellbore as a function of the asphaltene deposition that is locally occurring.

The model solution procedure is such, that for a given well geometry (considering either a clean well, or previously encountered asphaltene deposition), the two-phase flow inside the well is solved first. Using this flow field, the steady-state solution of equation (4.27) is obtained, which usually is found to set in much quicker than typical time scales over which the flow rate inside the wellbore change appreciably. For this reason, is can be assumed that the deposition rate of the asphaltenes is constant during one incremental step of the model. The diameter of the flow domain is reduced according to the net deposition rate that is predicted by the dispersed phase model, assuming a constant porosity of the deposit layer, where we have made sure that the relative decrease in the local diameter per incremental step is small enough to ensure the flow rate does not show very abrupt changes between subsequent steps.

4.4 Summary

Since one of the aims of this work is to use the fundamental insights that can be obtained using the Eulerian-Lagrangian model that is described in Chapter 3 to construct improved closure relations for simple engineering models for asphaltene deposition, the implementation of such a model was described in this chapter. The original implementation of the model described in this chapter was made in MATLAB by the TNO Heat Transfer and Fluid Dynamics group in Delft. To improve the computational efficiency, all routines were rewritten in Fortran 90.

The system that is considered in the model consists of an open-hole region inside an oil reservoir, the wellbore, and a choke valve that connects the top of the wellbore to a production pipeline. In the open-hole region, a linear relationship between the pressure drop and the mass flow rate is assumed, according to a fixed Productivity Index (PI). Inside the wellbore, that is represented by a one-dimensional discretisation in the streamwise direction, the drift-flux model by Shi et al. (2005) is used to determine the pressure distribution and the flow rates of the liquid and gas. The pressure drop over the valve is determined using the two-phase valve model due to Al-Safran and Kelkar (2009). The multiphase flow model is solved iteratively subject

to the boundary conditions posed by the reservoir pressure and the pressure in the flowline downstream of the choke valve.

The dispersed phase is modelled using a population balance equation, following the model proposed in Eskin et al. (2011). Collision kernels due to Brownian motion and turbulent velocity fluctuations are used. For the break-up kernel, the approach by Faraji and Solaimany-Nazar (2010) is used instead of the formulation proposed by Eskin et al., because we found that the break-up model by Eskin et al., (with the parameters proposed by these authors), predicted that agglomerate break-up would never occur under the conditions that are prevailing inside the wellbore.

Deposition and re-entrainment of agglomerates are handled in the same way as was proposed by Eskin et al. (2011), by considering that the flux of depositing particles is proportional to the local agglomerate concentration and the velocity of the particles towards the wall. This velocity is approximated by superposition of contributions due to Brownian motion and turbulent velocity fluctuations. Re-entrainment of agglomerates is taken into account by reducing the deposition flux depending on the relative intensity of the wall-shear stress and an yield-stress for the deposit layer above which re-entrainment is assumed to occur.

The model was improved and extended with respect to the implementation made by TNO, by coupling the deposition and re-entrainment formulation to the population balance equation, considering the loss of dispersed agglomerates upon deposition. Also, the reduction of the diameter of the wellbore as a result of deposition was taken into account in the drift-flux model. The resulting model can now be used in a quasi-steady transient mode, to investigate the temporal evolution of the deposit layer and the effects its presence has on the multiphase flow inside the wellbore. We also improved and extended the model by considering two-way coupling between the fluid- and dispersed-phase-solvers. In this way, the effects that the agglomeration and deposition of asphaltenes have onto the flow inside the wellbore are included in the model.

Chapter 5

Steady-state of agglomeration and break-up: Channel geometry

In this chapter, we study agglomeration and break-up in absence of deposition and re-entrainment using the Eulerian-Lagrangian model, as described in Chapter 3, for the channel flow geometry. We focus both on the properties of the agglomerates formed and the properties of the agglomeration and break-up processes. We also study the influence that the agglomerates have on the turbulent carrier-phase flow when two-way coupling is considered. A comparison to the results obtained in a pipe flow will be made in Chapter 6.

When interpreting the results of our simulations, special attention is paid to those properties of the agglomerates and the agglomeration and break-up processes that can be used to provide closure relations to engineering models, such as the one-dimensional drift flux population balance model that is described in Chapter 4. Since no models have been proposed before in the literature in which the structure of agglomerates are resolved during the formation and break-up of the agglomerates as induced by a turbulent flow, we will also study these processes from a more fundamental perspective. This is done to improve the overall insight in how these agglomeration and break-up processes interact with the turbulent flow.

5.1 Description of considered cases

Continuous carrier phase. We consider turbulent channel flows with Re_∇ (see equation (3.11) for its definition) ranging from 360 to 1080, corresponding to bulk Reynolds numbers (as defined in equation (3.13)) between 5700 and 19 400. These Reynolds numbers are representative for the flow inside wellbores or production pipelines for wells that produce relatively viscous oil at moderate production rates. Direct Numerical Simulations (DNS) are used at modest Reynolds numbers, whereas Large Eddy Simulations (LES) are used at elevated Reynolds number, where DNS becomes computationally very expensive. Periodic boundary conditions are used in the streamwise (x) and spanwise (y) directions and for the fluid flow, a no-slip boundary condition

Table 5.1: Overview of parameters associated with the continuous carrier-phase flow in the channel geometry. See Figure 3.1 for the definition of the grid parameters.

Re_∇	360	540	720	1080
$Re_{bulk\ (unladen/one-way)}$	5700	9000	12 500	19 400
$(n_x, n_y, n_z) = (96, 64, 48)$	LES			
$(n_x, n_y, n_z) = (192, 128, 96)$	DNS	LES	LES	LES
$(n_x, n_y, n_z) = (320, 224, 160)$			DNS	
L_x, L_y, H			5, 2, 1	

is used at the faces of the channel walls, that are located at $z = 0.0$ and $z = 1.0$ (see Figure 3.1). A uniform grid is used in the x- and y-directions. In the z-direction, the resolution is higher near the walls than in the centre of the channel. The turbulent flow is statistically steady before the dispersed phase is introduced.

The parameters associated with the continuous carrier-phase are given in Table 5.1. The associated grid resolutions (in wall-units, as defined in equation (3.14)), are given in Table 5.2. The grid resolutions used are similar or better than the ones used by van Haarlem (2000) in DNS studies using the DELFT code, and by Portela and Oliemans (2003) in LES mode. For $Re_\nabla = 360$, we compared the statistics of the single-phase flow to the DNS reference data by Moser et al. (1999). The maximum deviation of the mean streamwise fluid velocity ($+1.4\%$) occurs close to the walls of the channel. The maximum observed deviation in the Reynolds stresses is found for $u'u'$ (-12%), close the centre of the channel.

The one-way coupled simulations at $Re_\nabla = 720$ are conducted using DNS, whereas LES is used for the two-way coupled simulations. Cases labelled with «Re_∇ = XX» in the remainder of this chapter refer to large eddy simulations that are conducted at values of Re_∇ equal to 360, 540, 720 and 1080 at a fixed value of F_L or T_L to arrive at multiple values of the dimensionless strength of the inter-particle bonds (F_L^* and T_L^*), as defined in equation (5.1).

Dispersed-phase parameters. Apart from the parameters of the deposition and re-entrainment model, which will be discussed in Chapter 7, the dispersed-phase parameters of the Eulerian-Lagrangian model are given by: the radius of the primary

Table 5.2: Grid resolutions considered in this work, expressed in wall units, as defined in equation (3.14). Values printed in regular typeface represent grids that are used in DNS mode, and slanted values represent grids that are used in LES mode. The sequences of values reported correspond to $Re_\nabla = 360$, $Re_\nabla = 540$, $Re_\nabla = 720$ and $Re_\nabla = 1080$.

Grid (n_x, n_y, n_z)	(96, 64, 48)	(192, 128, 96)	(320, 224, 160)
Δ_x^+	*19, –, –, –*	*9.4, 14, 19, 28*	*–, –, 11, –*
Δ_y^+	*11, –, –, –*	*5.6, 8.4, 11, 17*	*–, –, 6.4, –*
$\Delta_z^+ \vert_{wall}$	*2.9, –, –, –*	*1.2, 1.8, 2.3, 3.5*	*–, –, 1.2, –*
$\Delta_z^+ \vert_{centre}$	*9.6, –, –, –*	*4.8, 7.3, 9.7, 15*	*–, –, 5.8, –*

particles (R_p), the volume fraction and number of primary particles, the added-mass corrected particle-fluid density ratio ($\breve{\rho}_p/\rho_f$), and the maximum stresses that the inter-particle bonds can withstand before breaking (F_L^N, F_L^S, T_L^B and T_L^T), as explained in Section 3.9.

Although our model has been constructed such that simulations can be conducted with polydisperse primary particle populations, we consider particles that are mono-disperse, with a radius equal to 0.5% of the channel height H. This relatively large primary particle size is adopted because it results in sufficiently large collision rates at moderate primary particle numbers, allowing the simulations to reach a steady-state within a reasonable simulation time. In each simulation, we study a constant amount of 250 000 primary particles, corresponding to a dispersed-phase volume fraction of 1.3%. The particles are individually introduced in the flow at random locations throughout the entire flow domain; their initial velocity is set equal to the local fluid velocity.

Typical asphaltene densities are about 1200 kg/m^3 (Yarranton and Masliyah, 1996), and, for light crude oils, oil densities can be as low as 800 kg/m^3. The density ratio ρ_p/ρ_f is therefore set equal to 1.5. This gives an effective, added-mass corrected density ratio $\breve{\rho}_p/\rho_f$ of 2.0.

The maximum stresses that the inter-particle bonds can withstand before breaking are the main parameters that are varied between simulations. For interpreting the results, the strengths of the inter-particle bonds (F_L and T_L) are scaled by the characteristic non-dimensional hydrodynamic force and torque acting on a single primary particle in a turbulent flow, which can be obtained by substituting u_∇ for $(\mathbf{U}_f - \mathbf{U}_p)$ in equation (3.40). The rescaled parameters can be expressed as:

$$F_L^* = \frac{F_L}{6\pi\mu_f R_p u_\nabla}; \qquad T_L^* = \frac{T_L}{6\pi\mu_f R_p^2 u_\nabla} \tag{5.1}$$

Multiple values of F_L^* and T_L^* are considered; their values are chosen such that the number of primary particles per agglomerate in steady-state is of $\mathcal{O}(100)$. Agglomeration numbers of this order were selected such that, on the one hand, a significant number of agglomerates can be simulated with a tractable number of primary particles, yet, on the other hand, it remains feasible to attribute macroscopic properties (e.g. shape, fractal dimension, etc.) to the agglomerates. Agglomerates are considered to be broken by only one single break-up mechanism in each simulation. The range of inter-particle bond strengths studied is given by F_L^* = [19.7, 222] and T_L^* = [172, 3092]. This corresponds to the bonds being able to withstand stresses that are significantly larger than those induced by the flow on a single primary particle.

The dimensions of the computational domain are equal for the dispersed phase and the continuous phase, and periodic boundary conditions are used for the particles in the streamwise and spanwise directions, like they are also used for the turbulent carrier phase.
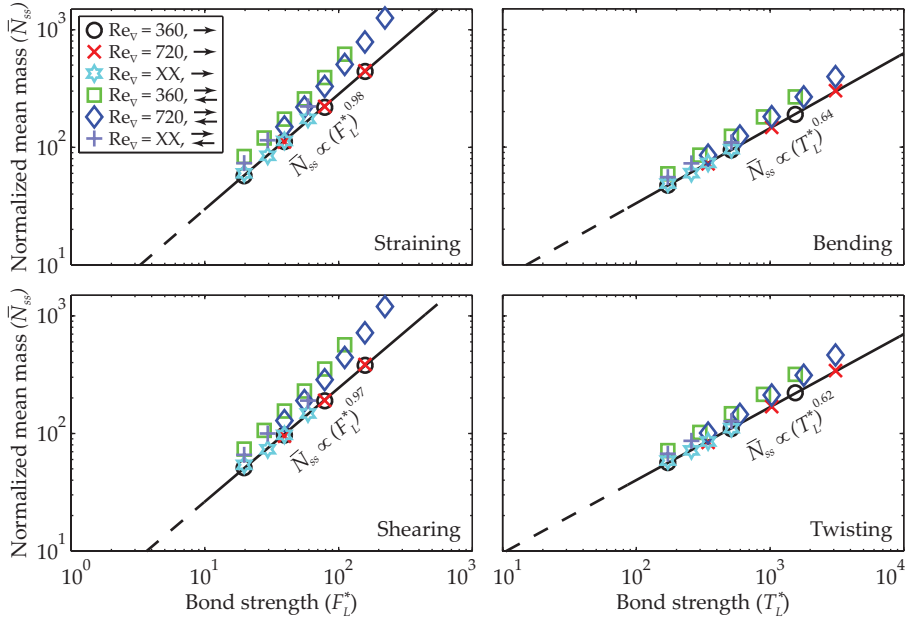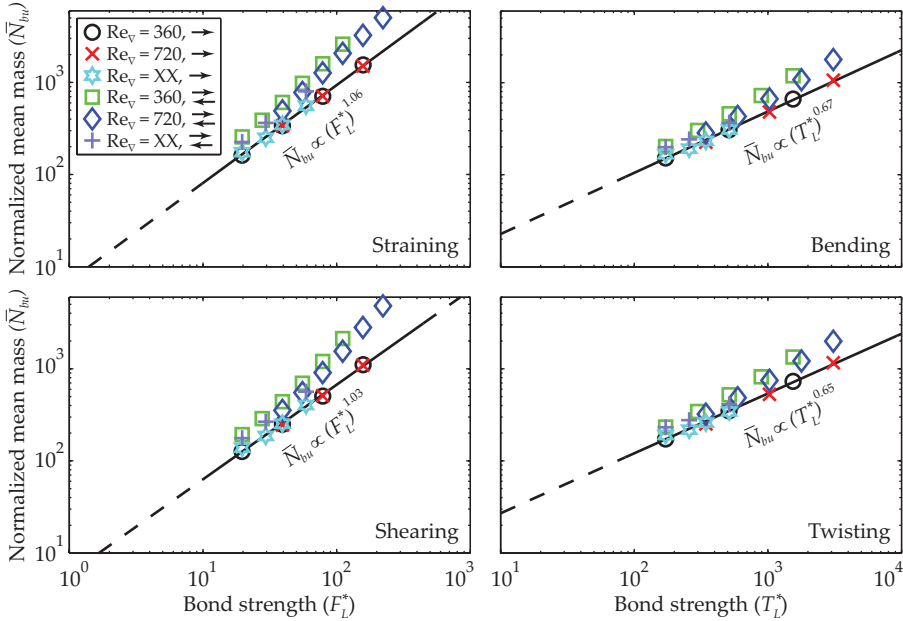
Figure 5.1: Scaling of the mean agglomerate mass *in steady-state* ($\bar{N}_{ss}$) with the characteristic strength of the inter-particle bonds, for different break-up mechanisms, one- and two-way coupling and multiple Reynolds numbers. The simulations labelled with «$Re_\nabla = XX$» have been conducted at a fixed value of F_L or T_L and for various Reynolds numbers to arrive at different values of F_L^* and T_L^*, as explained in Section 5.1.

5.2 Agglomerate properties

In absence of deposition and re-entrainment, the balance between agglomeration and break-up leads to a statistical steady-state (stationary state); in this thesis, we will simply refer to it as «steady-state». When the steady-state sets in, individual agglomerates still frequently undergo collisions, thereby forming new agglomerates, and agglomerates also are frequently broken. Overall, the effects of these processes cancel each other, such that the properties of the agglomerate population in a statistical sense remain unchanged. As a first property of the steady-state agglomerate population, we study the number-average steady-state mean mass of the agglomerates.

Scaling of steady-state mass of the agglomerates. Since we consider mono-dispersed primary particle populations, the mass of the agglomerates scales linearly with the number of primary particles that are part of the agglomerate, N. Therefore, all results presented in terms of the normalised mass of agglomerates correspond one-to-one to results in terms of the number of particles per agglomerate.

In Figure 5.1, the mean steady-state mass of the agglomerates ($\bar{N}_{ss}$) is shown as a

Figure 5.2: Scaling of the mean agglomerate mass *at agglomerate break-up* ($\bar{N}_{bu}$) with the characteristic strength of the inter-particle bonds, for different break-up mechanisms, one- and two-way coupling and multiple Reynolds numbers.

function of the characteristic strength of the inter-particle bonds for the different break-up mechanisms considered, for one- and two-way coupling, and for multiple Reynolds numbers. The solid lines in Figure 5.1 are least-square fits that relate the mean mass of the agglomerates to the value of F_L^* or T_L^* for one-way coupling: it is clear that for the range of parameters considered, interesting scaling relations between these quantities exist.

For one-way coupling, the mean mass of the agglomerates scales approximately linearly with F_L^* for the straining and break-up mechanisms; the scaling power for the steady-state mean mass of agglomerates that are broken due to bending and twisting is equal to approximately two-thirds. The steady-state mass is well described by scaling relations that are independent of the Reynolds number for all of the break-up mechanisms considered for one-way coupling. When considering two-way coupling, the scaling exponents relating the steady-state mean agglomerate mass to the strength of the inter-particle bonds increase with respect to one-way coupling for all break-up mechanisms considered; in this case, the scaling exponents do have some dependence on the Reynolds number.

Since the break-up of agglomerates directly depends on the strength of the inter-particle bonds inside the agglomerate, as well as on the break-up mechanism that is

considered, a natural way to proceed in explaining the scaling of the mean mass of the agglomerates is to consider the variation in properties of the agglomerates at the moment that they are broken.

Mean mass of agglomerates at break-up. In Figure 5.2, the dependence of the mean mass of the agglomerates measured at the moment that the agglomerates are broken ($\bar{N}_{bu}$) on the model parameters is presented.

To explain the results found in Figure 5.2, we will derive a simple model for the induced internal stresses in an agglomerate, which depends on (i) the number of primary particles that constitute the agglomerate and (ii) the hydrodynamic force that is acting on each of these particles. First, we will make the analysis for agglomerates that are broken by straining and shearing, and thereafter for agglomerates that are broken by bending and twisting.

Rewriting equation (3.47), it follows that the linear stress induced in an arbitrary bond b inside an agglomerate can be written in the form:

$$\mathbf{F}_b = \sum_m \left[\mathbf{F}_p - m_p \left(\frac{d\mathbf{U}_{cm}}{dt} + \frac{d\mathbf{\Omega}^S}{dt} \times \mathbf{r}_p + \mathbf{\Omega}^S \times \frac{d\mathbf{r}_p}{dt} \right) \right]$$

$$= -\sum_s \left[\mathbf{F}_p - m_p \left(\frac{d\mathbf{U}_{cm}}{dt} + \frac{d\mathbf{\Omega}^S}{dt} \times \mathbf{r}_p + \mathbf{\Omega}^S \times \frac{d\mathbf{r}_p}{dt} \right) \right] \tag{5.2}$$

where the summation ranges m and s are used to distinguish the two agglomerate branches that are linked by the bond b. If we now use:

$$\mathbf{I}^S \frac{d\mathbf{\Omega}^S}{dt} = \sum_{m\&s} [\mathbf{r}_p \times \mathbf{F}_p] - \frac{d\mathbf{I}^S}{dt} \mathbf{\Omega}^S \qquad \text{and} \qquad \frac{d\mathbf{U}_{cm}}{dt} = \sum_{m\&s} \left[\frac{\mathbf{F}_p}{m_a} \right]$$

equation (5.2) can be re-arranged as:

$$\mathbf{F}_b = \sum_m \left[\mathbf{F}_p - m_p \left(\sum_{m\&s} \left[\frac{\mathbf{F}_p}{m_a} \right] + [\mathbf{I}^S]^{-1} \left(\sum_{m\&s} [\mathbf{r}_p \times \mathbf{F}_p] \times \mathbf{r}_p \right) + \mathbf{C}_m \right) \right] \tag{5.3}$$

where the balance over branch s was omitted in favour of short-hand notion, and the term $\mathbf{C}_m$ represents all terms that do not depend on the hydrodynamic force $\mathbf{F}_p$.

The cross-products of $\mathbf{F}_p$ and $\mathbf{r}_p$ cross-correlate the individual component of $\mathbf{F}_b$ with all components of $\mathbf{F}_p$. If we assume, however, that characteristic values of the magnitude of the individual components of $\mathbf{F}_p$ are well represented by the characteristic values of the magnitude of $\mathbf{F}_p$ itself, equation (5.3) can be simplified to the form:

$$|\mathbf{F}_b| \propto N_m \left[|\mathbf{U}_f - \mathbf{U}_p|_m - \frac{N_m}{N_m + N_s} |\mathbf{U}_f - \mathbf{U}_p|_{m\&s} \right] + \mathbf{C}_m \tag{5.4}$$

where N_m represents the number of particles in agglomerate branch m and N_s the number of particles in branch s.

We have found that for all cases considered in this work, the constant term $\mathbf{C}_m$ (and, likewise, $\mathbf{C}_s$), which is associated with the centripetal acceleration that results from the solid body motion of the agglomerate, has a negligible ($< 5\%$) contribution to the magnitude of the total induced stress $|\mathbf{F}_b|$. Therefore, we can assume that the induced stresses inside the agglomerate effectively only depend on the slip velocity of the primary particles.

To arrive at a simple model that predicts the number of primary particles per agglomerate $N (= N_m + N_s)$ as a function of F_L^*, we further simplify equation (5.4). We assume that, at least for a particular break-up mechanism, the characteristic values of $|\mathbf{U}_f - \mathbf{U}_p|$ in branch m, in branch s, as well as over the entire agglomerate, change by a similar factor if the number of primary particles in the agglomerates changes. Furthermore, we assume that upon break-up, the relative fragmentation of the agglomerates (that is, the ratio of the number of primary particles that end up in the branches m and s), is independent of the value of F_L^*. In that case, our simple model predicts that the total number of primary particles N in an agglomerate that is broken at a given value of F_L^* is proportional to:

$$N \propto \frac{F_L^*}{|\mathbf{U}_f - \mathbf{U}_p|_{m\&s}} \tag{5.5}$$

According to this simple model, the dependence of the average of N over a large ensemble of break-up events (corresponding to $\bar{N}_{bu}$) on the value of F_L^* thus can be predicted from the characteristic magnitude of the slip velocity the primary particles inside those agglomerates.

Slip velocity of primary particles with respect to continuous carrier phase. Figure 5.3 shows the magnitude of the average slip velocity of the primary particles (in star units, as defined in equation (3.8)), as a function of the model parameters, both in steady-state, and at agglomerate break-up. In all cases, we find that the slip velocity is larger at the instant that the agglomerates are being broken than in steady-state. This effect can be contributed to two mechanisms. On the one hand, agglomerates are more likely to be broken when, temporarily, large gradients in hydrodynamic force act upon them, thus corresponding to larger magnitudes of the average slip velocity measured over the extent of the agglomerate. On the other hand, agglomerates consist of more primary particles when they are being broken when compared to the steady-state, and they thus experience fluid velocities from more different turbulent eddies.

Since the agglomerates have a very small non-dimensional density, and thus adapt quickly to changes in the fluid flow velocity, the agglomerates acts as a spatial filter to the fluid velocity along their perimeter. The more different branches of the agglomerates protrude through different turbulent eddies, the more the characteristic slip velocity therefore approaches the characteristic velocity difference between these eddies. The non-dimensional characteristic velocity difference between turbulent eddies is of the order of one, showing that the magnitude of the average slip velocity of the primary particles indeed approaches this characteristic velocity difference.
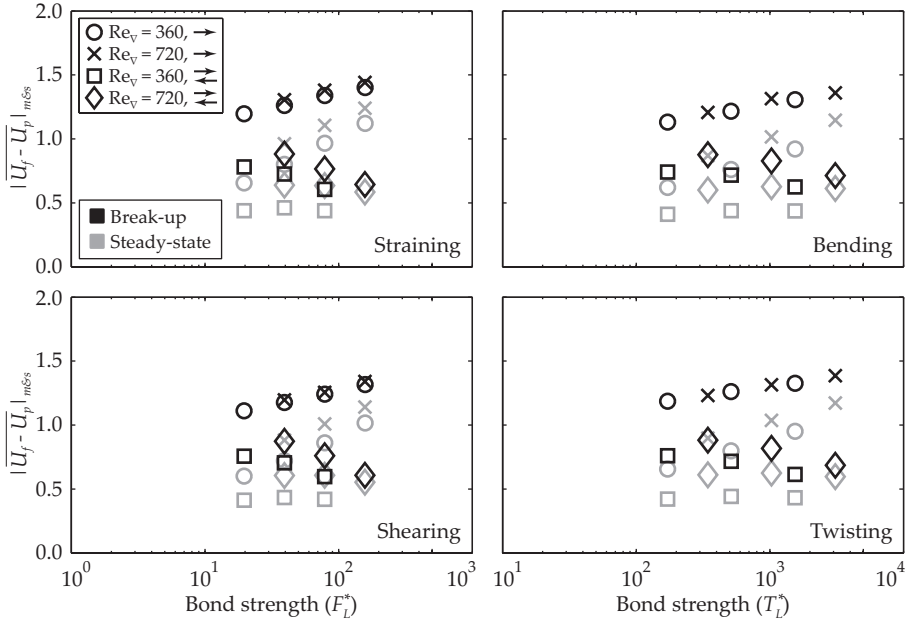
Figure 5.3: Average magnitude of the primary particle slip velocity measured in steady-state (grey) and at agglomerate break-up (black).

The feedback of the velocity filtering experienced by the agglomerates into the flow (when considering two-way coupling) causes local fluid velocity fluctuations to average out. This causes the overall slip velocity of the primary particles with respect to the fluid phase to decrease when two-way coupling is considered instead of one-way coupling. Since the agglomerates dampen turbulent velocity fluctuations more and more when they consist of larger numbers of primary particles, the magnitude of the slip velocity actually decreases with increasing values of F_L^* and T_L^* when two-way coupling is considered. As a result, the simple model in equation (5.5) predicts that the average number of primary particles per agglomerate at break-up scales with F_L^* with a power higher than one; this prediction agrees favourably to the actual results that were presented in Figure 5.2. The fact that the slip velocity depends on the Reynolds number when two-way coupling is considered also explains why $\bar{N}_{bu}$ is not independent of the Reynolds number in this case.

Similarly, the mean mass of the agglomerates at break-up found using one-way coupling should, according to equation (5.5), scale with the value of F_L^* to a power lower than one. This prediction is in contradiction with the results that are presented in Figure 5.2. We can explain this discrepancy by considering that equation (5.5) does not account for possible variations in the direction of the hydrodynamic force exerted on different primary particles in each of the branches of the broken agglomerate. In

the actual turbulent flow, the hydrodynamic force on each of the primary particles will not have an equally constructive contribution to the stress induced in the bond that is broken. Especially as the linear dimensions of the agglomerates increase, and primary particles within one branch of an agglomerate experience fluid velocities inside an increasing number of different turbulent eddies, the uniformity of the direction of the hydrodynamic force exerted on each of the particles will decrease.

Our results indeed show that the larger the value of F_L^*, the lower the fraction of the primary particles that constructively contribute to the stresses in the broken bond. Although the magnitude of the hydrodynamic force exerted on each individual primary particle increases with increasing values of F_L^* when one-way coupling is considered, the induced stresses therefore do not keep up with this increase. As a result, the mean mass of the agglomerates at break-up scales with F_L^* with a power slightly higher than one for the straining and shearing break-up mechanisms when one-way coupling is considered, even though the dependence of the slip velocity on the strength of the inter-particle bonds by itself suggests this should not be the case.

Scaling of mean mass for agglomerates that are broken due to bending or twisting. The dependencies of the average agglomerate mass at break-up on the value of F_L^*, on one- versus two-way coupling, and on the Reynolds number have been explained for the straining and shearing break-up mechanisms. Let us now consider how these results can be related to the dependence of $\bar{N}_{bu}$ on T_L^* for the bending and twisting break-up mechanisms.

The results in Figures 5.3 show that the dependence of the magnitude of the slip velocity on F_L^* and T_L^* is qualitatively the same. Likewise, our results show that the dependence of the fraction of the primary particles that constructively contribute to the stresses in the broken bond on F_L^* and T_L^* are not too different. The difference in the scaling exponents for the mean agglomerate mass as a function of the strength of the inter-particle bonds between the force- and torque-related break-up mechanisms thus has to be explained by the fact that the torque induced in the bonds of the agglomerates scales with the cross-product of the radius of the agglomerate and the induced force. This means that for the bending and twisting break-up mechanisms, the mean number of particles per agglomerate at break-up can be expected to scale with:

$$N \propto \frac{T_L^*}{\left| \mathbf{r}_p \times (\mathbf{U}_f - \mathbf{U}_p)_{m\&s} \right|} \approx \frac{T_L^*}{\left| \mathbf{r}_p \right| \left| \mathbf{U}_f - \mathbf{U}_p \right|_{m\&s}} \tag{5.6}$$

In Section 5.2, we relate the effective radius of the agglomerates to the number of primary particles by the fractal dimension. Using this relation, we can rewrite equation (5.6) as:

$$N \propto \left[\frac{T_L^*}{\left| \mathbf{U}_f - \mathbf{U}_p \right|_{m\&s}} \right]^{D_f/(1+D_f)} \tag{5.7}$$

where D_f is the fractal dimension of the agglomerates. Considering a typical fractal dimension of 2.0, the factor $D_f/(1 + D_f)$ can well explain the decreased scaling exponents of N_{ss} and N_{bu} with T_L^* with respect to F_L^* found in Figures 5.1 and 5.2.
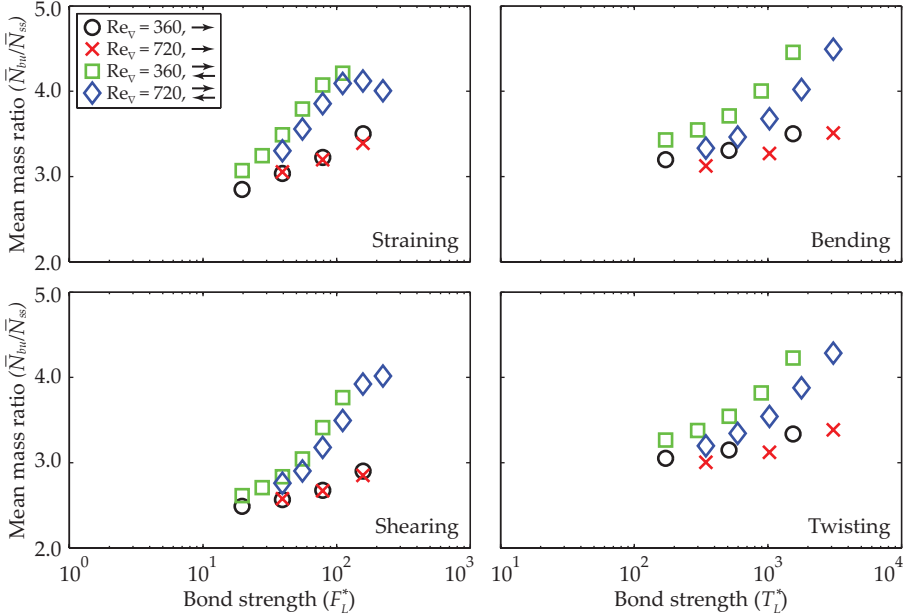
Figure 5.4: Ratio between the average agglomerate mass at break-up and steady-state mean agglomerate mass ($\bar{N}_{bu}/\bar{N}_{ss}$).

Ratio of mean masses at break-up and in steady-state. Figure 5.4 shows the dependence of the ratio $\bar{N}_{bu}/\bar{N}_{ss}$ on the model parameters. As expected, the mean mass of the agglomerates measured during agglomerate break-up is significantly larger than the steady-state mean mass of the agglomerates. Our results also show, however, that the ratio $\bar{N}_{bu}/\bar{N}_{ss}$ depends on the break-up mechanism, the strength of the bonds inside the agglomerates, and especially on whether one- or two-way coupling is used. These differences on the one hand stem from the fact that agglomerates are, on average, not broken in branches of equal numbers of primary particles (see Section 5.3). Variations in the lifetime of agglomerates with different N also contribute to the trends in $\bar{N}_{bu}/\bar{N}_{ss}$ found.

Let us consider a simple model in which agglomerates are broken in two parts with $N_m = f\bar{N}_{bu}$ and $N_s = (1-f)\bar{N}_{bu}$ primary particles. If we denote the lifetime of the original agglomerate and both of the formed branches as $\mathcal{T}_{bu}$, $\mathcal{T}_m$ and $\mathcal{T}_s$, the ratio of $\bar{N}_{bu}/\bar{N}_{ss}$ can be approximated by:

$$\frac{\bar{N}_{bu}}{\bar{N}_{ss}} = \frac{\mathcal{T}_{bu} + \mathcal{T}_m + \mathcal{T}_s}{\mathcal{T}_{bu} + f\mathcal{T}_m + (1-f)\,\mathcal{T}_s} \tag{5.8}$$

where we consider the lifetime of an agglomerate as the time interval between consecutive collisions or break-up events that the agglomerate undergoes. Since both

f and $1 - f$ are smaller than one, the ratio $\bar{N}_{bu}/\bar{N}_{ss}$ increases when the lifetime of the agglomerate branches $\mathcal{T}_m$ and $\mathcal{T}_s$ increase with respect to the lifetime $\mathcal{T}_{bu}$ of the agglomerate that is being broken.

The results of our simulations show that within an agglomerate population, agglomerates that consist of a large number of primary particles undergo collision and break-up events much more frequently than agglomerates that consist of a small number of primary particles. The lifetime of large agglomerates is thus shorter than that of small agglomerates. In all of the cases considered, the agglomerate lifetime-spectrum is such that the ratios $\mathcal{T}_m/\mathcal{T}_{bu}$ and $\mathcal{T}_s/\mathcal{T}_{bu}$ increase for increasing values of F_L^* and T_L^*. This explains why there is a general increasing trend of $\bar{N}_{bu}/\bar{N}_{ss}$ with increasing strengths of the inter-particle bonds.

Overall, the lifetime of the agglomerates increases when the value of F_L^* or T_L^* is increased. For one-way coupling, the increase in $\mathcal{T}$ with F_L^* and T_L^* is stronger for those agglomerates that consist of a large number of primary particles than it is for the agglomerates that consist of few primary particles. This counteracts the changes in $\mathcal{T}_m/\mathcal{T}_{bu}$ and $\mathcal{T}_s/\mathcal{T}_{bu}$ that occur for increasing values of F_L^* and T_L^*, thereby making the fraction $\bar{N}_{bu}/\bar{N}_{ss}$ only weakly dependent on the value of the strength of the inter-particle bonds. When two-way coupling is used, the relative increase in agglomerate lifetime as a function of the strength of the inter-particle bonds has a negligible dependence on the number of primary particles that make up the agglomerates. Therefore, the changes in $\mathcal{T}_m/\mathcal{T}_{bu}$ and $\mathcal{T}_s/\mathcal{T}_{bu}$ that occur for increased values of $\bar{N}_{bu}$ are not compensated, explaining why the ratio $\bar{N}_{bu}/\bar{N}_{ss}$ increases more strongly as a function of F_L^* and T_L^* than for the one-way coupling.

Radius of gyration and fractal dimension. In the literature, asphaltene agglomerates are frequently reported to have a fractal structure. Fractals are objects that exhibit a pattern that (almost) perfectly repeats itself at every scale. We characterise the agglomerates formed in our simulations using the mass-fractal dimension D_f, which is defined as:

$$m_a \propto R_g^{D_f} \tag{5.9}$$

where m_a represents the mass of an individual agglomerate and R_g is a representative radius of the agglomerates. In this work, we use the radius of gyration for representing the agglomerate radius, defined as:

$$R_g \equiv \sqrt{\frac{1}{N} \sum_p (\mathbf{r}_p \cdot \mathbf{r}_p)} \tag{5.10}$$

where the sum runs over all N primary particles in the agglomerate. Figure 5.5 shows the average radius of gyration for the steady-state agglomerate population as a function of the model parameters.

Since the mass of the agglomerates scales with the radius of gyration to the power of the fractal dimension, a quick comparison between the scaling exponents found in Figures 5.1 and 5.5 reveals that the fractal dimensions should approximately be equal to
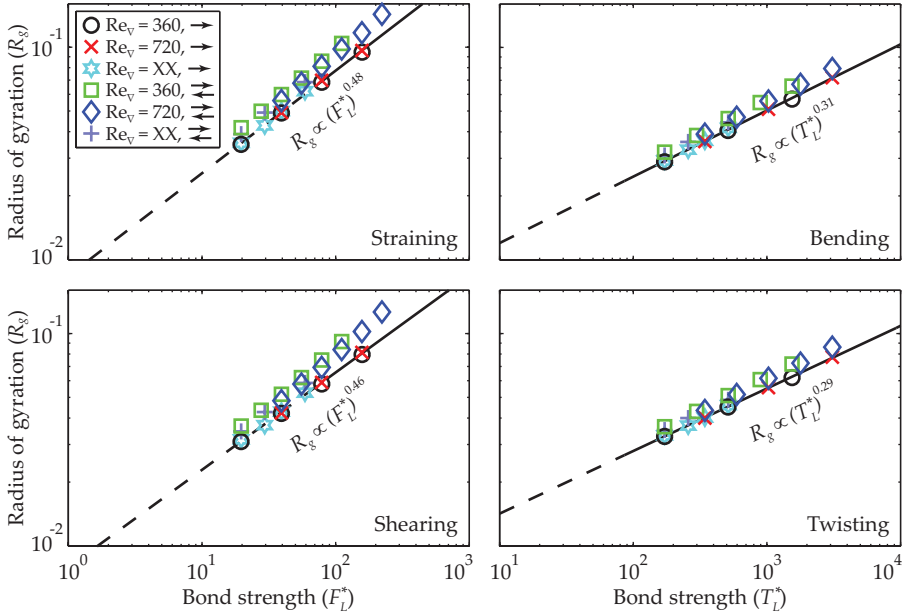
Figure 5.5: Scaling of the steady-state average radius of gyration of the agglomerates with the characteristic strength of the inter-particle bonds, for different break-up mechanisms, one- and two-way coupling and multiple Reynolds numbers.

two. To determine the actual fractal dimension of the agglomerates, a large ensemble of (m, R_g) data-points is obtained from steady-state agglomerate populations. This ensemble is subsequently divided into 100 sections of increasing agglomerate mass, and for each of these sections, the average value of R_g is determined; subsequently expression (5.9) is fit to these data to obtain the fractal dimension of the agglomerates. Figure 5.6 summarises the results obtained this way.

Indeed, we observe that the fractal dimensions are approximately equal to two. In general a monotonic increase is found with increasing values of F_L^* and T_L^*. Overall, the range values of D_f found in this work compare favourably to the larger end of the spectrum of asphaltene fractal dimensions that are reported in the literature for laboratory samples (Rahmani et al. (2005[†]) find fractal dimensions of 1.9 to 2.0). They are also similar to the classical results for ballistic cluster-cluster aggregation, for which $D_f \approx 1.95$ (Meakin and Jullien, 1988). Confirming visual observations, like the sample agglomerates shown in Figure 5.7, the range of fractal dimensions obtained indicates that the agglomerates have a very open, porous, structure.

There is a striking difference in the dependence of the fractal dimension on the model parameters between the straining and shearing break-up mechanisms on the one hand, and the bending and twisting break-up mechanisms on the other hand. The
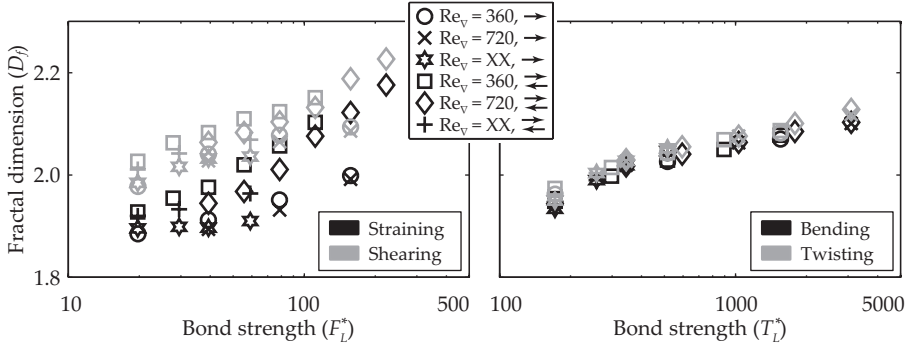
Figure 5.6: Fractal dimensions for steady-state agglomerate populations broken by straining and shearing (left), and bending and twisting (right).

change in fractal dimension when switching from one- to two-way coupling, as well as for different Reynolds numbers is virtually absent for the latter break-up mechanisms. Furthermore, the fractal dimensions for agglomerates that are broken by straining are distinctively smaller than those for agglomerates that break-up due to shearing. For the latter break-up mechanisms (viz. straining and shearing) two-way coupling is found to significantly increase the fractal dimensions compared to the values found for one-way coupling, and increasing the Reynolds number is found to decrease the fractal dimension.

Since the fractal dimension is a measure of the degree of compactness of the agglomerates, differences in the fractal dimension are related to the degree of inter-penetration that agglomerates attain before they actually collide. If agglomerates approach each other from a large distance, there overall structure, characterised by the fractal dimension, will determine the degree of inter-penetration that can be achieved before primary particles of both agglomerates actually collide. Since the fractal dimensions of the agglomerates do not deviate that much between different break-up mechanisms, we may expect that for agglomerates that approach each other from a relatively large distance, the inter-penetration at the moment of the actual collision will be weakly dependent on the break-up mechanism at most. The cause of the variations in the compactness of the agglomerates between different break-up mechanisms and at different values of the internal agglomerate strength is therefore more likely to be related to the chance that agglomerates collide upon being in close proximity prior to the collision.

We propose that the variation in the fractal dimension can be explained by differences in the likelihood that agglomerate branches, shortly after they are being created in a break-up event, re-collide, either at the same pair of primary particles, or with a different pair that is close to the broken bond. Agglomerate branches that consist of only a small number of primary particles can protrude much more easily into

the matrix of another, larger agglomerate branch. It therefore may be expected that the mechanism of agglomerate re-structuring, caused by subsequent break-up and collision events within the same agglomerate, is dominated by those break-up events in which one of the branches of the broken agglomerate contains much less primary particles than the other branch. If such an event occurs, the question whether the agglomerate will re-structure into a more compact form depends on the relative motion of both agglomerate branches after they are being broken apart.

After a break-up event, the chance that the agglomerate branches become less inter-penetrated (or even completely move apart) increases the quicker the branches separate along their initial line of contact (viz. along the direction through the bond that was broken). Only for the straining break-up mechanism, the relative acceleration of the branches in this direction is actually related to the characteristic strength of the inter-particle bonds that governs the agglomerate break-up. As a consequence, our results show that for this break-up mechanism, the relative acceleration of the agglomerate branches is significantly larger than for any of the other break-up mechanisms. As a result, the chance that the inter-penetration of agglomerate branches decreases after a break-up event is much greater for agglomerates that are broken by straining than for agglomerates that are broken by another mechanism of break-up. This explains why the straining break-up mechanism leads to a significantly lower fractal dimension than the other break-up mechanisms.

Accepting the agglomerate re-structuring mechanism sketched above also enables to explain the influence of two-way coupling and of the Reynolds number on the fractal dimension of the agglomerates. Since the inertia of the agglomerates is relatively low, and small agglomerate branches can quickly adapt to the local fluid velocity fluctuations that occur in the turbulent flow, the chance that a small agglomerate branch can escape from the vicinity of its large counterpart increases when the intensity of the turbulence increases. Agglomerates will thus become less compact (and have a smaller fractal dimension) when the Reynolds number is increased, and more compact (corresponding to a larger fractal dimension) when the turbulence fluctuations (and thus the local fluid velocity differences surrounding both agglomerate branches) are damped due to two-way coupling.

Agglomerate shape. To characterise the shape of the agglomerates, we here present results for the cumulative agglomerate shape distribution function, which represents the probability that a randomly selected agglomerate has a certain shape. To this end, the dimensions of each agglomerate are measured along its three primary axes of inertia, by finding the largest distance between any pair of primary particles that are part of the agglomerate along these axes. The ratios between these lengths can then be used to characterise the shape (form factor) of the agglomerates. Figure 5.7 shows the average cumulative agglomerate shape distribution functions for the different break-up mechanisms considered in this work, along with examples of agglomerates that are representative of certain regions of this distribution function.
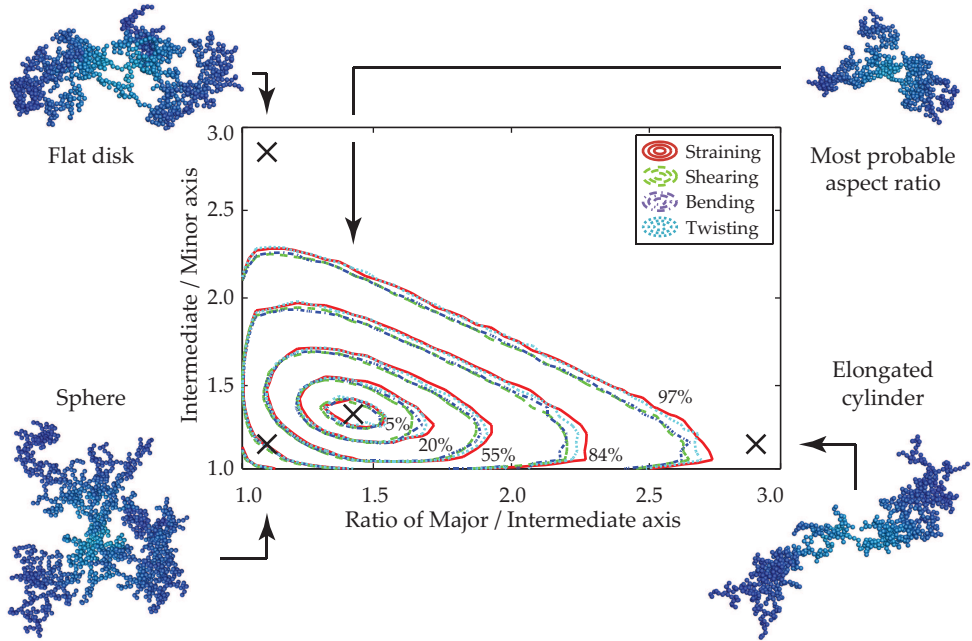
Figure 5.7: Steady-state cumulative agglomerate shape distribution functions averaged over all model parameters considered per break-up mechanism. The numbers indicated by the contours denote the percentage of the total agglomerate population that has a form factor contained within those contours (viz. the probability that an agglomerate picked at random has a particular form factor). The sample agglomerates shown provide a visual indication of representative agglomerate shapes for different regions of the distribution function.

It is found that the shape of the agglomerates is hardly dependent on the break-up mechanism considered. The most probable agglomerate shape has proportions of approximately 1.4/1.0/0.7 for the major, intermediate and minor axis, respectively, corresponding to slightly flattened and elongated sphere-like shapes. In Figure 5.8, the influence of one- and two-way coupling and of the Reynolds number on the agglomerate shape is shown. It can clearly be inferred that the shape of the agglomerates formed is similar when one- and two-way coupling are considered; likewise, the Reynolds number has a negligible influence on the agglomerate shape. In Figure 5.9, the influence of the strength of the bonds inside the agglomerates on the agglomerate shape is shown. Only a slight dependence of the agglomerate shape on the strength of the inter-particle bonds is found: for increasingly strong agglomerates, the shape distribution functions shift slightly towards lower values of the axes ratios (viz. the agglomerates become slightly more spherical).
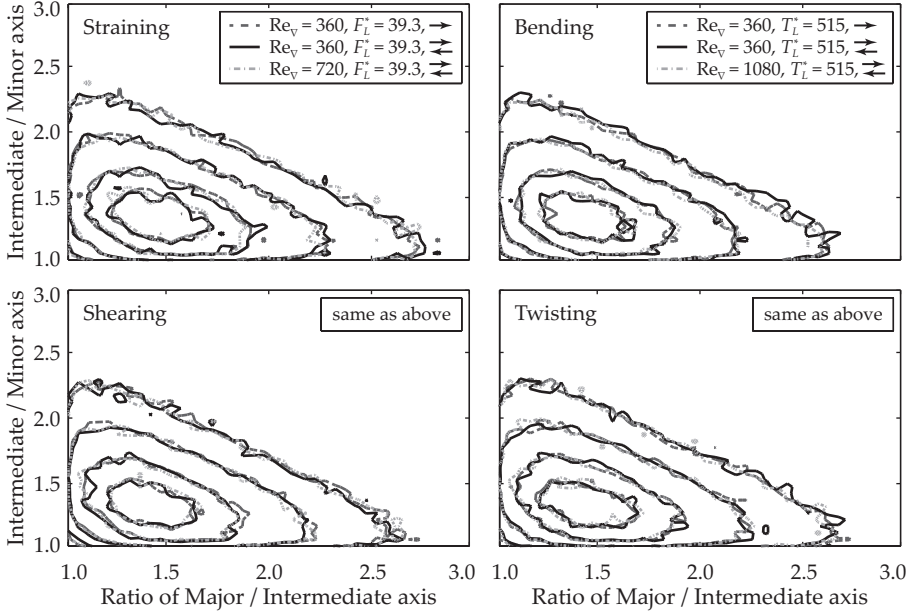
Figure 5.8: Steady-state cumulative agglomerate shape distribution functions for one- and two-way coupling and multiple Reynolds numbers. The contour levels are the same as in Figure 5.7; the 5% contour has been omitted to improve level-distinguishability.

5.3 Process properties

In terms of modelling, a good knowledge of the properties of the agglomeration and break-up processes is of high importance. Collision kernels, for instance, are important closure relations in population balance models that describe the evolution of a species that is undergoing agglomeration. Similarly, the fragmentation of agglomerates during break-up is an important closure to population balance models in which break-up is taken into account. In this section, we will discuss these aspects, as observed in our Eulerian-Lagrangian agglomeration and break-up model.

Overall collision and fragmentation kernel. In steady-state, the collision and break-up rate, measured over agglomerates that consist of arbitrary numbers of primary particles, are in balance and thus equal. To compare the overall rates of collision and break-up between different cases, we consider the overall collision kernel, independent of the number of primary particles per agglomerate. It is, by definition, given by:

$$C \equiv \Gamma \mathcal{N}^2 \tag{5.11}$$

where C is the collision rate (number of collisions per unit of time and unit of volume), and $\mathcal{N}$ represents the number of agglomerates per unit volume. Consequently, the
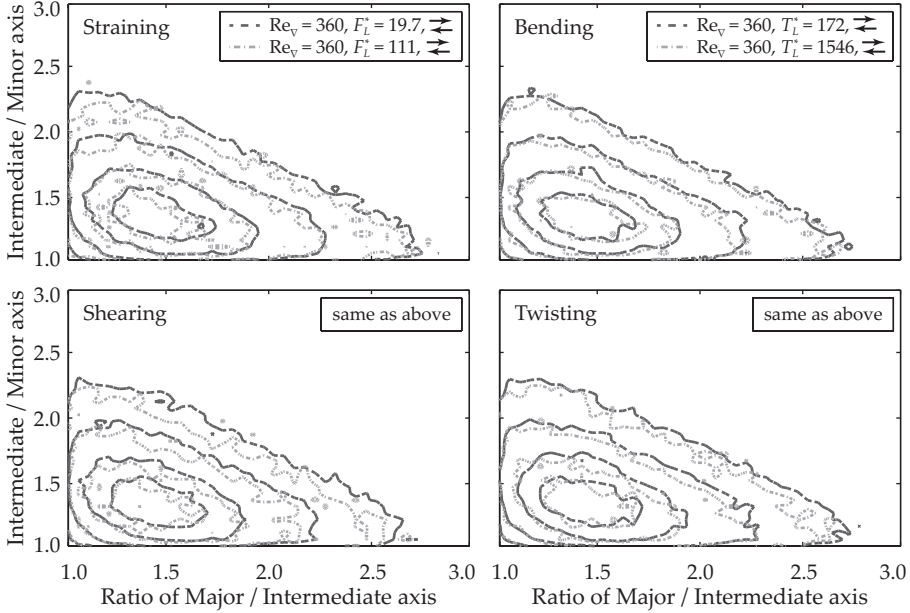
Figure 5.9: Steady-state cumulative agglomerate shape distribution functions for different values of F_L^* and T_L^*. The contour levels are the same as in Figure 5.7; the 5% contour has been omitted to improve level-distinguishability.

dimension of the collision kernel is unit of volume per unit of time.

Figure 5.10 summarises the dependence of this overall collision kernel on the strength of the inter-particle bonds, one- and two-way coupling and the Reynolds number. Here, the results are shown as a function of the value of $\bar{N}_{ss}$ instead of F_L^* or T_L^*, because collision kernels that have been proposed in the literature for fractal agglomerates often are assumed to depend on the number of primary particles that comprise the colliding agglomerates.

For each of the break-up mechanisms, the magnitude of the collision kernel is found to decrease by about 20% (shearing) to 25% (straining) and 30% (bending and twisting) if two-way coupling is used instead of one-way coupling. This indicates that the attenuation of turbulence caused by the back-forcing of the dispersed phase onto the turbulent carrier phase reduces the frequency at which agglomerates collide (and thus, in steady-state, are being broken). At constant values of $\bar{N}_{ss}$, the kernels for straining, bending and twisting are found to be about 40%, 25% and 20% smaller than those for agglomerates that are broken by shearing, respectively. This result supports the hypothesis that agglomerate branches that result from break-up due to straining have a lower probability to re-collide shortly after the break-up event than agglomerate branches that result from break-up due to the other mechanisms, as
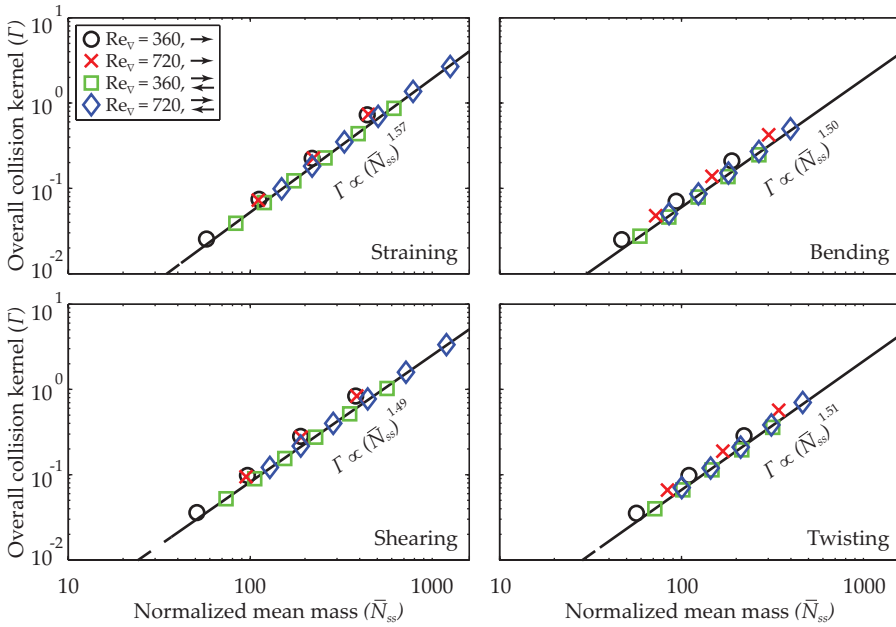
Figure 5.10: Overall collision and break-up kernel, for agglomerates that are broken at different values of the characteristic strength of the inter-particle bonds, using one- and two-way coupling at multiple Reynolds numbers. The solid lines represent least square error fits to all the two-way coupled simulation results.

posed when the results for the fractal dimension were discussed earlier.

Collision kernel correction factor as a function of the wall-normal coordinate. In the discussion of the one-dimensional drift-flux model in Chapter 4, collision kernels that predict the collision rate that occurs as a result of mean shear and turbulent velocity fluctuations were given in equations (4.31) and (4.32). To study the accuracy by which these collision kernels can predict the actual collision rates observed in our Eulerian-Lagrangian simulations, we introduce a correction factor $\mathcal{C}$ that is required to reconcile the model predictions to the actual collision rates found.

For statistical accuracy, we will not study the collision kernel correction factor as a function of the number of primary particles inside the agglomerates. Instead, only the overall correction factor for all agglomerate sizes will be considered. Like in Chapter 4, we here relate the collision cross-section of the agglomerates to the radius of the primary particles and the number of primary particles in the agglomerate:

$$\bar{d} = 2R_p \bar{N}_{ss}^{1/D_f} \tag{5.12}$$

The resulting overall collision kernel due to mean shear is given by:

$$\Gamma = \frac{4}{3} G \left(2R_p\right)^3 \bar{N}_{ss}^{3/D_f} \tag{5.13}$$

where G is the average shear rate. The overall collision kernel due to turbulent velocity fluctuations is given by:

$$\Gamma = \sqrt{\frac{8\pi}{15}} \sqrt{\frac{\epsilon}{\nu}} \left(2R_p\right)^3 \bar{N}_{ss}^{3/D_f} \tag{5.14}$$

where it is assumed that the agglomerates are smaller than the smallest eddies (viz. the Kolmogorov micro-scale) of the flow.

In the simulations, the dissipation rate of the turbulent kinetic energy that is needed to close the turbulent fluctuation collision kernel is computed by:

$$\epsilon = \frac{\nu}{2} \overline{\left(\frac{du_i}{dx_j} + \frac{du_j}{dx_i}\right) \left(\frac{du_i}{dx_j} + \frac{du_j}{dx_i}\right)} \tag{5.15}$$

in which u_i represents the turbulent velocity fluctuations in the direction i.

Since the agglomerates formed in our model are not smaller than the Kolmogorov micro-scale of the flow, they will collide as a result of both turbulent velocity fluctuations and macroscopic velocity gradients in the flow. The collision kernel given in equation (5.14), can easily be modified to take the mean velocity gradient in the channel into account as well. To this end, the turbulent energy dissipation ϵ is replaced by a fictitious dissipation term that has the form:

$$\hat{\epsilon} = \frac{\nu}{2} \overline{\left(\frac{dU_i}{dx_j} + \frac{dU_j}{dx_i}\right) \left(\frac{dU_i}{dx_j} + \frac{dU_j}{dx_i}\right)} \tag{5.16}$$

where the U_i represent the instantaneous fluid velocity components. The resulting collision kernel effectively describes the collision kernel as a superposition of the contributions of the turbulent eddies (equation (5.14)) and the time-averaged shear profile in the channel (equation (5.13), with $G = G(z)$).

For this final combined mean-shear and turbulent velocity fluctuation collision kernel, the collision kernel correction factor $\mathcal{C}$ can be written as:

$$\mathcal{C} = \frac{C}{\mathcal{N}^2 \sqrt{\frac{8\pi}{15}} \sqrt{\frac{\hat{\epsilon}}{\nu}} \left(2R_p\right)^3 \bar{N}_{ss}^{3/D_f}} \tag{5.17}$$

where C is the collision rate according to the simulations with the Eulerian-Lagrangian model. Before considering the collision kernel in further detail, we note that, for $D_f \approx 2.0$, the fractal collision kernels given in equations (5.13) and (5.14) predict that the collision kernel scales with $\bar{N}_{ss}$ to the power one and a halve, which compares favourably to the actual values reported in Figure 5.10.
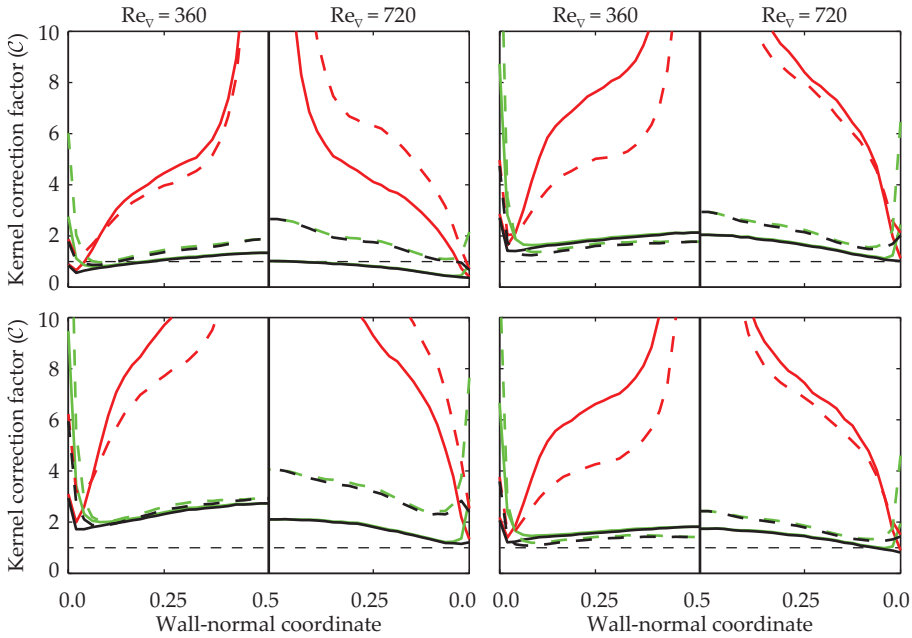
Figure 5.11: Collision kernel correction factor $\mathcal{C}$ as a function of the wall-normal coordinate in the channel, for different collision kernels. Red lines: mean-shear, green lines: turbulent fluctuations, black: mean-shear and turbulent fluctuations. Top to bottom, left to right: straining, shearing, bending, twisting. Solid lines represent one-way coupled results, and dashed lines represent two-way coupled results.

Figure 5.11 shows the value of $\mathcal{C}$ as a function of the wall-normal coordinate, for (i) the mean-shear collision kernel (5.13), (ii) the turbulent collision kernel, not taking into account the mean shear in the flow (5.14), and (iii) the full collision kernel, given in equation (5.14), with $\epsilon = \hat{\epsilon}$. Each line in each graph represents data that have been averaged across three to four simulations with different values of F_L^* or T_L^*, since we are mainly interested in the overall performance of the different collision kernels. The results in Figure 5.11 show that the mean-shear collision kernel significantly underestimates the collision rate of the agglomerates close to the centre of the channel, in the region where the mean shear rate is relatively small. The purely turbulent collision kernel is found to underestimate the collision rate close the walls of the channel, in the region where the mean shear rate of the flow is large. For any given case, the best match between the combined collision kernel prediction and the actual* collision rate is found using the combined mean shear and turbulent velocity fluctuations kernel, and therefore, we will study the predictions of this last kernel in more detail.

---

*The term «actual» refers to the simulation results as obtained with the Eulerian-Lagrangian model.
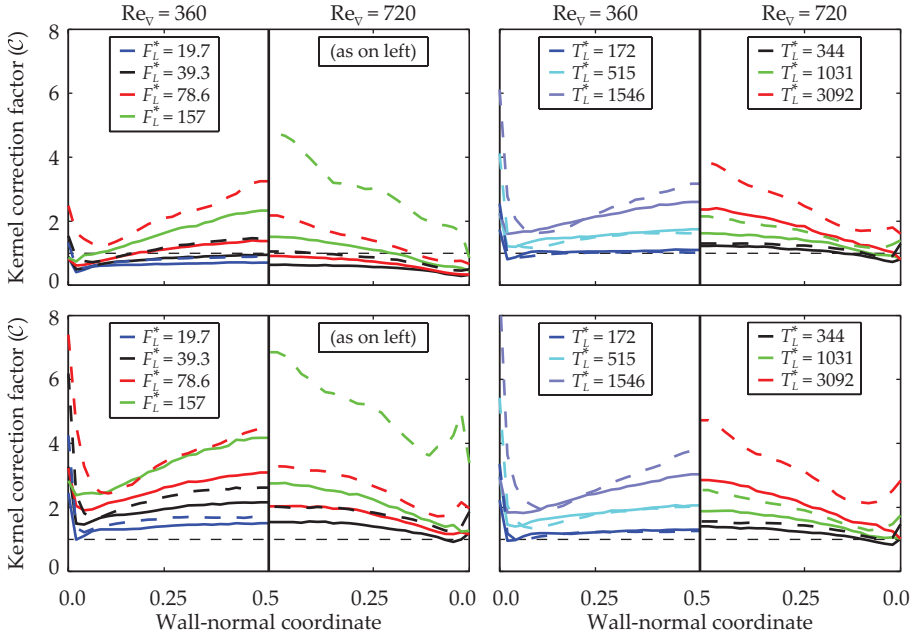
Figure 5.12: Collision kernel correction factor $\mathcal{C}$ as a function of the wall-normal coordinate in the channel. Top to bottom, left to right: straining, shearing, bending, twisting. Solid lines represent one-way coupled results, and dashed lines represent two-way coupled results.

In Figure 5.12, the average collision kernel correction factor given in equation (5.17) is shown as a function of the wall-normal coordinate for each value of F_L^* and T_L^* individually. The correction factor required to match the kernel predictions to the actual collision rates is typically of the order 0.5 to 5. In general, it is found that the collision kernel underpredicts the actual collision rate, except for these agglomerates that are broken by straining at a small values of F_L^*, where it overpredicts the collision rate. The deviation between the actual and predicted collision kernels increases when the strength of the inter-particle bonds increases. In general, the underprediction of the actual collision rate is most pronounced towards the centre of the channel, as well as close to the channel walls for $Re_\nabla = 360$. Note that the exact values of the collision kernel correction factor are quite sensitive to the exact value to the fractal dimension. Therefore, the results in Figure 5.12 should be interpreted qualitatively only.

Relative fragmentation of agglomerates during break-up events. Another important aspect of modelling a system of agglomeration and break-up is the relative fragmentation of agglomerates during break-up. A common assumption made in population balance models that are proposed in the literature is that agglomerates break in two branches of equal mass (binary breakage). To judge whether such a symmetrical branch distribution is also observed in our Eulerian-Lagrangian model,
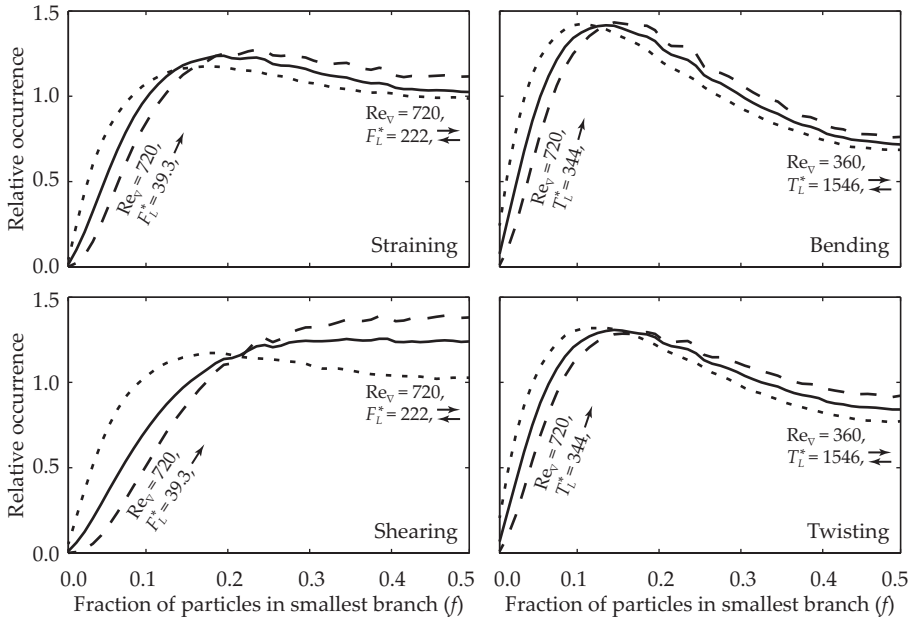
Figure 5.13: Histogram of the fraction of the primary particles that end up in the smallest agglomerate branch during a break-up event. Solid lines: averaged results over all cases considered per break-up mechanism, dashed lines: extreme cases as indicated by the labels shown.

Figure 5.13 shows the average fragmentation of the agglomerates observed for each of the break-up mechanisms considered in this work, complemented with extreme cases found per break-up mechanism. More specifically, the figure shows a histogram of the fraction of the number of primary particles of the agglomerate that end up in the branch that contains the smallest number of the primary particles.

The results in Figure 5.13 clearly show that binary breakage, which would be represented in the histograms by a δ-function at $f = 0.5$, is a poor representation of the relative fragmentation of the agglomerates for any of the break-up mechanisms. It is most closely approached by agglomerates that are broken due to shearing (where splitting of the agglomerate in two branches that contain an equal number of primary particles at least is one of the most probable outcomes of a break-up event). On average, however, the branch distribution is skewed towards forming one branch that contains a minority and one branch that contains the majority of the primary particles of the agglomerate that is being broken.

The scaling of the induced torque with respect to the radius of the agglomerates and the induced force in the inter-particle bonds explains why the branch distributions of agglomerates that are broken by bending and twisting are less symmetric than those

found for agglomerates that are broken by straining or shearing. A small branch of an agglomerate that is located relatively far away from the centre of mass of the agglomerate can more easily induce a large torque in the inter-particle bond that keeps it attached to the agglomerate than it can induce a large force. Therefore, small agglomerate branches more easily are formed by the torque-induced break-up mechanisms than by the force-induced break-up mechanisms.

In general, increasing values of F_L^* and T_L^* are found to produce more asymmetric fragmentation of the agglomerates, as do decreasing values of the Reynolds number, as well as two-way coupling instead of one-way coupling. We propose that these effects can be explained by the fact that any of the aforementioned parameter increases the $\bar{N}_{bu}$ of the agglomerates. In agglomerates that consist of a large number of primary particles, the number of bonds between primary particles that experience an induced stress that exceeds the strength of the bonds will be larger than in agglomerates that are made up of a smaller number of primary particles. Since, in our break-up model, the actual bond in the agglomerate that is being broken if multiple bonds in an agglomerate are eligible for break-up is selected at random, the chance that an agglomerate is broken in asymmetric branches can be expected to increase if the number of primary particles inside the agglomerate increases.

5.4   Modification of turbulence due the presence of agglomerates

When two-way coupling is considered, and the forces that the agglomerates exert on the fluid parcels of the turbulent carrier phase are thus taken into account, the presence of the agglomerates will influence the turbulent flow itself. To monitor to what extent the turbulence is modified by the presence of the dispersed phase we study (i) the bulk Reynolds number of the flow and (ii) the turbulence intensity as a function of the strength of the inter-particle bonds formed in the dispersed phase.

Flow rate / bulk Reynolds number. Figure 5.14 shows the increase in the overall flow rate in the channel upon including the influence of the dispersed phase on the flow using two-way coupling, as a percentage of the flow rate that is found when one-way coupling between the continuous phase and the dispersed phase is used (that is, when from the perspective of the fluid, the flow is not laden). Since the bulk Reynolds number is directly related to the average non-dimensional fluid velocity in the channel and the pressure-gradient Reynolds number (as defined in equation (3.11)), changes in the average flow rate translate one-to-one into changes in the bulk Reynolds number. To better separate between the effects of (i) the general lading of the flow with a dispersed phase and (ii) the fact that the dispersed phase is undergoing agglomeration and break-up, we have also included results obtained for a flow that is laden with two-way coupled non-interacting spherical point particles, with the same properties and volume fraction as in all other simulations.

The results shown in 5.14 clearly indicate that the overall flow rate is hardly affected by including the non-interacting dispersed phase using two-way coupling. For the simulations that are conducted at $Re_\nabla = 360$ (using DNS), we find a decrease in the overall flow rate by 0.6%, whereas in the simulations at $Re_\nabla = 720$ (using LES),
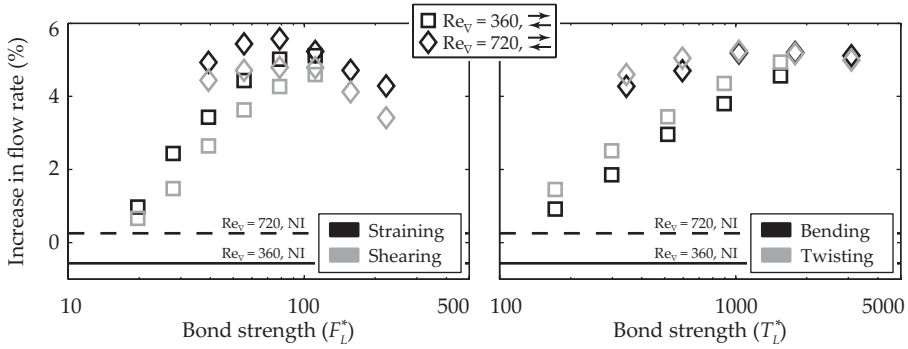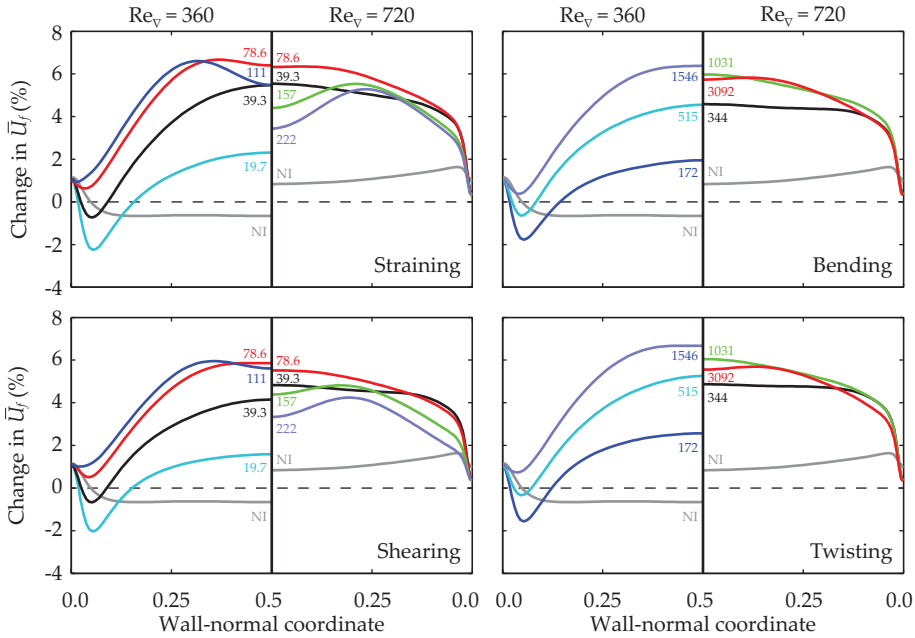
Figure 5.14: Change in the continuous carrier-phase flow rate with respect to non-laden flow upon including a dispersed phase using two-way coupling. The horizontal lines labelled «Re_∇ = 360 NI» and «Re_∇ = 720 NI» indicate results that have been obtained using a two-way coupled non-interacting dispersed phase with the same properties and volume fraction as in the agglomeration/break-up model, for reference.

an increase in the flow rate of 0.3% is found when compared to the non-laden or, equivalently, one-way coupled cases.

Upon including a two-way coupled dispersed phase that is undergoing agglomeration and break-up, a significant increase in flow rate occurs. The general increasing trend of the gain in flow rate that is found for small but increasing values of the strength of the inter-particle bonds does not carry through for arbitrarily large values of F_L^* and T_L^*; the maximum increase in the flow rate reaches a maximum of about 5.5%. A plateau at intermediate to large values of the strength of the inter-particle bonds is found, and, the gain reduces if the value of F_L^* or T_L^* is increased further. This effect is most pronounced for agglomerates that are broken by straining and shearing at Re_∇ = 720. In order to explain why the increase in flow rate does not grow monotonically when the strength of the inter-particle bonds is increased, we proceed to study the relative increase of the fluid velocity as a function of the wall-normal coordinate in the subsequent paragraphs.

Increase in flow rate as a function of wall-normal coordinate. In Figure 5.15, the relative increase in the streamwise velocity upon introducing two-way coupling is shown, as a function of the wall-normal coordinate. Since the average flow is symmetric in the centre plane of the channel, the results are only shown over half of the channel height for each Reynolds number.

The results in Figure 5.15 show that the increase in overall flow rate mainly results from an increase in the streamwise velocity near the centre of the channel. Like for the overall flow rate, the maximum increase in fluid velocity that can be achieved upon adding the two-way coupled dispersed phase is limited, at about six to seven percent. For agglomerates that have a very large strength (and thus consist of a very

Figure 5.15: Change in the average continuous phase streamwise velocity as a function of the wall-normal coordinate with respect to non-laden flow upon including a dispersed-phase using two-way coupling. The labels along the lines indicate the values of F_L^* and T_L^* used to obtain the respective results, «NI» indicates results obtained using a two-way coupled non-interacting dispersed phase.

large number of primary particles), the maximum increase in the fluid velocity does not occur at the centre of the channel, but rather at an intermediate location between the centre and the wall.

Close to the channel walls, a reduction of the fluid velocity, or a small increase at most, is found for $Re_\nabla = 360$, whereas a sharp increase in the flow rate as a function of the wall-normal coordinate is found in the same region for $Re_\nabla = 720$. The sharp increase of the flow rate in the latter cases may be caused by the spatial resolution of the computational grid of the Large Eddy Simulations that were used to obtain these results, which could be insufficient to fully capture the changes in the boundary layer as induced by the two-way coupling of the dispersed phase.

Turbulence modification by dispersed phase. Since the pressure gradient, which is the driving force of the flow, remains unchanged upon including a two-way coupled dispersed phase, the changes in flow rate and fluid velocity found above ultimately must be related to the quantity that relates the streamwise pressure gradient to the gradients in the fluid velocity in the wall-normal direction: the (effective) fluid viscosity.

95

In a non-laden turbulent flow, the effective viscosity is comprised of the molecular viscosity and the turbulent eddy viscosity. It has been reported before in the literature that the addition of a dispersed phase with non-spherical structures (such as polymers (Sureshkumar et al., 1997; Ptasinksi et al., 2001), or non-elastic rods (Paschkewitz et al., 2004)) can cause a drag reduction in turbulent flows by reduction of the turbulent stresses. Since the molecular viscosity is constant in our simulations (it is determined by the value of $Re_\bigtriangledown$), the changes in the fluid flow rate must either result from changes in the turbulent eddy viscosity, or from changes in the effective viscosity that are in some other way related to the presence of the dispersed phase.

As a simple estimate of how the magnitude of the turbulent viscosity of the continuous phase changes upon two-way coupling with the dispersed phase, we here consider the turbulent kinetic energy $\mathbb{K}$:

$$\mathbb{K} = \frac{1}{2}\left(\overline{u'u'} + \overline{v'v'} + \overline{w'w'}\right) \tag{5.18}$$

where u', v' and w' denote the turbulent velocity fluctuations in the streamwise, spanwise and wall-normal directions, respectively.

Figure 5.16 shows the percentage decrease of the turbulent kinetic energy as a function of the wall-normal coordinate for the two-way coupled approach compared to non-laden flows. To large extent, the decrease in the eddy viscosity that is associated with the presence of the dispersed phase can explain the changes in the fluid velocity that are found in Figure 5.15. The turbulence intensity decreases sharply for both Reynolds numbers upon including two-way coupling near the centre of the channel, for instance, which is also the region where the largest increase in the fluid velocity is observed. For very large values of F_L^* and T_L^*, the reduction of the turbulent kinetic energy approaches a saturation close to the centre of the channel, although it is still decreasing further with increasing strengths of the inter-particle bonds. However, we find that the increase in the fluid velocity in this region as well as the increase in the overall flow rate through the channel show a maximum (or plateau) at intermediate values of F_L^* and T_L^*. This effect cannot be explained by considering only the influence of the dispersed phase on the turbulent eddy viscosity.

We propose that the presence of the agglomerates itself increases the apparent viscosity of the fluid, as it induces coupling in the continuous phase velocity field over distances that are relatively large compared to the typical turbulent eddies. The viscosity is a measure of the resistance of the fluid against velocity gradients, and the filtering of the fluid velocity that results from the two-way coupling of the agglomerates with the fluid will increase this resistance. This hypothesis is supported by the results of some simulations that were conducted in laminar flows (in which the turbulent eddy viscosity does not play a role), where we find that the flow rate decreases significantly (by around 25%) upon lading the flow with the two-way coupled dispersed phase that is undergoing agglomeration and break-up.

The results that were found in Figures 5.14 and 5.15 can therefore be explained by a balance of the decrease of the effective viscosity due to turbulence attenuation and
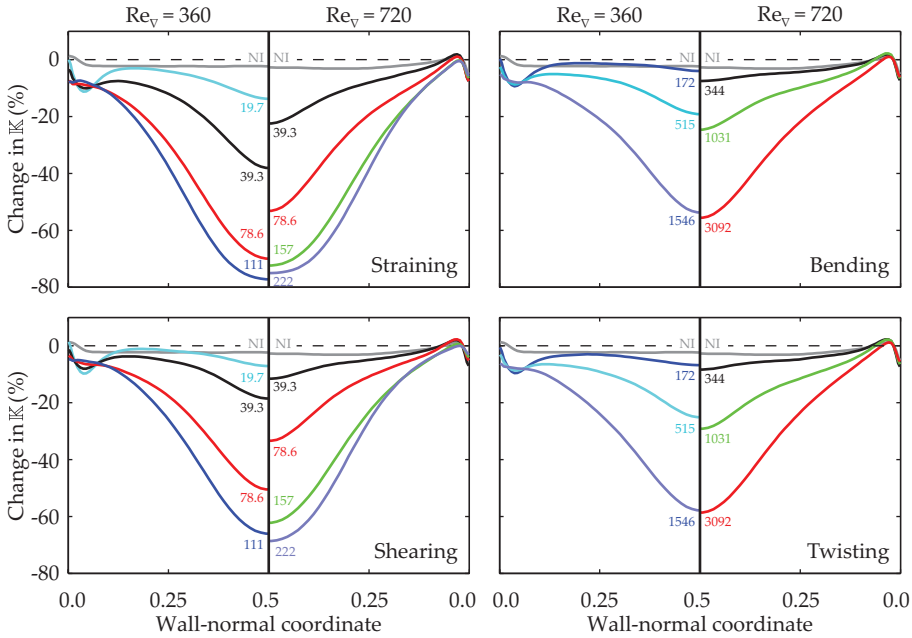
Figure 5.16: Change in the turbulent kinetic energy as a function of the wall-normal coordinate with respect to non-laden flow upon including a dispersed phase using two-way coupling. The labels along the lines indicate the values of F_L^* and T_L^* used to obtain the respective results, «NI» indicates results obtained using a two-way coupled non-interacting dispersed phase.

the increase that directly results from the presence of the dispersed phase. Once the turbulent eddy viscosity has already vanished to a large extent for increasing values of F_L^* and T_L^*, it can no longer compensate for the increased long-range apparent viscosity that results from the increase in $\bar{N}_{ss}$ if F_L^* and T_L^* are further increased.

5.5 Laminar and transitional flows

Although laminar and transitional flows are not of primary interest in this work, it is interesting to assess whether the universal character of the agglomerates as a function of the Reynolds number that we have found in many of the agglomerate properties also hold true if the continuous carrier-phase flow is not turbulent. As an example, let us consider the scaling of the mean mass of the agglomerates in steady-state with the value of F_L^* or T_L^*.

In one-way coupled laminar flow simulations, the streamwise fluid velocity profile is purely parabolic. Due to the lack of spanwise and wall-normal velocity components, agglomerates will grow to infinite size, as is confirmed by our simulations. This means that the scaling relations for the mean agglomerate mass using one-way coupling
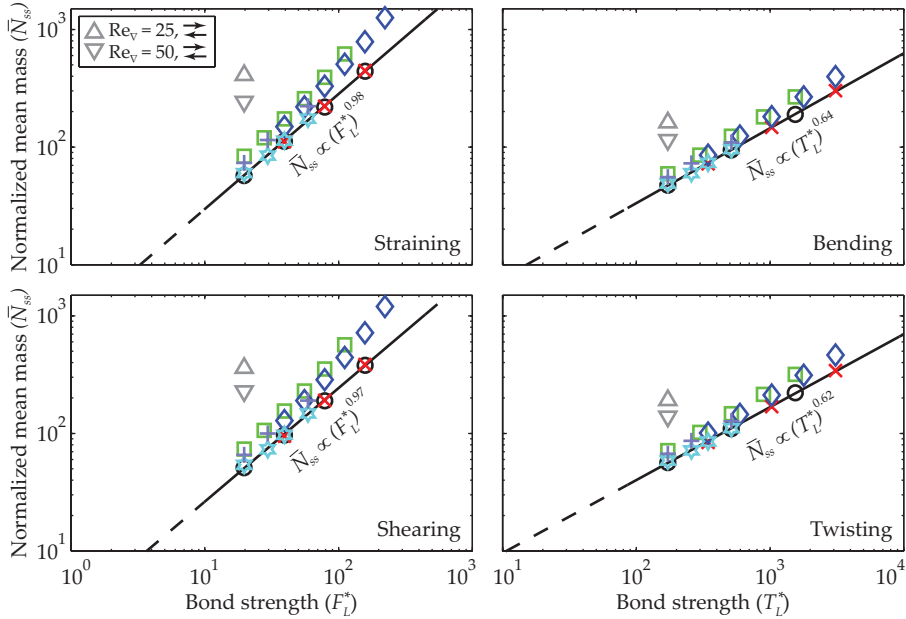
Figure 5.17: Scaling of the mean agglomerate mass in steady state ($\bar{N}_{ss}$), shown in Figure 5.1, complemented with results obtained in laminar and transitional flows. The labelling of the data that is obtained in turbulent flows is the same as in Figure 5.1.

break down if the flow becomes laminar. With two-way coupling, the presence of the agglomerates changes the parabolic velocity profile of the flow, and, therefore, the situation becomes more complex.

In Figure 5.17, we have complemented the results previously presented in Figure 5.1 with two-way coupled simulations that have been obtained at Re_∇ equal to 25 and 50. These results show that the $\bar{N}_{ss}$ disproportionately changes if the Reynolds number is reduced such that the flow becomes transitional or laminar. Furthermore, our results show that for the non fully turbulent Reynolds numbers, the agglomerates are sometimes prone to form very large, channel-filling structures even if two-way coupling is considered. In fact, this occurred in all simulations with $Re_\nabla = 100$ we considered, such that no results on the steady-state agglomerate mass are shown for these cases in Figure 5.17. The inherent irregular motion that is present in turbulence thus is an important feature in determining the characteristics of the agglomerates that are formed in our model, even though the properties of the agglomerates are not too sensitive to the exact magnitude of the Reynolds number, provided the flow is turbulent.

5.6   Summary

In this chapter, we have studied agglomeration and break-up in absence of deposition and re-entrainment using the Eulerian-Lagrangian model, as described in Chapter 3, in the channel flow geometry. We have focused both on the properties of the agglomerates formed and the properties of the agglomeration and break-up processes. We have also studied the influence that the agglomerates have on the turbulent carrier phase when two-way coupling is considered. In the simulations, periodic boundary conditions have been used for the continuous carrier phase, as well as for the dispersed phase. The number of primary particles, and thus the dispersed-phase volume fraction was kept constant in time.

Under these conditions, the balance between agglomeration and break-up gives rise to a statistical steady-state. In this steady-state, individual agglomerates still frequently undergo collisions, thereby forming new agglomerates, and also, agglomerates are frequently broken. Overall, the effects of these processes cancel each other, such that the properties of the agglomerate population in a statistical sense remain unchanged. Considering all results that have been presented in this chapter, the following concluding remarks can be made.

Break-up mechanisms. By considering different break-up mechanisms independently, we effectively have investigated how the properties of the agglomerates change if their resistance against break-up is much smaller for one particular break-up mechanism than it is for all other break-up mechanisms. Our results show that the properties of the agglomerates do not change that much depending on which mechanism governs the break-up of the agglomerates. The largest differences can be found for the fractal dimension, and the relative fragmentation during break-up. Even these differences, however, are small. This means that when constructing an engineering model for asphaltene evolution under flow conditions, the exact knowledge on the most relevant break-up mechanism is not required.

Scaling of agglomerate properties with strength of inter-particle bonds and Reynolds number. For all of the break-up mechanisms, we have found that the mean mass of the agglomerates, both when measured in steady-state and during break-up follow scaling relations that are independent on the Reynolds number when one-way coupling is considered. For two-way coupling, there is a weak dependence on the Reynolds number. The differences in the scaling exponents for different break-up mechanisms and Reynolds numbers under two-way coupling can be understood from differences in the slip velocity of the primary particles with respect to the turbulent carrier phase. By contrast, the properties of the agglomerates are found to change a lot when the continuous-phase flow is laminar or transitional instead of turbulent.

Collision rate and fragmentation. We have found that the collision rate of the agglomerates is underestimated by collision kernels that are proposed in the literature (and are also frequently applied in engineering models for the asphaltene evolution) by up to a factor of about 5, especially towards the centre of the channel. Likewise, it is found that the relative fragmentation during break-up deviates a lot from the

typical assumption of binary breakage, in which agglomerates are assumed to be broken in two parts of equal mass. In Chapter 8, we will address how this information can be used for the benefit of predictive engineering models.

Modification of turbulence. We found that the turbulence can be significantly attenuated by the presence of a dispersed phase that is undergoing agglomeration and break-up. This results in an increase in the flow rate in the channel, that is limited for very large agglomerates due to the increase of the apparent viscosity that is caused by the long-range interactions that result from the presence of large agglomerates. The effects that the dispersed phase that is undergoing agglomeration and break-up have on the continuous liquid carrier-phase are much stronger when compared to flows that are laden with non-agglomerating dispersed phases with otherwise equal properties.

Chapter 6

Steady-state of agglomeration and break-up: Pipe geometry

In addition to the study of agglomeration and break-up in the absence of deposition and re-entrainment in the channel geometry, as described in Chapter 5 of this thesis, we have also performed simulations of agglomeration and deposition in the absence of deposition and re-entrainment in a cylindrical pipe geometry. In this chapter, we will present the similarities and differences that are found between both geometries.

6.1 Description of considered cases

Continuous carrier phase. We consider flows in the cylindrical pipe geometry with Re_{∇}, as defined in equation (3.11), equal to 360 and 720. Due to the increase of the ratio of the wall circumference to the cross-sectional flow area in the cylindrical pipe in comparison to the channel flow domain, the bulk Reynolds numbers in the cylindrical pipe are slightly lower than they are in the channel. The bulk Reynolds numbers (see equation (3.13)) that are found in the non-laden pipe flows are equal to 5400 and 12 400 for the aforementioned pressure gradient Reynolds numbers, respectively.

In the pipe, all simulations at $Re_{\nabla} = 360$ were performed using DNS, whereas LES were used for all simulations at $Re_{\nabla} = 720$. The flow is periodic in the streamwise direction, and a no-slip condition is applied at the face of the pipe wall, which is located at the radial coordinate $r = 0.5$. The motion of the continuous carrier phase is discretised on a cylindrical grid, with a uniform resolution in the streamwise direction and uniform angular resolution in the circumferential direction. In the radial direction, the grid resolution is highest near the wall of the pipe and gradually decreases towards the pipe centreline. Like in the simulations that were performed in the channel, the turbulent flow is left to reach a statistical steady-state before the dispersed phase is introduced.

A summary of the parameters associated with the simulation of the continuous carrier phase and the grid resolution in wall- ($^{+}$-)units in the pipe are given in Table 6.1. The

Table 6.1: Overview of parameters associated with the continuous carrier-phase flow in the pipe. See Figure 3.1 for the definition of the grid parameters.

Re_∇	360	720
$\mathrm{Re}_{\text{bulk (unladen/one-way)}}$	5400	12 400
$(n_x, n_\theta, n_r) = (192, 128, 64)$	DNS	LES
Δ_x^+	9.4	18.8
$\Delta_r^+ \vert_{\text{wall}}$	1.1	2.2
$\Delta_r^+ \vert_{\text{centre}}$	4.3	9.5
L_x, L_θ, R		$5, 2\pi, 0.5$

grid-resolutions used in DNS mode are similar to the ones used by Eggels (1994) in the DELFT code. For $\mathrm{Re}_\nabla = 360$, we compared the statistics of the single-phase flow to the high-resolution DNS data obtained by Khoury et al. (2013). We found that the maximum deviation of the mean streamwise fluid velocity ($+1.0\%$) occurs at around $r = 0.2$. The maximum deviation observed in the Reynolds stresses is found for $w'w'$ (-8.4%), close the wall of the pipe.

Dispersed-phase parameters. The dispersed phase parameters that were considered in the pipe are the same as in the channel, as outlined in Section 5.1. The only difference is the number of primary particles that was considered (98 175 in the pipe versus 250 000 in the channel), to ensure that the volume fraction of the dispersed phase is the same in both geometries (1.3%). Like in the channel, primary particles are introduced individually in the flow at random locations throughout the entire flow domain in the pipe; their initial velocity is set equal to the local fluid velocity.

Throughout this chapter, we will show the results that are obtained in the channel unlabelled and greyed out in the background of the various figures that show the labelled pipe results in the foreground. For convenience, a reference to the corresponding graphs for the channel flow regime in Chapter 5 is included in the respective figure captions.

6.2   Differences in fluid flow between the pipe and the channel

Before considering how the properties of agglomerates that are formed in the pipe flow differ from those formed in a channel flow, it is useful to first summarise the differences that occur in non-laden flows in both geometries. Figure 6.1 shows the time-averaged streamwise fluid velocity and the turbulent kinetic energy, as defined in equation (5.18), as a function of the wall-normal coordinates in the two geometries, both for Re_∇ equal to 360 and 720. Both the mean velocity and the turbulent kinetic energy have been normalised with the pressure-gradient velocity u_∇, that is defined in equation (3.12).

The results in Figure 6.1 show that both the average streamwise fluid velocity and the turbulent kinetic energy have a similar dependence on the wall-normal distance in the pipe and channel. Due to the round shape of the pipe, however, the region that
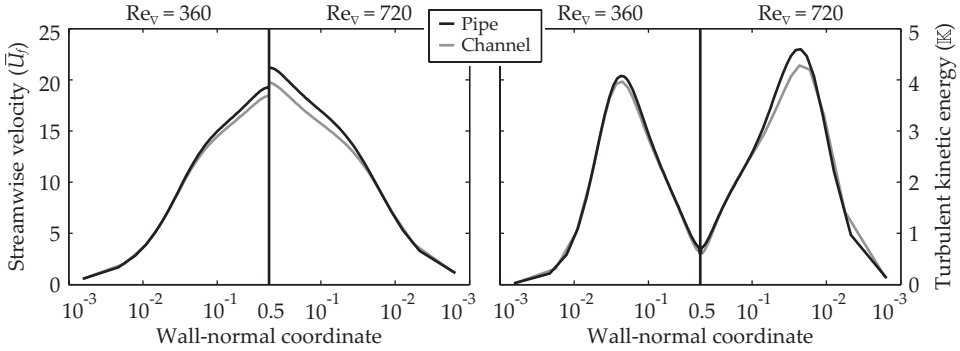
Figure 6.1: Comparison of the non-dimensional time-averaged streamwise velocity (left) and the turbulent kinetic energy (right) for non-laden flows in the pipe and channel geometries.

corresponds to small values of the wall-normal coordinate occupies a much larger volume fraction of the computational domain than it does in the channel geometry. This so-called inner layer of the flow, which is characterised by a relatively low average velocity, a large wall-normal streamwise velocity gradient, and large values of the turbulent kinetic energy, will thus have a much larger potential to interact with the dispersed phase in the pipe geometry than it has in the channel. The implications of this on the properties of the agglomerates formed in the dispersed phase will be discussed later in this chapter.

6.3   Agglomerate properties

**Scaling of steady-state mean mass and mean mass at break-up of the agglomerates**. In Figure 6.2, the mean steady-state mass of the agglomerates ($\bar{N}_{ss}$) formed in the pipe is shown as a function of the characteristic strength of the inter-particle bonds for the different break-up mechanisms considered, one- and two-way coupling, and for multiple Reynolds numbers. In Figure 6.3, the dependence of the mean mass of the agglomerates measured at the moment that the agglomerates are broken in the pipe ($\bar{N}_{bu}$) is presented.

For a given break-up mechanism and strength of the inter-particle bonds, the mean mass of the agglomerates is in general smaller when the agglomerates are formed in the pipe instead of the channel. This is true both for the mean mass of the agglomerates in steady-state, as well as for the mean of the mass that is measured at the moment of agglomerate break-up. An exception to this trend is found for the values of $\bar{N}_{bu}$ for agglomerates that are formed using two-way coupling, at relatively large values of the strength of the inter-particle bonds. For all four break-up mechanisms, larger values of $\bar{N}_{bu}$ are found in the pipe than in the channel for this particular regime.

In order to explain the differences found in the values of $\bar{N}_{ss}$ and $\bar{N}_{bu}$ between both geometries, let us consider the differences in the average magnitude of the slip velocity
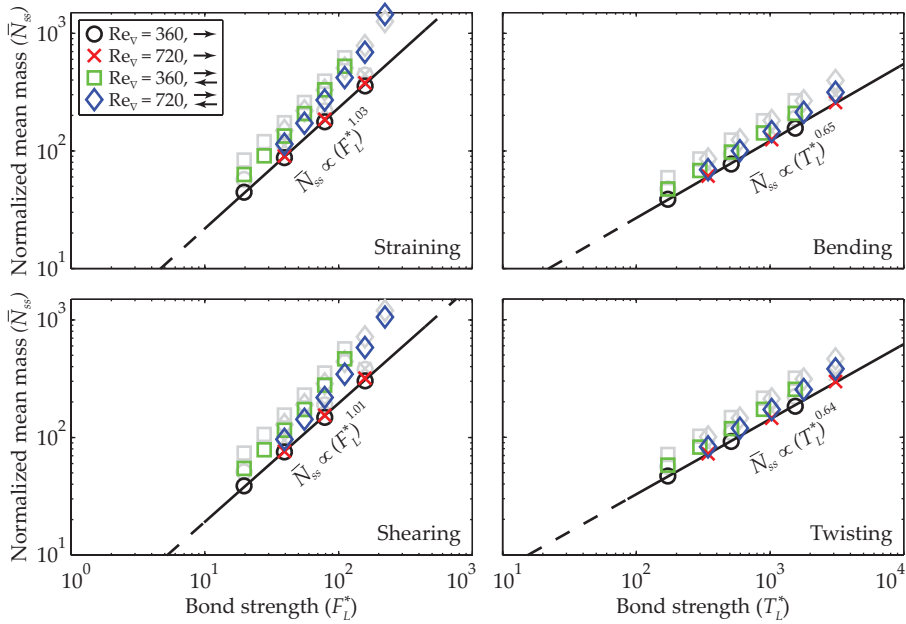
Figure 6.2: Scaling of the mean agglomerate mass in *steady-state* ($\bar{N}_{ss}$) with the characteristic strength of the inter-particle bonds, for different break-up mechanisms, one- and two-way coupling and multiple Reynolds numbers. The greyed out results in the background correspond to the channel flow regime and thus were presented in Chapter 5 in Figure 5.1.
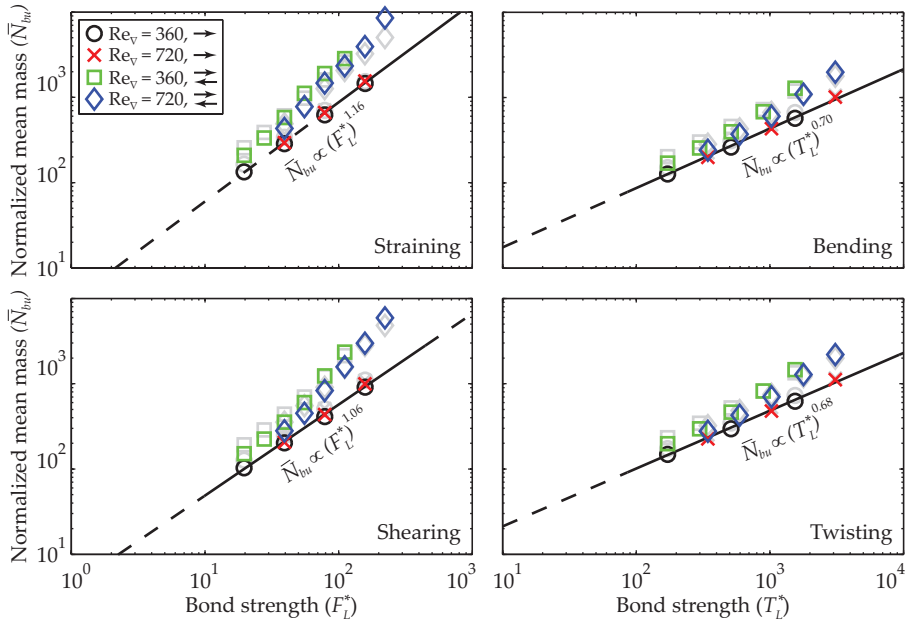
Figure 6.3: Scaling of the mean agglomerate mass *at agglomerate break-up* ($\bar{N}_{bu}$) with the characteristic strength of the inter-particle bonds, for different break-up mechanisms, one- and two-way coupling and multiple Reynolds numbers. (Channel flow: Figure 5.2)
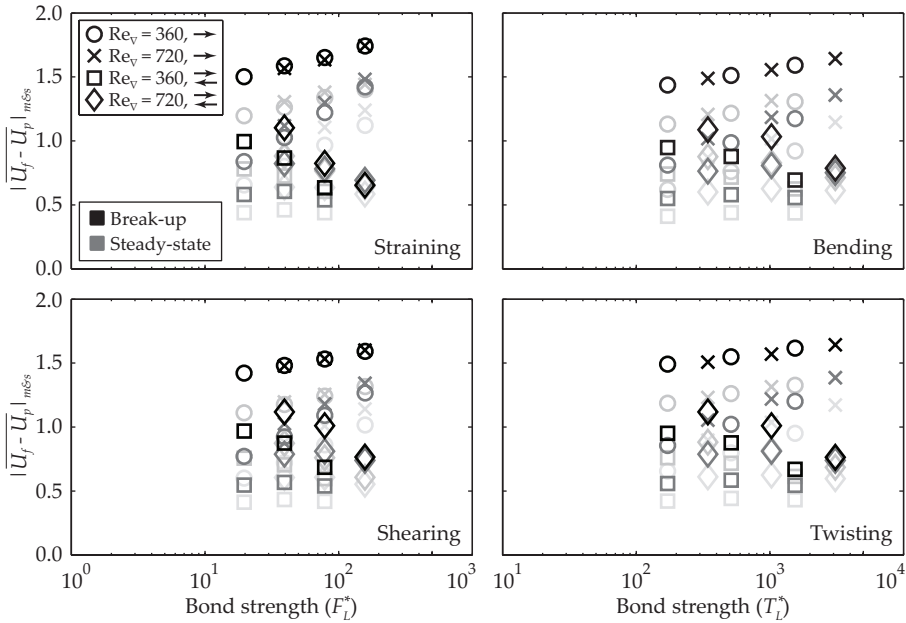
Figure 6.4: Average magnitude of the primary particle slip velocity measured in steady-state (dark grey) and at agglomerate break-up (black). (Channel flow: Figure 5.3)

of the primary particles that occur between agglomerates that are formed in a pipe or channel.

Slip velocity of primary particles with respect to the continuous carrier phase. In Figure 6.4, the magnitude of the slip velocity of the primary particles, averaged over entire agglomerates, is shown as a function of the model parameters, measured both in steady-state, and at agglomerate break-up.

The average magnitude of the slip velocity of the primary particles is larger in the pipe than in the channel. This is explained by the fact that the inner layer of the turbulent flow occupies a larger fraction of the domain in the pipe than it does in the channel. Because of this, the strong wall-normal gradient in the streamwise velocity and the strong turbulent velocity fluctuations that are characteristic to the turbulent inner layer are more likely to interact with the agglomerates in the pipe than they are in the channel, simply because a larger fraction of the agglomerates will be present in this region. The agglomerates on average have a negligible slip velocity with respect to the continuous carrier phase. Therefore their presence in a region with both a stronger mean velocity gradient and more intense turbulence fluctuations will increase the characteristic magnitude of the slip velocity of the primary particles inside the agglomerates with respect to the continuous carrier phase.

For simulations with one-way coupling, the differences between the slip velocities in both geometries have a negligible dependence on the value of F_L^* and T_L^*. When two-way coupling is used, the slip velocities found in the pipe show a stronger decrease upon increasing the strength of the inter-particle bonds than they do in the channel. Revisiting the simple model for the scaling of the agglomerate mass at break-up proposed in equation (5.5), the former effect can explain why the mean mass of the agglomerates at break-up is generally smaller in the pipe than it is in the channel. The latter effect explains why the increase of $\bar{N}_{bu}$ with F_L^* and T_L^* under two-way coupling is stronger in the pipe than in the channel, as smaller magnitudes of the slip velocity lead to agglomerates that consist of a larger number of primary particles at fixed values of the strength of the inter-particle bonds.

Since the forces that the particles exert onto the fluid when two-way coupling is considered follow from the application of Newton's third law to the hydrodynamic force that is acting on the particles itself (see equation (3.17)), an increase in the magnitude of the slip velocity corresponds to an increase in the strength of the back-forcing of the dispersed phase onto the liquid phase. The increase in magnitude of the slip velocity that is found using one-way coupling, therefore suggests that the effect of two-way coupling will be stronger in the pipe than in the channel. In Chapter 6 we have argued that the main effect of the two-way coupling on the liquid carrier phase is the damping of the turbulence intensity, which leads to a decrease of the magnitude of the slip velocity of the primary particles. Correspondingly, the overall increase in the slip velocity that is found in the pipe when compared to the channel should lead to larger differences in the slip velocity between one- and two-way coupling. This is indeed in line with the results presented in Figure 6.4.

Our results show that the differences in the fraction of the primary particles that have a hydrodynamic force exerted on them that constructively contributes to the stresses in the broken inter-particle bonds are smaller than the differences in the magnitude of the slip velocity between both geometries. This indicates that the latter mechanism is dominating the differences in the mean agglomerate mass. Still, both mechanisms have a positive contribution to the fact that the mass of the agglomerates shows a stronger increase with increasing values of F_L^* and T_L^* in the pipe than in the channel.

Ratio of mean masses at break-up and in steady-state. Figure 6.5 shows the dependence of the ratio $\bar{N}_{bu}/\bar{N}_{ss}$ on the model parameters for the pipe. For agglomerates that have small to moderate internal strengths, we find that the ratio $\bar{N}_{bu}/\bar{N}_{ss}$ does not significantly differ between the pipe and channel geometries. For agglomerates that are formed using large values of F_L^* and T_L^*, however, the ratio between the mean mass at break-up and in steady-state is significantly larger in the pipe geometry than it is in the channel.

In the channel geometry, we found that the large variations in $\bar{N}_{bu}/\bar{N}_{ss}$ between cases can be attributed to large variations in the lifetime between agglomerates that contain small and large numbers of primary particles within one agglomerate population. Our results show that the lifetime of the agglomerates is shorter in the pipe than in the channel by up to as much as 60%. For each break-up mechanism, we find that
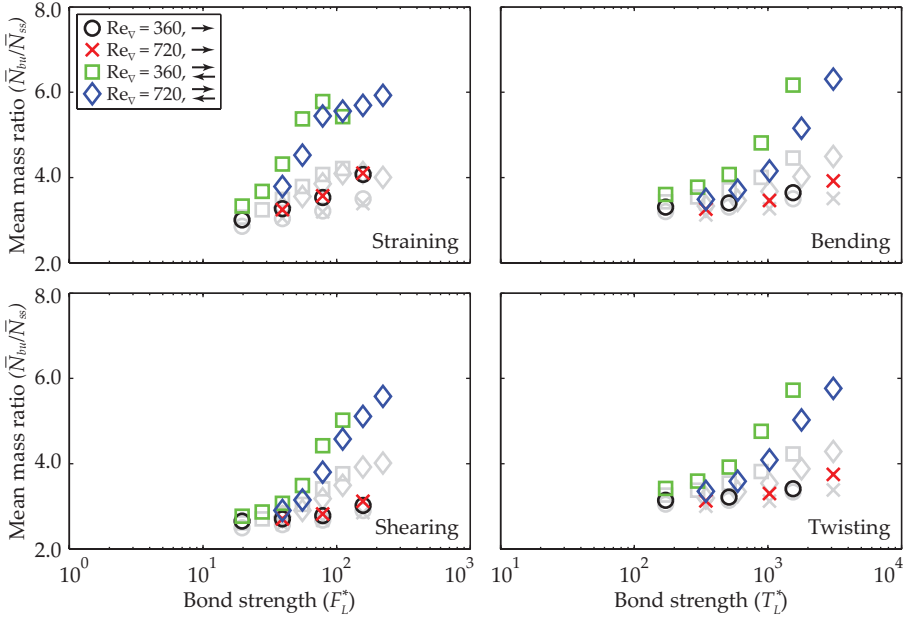
Figure 6.5: Ratio between the average agglomerate mass at break-up and steady-state mean agglomerate mass ($\bar{N}_{bu}/\bar{N}_{ss}$). (Channel flow: Figure 5.4)

the largest decrease in lifetime occurs for those agglomerates in the population that contain the largest number of primary particles. According to the simple model that was derived in equation (5.5), such a shift in relative lifetime within the agglomerate population leads to larger values of $\bar{N}_{bu}/\bar{N}_{ss}$, thereby explaining the differences that are found between both geometries in Figure 6.5. We will come back to the cause of these differences in agglomerate lifetime later when the differences in the collision kernel between both geometries are discussed in Section 6.4.

Fractal dimension. Figure 6.6 summarises the fractal dimensions found in the pipe. For all break-up mechanisms, the fractal dimensions of the agglomerates with the smallest values of F_L^* and T_L^* considered are smaller in the pipe than in the channel. Upon increasing the strength of the inter-particle bonds, the fractal dimensions show a stronger increase in the pipe than in the channel; this is particularly true for straining and shearing and when two-way coupling is considered.

In the channel, we have already found that two-way coupling gives higher fractal dimensions than one-way coupling. Since the impact of two-way coupling over one-way coupling is stronger in the pipe than it is in the channel, this effect can explain the stronger increase of the fractal dimension with the strength of the inter-particle bonds found in the two-way coupled pipe flow simulations. Similar to the results found in the channel flow, the variations of the fractal dimension with one- or two-way
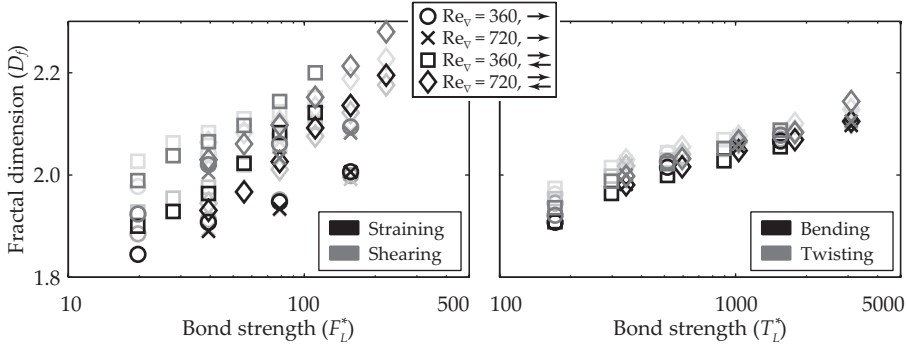
Figure 6.6: Fractal dimensions for steady-state agglomerate populations broken by straining and shearing (left), and bending and twisting (right). (Channel flow: Figure 5.6)
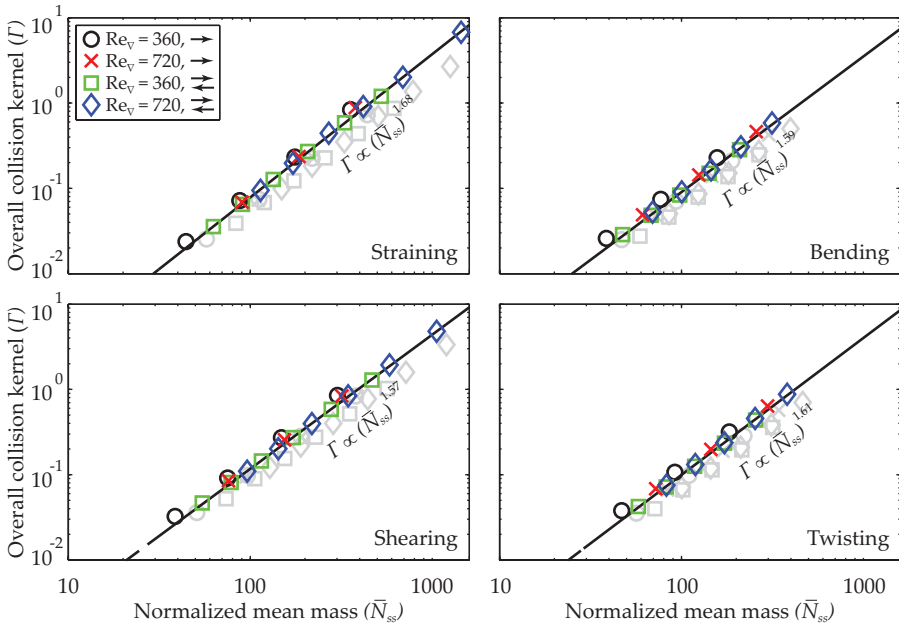
coupling are smaller for agglomerates that are broken due to bending and twisting, than they are for agglomerates that are broken by straining or shearing.

Our results show that agglomerate populations that are characterised by smaller values of $\bar{N}_{ss}$ have smaller fractal dimensions than agglomerate populations in which $\bar{N}_{ss}$ is large. The reduction of the mean mass of the agglomerates in steady-state in the pipe compared to the channel can therefore partly explain why in general, smaller fractal dimensions are found in the former geometry for agglomerates that have relatively weak inter-particle bonds. Furthermore, we have found that an increase in the turbulence intensity leads to smaller values of D_f. As the effective turbulence intensity as felt by the dispersed phase is larger in the pipe than in the channel due to the relative expansion of the turbulent inner layer, this effect also contributes to the decrease of D_f in the pipe compared to the channel.

Agglomerate shape. The results of our simulations show that the average shape of the agglomerates, as measured by the distribution function of the ratio of the lengths of the agglomerate along its primary axes of inertia, is very similar for agglomerates formed in the pipe and in the channel. The trends found in the shape of the agglomerates in the pipe are thus well represented by the results shown in Figures 5.7, 5.8 and 5.9 and therefore, we do not separately report the results found in the pipe here.

6.4   Process properties

Figure 6.7 shows a comparison between the overall collision kernels found in the pipe and channel, as a function of the mean mass of the agglomerates in steady-state. Comparing the scaling exponents that relate the collision kernel found using two-way coupling to the value of $\bar{N}_{ss}$ in both geometries (as shown in Figure 5.10 for the channel geometry), we find that the value of Γ shows a stronger increase with an increasing mean mass of the agglomerate population for agglomerates that are broken by shearing, twisting, and, particularly, bending. The collision kernels found in the

Figure 6.7: Overall collision and break-up kernel for agglomerates that are broken at different values of the characteristic strength of the inter-particle bonds, using one- and two-way coupling, and at multiple Reynolds numbers. The solid lines represent least square error fits to all the two-way coupled simulation results. (Channel flow: Figure 5.10)

pipe are higher by about 40% (bending and twisting) to 50% (straining and shearing) than in the channel if one-way coupling is considered. For two-way coupling, the increase amounts to about 60% (straining, bending and twisting) to 80% (shearing).

To investigate these differences further, we will again consider the correction factor needed to match the predicted collision kernel to the actual collision kernel that follows from the simulation results, as a function of the wall-normal coordinate in the pipe.

Collision kernel correction factor as a function of the wall-normal coordinate. In Figure 6.8, the average collision kernel correction factor $\mathcal{C}$, as defined in equation (5.17) is plotted as a function of the wall-normal coordinate in the pipe. In general, we find that the values of $\mathcal{C}$ needed to reconcile the kernel predictions to the actual collision rates observed in the simulations are larger in the pipe than in the channel. The combined mean-shear and turbulent velocity fluctuation collision kernel that is given by equation (5.14) underpredicts the collision rate in the pipe by up to a factor of 10. The profiles of the correction factors as a function of the wall-normal coordinate are such, however, that the ratio between the correction factors in both geometries is not strongly dependent on the distance to the wall of the flow domain. Still, the
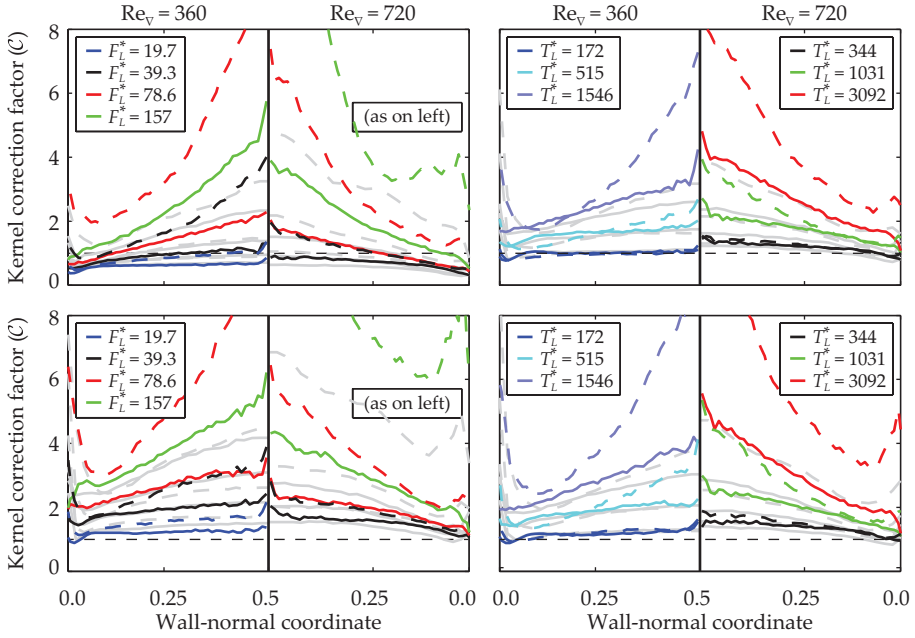
Figure 6.8: Collision kernel correction factor $\mathcal{C}$ as a function of the wall-normal coordinate in the pipe. Top to bottom, left to right: straining, shearing, bending, twisting. Solid lines represent one-way coupled results and dashed lines show two-way coupled results. (Channel flow: Figure 5.12)

relative correction that is required in the pipe is slightly larger near the centre than towards the wall.

Spatial concentration of particles and agglomerates. Since we define the agglomerate lifetime as the time interval in which an agglomerate neither undergoes an agglomeration event, nor is being broken, the lifetime of an agglomerate is strongly correlated with the collision kernel. When discussing the results for the $\bar{N}_{bu}/\bar{N}_{ss}$ earlier in this chapter, it was already mentioned that the strongest decrease in lifetime in the pipe when compared to the channel is found for agglomerates that contain large numbers of primary particles.

To explain this result, Figure 6.9 shows a comparison of the concentration of primary particles as a function of the wall-normal coordinate in both geometries. Even though the concentrations are volumetrically the same, the concentration of primary particles is larger in the pipe than in the channel, at every wall-normal coordinate. This is a result of the curved geometry in the pipe, combined with the increase of the concentration in both geometries towards the centre of the domain. The latter preferential concentration is found to be stronger for agglomerates that are formed using increasing values of F_L^* or T_L^*, as well as when using two-way coupling instead of one-way
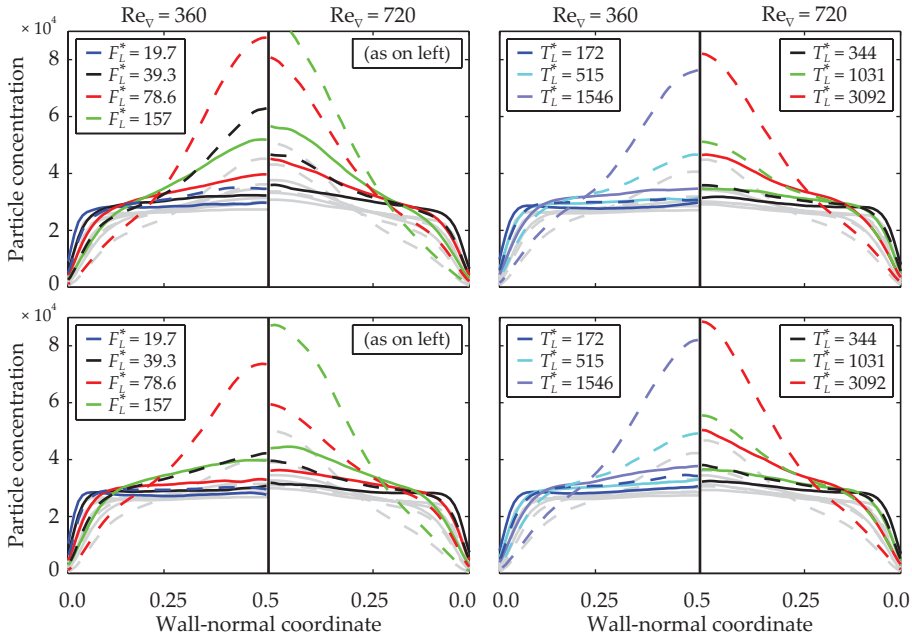
Figure 6.9: Concentration of primary particles (number per unit volume) as a function of the wall-normal coordinate in the cylindrical pipe geometry. Top to bottom, left to right: straining, shearing, bending, twisting. Solid lines represent one-way coupled results and dashed lines show two-way coupled results. The grey lines in the background indicate results that are obtained in channel flow. No corresponding figure is shown in Chapter 5.

coupling, as shown in Figure 6.9. We propose that the wall-normal concentration profile, in conjunction with the fact that the cross-sectional area of centre of the cylindrical pipe geometry is a lot smaller when compared to the area centred around the midplane of the channel, explains the differences in the collision rate and agglomerate lifetime that are observed between both geometries.

As an example, let us consider an agglomerate that is located at a wall-normal coordinate of 0.45 in both geometries (viz. at $z = 0.45$ or $z = 0.55$ in the channel, or at $r = 0.05$ in the pipe). Upon break-up, the agglomerate branches that are moving apart in the transversal direction have the full channel width at their disposal, equal to 2 times the height of the channel, before touching again at the other side due to the periodic boundary conditions. The equivalent distance in the pipe geometry, also caused by the periodic boundary conditions but now in the circumferential direction, is 0.05π times the pipe diameter, which is just 8% of the distance available in the channel. Only from a wall-normal coordinate of 0.18 outwards, the circumference of the pipe becomes larger than the width of the channel.

Agglomerates that are present close the centre of the pipe thus have a larger chance of

re-colliding shortly after they are being broken. The internal stresses inside the bonds of the agglomerates is thus likely to again be exceeding the limit set by the value of F_L^* or T_L^*. Consequently, the agglomerates will be broken quickly once more, thereby increasing the collision and break-up count per unit of time and thus decreasing the lifetime of the agglomerates. Indeed, we find that the actual values of the maximum stress in inter-particle bonds measured at break-up exceeds the set values of F_L^* or T_L^* by a larger factor in the pipe than in the channel. This forms another indication that agglomerates are less effectively broken upon first exceeding the threshold stress level in their bonds in the former geometry.

Based on the considerations given above, we may expect agglomerates that have small wall-normal coordinates to have a larger lifetime in the pipe than in the channel, and visa versa. The results of our simulations also show that agglomerates which consist of a large number of primary particles are more likely to concentrate near the centre of the channel and the pipe than agglomerates with small N. Combined, these effects explain why the lifetime of agglomerates that consist of a large number of primary particles decreases more in the pipe compared to the channel than the lifetime of small agglomerates does. This is also the underlying cause of the differences in $\bar{N}_{bu}/\bar{N}_{ss}$ between both geometries, and it thus explains why the values of $\bar{N}_{bu}$ increase so much more strongly in the pipe than in the channel at large values of F_L^* and T_L^*.

Relative fragmentation of agglomerates during break-up events. Figure 6.10 shows a histogram of the fraction of the primary particles of the agglomerates that end up in the branch that contains the smallest number of the primary particles during break-up events in the pipe. In general, the fragmentation of the agglomerates is very similar in the pipe and in the channel. Like in the channel, binary breakage is a poor representation of the actual break-up process in the pipe for all of the break-up mechanisms that have been considered. We find that the break-up distribution in the pipe is shifted towards a slightly more asymmetric break-up when compared to the channel geometry, especially for the cases with two-way coupling, $Re_\nabla = 720$, and large values of F_L^* and T_L^*.

When discussing the results found in the channel in Chapter 5, we have hypothesised that the stronger break-up asymmetry for the latter cases is caused by the large values of $\bar{N}_{bu}$ that occur in these cases. This increases the chance that small agglomerate branches are broken of the agglomerate when a random bond is selected in which the characteristic strength is exceeded. Since for the two-way coupled $Re_\nabla = 720$ cases with large values of F_L^* or T_L^*, the values of $\bar{N}_{bu}$ found in the pipe are larger than those in the channel, the same argument can explain why the break-up of these agglomerates is more asymmetric in the former geometry.

6.5 Modification of turbulence by the presence of agglomerates

Flow rate / bulk Reynolds number. The increase in the overall flow rate in the pipe due to the inclusion of the dispersed phase using two-way coupling is shown as a percentage of the non-laden flow rate in Figure 6.11. Results that are obtained upon
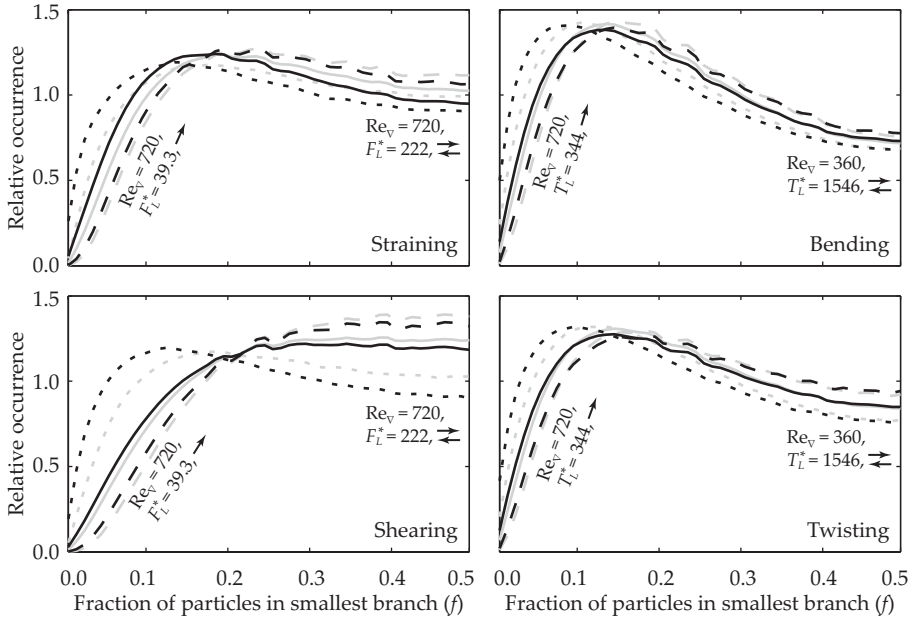
Figure 6.10: Histogram of the fraction of the primary particles that end up in the smallest agglomerate branch during a break-up event. Solid lines: averaged results over all cases considered per break-up mechanism, dashed lines: extreme cases as indicated by the labels shown. (Channel flow: 5.13)
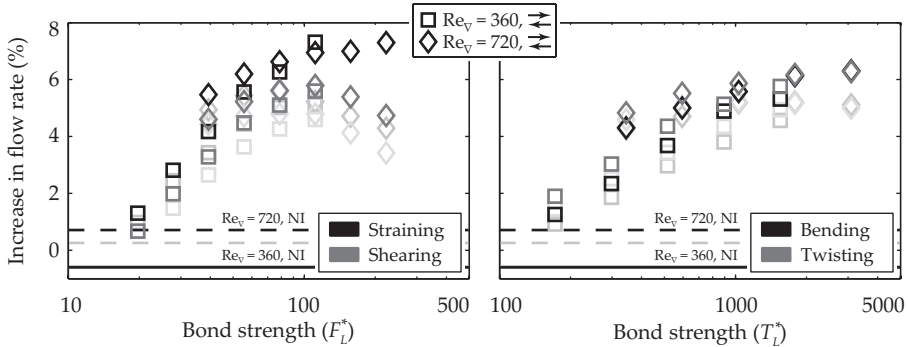
Figure 6.11: Change in liquid flow rate with respect to non-laden flow upon including a dispersed-phase using two-way coupling. The horizontal lines labelled «Re_∇ = 360 NI» and «Re_∇ = 720 NI» indicate results that have been obtained using a two-way coupled non-interacting dispersed phase with the same properties and volume fraction as in the agglomeration/break-up model, for reference. (Channel flow: Figure 5.14)
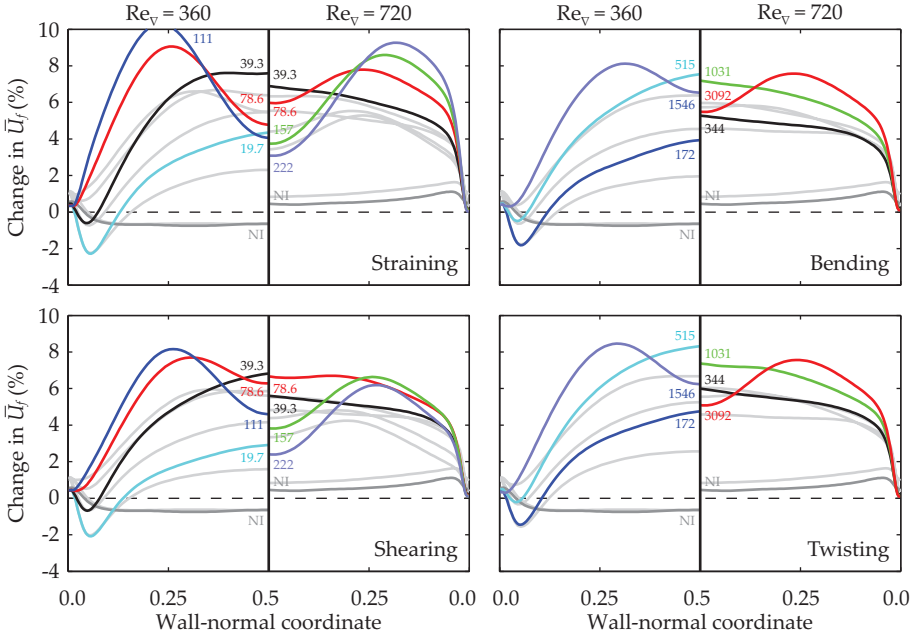
Figure 6.12: Change in the average continuous phase streamwise velocity as a function of the wall-normal coordinate with respect to non-laden flow upon including dispersed-phase using two-way coupling. The labels by the lines indicate the values of F_L^* and T_L^* used to obtain the respective results, «NI» indicates results obtained using a two-way coupled non-interacting dispersed phase. (Channel flow: Figure 5.15)

lading the flow with the same volume fraction of two-way coupled non-interacting particles have again been included for reference.

Like in the channel, we find that the non-interacting particles hardly change the flow rate in the pipe: for $Re_\nabla = 360$, a decrease by 0.6% is found, whereas for $Re_\nabla = 720$, an increase in the flow rate of 0.7% is observed. The increase in the flow rate upon lading the flow with the two-way coupled dispersed phase that is undergoing agglomeration and break-up is much more significant, and is found to be larger in magnitude in the pipe than in the channel flow. The maximum increase in the bulk Reynolds number that is achieved in the pipe is about 7%. To explain why this is the case, we will proceed to study the relative increase in the fluid velocity as a function of the wall-normal coordinate in the subsequent paragraphs.

Increase in flow rate as a function of wall-normal coordinate. Figure 6.12 shows the increase in flow rate caused by including the two-way coupled dispersed phase as a function of the wall-normal coordinate in the pipe. Loosely speaking, the results that are found in the pipe look like exaggerations of the results that were found in the channel. Close to the walls, the increase in flow rate is similar in both geometries.
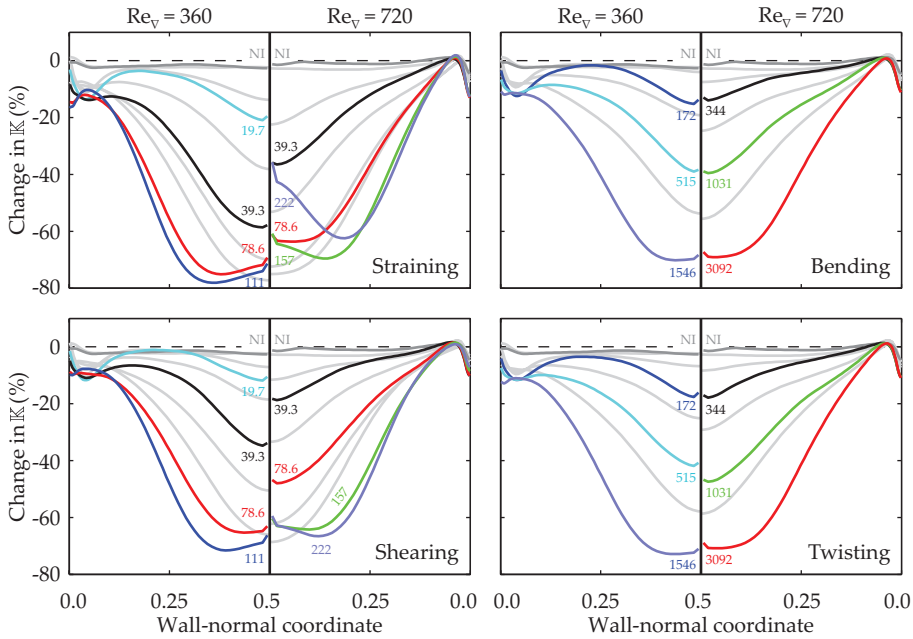
Figure 6.13: Change in the turbulent kinetic energy as a function of the wall-normal coordinate with respect to non-laden flow, upon including the dispersed phase using two-way coupling. The labels along the lines indicate the values of F_L^* and T_L^* used to obtain the respective results, «NI» indicates results obtained using a two-way coupled non-interacting dispersed phase. (Channel flow: Figure 5.16)

At intermediate wall-normal coordinates, the fluid velocity increases much more strongly in the pipe than it does in the channel. For flows that are laden with large agglomerates, that are formed at large values of F_L^* and T_L^*, the decline in the increase in flow rate towards the centre of the pipe is also much more intense than it is towards the centre of the channel. When presenting the results that were obtained in the channel in Chapter 5, we proposed that the latter effect is caused by the increase in the apparent fluid viscosity that results from the long-range fluid velocity coupling that is associated with two-way coupling of large agglomerates that act as spatial filters to the fluid velocity. In Section 6.4, we have found that large agglomerates tend to concentrate more strongly near the centre of the pipe then near the centre of the channel. This explains why the increase in the effective viscosity is larger near the centre of the pipe than near the centre of the channel upon lading the flows with agglomerates with large values of F_L^* or T_L^*.

The increased magnitude of the slip velocities of the primary particles that is found in the pipe compared to the channel implies that the effects of two-way coupling over one-way coupling are stronger in the pipe than in the channel. So far, we have found

that the increase in the bulk flow rate, as well as the changes in the fluid velocity upon including two-way coupling are indeed stronger in the pipe then in the channel. To see whether the same mechanism follows through for the attenuation of the turbulent kinetic energy, we will consider the change in the turbulent kinetic energy upon including two-way coupling as a final parameter in this chapter.

Turbulence intensity. Figure 6.13 shows the percentage decrease of the turbulent kinetic energy in the pipe for two-way coupled with respect to non-laden flows as a function of the wall-normal coordinate.

Overall, the decrease in the turbulent kinetic energy upon including a two-way coupled agglomerating disperse phase is indeed much stronger in the pipe than in the channel. For all of the break-up mechanisms, similar levels of attenuation are found close to the walls of the flow domain (in the region where also similar increases in fluid velocity where observed in Figure 6.12). At intermediate wall-normal coordinates, where the largest increase in the streamwise fluid velocity in the pipe was observed, the reduction of the turbulent kinetic energy indeed is much stronger in the pipe than in the channel. Surprisingly, the attenuation of the turbulence decreases again towards the centre of the pipe for the straining and shearing break-up mechanisms when the strength of the inter-particle bonds exceeds a certain threshold. It is not clear what is the cause of this effect.

6.6   Summary

In this chapter, we have studied agglomeration and break-up in the absence of deposition and re-entrainment in the pipe-flow geometry using the Eulerian-Lagrangian model that was described in Chapter 3. Special attention was given to the differences that are found for agglomerates that are formed in the pipe flow compared to the channel-flow results that were presented in Chapter 6.

Overall, we find that the main cause for the differences that are found between both geometries in terms of the properties of the agglomerates and the agglomeration and break-up processes are caused by the fact that the inner layer of the turbulent flow occupies a larger fraction of the cross-sectional area of the pipe than it does in the channel. The turbulent inner layer is characterised by large time-averaged wall-normal gradients in the streamwise fluid velocity and by intense turbulent velocity fluctuations. Even though the primary particles concentrate at the centre of the pipe and channel, and the concentration in the centre of the pipe is larger than the concentration at the centre of the channel, more particles are present close to the pipe wall than close to the channel wall due to curved geometry in the pipe. As a result, a larger fraction of the agglomerates is inside the inner layer of the flow in the former geometry. The characteristic slip velocity of the primary particles is thus larger in the pipe than in the channel, as is confirmed by the results from our simulations.

The implications of this difference in slip velocity are widespread. On the one hand, it causes the internal stresses that are induced inside the agglomerates to increase, thereby lowering the mean mass of the agglomerates, both in steady-state and at

break-up, at fixed values of the strength of the inter-particle bonds. On the other hand, the increased slip velocity enhances the damping of the turbulent velocity fluctuations that is introduced by the dispersed phase when two-way coupling is considered, thereby giving rise to a stronger increase of $\bar{N}_{ss}$ and $\bar{N}_{bu}$ with F_L^* and T_L^*, and also to a larger increase in flow rate.

The increased presence of the turbulent inner layer also causes agglomerates to undergo collisions more frequently in the pipe, giving rise to shorter agglomerate lifetimes and larger values of the collision kernel. This translates into larger correction factors that are needed to reconcile the collision rate predictions based on existing collision kernels to the collision rate found in the Eulerian-Lagrangian model. The combined mean shear and turbulent velocity fluctuations collision kernel under-predicts the collision rate in the pipe by up to a factor of 10 instead of a factor of 5, as found in the channel. The additional correction factor that is required when compared to the channel flow is fairly invariant to the parameters of the dispersed phase and the Reynolds number.

Since the shape of the agglomerates and the relative fragmentation are also very similar in both geometries, we find that the properties of the agglomerates and the agglomeration and break-up processes are similar enough such that from an engineering perspective, channel flow results can be used to predict how the agglomeration proceeds in a cylindrical pipe.

Chapter 7

Deposition and re-entrainment

In this chapter, the Eulerian-Lagrangian model described in Chapter 3 is used to study deposition and re-entrainment. To this end, particle-wall interactions are taken into account as outlined in Section 3.10. Our main focus will be on the dependence of the rates of deposition and re-entrainment, as well as of the properties of the deposit layer formed, on the strength of the particle-wall interaction and on the internal strength of the agglomerates, as well as on the Reynolds number. Also the influence of the deposit layer on the flow itself will be studied, by monitoring the additional pressure drop that is induced in the flow domain.

To monitor the properties of the deposit layer as a function of the downstream distance from the location where primary particles are released into the flow, periodic boundary conditions are no longer used for the dispersed phase in simulations in which deposition and re-entrainment are considered. Instead, primary particles are injected somewhere close to the upstream end of the flow domain, and they flow out of the domain at the downstream end. As a result, the properties of the deposit layer that is formed varies as a function of the streamwise coordinate. Periodic boundary conditions for the fluid phase therefore can no longer be applied when two-way coupling is used. When using two-way coupling, in- and outflow boundary conditions are used for the continuous carrier-phase solver as well, and the flow has to be solved for the full length of the domain over which the deposition is monitored.

It is desirable to study the deposition over a distance equal to at least a couple of dozen times the diameter of the pipe or the height of the channel. Therefore, a very large number of grid-cells has to be used to represent the fluid phase. Also, very large numbers of primary particles are needed to form a deposit layer of considerable thickness. The large computational power that is needed to solve such simulations limits the maximum time interval for which the deposition and re-entrainment processes can be studied. Achieving a steady-state between deposition and re-entrainment is therefore not feasible in these simulations. We thus only study the initial stages of the deposition and re-entrainment processes here.

Table 7.1: Overview of the parameters that are considered in the initial evaluation of the deposition and re-entrainment model.

| Parameter	Reduced	Base	Increased
F_L^*		78.6	
T_L^*		1 546	
γ		0.1	0.3, 0.75
δ_c	$2.5 \cdot 10^{-2}$	$5.0 \cdot 10^{-2}$	
t_{rns}		$2.5 \cdot 10^{-4}$	$1.0 \cdot 10^{-3}$
ζ	0.5	1.0	2.0
$\dot{N}_p$		50 000	100 000

7.1 Model sensitivity with respect to free parameters

As was outlined in Section 3.10, the free parameters of the deposition model are: (i) the ratio of the particle-wall adhesion force to the internal strength of the agglomerates, γ, (ii) the particle wall-interaction range, δ_c, (iii) the damping ratio of the damped harmonic oscillator, ζ, (iv) the relaxation time, t_{rns}, and (v) the primary particle injection rate per unit time, $\dot{N}_p$.

To first study the sensitivity of the deposition model with respect to these parameters, we present results that are obtained using one-way coupling, with a preliminary version of the model. The differences with respect to the final version of the model, as it was presented in Section 3.10, will be explained later on. Since the fluid flow is unaffected by the deposition when one-way coupling is used, periodic boundary conditions for the fluid phase can be used in these simulations. The simulations are conducted using DNS for channel flow at $Re_\nabla = 360$, with $L_x = 5$, $L_y = 2$ (normalised by the channel height H), and $n_x = 192$, $n_y = 128$ and $n_z = 96$. This is the same configuration as was used for the DNS cases at $Re_\nabla = 360$ that were considered in Chapter 5. For the dispersed phase, an outflow boundary condition was used at the downstream end of the computational domain, which is located at $L_x = 55$.

The parameters of the deposition model that have been considered are summarised in Table 7.1. Primary particles are injected in the flow over the time interval between $t^* = 0$ and $t^* = 5$, at random uniform locations between $x = 0$ and $x = 2.5$, over the entire width and height of the channel. The properties of the deposit layer are considered at five units of t^* after the final primary particles have been injected (viz. at $t^* = 10$). By this time, all of the primary particles that have not deposited at the walls have left the computational domain at the downstream end.

We characterise the morphology of the deposit layer by (i) the velocity magnitude of the primary particles, (ii) the number of primary particles per agglomerate, N, (iii), the percentage of the wall-area that is covered by deposits, $\mathcal{A}$, (iv) the minimum wall-normal coordinate of the deposit layer, δ_w, and (v) the thickness of the deposit layer, Θ. Along with the amount of primary particles that have deposited, expressed as a percentage of the total number of particles that have been injected into the flow,
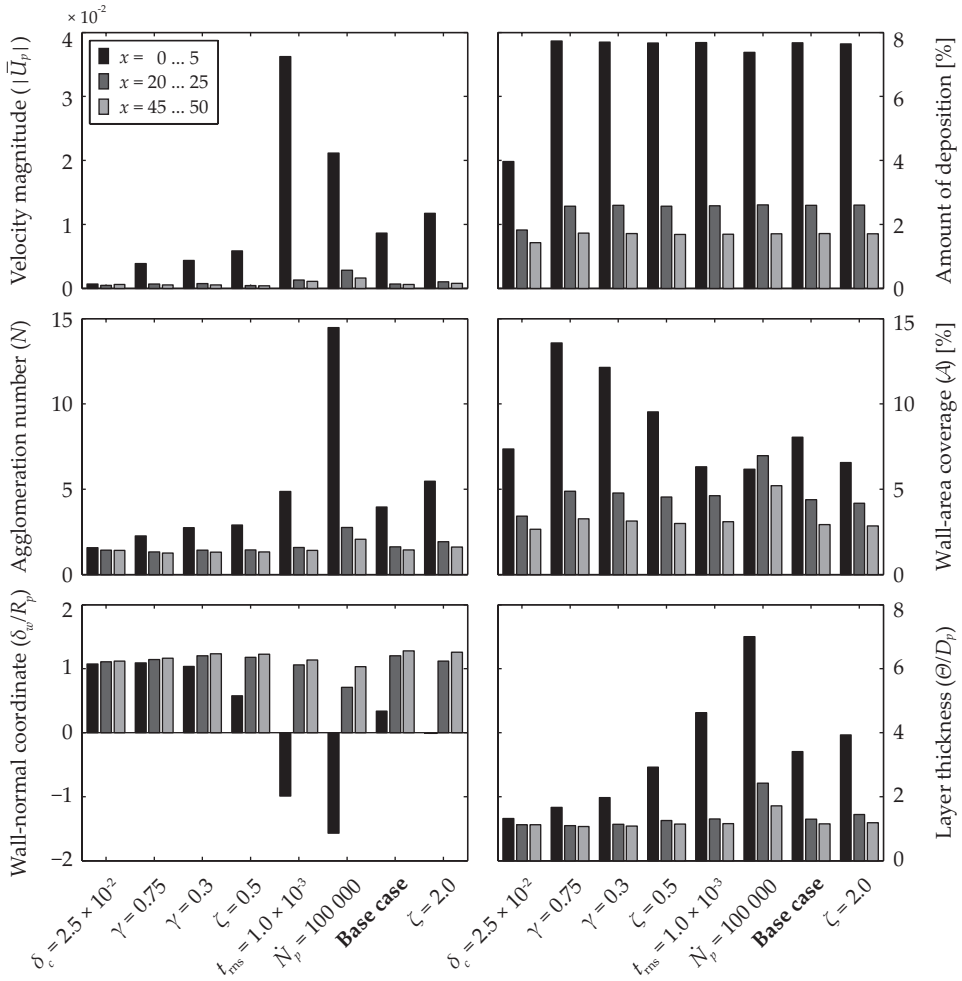
Figure 7.1: Dependence of the deposit layer morphology and the amount of deposited primary particles on deposition model parameters, for three segments of the channel wall. The results shown are obtained using a preliminary version of the Eulerian-Lagrangian model, in a one-way coupled channel domain at Re_∇ equal to 360.

the dependence of these characteristics on the model parameters are shown in Figure 7.1.

The thickness Θ of the deposit layer is determined by dividing the walls of the computational domain into square patches, with edge lengths equal to ten times the primary-particle diameter. Subsequently, the minimum and maximum wall-normal

coordinate for all deposited primary particles that have their centre located in each patch is determined. The value of Θ is then found by averaging the inner and outer coordinates over the isotropic spanwise direction, and subtracting these values from each other. The area fraction $\mathcal{A}$ of the walls that is covered by deposited particles is approximated by the intersected area of all primary particles that are part of the deposit layer and a plane parallel to the walls of the flow domain, located one particle radius inside of it. Finally, the minimum wall-normal coordinate of the deposit layer (which might be negative if particles penetrate into the wall) is defined as the minimum of all wall-normal coordinates of primary particles located in a certain downstream segment.

The results in Figure 7.1 show that, for the set of parameters considered, the total fraction of the injected particles that forms a deposit somewhere inside the domain depends only on the wall-adhesion interaction range δ_c. Since the value of δ_c determines the extent of the region near the channel walls in which particles experience attractive forces towards the wall, this result indicates that the transport of primary particles towards the wall rather than the adhesion is the limiting factor for deposition under the conditions considered. This is confirmed by the fact that the fraction of primary particles that deposit is practically independent of the particle injection rate $\dot{N}_p$, such that twice as many particles deposit on the walls when the supply of particles is doubled.

In general, our results show that the local number-concentration of primary particles that deposit and the mobility of these particles after deposition (as characterised by the velocity magnitude of the primary particles) are very important parameters that largely determine the morphology of the deposit layer. This for instance explains the large increase in N that is found for the doubled particle injection rate in Figure 7.1. The mobility of the deposited primary particles decreases when the strength of the particle wall-adhesion is increased, which occurs for increasing values of γ and/or F_L^*. Contrarily, the mobility of the deposit layer increases if the value of t_{rns} is increased, since this allows agglomerates to adapt their velocity to the stationary walls over a larger time interval. Finally, our results show that the particle mobility slightly increases with respect to the base case if the damped harmonic oscillator is overdamped ($\zeta = 2$), and that it slightly decreases if the system is underdamped ($\zeta = 0.5$).

Since, from the perspective of deposition, the walls of the flow domain are modelled as soft barriers, which do not force particles to stop moving completely upon reaching the coordinate of the walls, a significant amount of particles may protrude through the walls. These particles thus finally end up at locations outside of the actual flow domain (note that in this case, the hydrodynamic force is calculated by assuming that the fluid velocity is zero). The results in Figure 7.1 show that deposited particles reside on the face of the walls ($\delta_w/R_p \approx 1$) only if the agglomerates consist of few primary particles. As soon as the agglomerates consist of more primary particles and the deposit layer becomes thicker, agglomerates significantly penetrate into the walls. This non-physical behaviour of the preliminary deposition and re-entrainment model

was corrected by modifying the formulation of the particle-wall interaction potential, as will be explained in the next paragraphs.

Revision of deposition model. The preliminary deposition model that was used to obtain the results that were presented above, differs from the final version of the deposition model that was described in Section 3.10 in the following two aspects: (i) the value of the parameter ξ, given in equation (3.58), inside the wall, and (ii) the direction of the force $\mathbf{F}_{\text{rns}}^{\text{wall}}$, given in equation (3.60). Both of these aspects of the deposition model were modified following the initial parameter study of the deposition and re-entrainment model, to prevent the excessive penetration of primary particles into the wall that was found above.

In the preliminary model, the maximum repulsive force that is exerted by the wall on primary particles that have negative wall-normal coordinates was limited to the value of γF_L^*. This means that a value of $\xi = 1$ was used inside the wall in equation (3.58). The maximum strength of the repulsive force was raised in the revised model by increasing the value of ξ to 25 inside the wall. Physically, the repulsive force is compressive, and it thus does not have to be limited to the adhesion strength between the particles and the wall. It is purely for reasons of numerical stability that the value of ξ cannot approach infinity inside the wall. We found that a value of 25 was adequate for resolving the wall penetration of the primary particles, and this value was not found to jeopardise the stability of the calculations.

The additional particle-wall interaction force $\mathbf{F}_{\text{rns}}^{\text{wall}}$, which ensures that the velocity of deposited primary particles relaxes towards that of the wall, was proportional to the full predicted velocity vector of the depositing primary particles in the preliminary model. As a result, it consisted both of wall-parallel and wall-normal components, and the effective particle-wall interaction in the wall-parallel direction was given by a superposition of the force due to the damped harmonic oscillator, given in equation (3.57), and an additional contribution that results from equation (3.60). By eliminating the wall-normal component of $\mathbf{F}_{\text{rns}}^{\text{wall}}$, the wall-normal and wall-parallel components of the interaction potential have been completely decoupled in the revised model. The wall-normal component of the particle-wall interaction potential thus is exclusively determined by the damped harmonic oscillator as described in equation (3.57), which ensures that the stable neutral point for the wall-normal interaction force now coincides with $\delta_s = R_p$.

Change of parameters with respect to preliminary model. Apart from improving the formulation of the particle-wall interaction potential, the results of the initial set of simulations described above also allow us to re-define the parameter space that will be explored in the rest of this chapter. Since we have found that the influence of the damping ratio on the properties of the deposit layer is minor, we use the base-case value of this parameter described above ($\zeta = 1$, critical damping) in all the simulations that will follow from this point onward. Because increasing the value of t_{rns} increases the deposit mobility, and we did not encounter any stability issues with the base-case value of $2.5 \cdot 10^{-4}$, we keep the relaxation time of the deposition interaction at the latter value for the rest of the simulations.

Selecting a value of δ_c follows from a delicate balance of competing interests. It is clear that physically, the interaction range should be microscopically large. However, to ensure that any particles are captured by the wall, this would require a very small time step, that, from a practical perspective, is not feasible. Small values of δ_c will lead to a smaller total number of primary particles that deposit on the wall and thus to a less good statistical accuracy for a given number of injected primary particles. As a compromise, we consider slightly smaller values of δ_c ($1.5 \cdot 10^{-2}$ and $3.0 \cdot 10^{-2}$) in all further simulations when compared to the initial simulation set. To compensate for the loss of depositing particles, primary particles will be injected over twice the original time interval, between $t^* = 0$ and $t^* = 10$. To prevent a very strong peak of the deposition rate inside the phase separation region, we will inject particles with a minimum wall-normal coordinate equal to 0.1 instead of the primary particle radius. Also, the increased value $\dot{N}_p$ (100 000) will be used as a default in all further simulations.

The main parameter that will be studied is the adhesion strength between the particles and the walls. Both the values of γ and F_L^* and T_L^* are varied, to study whether the deposition and re-entrainment mainly depend on the actual strength of the interaction between the walls and the agglomerates, or on the balance between the latter interaction and the strength of the bonds inside the agglomerates. The fact that the amount of deposition in the exploratory cases was invariant to adhesion parameters shows that the strength of the particle-wall interaction was too large for a significant amount of re-entrainment to occur. Therefore, we extended the range of both γ and F_L^* and T_L^* towards smaller values, to determine the minimum conditions under which agglomerates still can form deposits.

For interpreting the simulation results, we introduce the *effective* (normalised) particle-wall adhesion parameter $\mathcal{W}$, which combines the effects of varying the internal strength of the agglomerates and γ. It is defined as:

$$\mathcal{W} \equiv \frac{\gamma F_L^*}{[\gamma F_L^*]_{\text{base}}} \tag{7.1}$$

Two-way coupling is used in all further simulations. Therefore, we now consider in- and outflow boundary conditions for the continuous carrier phase as well. Since such simulations require a very large number of computational cells if a considerable length of the computational domain is to be considered, we use LES instead of DNS, as this allows to use a lower grid resolution. In each case, the inflow conditions for the actual flow domain are obtained from a fixed cross-section of a domain with periodic boundary conditions (and $L_x = 5$) that is co-solved with the actual flow domain, using the same value of the time step Δt. Since the pressure drop now is no longer the driving force of the flow in the main domain, the prescribed pressure gradient numbers refer to the co-solved periodic inlet domain.

Simulations have been conducted using a computational domain with $L_x = 30$ at Re_∇ equal to 360, 540, 720 and 1080, whereas for $Re_\nabla = 360$ also simulations have

Table 7.2: Configuration of the numerical grids that are used in the deposition and re-entrainment simulations. All simulations are conducted in LES mode. The sequences for the grid resolutions Δ^+ correspond to $\mathrm{Re}_\nabla = 360$, $\mathrm{Re}_\nabla = 540$, $\mathrm{Re}_\nabla = 720$ and $\mathrm{Re}_\nabla = 1080$, respectively.

Domain size (L_x, L_y, H)	55, 2, 1	30, 2, 1
n_x, n_y, n_z	1056, 64, 48	864, 96, 72
Δ_x^+	19, –, –, –	12.5, 19, 25, 38
Δ_y^+	11, –, –, –	7.5, 11, 15, 23
$\Delta_z^+ \mid_{\text{wall}}$	2.9, –, –, –	1.7, 2.5, 3.4, 5.1
$\Delta_z^+ \mid_{\text{centre}}$	9.6, –, –, –	6.4, 9.7, 13, 19

been conducted in a domain with a larger length ($L_x = 55$), at the expense of grid resolution. The parameters and grid resolutions are summarised in Table 7.2.

The parameters that are used for the dispersed phase are summarised in Table 7.3. In the pipe two values of $\dot{N}_p$ are considered. For $\dot{N}_p$ equal to 100 000, the injection rate per unit of volume is equal in the pipe and in the channel. The injection rate per unit of wall area is 50% smaller in the pipe than in the channel, however. For this reason, we also studied $\dot{N}_p = 200\,000$ in the pipe, as this ensures that the injection rate per unit of wall area is the same in both geometries. Quantitative results of the simulations that have been considered in the pipe will be reported in a future publication, because these simulations took too long to finish before the completion of this thesis.

7.2 Properties of deposition and re-entrainment processes

Figure 7.2 shows examples of deposit layers formed, for different values of the model parameters.

Deposition process. We distinguish between agglomerates that are being transported to the wall by the flow for the first time (primary deposition), by the flow after being

Table 7.3: Overview of dispersed-phase parameters used in the simulations to study deposition and re-entrainment. The values of F_L^* and T_L^* are always changed proportionally between cases.

Parameter	Minimum	Base	Maximum
$\mathcal{W}$	$3.2 \cdot 10^{-2}$	1	3.2
F_L^*	3.9	78.6	248
T_L^*	5.2	1546	4885
γ	$1 \cdot 10^{-2}$	$3.2 \cdot 10^{-2}$	0.32
δ_c	$1.5 \cdot 10^{-2}$	$3.0 \cdot 10^{-2}$	
t_{rns}		$2.5 \cdot 10^{-4}$	
ζ		1.0	
$\dot{N}_p$ (channel)		100 000	
$\dot{N}_p$ (pipe)		100 000	200 000
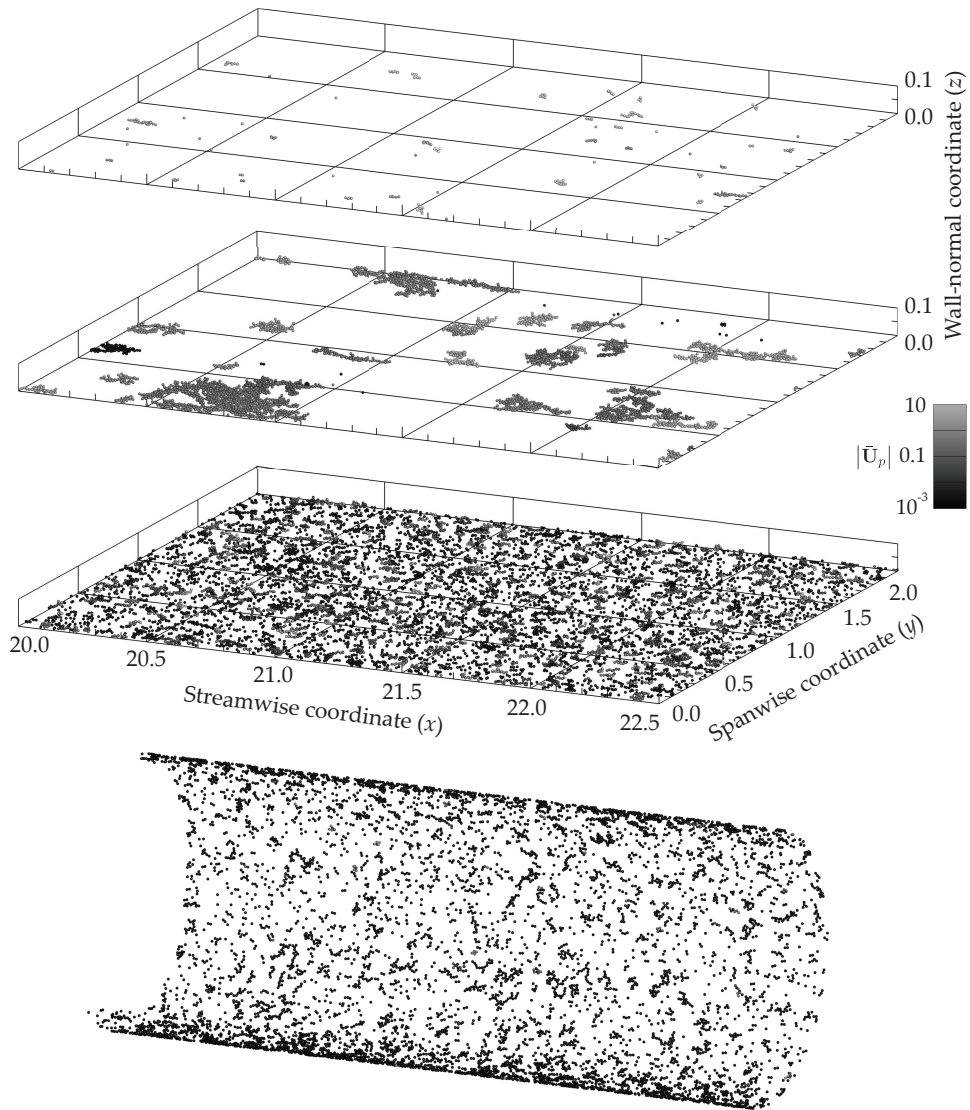
Figure 7.2: Visual representation of deposit layers formed at $Re_\nabla = 360$, using $\delta_c = 0.030$ in the channel. From top to bottom: $\gamma = 0.032$, $F_L^* = 7.9$, $T_L^* = 155$; $\gamma = 0.032$, $F_L^* = 78.6$, $T_L^* = 1546$ and $\gamma = 0.32$, $F_L^* = 78.6$, $T_L^* = 1546$. The deposit layer formed in the pipe shown at the very bottom of the image is obtained using the same parameters as the last presented channel case.
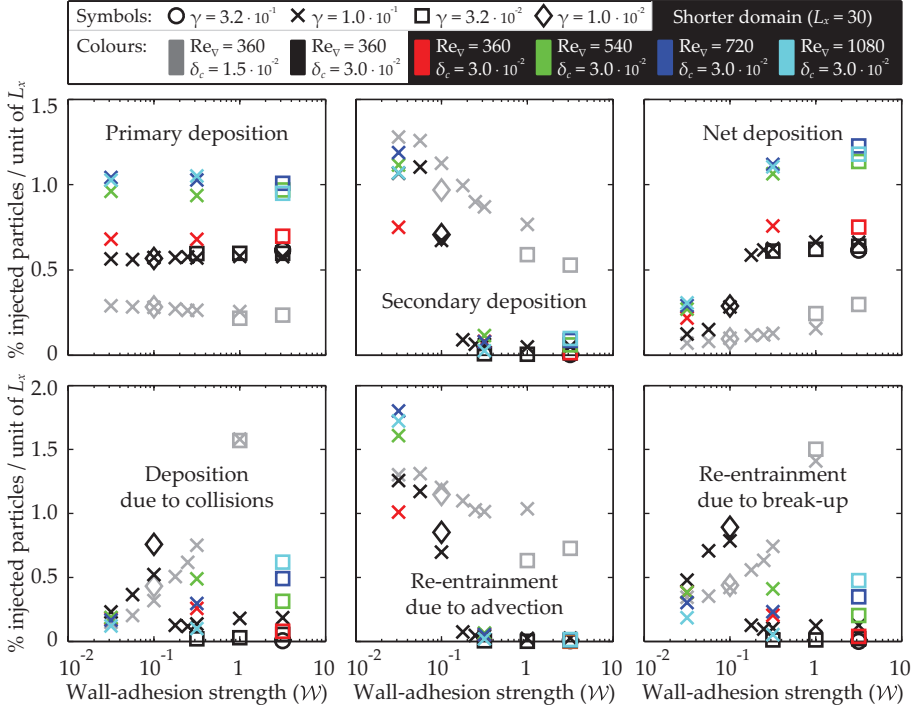
Figure 7.3: Amount of deposition and re-entrainment (as a percentage of the number of injected primary particles), accumulated over the entire length of the computational domain. The different deposition and re-entrainment mechanisms are explained in the text.

re-entrained (secondary deposition), or by colliding to an agglomerate that already has deposited at the wall before. Similarly, for re-entrainment we distinguish between agglomerates that are removed from the wall by the flow by itself, and those that are removed because a part of a deposited agglomerate is broken of the wall when an inter-particle bond is broken. We mark an agglomerate that contains at least *one* primary particle that is closer than a distance δ_c to the wall as being deposited, and consider re-entrainment of an agglomerate to occur as soon as *all* of the primary particles of the agglomerate have a distance larger than δ_c to the wall.

Figure 7.3 shows an overview of the overall deposition and re-entrainment rates, measured over the entire length of the computational domain, for each of the aforementioned mechanisms. Figure 7.4 shows the average number of primary particles per agglomerate that undergoes deposition or re-entrainment. We will first focus on the role of the effective particle-wall adhesion strength $\mathcal{W}$ for Re_∇ equal to 360, and $\delta_c = 0.030$, in the channel with $L_x = 55$. Differences that are found in the process and deposit layer properties at elevated Reynolds numbers, and at the decreased value of
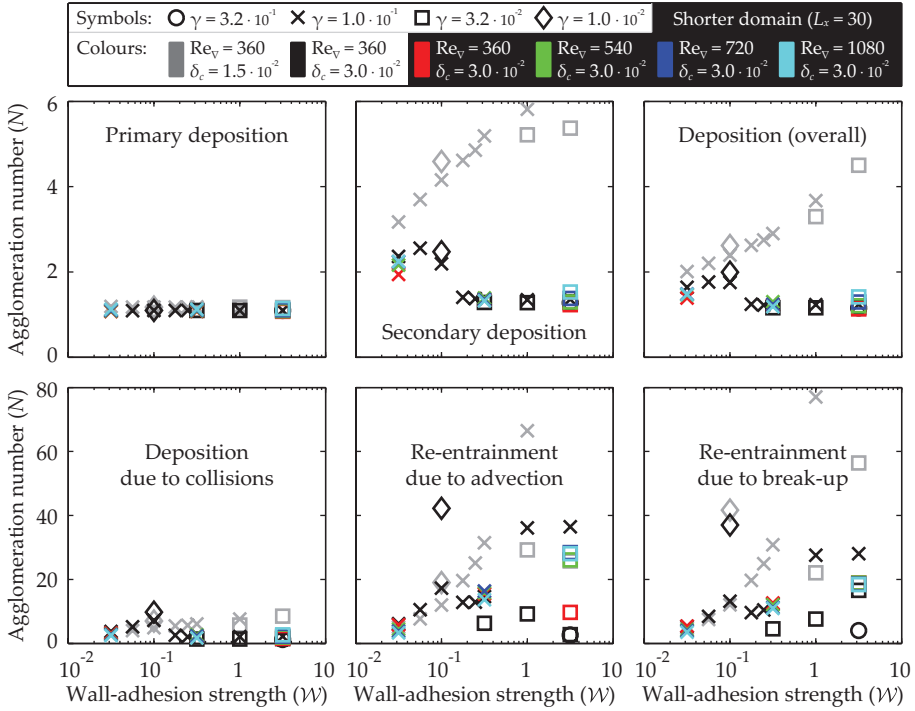
Figure 7.4: Number of primary particles per agglomerate during deposition and re-entrainment, averaged over the entire length of the computational domain, for different deposition and re-entrainment mechanisms, as explained in the text.

the particle-wall interaction range $\delta_c = 0.015$, will be discussed thereafter.

The results in Figures 7.3 and 7.4 show that the primary deposition of agglomerates is almost independent of the effective particle-wall adhesion strength $\mathcal{W}$, both in terms of the amount of deposition, as well as the value of N for the agglomerates that deposit this way. This is because during primary deposition, almost exclusively single primary particles and doublets of primary particles deposit at the wall, which are not affected by the break-up of agglomerates and thus also not by the strength of the inter-particle bonds inside the agglomerates. Also, these agglomerates are not affected by the strength of the particle-wall adhesion, as they just have passed the plane where the particle-wall interaction potential becomes non-zero for the first time.

The strength of the particle-wall adhesion is insufficient to keep deposited primary particles firmly attached to the wall of the flow domain if the value of $\mathcal{W}$ is small. As a result, re-entrainment of deposited agglomerates frequently occurs in this regime, and secondary deposition of re-entrained agglomerates amounts to a larger fraction of the total primary particle flux towards the wall than primary deposition does. Along

with the decrease in the amount of secondary deposition for increasing values of $\mathcal{W}$, a decrease in the value of N of the agglomerates that deposit by this mechanism is found. The latter effect can be attributed to the fact that, agglomerates that contain a relatively large numbers of primary particles can more easily re-entrain into the flow at small values of $\mathcal{W}$ than at larger values of $\mathcal{W}$. Therefore, there is also a larger probability that agglomerates that contain more primary particles re-deposit at the wall during secondary deposition.

For all values of $\mathcal{W}$ that have been considered at $Re_\nabla = 360$ and $\delta_c = 0.030$, the amount of deposition due to collisions of suspended agglomerates with elements of the deposit layer is smaller than the amount of deposition that is caused by the advection of agglomerates towards the wall without colliding to previously deposited agglomerates. In general, we find that the amount of collision-induced deposition decreases with increasing values of γ, and increases with increasing values of $\mathcal{W}$. The latter trend, however, shows a distinctive break around $\mathcal{W} = 0.1$, where many of the properties of the deposition process and the deposit layer undergo transitions. The cause of this will be addressed when we discuss the properties of the deposit layer itself. Averaged over all deposition mechanisms, the mean agglomeration number of depositing agglomerates is very small (< 4), showing that predominantly agglomerates that contain very few primary particles deposit at the wall.

In general, we find that re-entrainment is mostly occurring due to entire agglomerates being transported from the wall by the flow for small values of $\mathcal{W}$, whereas for large values of $\mathcal{W}$, re-entrainment mainly occurs because flow-protruding branches of the deposit layer are breaking loose. For both re-entrainment mechanisms, an increase in N with increasing values of $\mathcal{W}$ is found, whereas it decreases with increasing values of γ. Like for the deposition due to collisions, a pronounced break in the trend that relates the re-entrainment rate for both mechanisms to the value of $\mathcal{W}$ is found at around $\mathcal{W} = 0.1$ for $Re_\nabla = 360$ and $\delta_c = 0.030$.

Given our definition of re-entrainment, the breaking loose of an agglomerate branch that still contains at least one primary particle that is within a distance equal to δ_c from the wall is not being counted as re-entrainment. If this branch later is advected away from the wall, the re-entrainment is counted as being caused by advection rather than break-up, no matter how quickly this occurs after the break-up event. It is difficult to determine accurately what fraction of the advection-attributed re-entrainment actually originates from break-up of deposit layers closer to the wall. The similarities in relations between N and $\mathcal{W}$ for both re-entrainment mechanisms suggest, however, that the underlying cause of the re-entrainment is similar for both mechanisms. This may be an indication that most of the re-entrainment that is attributed to advection actually results from the break-up rather than from the actual removal of complete agglomerates from the wall.

Influence of particle-wall interaction range. As was already observed in the preliminary simulations that were presented at the start of this chapter, a decrease in the particle-wall interaction range δ_c leads to a decrease in the total amount of deposition that occurs in the channel. Apart from this difference, the results that have been

obtained at $\delta_c = 0.015$ and $\delta_c = 0.030$ at $Re_\nabla = 360$ for the $L_x = 55$ domain are rather similar if the value of the effective strength of the particle-wall interaction is small. For increasing values of $\mathcal{W}$, the sharp discrepancies in the process or in the deposit layer properties that were found for $\delta_c = 0.030$ are not observed for $\delta_c = 0.015$ (at least not within the range of values of $\mathcal{W}$ that is studied). We will come back to the differences between the two values of δ_c when we are discussing the properties of the deposit layer in more detail in Section 7.3.

Influence of the Reynolds number. To be able to make a fair comparison to the simulations at elevated Reynolds numbers that have been obtained in the domain with $L_x = 30$, $Re_\nabla = 360$ simulations were also conducted in the shortened higher-resolution computational domain that was used for the $Re_\nabla = 540$, 720 and 1080 simulations. Comparing the results that have been obtained at $Re_\nabla = 360$ with $\delta_c = 0.030$ in the $L_x = 55$ and $L_x = 30$ domains, we find that in the latter case, more deposition of primary particles occurs, as well as deposition due to collisions of agglomerates, whereas there is less re-entrainment and secondary deposition. The net amount of particles that are deposited at the wall slightly increases. These effects in the shortened domain are caused by the fact that primary deposition mainly occurs closer to the region where primary particles are injected into the flow, whereas secondary deposition and re-entrainment are mainly occurring further downstream.

Comparing the results shown in Figures 7.3 and 7.4 for the different Reynolds numbers that were considered, we find that for all values of $\mathcal{W}$ there is a significant enhancement of the deposition and re-entrainment processes for the Reynolds numbers that are elevated above $Re_\nabla = 360$. For Re_∇ beyond 540, however, the net deposition does not increase significantly any more.

Wall-normal velocity during deposition. In terms of modelling, the wall-normal velocity of the agglomerates as they approach the wall during deposition is an important parameter. In engineering models, the rate of deposition of the agglomerates is typically computed by a relation that involves this velocity. Also, it is commonplace to approximate the wall-normal velocity of the dispersed phase to the wall-normal velocity fluctuations of the liquid carrier phase in such models, like it was also done in the drift-flux model that was described in Chapter 4.

Figure 7.5 shows the actual average wall-normal velocity of agglomerates during primary and secondary deposition as found in our simulations, as a function of the effective strength of the particle-wall interaction $\mathcal{W}$. These deposition velocities are measured at the moment that the agglomerates pass the plane that is located at a distance δ_c from the wall. For all cases that have been considered, the average wall-normal velocity of agglomerates during secondary deposition is somewhat smaller than that of agglomerates that undergo primary deposition. This effect is caused by the fact that a certain part of the agglomerates undergoes secondary deposition at a very small time interval after being re-entrained into the flow. Therefore, these agglomerates have a negligible velocity component directed towards the wall. The deposition velocity does not depends much on the value of $\mathcal{W}$ and neither on the internal strength of the agglomerates, both for primary and secondary deposition.
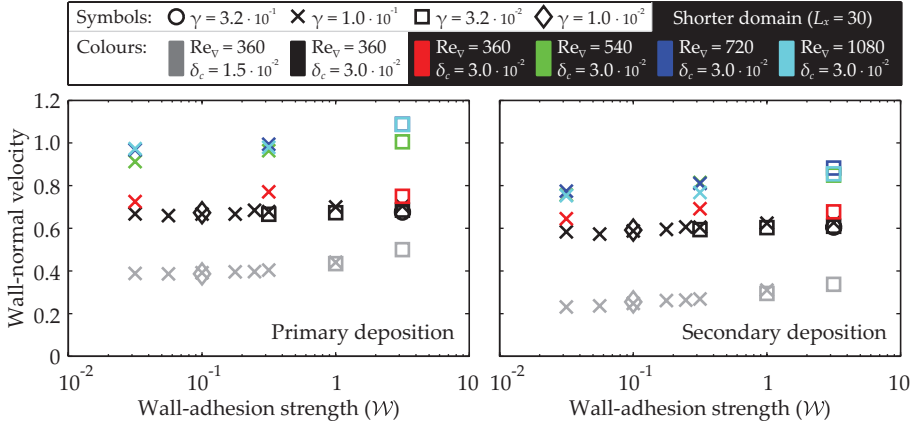
Figure 7.5: Wall-normal velocity of agglomerates that are advected to the wall by the flow during primary and secondary deposition.

For the increased Reynolds numbers in the shortened flow domain, we find that the deposition velocity significantly increases when Re_∇ = 360 is increased to 540, but no strong further increase is found for Re_∇ equal to 720 and 1080, which is similar to the previous result that was found for the amount of deposition. The decrease in the mean wall-normal velocity that is found when δ_c is reduced from 0.030 to 0.015 in the L_x = 55, Re_∇ = 360 simulations can be explained by the fact that the deposition velocities are measured at different wall-normal locations if the value of δ_c is varied.

The values of $\mathcal{V}_T$ that are calculated using equation (4.44) with the turbulent velocity fluctuations calculated at a wall-normal coordinate equal to 0.030 are equal to 0.36, 0.38, 0.42 and 0.53, for Re_∇ equal to 360, 540, 720 and 1080, respectively. At Re_∇ = 360 and δ_c = 0.015, the predicted $\mathcal{V}_T$ is equal to 0.13. We thus find that the relation given in equation (4.44) (which is used as part of the deposition closure in the one-dimensional model presented in Chapter 4) underestimates the actual deposition velocities due to the turbulence to some extent, but not severely.

7.3 Properties of deposit layer

Figures 7.6 and 7.7 show the properties of the deposit layer that is formed, as a function of the effective adhesion strength $\mathcal{W}$, at t^* = 15. Results are presented for three different segments of the wall: a segment upstream in the domain ($x = 5 \ldots x = 10$), a midstream segment ($x = 20 \ldots x = 25$), and a downstream segment ($x = 45 \ldots x = 50$). For the simulations with L_x = 30, no results for $x = 45 \ldots x = 50$ are shown; the «mid-stream» segment ($x = 20 \ldots x = 25$) here effectively is the downstream-segment, located equally far from the end of the computational domain as the aforementioned downstream segment is for L_x = 55. The values of $\mathcal{A}$, δ_w and Θ are obtained the same way as was explained in Section 7.1.

131
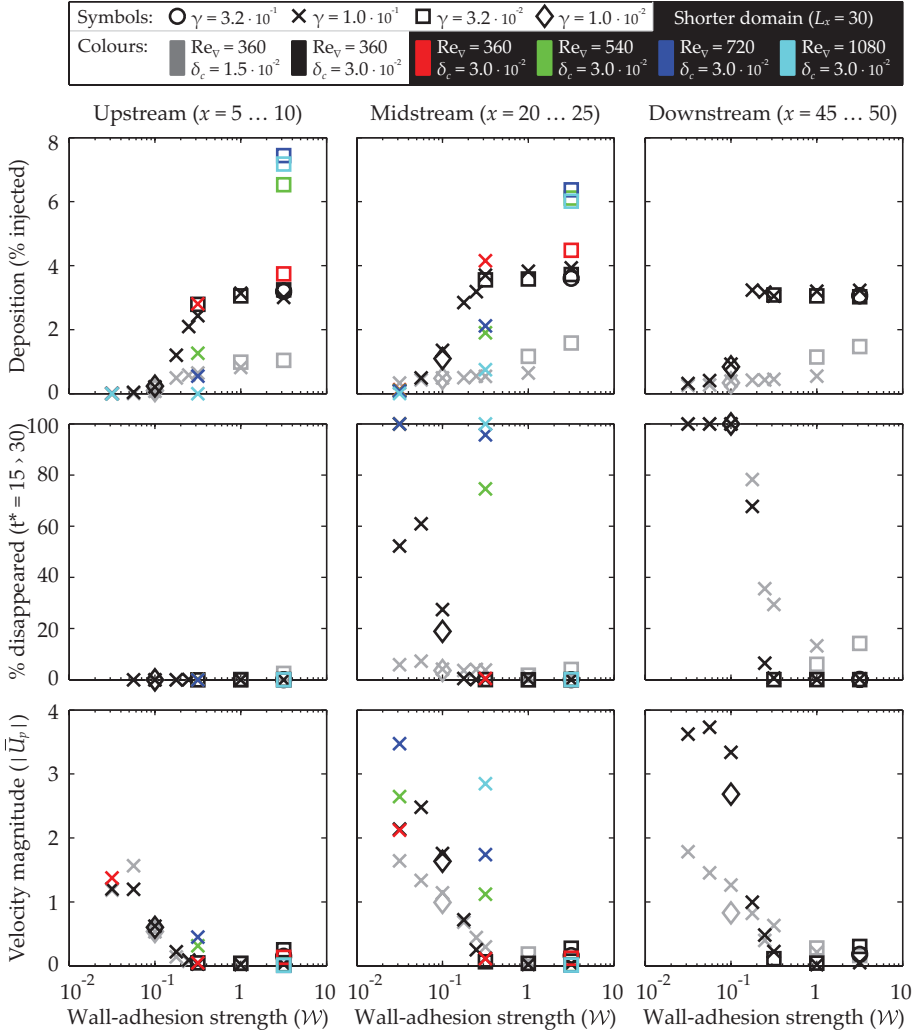
Figure 7.6: Properties of the deposit layer, measured at $t^* = 15$, for different segments of the wall. More properties are shown in Figure 7.7.
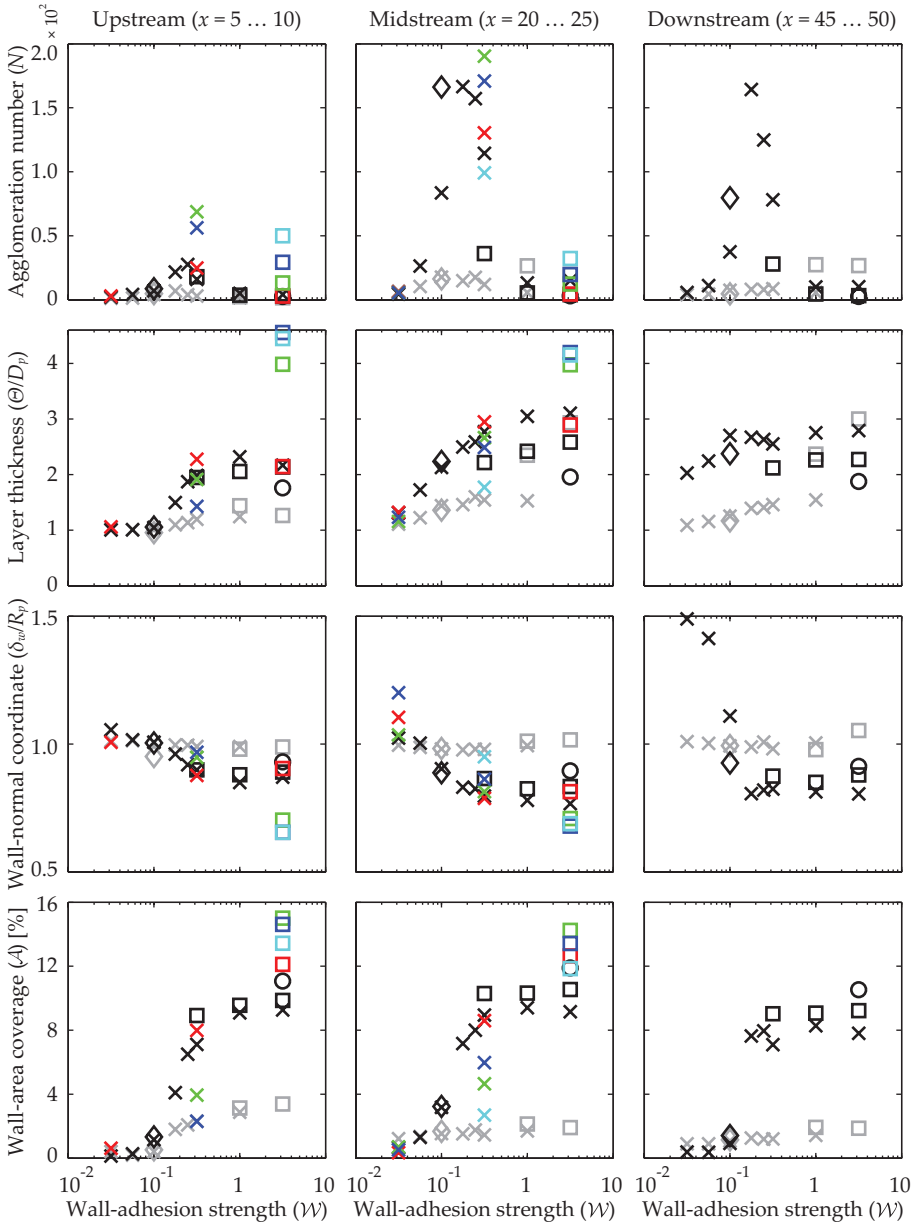
Figure 7.7: Properties of the deposit layer, measured at $t^* = 15$, for different segments of the wall. Continuation of the properties shown in Figure 7.6.

Again, we will first focus on the results that have been obtained at $Re_\nabla = 360$ and $\delta_c = 0.030$ before discussing the influence of the Reynolds number and the particle-wall interaction range on the properties of the deposit layer. Three distinctively different regimes can be observed depending on the value of $\mathcal{W}$; we will discuss these regimes one by one.

First regime: small $\mathcal{W}$ (< 0.1). Visual inspection of snapshots of the deposit layer that have been made throughout the deposition and re-entrainment process reveal that at $Re_\nabla = 360$ and $\delta_c = 0.030$, all deposited agglomerates continuously move over the wall if the value of $\mathcal{W}$ is small. As a consequence, the velocity magnitude of the deposited primary particles is very large in this regime. Note that the maximum values of $\left|\bar{U}_p\right|$ shown in Figure 7.6 are about 100 times larger than those found in Figure 7.1, which is a result of the decreased strength of the particle-wall interaction. Because the deposited agglomerates move at similar velocities, there are relatively little mutual collisions between them. The agglomeration number of the deposited particles thus does not increase significantly with respect to the value of N that is representative for the agglomerates during their initial deposition. Effectively, the entire deposit layer is traversing to farther downstream coordinates over time. Consequently, there is no deposit layer left at the wall in the upstream segment of the flow domain at $t^* = 15$ in this regime. For the same reason, a large percentage of those primary particles that were deposited at that time has been removed from the simulation domain by $t^* = 30$, simply because large parts of the deposit layer slide over the wall out of the computational domain at the downstream end.

Due to the small strength of the particle-wall interaction in the wall-normal direction, the hydrodynamic stresses that are acting on the deposit layer are frequently strong enough to overcome the adhesive force between the deposit layer and the wall. Re-entrainment of agglomerates is therefore frequently occurring in the small-$\mathcal{W}$-regime. Also, we observe that agglomerates frequently pass the deposition measurement plane only partially if $\mathcal{W}$ is small, indicating that they are very loosely attached to the wall. The relatively small values of N in the deposit layer nevertheless causes the thickness of it to remain rather small.

In the downstream wall segment, we find that the normalised value of the minimum wall-normal coordinate of the deposit layer is much larger than unity if the value of $\mathcal{W}$ is very small. This apparent sign of detachment of the deposit layer from the wall is caused by the fact that downstream in the domain, re-entrainment is still frequently taking place at $t^* = 15$. In some of the wall patches that are used to determine the minimum wall-normal coordinate of the deposit layer, only agglomerates that are in the process of being re-entrained have remained at the wall at $t^* = 15$. Since these agglomerates have relatively large wall-normal coordinates, this causes a bias in the measurement of δ_w towards larger values than actually are representative of the deposit layer itself.

Second regime: intermediate $\mathcal{W}$ (0.1 < 0.8). At intermediate values of $\mathcal{W}$, the wall-parallel component of the particle-wall adhesion is of sufficient magnitude to retain agglomerates that contain a relatively small number of primary particles firmly

attached to the wall, at least for most of the time. The motion of the deposit layer therefore becomes intermittent, as some of its elements every now and then do travel downstream over the wall upon being exposed by a temporary burst in the wall shear stress caused by velocity fluctuations of the turbulent flow. As a result, relative motion between different agglomerates that have been deposited at the wall becomes an important factor in this regime, causing collisions between different elements of the deposit layer and thus a (strong) temporal increases in $N_{p|a}$. Ultimately, large, sheet-like structures that contain large numbers of primary particles ($\mathcal{O}\,(100 - 1000)$) are formed in this regime, that can no longer be retained by the wall-parallel component of the particle-wall interaction and thus continuously move over the wall. In fact, these sheet-like structures frequently break and re-attach, such that each of them actually consists of several separate agglomerates that lay almost adjacent to each other.

The formation of large sheet-like structures is key to explaining the sudden trend breaks in the deposition and re-entrainment process parameters, as well as in the properties of the deposit layer formed, that occur around $\mathcal{W} = 0.1$ for $Re_{\bigtriangledown} = 360$ and $\delta_c = 0.030$. First of all, large layers of deposited particles are far more difficult to re-entrain into the flow than smaller individual agglomerates, which explains why the re-entrainment suddenly drops at around $\mathcal{W} = 0.1$. Likewise, the chance that relatively large agglomerate branches can re-entrain into the flow when they are broken loose from the deposit layer significantly reduces. Therefore, these branches are no longer available to re-deposit at the wall by re-colliding with other elements of the deposit layer. This explains the sudden trend breaks that are found at around $\mathcal{W} = 0.1$ in Figure 7.3 in the re-entrainment rate due to break-up, as well as in the deposition rate due to collisions. It also causes the sudden decrease of N with increasing value of $\mathcal{W}$ that is found during secondary deposition, during deposition due to collisions, and during re-entrainment due to advection, as well as during re-entrainment due to break-up.

The increased strength of the particle-wall interaction when compared to the first regime causes the velocity magnitude of the deposit layer to reduce in magnitude. Therefore the amount of deposition that remains at the wall is higher for a longer period of time. The thickness of the deposit layer increases, and the minimum wall-normal coordinate of the layer decreases slightly, such that the deposit layer very mildly gets pushed into the wall of the flow domain. The minimum value of δ_w/R_p of $+0.8$ that is found in the revised model is much less extreme than the minimum value of -1.6 that was found in the preliminary simulations, which shows that the modifications that were made to the model to prevent wall-penetration are performing satisfactory. Since the thickness of the deposit layer increases, the wall-area coverage $\mathcal{A}$ increases less with increasing values of $\mathcal{W}$ than the amount of deposited primary particles does when comparing the intermediate-$\mathcal{W}$-regime to the small-$\mathcal{W}$-regime.

Third regime: large $\mathcal{W}$ (> 0.8). At even larger values of $\mathcal{W}$, fluctuations in the wall shear stress are less likely to be strong enough to drag small deposited agglomerates along the wall intermittently, thereby reducing the precursor the formation of large

the large sheet-like structures that occurs in the intermediate-$\mathcal{W}$-regime. As a result, both the mobility of the deposit layer and the value of N inside the deposit layer reduce if $\mathcal{W}$ is increased above a certain threshold. For sufficiently large values of $\mathcal{W}$, the deposited agglomerates remain at the wall as individual entities for very long time intervals, and the total amount of deposition does therefore hardly change over time once the deposit layer has settled in.

In contrast to the regimes of small and intermediate $\mathcal{W}$, where the properties of the deposit layer were found to hardly depend on the value of γ, we observe more pronounced differences when the internal strength of the agglomerates is varied at fixed values of $\mathcal{W}$ if $\mathcal{W}$ is large. At a given value of $\mathcal{W}$, the thickness of the deposit layer increases if the internal strength of the agglomerates increases (viz. at lower values of γ). This is caused by the fact that branches of the deposit layer that extend significantly into the flow can better withstand the stresses induced inside them if the values of F_L^* and T_L^* are larger, and thus are less likely to be broken free from the wall.

The characteristic slip velocity of primary particles that are protruding far into the flow is larger than of those primary particles that are relatively close to the wall, because the average fluid velocity increases for increasing wall-normal coordinates. The hydrodynamic stresses that are induced on these protruding branches are therefore relatively strong. Since these stresses are being transferred all the way to the wall if the internal strength of the agglomerates is large enough, this increases the chance that they can overcome the wall-parallel adhesion when compared to the case in which the internal strength of the agglomerates is smaller. For the same reason, the value of N inside the deposit layer is smaller if the internal strength of the agglomerates decreases (or, equivalently, if γ increases). Effectively, the crossover between the intermediate- and large-$\mathcal{W}$-regimes (with intermittent and stable deposition, respectively) occurs at larger values of $\mathcal{W}$ if the internal strength of the agglomerates increases.

The trend of increasing deposit stability with increasing values of $\mathcal{W}$ that is found in our simulations qualitatively agrees with the observations by Boek et al. (2008, 2010), who found that for an increasing strength of the particle-wall interaction, transient and eventually permanent blocking occurs for simulated asphaltene deposition in square capillaries.

Differences for different downstream coordinates. Since primary particles are injected at a minimum wall-normal coordinate of 0.1 in the present simulations, primary particles require some streamwise distance before they can deposit at the wall. The amount of deposition in the upstream segment is therefore relatively moderate when compared to the midstream and downstream segments. As a result, the number of deposited primary particles per unit of wall area is limited in this region. Because they are farther apart, the deposited agglomerates are less likely to collide into each other in the upstream segment when compared to the other segments, even when they have similar relative velocities. All of the effects that have been explained above are therefore less intense in the upstream region of the computational domain when compared to the mid- and downstream regions. This is in correspondence with the results that are shown in Figures 7.6 and 7.7.

Influence of δ_c. For small values of $\mathcal{W}$, the behaviour of the deposit layer that is found for $\delta_c = 0.015$ is very similar to the results that are found in the small-$\mathcal{W}$-regime for $\delta_c = 0.030$. For values of $\mathcal{W}$ that increase above 0.1, the movement of the deposit layer becomes intermittent at $\delta_c = 0.015$, like it does for $\delta_c = 0.030$. However, this intermittency does not translate into the formation of large sheet-like structures, but rather into the re-entrainment of large agglomerate chunks, that continues up to large values of $\mathcal{W}$. This difference is caused by the smaller interaction range between the particles and the wall, where in the initial stage of intermittent deposit motion, agglomerates are far more easily being re-entrained into the flow because the interaction range is too small to retain them at the wall. Since large sheet-like structures are no longer formed upon increasing the value of $\mathcal{W}$, the properties of the deposit layer change far more gently as a function of $\mathcal{W}$ for $\delta_c = 0.015$ than for $\delta_c = 0.030$. The general decrease in the thickness of the deposit layer, the reduction of the area of the wall that is covered by the deposit layer, and the better compliance of the non-dimensional minimum coordinate of the deposit layer δ_w/R_p to unity can be attributed to the general decrease of the deposition with decreasing values of δ_c.

Even at the largest values of $\mathcal{W}$ that have been considered in this work, no stable deposition regime exists for $\delta_c = 0.015$. Despite this, we do find that the properties of the deposit layer become dependent on the relative magnitude of the internal agglomerate strength when compared to the strength of the particle-wall adhesion interaction when the value of $\mathcal{W}$ is large. An increase in the internal strength of the agglomerates at large values of $\mathcal{W}$ incurs hydrodynamic stresses an the wall that cannot be sustained by the particle-wall interaction if $\delta_c = 0.015$, simply because a too small fraction of the primary particles inside the deposit layer is actually attracted to the wall. Decreasing the value of γ at fixed values of $\mathcal{W}$ (through increasing F_L^* and T_L^*) thus significantly increases the rate at which agglomerates are removed from the wall. Since, by contrast to the results found at $\delta_c = 0.030$, re-entrainment in general still frequently occurs for large values of $\mathcal{W}$ if $\delta_c = 0.015$, this explains why the net deposition rate significantly increases when the value of γ is increased at large values of $\mathcal{W}$ for $\delta_c = 0.015$. The same mechanism thus also causes the amount of primary particles that can remain attached to the walls for prolonged periods of time to show a significant dependence on the value of γ.

Influence of Re_∇. We find that for increasing Reynolds numbers, the crossover between the small- and intermediate-$\mathcal{W}$-regime, as well as the crossover between the intermediate- and large-$\mathcal{W}$-regime shift to larger values of $\mathcal{W}$. Consequently, small agglomerates that all move with respect to the wall are present in the deposit layer at $\mathcal{W} = 0.32$ at the Reynolds numbers above 360 and at $\mathcal{W} = 3.2$, very large sheet-like structures are formed that also move with respect to the wall. The overall increase in the agglomeration number of the deposit layer can be explained from the fact that the shear stress at the wall increases if the Reynolds number is increased (thereby allowing even larger deposited agglomerates to undergo significant movement with respect to the wall). Combined with the larger overall deposition rate, this results in a larger thickness of the deposit layer, and explains the increased mobility, and the larger rate at which deposited agglomerates disappear at $x = L_x$. The delayed

crossover between the small- and intermediate-$\mathcal{W}$-regime explains why the value of N of the deposit layer is still smaller at $Re_\triangledown = 1080$ than it is at $Re_\triangledown = 360$ for $\mathcal{W} = 0.32$, because here the formation of deposit-sheets has not completely set in yet.

The increased thickness of the deposit layer that is found at elevated Reynolds numbers also caused the value of δ_w/δ_c to decrease considerably, even with the enforced repulsive particle-wall interaction that was introduced in the revised model. Still, the deposit layer is pushed into the wall by only about 10% of its thickness in the worst case that was observed.

7.4   Modification of pressure drop due to deposit layer formation

In the Eulerian-Lagrangian model, we use the point-particle approach. Although the primary particles have a radius attributed to them, their volume is not explicitly taken into account in the continuous carrier-phase solver. As such, the formation of a deposit layer does not lead to a formal reduction of the channel height or the pipe diameter, contrary to the approach adopted in the one-dimensional drift-flux model. Still, the force distribution that the dispersed phase exerted on the fluid when using two-way coupling ensure that the continuous carrier-phase flow is affected by the occurrence of deposition.

Since we consider in- and outflow boundary conditions for the non-compressible continuous carrier phase when simulating deposition and re-entrainment, the total mass flux of liquid through each cross-sectional plane of the computational domain is by construction equal to the mass flux that is imposed at the inlet plane. Instead the pressure gradient over the domain changes under the influence of the deposition and re-entrainment.

Figure 7.8 shows the increase in the pressure drop over the entire domain (excluding the periodic inlet region) when a deposit layer is present, when compared to the case where there is no dispersed phase present in the channel. We find that the total pressure drop in the channel can increase by as much as 90% as a result of deposition for the range of parameters that is studied in this work. The additional pressure drop increases with increasing values of $\mathcal{W}$, because more primary particles remain deposited inside the domain for long periods of time when the strength of the particle-wall interaction increases. Contrarily, the additional pressure drop decreases with increasing values of γ, and it thus increases with increasing values of the internal strength of the agglomerates. This is a result of the decrease of the deposit layer thickness that is found with increasing values of γ. More protrusion of the deposited primary particles into the flow will give a larger the slip velocity between the particles and the undisturbed flow. The latter effect results in an increased magnitude of the body force that is exerted by the deposit layer onto the continuous carrier phase, and thus into a larger pressure drop.
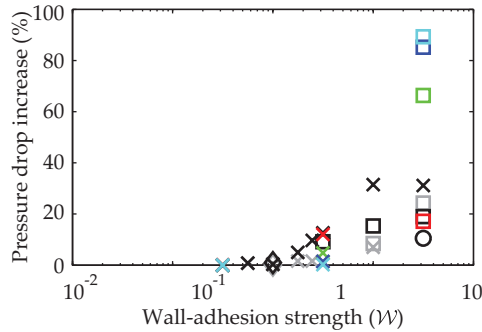
Figure 7.8: Increase in the pressure drop incurred by the deposit layer with respect to a non-laden flow. Results are averaged over the entire length of the computational domain, between $t^* = 15$ and $t^* = 30$. The legend is the same as in Figures 7.3 to 7.7.

7.5   Summary

In this chapter, we have considered deposition and re-entrainment using the Eulerian-Lagrangian model described in Chapter 3, as it occurs when particle-wall interactions are taken into account as outlined in Section 3.10. We have focused on the dependence of the properties of the deposit layer formed, as well as of the rates of deposition and re-entrainment, on the particle-wall interaction strength, on the internal strength of the agglomerates, and on the Reynolds number. In these simulations, in- and outflow boundary conditions were used, such that the total flow rate of the continuous carrier phase is fixed.

Because of computational time constraints induced by the increased length of the computational domain that is associated with in- and outflow boundary conditions, it was not feasible to achieve a steady-state between deposition and re-entrainment in these simulations. Instead, we have studied the initial stages of the deposition and re-entrainment processes, as they occur when primary particles are injected into the flow domain in a certain region for specified amount of time. The model was applied both to channel and pipe flows, but only channel flow results are reported here because the pipe flow simulations have not been finished before completing this thesis. Still, a few interesting observations have been made.

Our results show that only small agglomerates deposit at the walls of the flow domain, especially during primary deposition. This is in agreement with the hypothesis by Eskin et al. (2011), which states that only agglomerates with a radius smaller than a critical deposition radius contribute to the formation of a deposit layer. Furthermore, we have found that the deposition velocity of the agglomerates is underpredicted by empirical correlations that are used in one-dimensional models that have been proposed in the literature. The same closure relations have also been used in the drift-flux model described in Chapter 4.

Based on the adhesion strength between the dispersed phase and the walls, we have identified three regimes for the evolution of the deposit layer after the initial deposition of the agglomerates at the walls. If the particle-wall adhesion strength is very small, all agglomerates that constitute the deposit layer continuously move over the wall. As there is limited relative motion between the agglomerates, further agglomeration inside the deposit layer is not frequently occurring in this regime. For larger strengths of the particle-wall interaction, the motion of the deposit layer becomes intermittent. The strong increase in relative motion in the deposit layer that is associated with this intermittency leads to vastly increased mutual deposit agglomeration, which ultimately results in the formation of large sheet-like structures. For even larger strengths of the particle-wall interaction potential, depositing agglomerates remain as stable separate entities at the wall for prolonged periods of time. In this regime, the internal strength of the agglomerates is found to become an important parameter in determining the deposit layer morphology.

Because the volume of the primary particles is not explicitly taken into account in the continuous carrier-phase solver, the dimensions of the flow domain do not change when a deposit layer is formed. However, the force interaction that occurs if two-way coupling is considered ensures that the deposition does have an influence on the flow of the carrier phase. Since the flow rate is fixed by the inflow boundary condition, the pressure drop over the domain was monitored to study the influence of the deposit layer on the flow. The increase in the pressure drop is found to be higher when the particle-wall adhesion strength is increased, whereas at a fixed strength of the particle-wall adhesion strength, a decrease in the internal strength of agglomerates is found to reduce the increase in pressure drop. This is caused by the fact that the thickness of the deposit layer is strongly dependent on the internal strength of the agglomerates.

Increasing the Reynolds number beyond $Re_\nabla = 360$ is found to increase the percentage of the agglomerates that deposit at the wall, although the increase stagnates if Re_∇ is increased beyond 540. Similar results are found for the deposition velocity. Increasing the Reynolds number is found to delay the onset of the formation of stable deposit layers with respect to the effective particle-wall adhesion-strength $\mathcal{W}$. This shows that specifying the particle-wall interaction strength non-dimensionalised by the characteristic hydrodynamic force that is exerted on a freely moving spherical particle in the turbulent flow is insufficient to fully characterise the deposit layer behaviour for arbitrary values of the Reynolds number.

Chapter 8

Critical review, verification, and validation of models and parameters

In Chapters 3, 5, 6 and 7, we have only sporadically questioned the accuracy with which the Eulerian-Lagrangian model can represent the evolution of real asphaltene agglomerates under field production conditions. In this chapter, a critical review of the model in this respect is made. Furthermore, we will outline the steps that need to be taken to fully verify and validate the model, and discuss what steps have been taken in this direction so far. Also, the verification and validation of the one-dimensional drift-flux model will be discussed. At the end of the chapter, we discuss to what extent the fundamental insights that have been obtained on the agglomeration, break-up, deposition and re-entrainment processes using the Eulerian-Lagrangian model can be used to obtain improved closure relations in predictive engineering models for asphaltene deposition.

8.1 Applicability of the Eulerian-Lagrangian model to real asphaltenes

The verification of the accuracy with which the Eulerian-Lagrangian model proposed in Chapter 3 can represent the evolution that real asphaltenes undergo after they separate from a crude oil consists of several aspects. First of all, we will consider whether the simplified hydrodynamic force model that is adopted in the Eulerian-Lagrangian model can accurately describe the forces that are exerted on agglomerates with complex shapes. Secondly, we assess whether the model parameters that have been used in Chapters 5, 6 and 7 are representative of asphaltenes. Finally, we consider the challenging task of the actual validation of the model results to experimental data for asphaltenes or, where necessary, for model compounds.

Hydrodynamic force model and free-draining approximation

Because a point-particle approach is used to represent the primary particles in the Eulerian-Lagrangian model, the flow around (and inside) the agglomerates is not

resolved. A sub-model is thus required to compute the hydrodynamic force that is exerted on the individual primary particles that form an agglomerate. For simplicity and efficiency, the model that we adopted does not take into account shielding effects between nearby primary particles, and it only considers Stokes drag with a simplified added mass correction. It is therefore useful to check to what extent the hydrodynamic force distribution inside an agglomerate is representative for the actual hydrodynamic force that would be found if the flow around and inside the agglomerates is *resolved*. To this end, Martin Ernst of the Martin Luther University in Halle-Wittenberg was so helpful to conduct fully-resolved simulations for an agglomerate that was formed using our model.

A Lattice-Boltzmann method, that is described by Ernst et al. (2013), was used in the resolved simulations, in which a steady laminar shear flow over a stationary agglomerate was considered in a square box with periodic boundary conditions in the streamwise and spanwise directions. Four levels of local grid refinement are used, such that at the finest level, that is applied near the agglomerate, the diameter of a single primary particle is spanned by as much as 10 grid cells. Similar to the primary particle Reynolds numbers that were considered in Chapters 5, 6 and 7 of this thesis, a Reynolds number of the individual primary particles of about 10 is considered. The same flow conditions were reproduced in our Eulerian-Lagrangian model, and a comparison of the hydrodynamic force per individual primary particle along the three Cartesian coordinates is shown in Figure 8.1.

The results of the comparison in Figure 8.1 show that using one-way coupling, the streamwise hydrodynamic force in the Eulerian-Lagrangian model is substantially overpredicted for all of the primary particles in the agglomerate. Since flow is directed purely in the streamwise direction, the slip velocity in the spanwise and wall-normal directions is equal to zero in this case. The forces that are induced onto the agglomerate in these directions, as found in the fully-resolved simulations, are therefore not captured by our Eulerian-Lagrangian model.

When two-way coupling is used, however, we find that the overall trends in the hydro-dynamic force are captured with satisfactory accuracy. The streamwise forces on the individual primary particles that are located at the downstream side of the agglomerate are under- or overpredicted by our model by up to a factor five. Nevertheless, our model is able to represent the force distribution at the front of the agglomerate as well as the average force components over all particles with reasonable accuracy when two-way coupling is considered. The average force in the streamwise, spanwise and wall-normal directions is underpredicted by 20, 40 and 44%, respectively, when compared to the fully-resolved simulations. It is thus reasonable to apply the hydro-dynamic force model that was described in Chapter 3 to compute the force exerted by the flow onto the agglomerates.

Review of the model parameters used in Chapters 5, 6 and 7

Tracking the formation, break-up, deposition and re-entrainment of agglomerates in the Eulerian-Lagrangian framework is a computationally intensive task. Therefore,
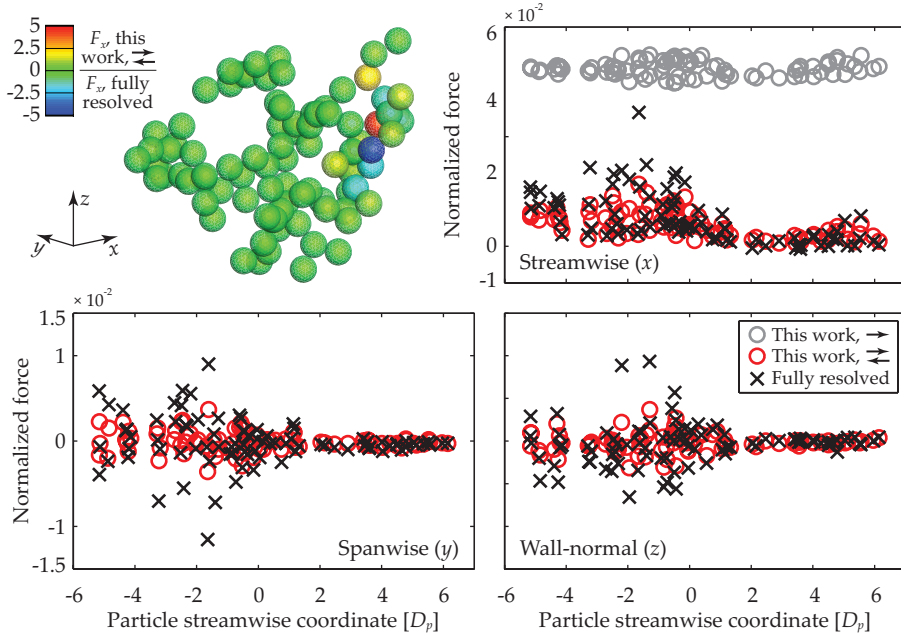
Figure 8.1: Comparison of the hydrodynamic force as predicted in the Eulerian-Lagrangian model to results from fully-resolved Lattice-Boltzmann simulations conducted by Martin Ernst.

some compromises had to be made in the parameter space that was studied in this work. We will discuss these compromises one by one.

Continuous liquid carrier phase Reynolds number. The bulk Reynolds numbers that have been studied in Chapter 5, 6 and 7 are in the range of 5400 to 19 400. These Reynolds numbers are somewhat on the lower end of the spectrum of the typical conditions in wellbores and oil production flowlines. However, they are reasonable for wells in which relatively viscous oil is produced at moderate production rates. Since the results of our simulations show that the properties of the agglomerates and the deposit layers formed do not strongly depend on the Reynolds number as long as the flow is turbulent, we have confidence that the range of Reynolds numbers studied in this work is well representative of field-relevant conditions.

Primary particle radius. One of the limitations of the present, single-core implementation of the Eulerian-Lagrangian model is that it requires a significant volume fraction of the dispersed phase in order to achieve a steady-state between agglomeration and break-up within a reasonable amount of computational time. Therefore, dispersed-phase fractions of over 1% were used in the Chapters 5 and 6 of this thesis.

By itself, this volume fraction is reasonable considering the typical asphaltene content of crude oils. However, the number of primary particles that can practically be

considered in the present model formulation is limited to about one million. However, the minimum volume of the computational domain that has to be considered is limited by the requirement that the turbulent flow should de-correlate well within the length of the computational domain in the periodic directions. As a consequence, relatively large primary particles have to be used to arrive at the required volume fraction of the dispersed phase.

In all of the simulations that have been conducted using the Eulerian-Lagrangian model in this work, a primary particle radius equal to 0.5% of the channel height (or of the pipe diameter) was therefore considered. Translated to typical dimensions of a wellbore or production pipeline of, say, 10 centimetres, the radius of these primary particles is equal to 500 micrometres. The linear dimensions of the largest asphaltene agglomerates that have been reported in the literature do not even surpass this dimension. The primary particle radius that is presently used can therefore hardly be considered to be representative for real primary asphaltene particles that are the building blocks for asphaltene agglomerates.

Due to the increased dimensions of the primary particles, the dimensions of the agglomerates that are formed in our simulations are also significantly larger than those of real asphaltene agglomerates. Consequently, the relative scale of the agglomerates with respect to the cascade of turbulent flow structures is also different. The dynamics of the real asphaltene evolution will more strongly depend on the smallest eddies in turbulent flow under actual production conditions than in our simulations, and less on the larger eddies.

Strength of inter-particle bonds and particle-wall interaction parameters. To investigate whether the range of strengths for the inter-particle bonds considered in this work is reasonable for actual asphaltenes, tensile test have been conducted at TNO Eindhoven by Hartmut Fisher for an asphaltene sample that was collected from a separator by a solvent wash. As preparation for the tensile tests, the asphaltene sample was pressed into a thin (1.5 mm) plate at room temperature. Strips of this plate with a width of 10 mm are subsequently cut and they are clamped into the measurement chamber of the tensile test device at a temperature of 65°C. The measurement chamber is thereafter cooled to 23°C, and the clamps are adjusted to accommodate for a slight shrinkage of the samples. The tensile tests are thereafter performed at a strain rate of ±0.01% per second. Three specimens from the same source were tested, and the maximum stresses that these samples could withstand were found to be 27, 43 and 50 kPa, respectively.

To see how these maximum tensile stresses compare to the values of F_L^* that have been used in Chapters 5, 6 and 7, let us consider the following situation. Assume that asphaltene agglomeration is occurring inside a wellbore, again with a typical internal diameter of 10 cm, through which crude oil is produced at a bulk Reynolds number of 10 000. If the viscosity of the oil is 50 mPas and the density is 800 kg/m^3, the bulk flow velocity will be just over 6 m/s, corresponding to a pressure gradient velocity u_∇ of the order of 0.4 m/s. If we assume that the bonds between the primary particles inside the agglomerates have an area equal to 2.5% of the cross-section of

the particles itself, a bond being able to withstand a physical stress equal to $\mathcal{S}$ would translate into a value of F_L^* equal to:

$$F_L^* = 2.5 \cdot 10^{-2} \frac{\mathcal{S}\pi R_p^2}{6\pi\mu_f R_p u_\nabla} = 42$$

if we take $\mathcal{S} = 40 \cdot 10^3$ Pa. This value of F_L^* falls within the range that is considered in Chapters 5, 6 and 7. Using similar tests, by applying stresses in different directions, the maximum resistance of asphaltenes against shearing, bending and twisting, could also be determined, to obtain approximations of the value for T_L^*. However, such experiments have not been conducted yet.

Using the same sample, the adhesion strength between the asphaltenes and an un-coated stainless steel surface was compared to the adhesion strength of the asphaltenes to a stainless steel surface that was previously coated with a layer of asphaltenes. As the asphaltene-asphaltene adhesion strength can be compared to the strength by which the asphaltenes adhere to a clean stainless steel surface, this allows to estimate the value of γ that appears in the spring-dashpot wall-interaction potential given in equation (3.57).

In the adhesion experiments, the asphaltene sample was dissolved in toluene on a one-to-one mass basis; a droplet of the solution was applied onto the stainless steel surface, after which it was left to dry under a warm stream of air. It is found that the adhesion strength between two asphaltene coated stainless steel surfaces is about three times larger than the adhesion strength between one asphaltene-coated surface and one clean surface. These results thus indicate that values of γ of around 0.3 are reasonable for asphaltenes, similar to the largest values used in Chapter 7.

The tensile stress test and the adhesion experiments seem to be promising techniques to estimate the Eulerian-Lagrangian model parameters for asphaltenes. We are not aware of any literature in which similar experiments have been performed before.

Verification and validation of the Eulerian-Lagrangian model

Now that we have reviewed the applicability of the model parameters that have been considered using the Eulerian-Lagrangian model for asphaltenes, the next step is to consider a full verification and validation of the model with respect to experimental data. We will first describe the type of experimental data that is required for the model validation, and thereafter we will discuss the validation of several aspects of the Eulerian-Lagrangian model one by one. For those model aspects for which suitable data are lacking in the literature, a description will be given of the types of experiments that look most propitious to overcome this shortcoming in future research.

Requirements for the experimental data that can be used as model validation. Ideally, the experimental data that are used to validate the Eulerian-Lagrangian model have to be obtained under well-defined flow conditions that can be reproduced in the model. Since experimentally, there are no such things as periodic boundary

conditions and infinitely long channels or pipes, first of all, a more practically applicable flow geometry should be selected. It should produce a well-defined flow field and still be simple enough to be represented in the Eulerian-Lagrangian model. The Taylor-Couette flow cell, in which moving walls provide the driving force of the flow, is a promising experimental apparatus in this respect. It does not involve any pumps that can disrupt the agglomerates in an unpredictable way, and it also typically has a fluid-filled volume that is small (and simple) enough to be represented in the model.

Taylor-Couette flow cells are classical experimental setups that consists of co-axial cylinders, of which one can rotate, or both can rotate independently. It is characterised by the inner and outer Reynolds numbers, the gap ratio η, and the aspect ratio $\mathcal{Z}$ (Andereck et al., 1986):

$$Re_i = \frac{\rho_f R_i \omega_i (R_o - R_i)}{\mu_f} \qquad \eta = R_i/R_o$$

$$Re_o = \frac{\rho_f R_o \omega_o (R_o - R_i)}{\mu_f} \qquad \mathcal{Z} = \mathbb{L}/(R_o - R_i) \qquad (8.1)$$

where R_i and R_o are the radii of the inner and outer cylinder, respectively, $\mathbb{L}$ is the height of the cylinders and ω denotes the angular velocity of the cylinders.

If the rotation rate of the cylinders is small enough, the flow pattern that occurs in a Taylor-Couette device is pure Couette flow. For such flow, apart from deviations that occur near the top and bottom plates of the device, the circumferential velocity of the fluid is a function of the axial position in the device only. For larger rotation rates, secondary flow patterns occur, like Taylor vortices, that form circulation patterns in the direction perpendicular to the mean flow and the axis of the device.

With a few relatively simple modifications, the implementation of the Eulerian-Lagrangian model in the pipe geometry can be (and has been) adapted to simulate Taylor-Couette flow. This is done by including an inner cylinder in the model, that rotates with a prescribed velocity, and thus provides a driving force to the flow in the circumferential direction of the computational grid. The top and bottom lids of the flow cell are created by considering no-slip boundary conditions instead of periodic boundary conditions in the direction that corresponds to the streamwise direction in the original pipe flow. With these modifications, agglomeration and break-up of agglomerates in the Taylor-Couette geometry can be simulated accurately with relative ease.

Mean agglomerate size and agglomerate size distribution

The first property of the agglomerates that was studied in Chapters 5 and 6 was the steady-state mean mass of the agglomerates. The associated mass distributions and temporal evolutions were not shown in these chapters, but of course these can be easily extracted from the results of our simulations. Experiments that characterise this mean mass and the mass distribution would therefore be very useful to validate the

transport, agglomeration and break-up in our Eulerian-Lagrangian model. Experimentally, these are relatively hard to measure, however, and it is close to impossible to find the temporal evolution of these properties in situ during an experiment.

Alternatively, measurements of the mean size or the size distribution of the agglomerates can be used, which can be monitored much more easily. Provided that the fractal dimension of the agglomerates in the simulations is similar to the fractal dimensions that are found experimentally for asphaltenes (in Chapters 5 and 6 we have already shown that this is the case) we can expect that the mass distribution is more or less correct if the size distribution is correctly predicted. Although reports on asphaltene experiments that have been gathered under well-defined flow conditions are scarce in the literature, Rahmani and co-authors and Solaimany-Nazar and Rahimi conducted experiments in Taylor-Couette flow cells that provide a good lead towards validating the model with respect to the size of the agglomerates formed.

Taylor-Couette experiments on asphaltenes in model oil mixtures. Rahmani et al. (2003, 2004) studied the agglomeration and break-up of asphaltene agglomerates in a Couette-Taylor flow device in which only the inner cylinder is rotating. Shear rates between 1.2 and 12.7 s^{-1}, different heptane to toluene ratios for the model oil mixture, and asphaltene volume fractions of $\mathcal{O}\left(10^{-6}\right)$ are considered. The inner Reynolds number that corresponds to these experimental conditions ranges from 50 to 550. The flow patterns that correspond to this range of Reynolds numbers are, according to the regime map by Andereck et al. (1986), Couette flow, Taylor-vortex flow and wavy-vortex flow.

Microscopic videography, which is capable of detecting agglomerates larger than thirty micrometres, provides the temporal evolution of the average diameter of the asphaltene agglomerates (Rahmani et al., 2003, 2004), as well as the agglomerate size distribution (Rahmani et al., 2004). The time evolution of the mean agglomerate diameter that was obtained this way at an asphaltene concentration of 12.8 mg/l in a 1:15 volumetric mixture of toluene and heptane is reproduced in Figure 8.2.

Solaimany-Nazar and Rahimi (2008, 2009) performed experiments in a Taylor-Couette flow-cell similar to Rahmani and co-workers, and they also found that the average agglomerate diameter is of $\mathcal{O}\left(100\right)$ µm. Furthermore, they also report a maximum in the average agglomerate diameter at intermediate time scales, and a subsequent decrease in the mean agglomerate size. The results of these experiments are thus very similar to the ones found by Rahmani et al. that are presented in Figure 8.2.

Reproduction of the Taylor-Couette flow experiments in the Eulerian-Lagrangian model. Even though adapting the Eulerian-Lagrangian model to the Taylor-Couette flow geometry is relatively easy, reproducing the experimental conditions that were considered by Rahmani and co-authors and Solaimany-Nazar and Rahimi is not straightforward.

First of all, the concentrations of the dispersed phase that are considered by Rahmani and co-workers and Solaimany-Nazar and Rahimi are much smaller than the concentrations considered in Chapters 5 and 6 of this thesis. The typical time it takes for the
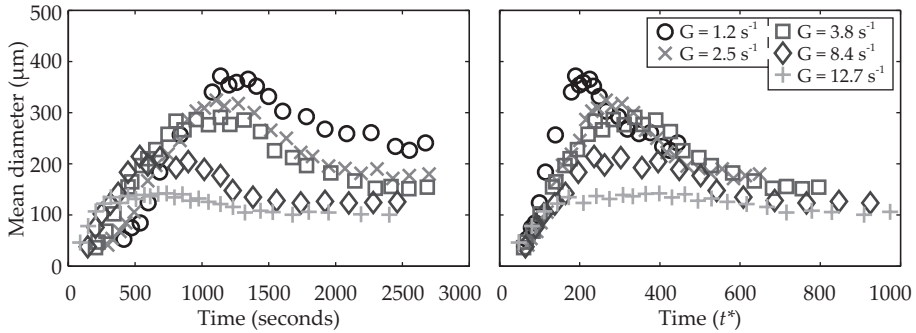
Figure 8.2: Temporal evolution of mean agglomerate diameter as observed for various shear rates in laminar Couette-flow experiments by Rahmani et al. (2003, 2004), for asphaltenes concentrated at 12.8 mg/l in a 1:15 mixture of toluene and heptane.

steady-state between agglomeration and break-up to set in scales with the inverse of the concentration of the dispersed phase. Reaching the steady-state therefore takes a lot of (wall-)time for the considered experimental conditions (as also shown in Figure 8.2). Simulating the flow over time scales as long as shown in Figure 8.2 is especially challenging because achieving a steady-state between agglomeration and break-up in laminar flow requires the use of two-way coupling (as discussed in Section 5.5). We thus cannot get away with using a small number of grid nodes for the carrier phase, which would be possible if one-way coupling could be used. The combination of the requirement of a fine computational grid and a very long simulated time interval results into an enormously long computational time that is required to reproduce the experimental results in the Taylor-Couette cell for the validation of our Eulerian-Lagrangian model. Single simulations are estimated to last for up to one year or more (assuming similar computational resources as used for the other simulations presented in this thesis). Conducting such long-running simulations is not feasible in the context of the present research project.

Still, the results shown in Figure 8.2 can be used to indicate one aspect of the actual asphaltene evolution that is not represented by our Eulerian-Lagrangian model in its present form. Our model never predicts a peak in the temporal evolution of the mean agglomerate diameter, which is observed in the experiments at intermediate time scales. In our simulations, agglomerates grow as long as the rate of agglomeration is larger than that of agglomerate break-up. As soon as the collision and break-up rates become balanced, the mean size of the agglomerates stops increasing in our simulations, but no subsequent decrease in size is observed. Most likely, the intermediate diameter peak that is found in the experiments is the result agglomerates becoming more compact over time by flexible restructuring (this mechanism is also hypothesised by Rahmani et al. (2003)). Alternatively, the peaks can be explained by a temporal change in the ability of the asphaltene agglomerates to bond to each other.

The latter mechanism could by enhanced by the possible effect that agglomerates might mainly break at very specific locations inside the Taylor-Couette flow cell, where they are not frequently passing through. These locations for instance could be the gaps between the inner cylinder and the outer casing of the cell at its axial ends. These effects are not taken into account in our model.

Experiments in turbulent Taylor-Couette flow. The steady-state between agglomeration and break-up can be more easily achieved in the Eulerian-Lagrangian model if turbulent flows are considered and larger dispersed-phase volume fractions are used. A Master student (de Combe, 2013) therefore conducted additional experiments in a Taylor-Couette flow cell, using a dispersed-phase volume fraction which is similar to the values used in Chapters 5 and 6 of this thesis (1%). Studying real asphaltenes unfortunately was not possible in equipment that was available for these experiments. Therefore, a model substance was used instead.

Polystyrene particles, mixed with ethane, hexane, toluene and/or CO_2, have previously been used in the literature as asphaltene substitutes (Ting, 2003; Sirota and Lin, 2007; Vargas et al., 2009), because they show a good resemblance in their behaviour and morphological characteristics. In the actual experiments by de Combe, polystyrene latex agglomerates were used, combined with water-glycerol mixtures as the continuous carrier phase. Because it was not possible to form the agglomerates inside the flow cell, only the break-up of the agglomerates was monitored over time from the moment that the rotation of the cylinders commences. A camera was used to make snapshots at regular time intervals of the agglomerate size distribution in a small region halfway the height of the Taylor-Couette device. The initial mean diameter of the agglomerates was approximately equal in all the experiments.

The Taylor-Couette flow-cell that was used by de Combe (2013) has a gap ratio η of 11/12 and an aspect ratio $\mathbb{Z}$ of 44. In contrast to the experiments by Rahmani and co-authors and Solaimany-Nazar and co-authors, both the inner and outer cylinders are rotated, in opposite directions. The inner and outer Reynolds numbers that are given in equation (8.1) can be translated into a Reynolds number that is based on the mean shear in the gap, and the rotation number R_Ω (Dubrulle et al., 2005):

$$Re_s = 2\frac{|\eta Re_o - Re_i|}{1 + \eta} \qquad R_\Omega = (1 - \eta)\frac{Re_i - Re_o}{\eta Re_o - Re_i}$$

In the experiments by de Combe (2013), the rotation number was kept at zero, and multiple values of the mean-shear Reynolds number Re_s were used.

Figure 8.3 shows the temporal evolution of the mean agglomerate diameter that was observed in the experiments. As the initial size distribution was the similar for all values of Re_s, the average diameter of the polystyrene latex agglomerates shows a very strong initial decrease, that is not captured by the temporal resolution of the experiments. However, especially for relatively small values of Re_s, the decrease in the average diameter persists for very long time intervals (more than 1000 units of t^*).

To mimic the procedure that was used in the experiments, simulations using the Eulerian-Lagrangian model were conducted in which the internal strength of the
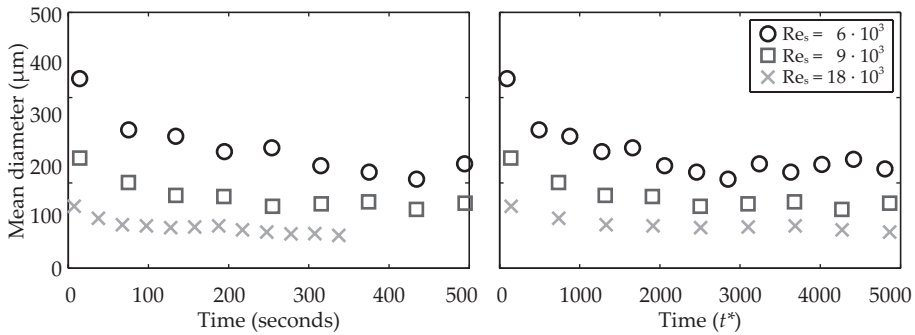
Figure 8.3: Temporal evolution of the mean agglomerate diameter under break-up as observed in turbulent Couette-flow experiments by de Combe (2013).

agglomerates is abruptly lowered. The moment of the decrease of the internal strength of the agglomerates resembles transferring the agglomerates to the Taylor-Couette flow cell, and turning it on.

Using a preliminary version of the Eulerian-Lagrangian model, de Combe (2013) compared the model results for the break-up of a pre-formed agglomerate population to the results that were obtained in his experiments. Even though the Reynolds numbers and volume fraction of the dispersed phase are similar in the simulations and the experiments, the time scale after which a new steady-state sets in was found to be much shorter in the simulations. The lack of two-way coupling and the inability of the preliminary model version to consider break-up due to torque-related break-up mechanisms were put forward by de Combe as the most likely causes for the mismatch between the model prediction and the experimental results. Results of simulations that have been conducted since the report by de Combe was written show that the time scale of the agglomerate break-up does not significantly change when these effects are included in the model.

We hypothesise that the most likely explanation for the difference in the time scale that is observed is caused by the fact that we consider agglomerates to be completely rigid in the model, whereas the polystyrene latex agglomerates used by de Combe (2013) were in fact quite flexible. The implication of the agglomerate rigidity is two-fold. On the one hand, the flexibility of the agglomerates by itself will partly absorb the stresses that are induced in those locations where the individual polystyrene latex particles are bonded to each other. On the other hand, flexibility during the formation of the agglomerates will make it very likely that multiple bonds between different agglomerate branches are present. Since all of these bonds need to be broken before the agglomerate is split into two pieces (either simultaneously, or consecutively), the presence of multiple-linked structures inside the agglomerates will increase the characteristic time scale of the break-up process.

Collision and break-up rate

The results of our simulations indicate that the collision rate of the agglomerates that is occurring in our Eulerian-Lagrangian model is underpredicted by empirical correlations that are used in engineering models for asphaltene deposition. Direct experimental measurements of the collision and break-up rate is virtually impossible, however. These aspects of the Eulerian-Lagrangian model can therefore only be validated indirectly, through their influence on other properties of the agglomerates or of the agglomeration process.

Fragmentation of agglomerates

The results that have been obtained using our Eulerian-Lagrangian model show that the mass distribution of the fragments of the agglomerates that are produced during break-up events is highly asymmetric. This is in contrast to common assumptions made in the literature, in which agglomerates are considered to be broken in two equal fragments. Furthermore, we have found that the properties of the agglomerates are rather insensitive to the break-up mechanism by which agglomerates are broken. It is therefore very difficult to determine which break-up mechanism is most relevant for asphaltenes, but, from a pragmatic perspective, it is also not important to obtain this knowledge. Data on the mass or size distribution that results from the break-up of agglomerates by any combination of break-up mechanisms are valuable for the validation of our model. Unfortunately, no such experimental data can be found in the literature for asphaltenes.

Still, the experimental results that have been obtained by Saha et al. (2014) give a qualitative validation of the results that were found in this respect in Chapters 5 and 6. These authors used particle tracking velocimetry to study the break-up of white sulphate polystyrene latex particles in the extensional flow that occurs inside a nozzle. They report data on the fragment distribution function, that is expressed by the diameter of the largest branch of an agglomerate that emerges from a break-up event as a fraction of the agglomerate diameter before break-up.

Similarly to the results that were shown in Chapters 5 and 6 of this thesis, Saha et al. find that break-up of agglomerates is very asymmetric. The most probable fragmentation ratio is characterised by $D_{\text{large}}/D_0 = 0.78$. Qualitatively, this compares favourably to the results presented in Figures 5.13 and 6.10 in terms of the fraction of the amount of primary particles that end up in the smallest agglomerate branch during break-up events in the Eulerian-Lagrangian model.

Deposition and re-entrainment

For asphaltenes, no suitable data for validating the deposition and re-entrainment as predicted by the Eulerian-Lagrangian model are available in the literature. Detailed experimental results are reported by Boek et al. (2008, 2010), but those are obtained in a capillary. On the other hand, field-scale deposit layer profiles like the ones reported by Haskett and Tartera (1965) cannot be represented by the Eulerian-Lagrangian

model, because they occur on a much too large scale both in a spatial and temporal sense.

There are other fields of science and engineering in which deposition or settling of agglomerates has been studied, like in environmental flows, or in the flow inside the human respiratory system. The flow conditions that occur in these systems cannot be represented in our model without making substantial modifications, however, and furthermore, detailed reports on the deposit formation and the structure of the deposit layers in these systems also seem to be lacking in the literature. Since we are not aware of any other numerical models for the deposition and re-entrainment of agglomerates with a complex structure, we also cannot use other numerical results for the validation of the spring-dashpot wall-interaction model. What we can do, however, is to provide our views on the recommended type of experiments to be obtained in future research.

Again, Taylor-Couette flow-cell experiments seem promising in this respect. In fact, Akbarzadeh and co-authors (Akbarzadeh et al., 2009, 2012; Eskin et al., 2011) already studied the deposition and re-entrainment of asphaltenes in a Taylor-Couette flow cell. Unfortunately, these authors do not report measurements on the characteristics of the deposit layer or of the deposition process itself. However, it should be possible to gather such information in future experiments. The Taylor-Couette flow-cell that was used by Akbarzadeh and co-authors is commercially available. Incorporating sensors that can monitor the deposition rate of agglomerates and the properties of the agglomerates into the apparatus would be a promising step in the direction of obtaining suitable validation data for the deposition and re-entrainment model.

As a first step, which should be relatively easy to achieve, we recommend to examine the properties of the deposit layer after the experiments, as this is easier than conducting in-situ observations. Examining the deposits formed using a microscope would already allow the verification of the hypothesis that large agglomerates do not contribute to the deposition. Also, it would allow for the structure of the deposit layers to be compared to the results of our model. As a next step, in-situ examination can be considered. By using a transparent outer cylinder in the Taylor-Couette flow cell and working fluids that are not too opaque, this would allow monitoring the evolution of a two-dimensional projection of the deposit layer during the experiments. Due to practical constraints (viz. project budget and time), proceeding along these lines was not possible within the scope of the present project, but it could still be pursued in the future.

Opportunities for model improvements

Until we arrive at a complete verification and validation of the Eulerian-Lagrangian model, it remains speculative to what extent the insights that have been obtained in Chapters 5, 6 and 7 are truly applicable to the actual evolution of asphaltenes after phase separation. When discussing experimental data that can be used to verify and validate the model, we often found that the experimental conditions for which data are available cannot be represented by the model. Above, we already outlined how

the experiments can be adapted to match the conditions that can be achieved in the present implementation of the model. Here, we will consider how the present model formulation can be modified to be able to represent the experimental conditions for which data are already available in the literature.

Code parallelisation. Using the present model formulation, simulations that are conducted using the Eulerian-Lagrangian model will take much too long when reproducing the experimental conditions by Rahmani and co-authors and Solaimany-Nazar and Rahimi. Bridging this gap can only be achieved if the computational power that can be invested in the simulations is highly increased, at least by one, but preferentially by multiple orders of magnitude. It is unrealistic to expect that the computational power of individual processor cores will increase by these factors within the foreseeable future. The only way to achieve this goal therefore is the parallelisation of the algorithm that underlies the numerical model. Some thoughts on how this can be achieved are given in Section 3.13 of this thesis. If this route is successfully pursued for the two-way coupled model, this enables either simulating significantly smaller volume fractions of the dispersed phase, or similar volume fractions using much smaller primary particles within a tractable amount of time.

The ability to consider much smaller primary particles is highly desirable, because it allows the agglomerates to better represent typical dimensions of asphaltene agglomerates. Parallelisation would also allow the model to reproduce the experimental conditions of the Taylor-Couette experiments by Rahmani et al. (2003, 2004). Possibly, it even could enable exploring the steady-state that ultimately sets in between deposition and re-entrainment. We therefore highly recommend proceeding along these lines in future research. Expectations should be realistic, however. Under no circumstance, the model will ever be able to simulate the asphaltene evolution from the nanometre-scale onwards. Even if perfect scaling across CPU's could be achieved, a reduction of the primary particle size by at most one or two orders of magnitude is possible. This would still, however, make a substantial difference in relation to the actual size of asphaltene agglomerates.

Rigidity or flexibility? We came across agglomerates flexibility as a possible cause for the discrepancies in the Eulerian-Lagrangian model predictions and experimental results that are obtained for asphaltenes or asphaltene model compounds. Introducing flexibility of the agglomerates into the Eulerian-Lagrangian model may therefore be helpful to overcome this discrepancies in the future. Doing so is not trivial, however, since the basis of the dispersed phase solver is built on the assumption that the motion of individual primary particles is given by the laws of solid body motion.

In order to incorporate the agglomerate flexibility, we recommend to move away from the solid-body based model implementation that was made in the present work. Instead, inter-primary-particle contact can best be modelled using a soft-sphere approach, similar to the current implementation of the particle-wall interaction. In this way, the cell-index technique can be used to determine for which primary-particle pairs interaction forces need to be taken into account. Collisions between particles no longer need to be captured, and the limiting strength of the inter-particle bonds can

be naturally incorporated into the interaction potential. Therefore, there no longer will be a need to explicitly resolve the break-up of agglomerates.

A possible pit-fall of this approach could be that severe time step constraints need to be imposed to ensure the numerical stability if the repulsive force that is associated with the overlap between primary particles is chosen too large. If the repulsive force is chosen too small, however, excessive overlap will occur. It is not a priori clear whether a suitable balance between these competing interests exists that will give satisfactory results.

8.2   One-dimensional drift-flux model

Because the one-dimensional drift-flux model described in Chapter 4 represents the formation, break-up, deposition and re-entrainment of asphaltenes at a much lower level of detail than the Eulerian-Lagrangian model, the requirements for experimental data that can be used to validate this model are much less stringent. We here compare the predictions that are obtained using this one-dimensional model with the asphaltene deposit layer profile measurements reported in the literature by Haskett and Tartera (1965) for the Hassi-Messaoud oil field in Algeria. The model results are also compared with both OLGA simulations and actual production data of an oil field that were made available to us but are not reported in the literature.

Incremental steps for the deposition on the order of 24 hours can confidently applied for the cases that have been considered. For computing the thickness of the asphaltene deposit layer, we assume that its porosity is 40%.

Hassi-Messaoud deposition profiles

The Hassi-Messaoud field in Algeria provides one of the rare examples for which asphaltene deposition profiles have been reported in the literature. Haskett and Tartera (1965) studied the MD4 well in particular, such that this well was selected for the validation of the one-dimensional model in this work.

Haskett and Tartera report the evolution of the deposit layer profile over a period of 100 days, with a probing interval of approximately 25 days. The profiles are acquired by descending gauge rings into the well, and they show a maximum deposit layer thickness of about 1.4 inches in the 4.5 inch well tubing. The well is completely vertical, and the reservoir, which is completed open-hole, is located at a depth of approximately 3400 metres. The so-called *pay-zone* (which is the layer in the reservoir from which oil is actually produced) is reported to be 100 to 300 feet thick by Haskett and Tartera (1965); therefore we assume a thickness of 60 metres in our model. The profiles of the deposit layer that are reported for the MD4 well have been obtained when the surface choke was removed from the production system. Therefore, we also disabled the choke in the model that was used for the MD4 simulations.

The actual reservoir pressure at the time that the deposit layer measurements were taken is not specified by Haskett and Tartera (1965). We assume that the reservoir pressure has not significantly decreased when compared to the original value of 470.6

Table 8.1: Overview of the parameters that are used in the drift-flux simulations for the Hassi-Messaoud MD4 well. The base values of the dispersed-phase model parameters are given by the values used by Eskin et al. (2011) for «oil C».

Parameter \ parameter set	Base values	Oil B	Matched
n_x	500		
# of size classes (K)	20		
R_{pri}	$8 \cdot 10^{-9}$ m		
D_f	1.8		
valve opening	valve removed		
P_{onset}	236 bar	236 bar	209 bar
P_{lower}	152 bar	152 bar	189 bar
collision efficiency (ς)	$5 \cdot 10^{-6}$	$3.5 \cdot 10^{-5}$	$1 \cdot 10^{-3}$
break-up efficiency (β)	0	0	0
deposition efficiency (ϕ)	$1 \cdot 10^{-6}$	$3.55 \cdot 10^{-6}$	$2 \cdot 10^{-4}$
re-entrainment coefficient (ϑ)	0.43	0.43	1.29
yield stress $\left(\tau_w^0\right)$	∞	∞	300 Pa
deposition cut-off (R_{max})	$3.6 \cdot 10^{-8}$ m	$1.5 \cdot 10^{-8}$ m	$3.6 \cdot 10^{-8}$ m

bar that was measured at the start of the production from the field. In our model, the Productivity Index of the reservoir was changed such that the initial flow rate of oil matches the reported value of Haskett and Tartera (1965) (9700 barrels per day). The PI value found is equal to 2.8 barrels per psi per day (6.4 m^3/bar/day). Furthermore, since we do not take into account heat transfer in our model, we have assumed a uniform temperature of 96°C inside the entire well, which is midway in the range that was specified by Haskett and Tartera (76–116°C). Based on the fluid composition data that are reported by Haskett and Tartera, PVTsim was used by TNO to construct a PVT-table for the Hassi-Messaoud reservoir fluid. This table has been used in our model as well to obtain the phase behaviour of the fluid inside the well.

Kurup et al. (2011) conducted simulations using Statistical Associating Fluid Theory to determine the asphaltene phase-separation window for the Hassi-Messaoud crude oil. The onset and lower limit of the phase separation pressure reported by Kurup et al. are used as base-case values in our model; they are equal to approximately 236 and 152 bar, respectively, for the temperature conditions inside the well. We assume that within the phase-separation pressure-window, all of the asphaltenes that are contained in the crude oil (500 mg/l, (Haskett and Tartera, 1965)) are released as primary particles, which will take part in the agglomeration and/or in the deposition.

As base parameters for the population balance model, we use the parameters that Eskin et al. (2011) determined for «oil C». The parameters of the population balance model that have been used for the simulations of the Hassi-Messaoud field case are summarised in Table 8.1. Figure 8.4 shows a comparison between the deposition profile predicted by the one-dimensional model and the actual deposition profile as reported by Haskett and Tartera for the MD4 well on the 8th of May 1963.
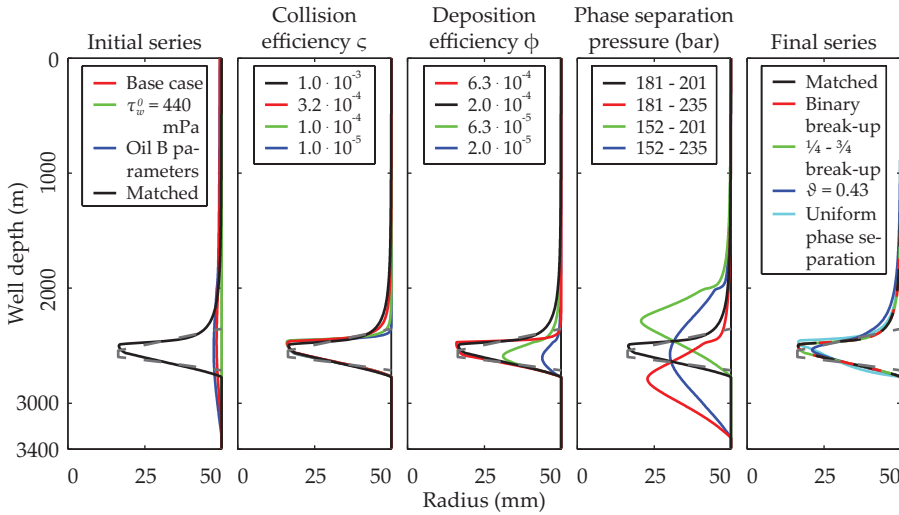
Figure 8.4: Comparison of the predicted deposition profiles (solid lines) as a function of the depth inside the well to experimental data by Haskett and Tartera (1965) (dashed line) for the Hassi-Messaoud MD4 well on the 8th of May 1963. In the leftmost graph, all cases (except the «oil B» and «matched» cases) are based on the base case parameters outlined in Table 8.1. In the rightmost graph, all cases are based on the matched-case parameters given in the same table.

The results in the leftmost graph of Figure 8.4 show that the model parameters for the dispersed phase that have been found by Eskin et al. cannot represent the deposition that is occurring in the Hassi-Messaoud MD4 even with approximate accuracy. The maximum thickness of the deposit layer is much too small, whereas its spatial extent is too large. When re-entrainment is considered with the same value for the yield-stress that was determined by Eskin et al. (440 mPa), all depositing agglomerates are immediately re-entrained. This is caused by the fact that the wall shear-stress in the entire well exceeds this value of the yield-stress at least by a factor of 10.

The simulation that has been conducted with the «oil B» parameters of Eskin et al. instead of the «oil C» parameters approaches the deposition profile in the Hassi-Messaoud field more closely. Based on these results, the inter-particle collision and deposition efficiencies, as well as the yield-stress for re-entrainment, were increased to match the model prediction of the deposit layer to the shape reported by Haskett and Tartera (1965). Likewise, the re-entrainment coefficient ϑ in equation (4.41) was increased three-fold with respect to the value used by Eskin (from 0.43 to 1.29), and the upper and lower limits of the phase separation pressure window were narrowed to 209 bar and 189 bar, respectively. Using this matched set of parameters, the deposit layer model provides a reasonably good reproduction the deposit layer profile that was measured on the 8th of May 1963, as shown in the left graph of Figure 8.4.

The three central graphs in Figure 8.4 show the influence of variations of the collision

efficiency ς (in equation (4.41)), the deposition efficiency ϕ and the phase-separation pressure boundaries on the profile of the deposit layer. All other parameters for these cases are equal to the «matched» set of parameters given in Table 8.1, without considering agglomerate break-up. The results show that changes in the collision efficiency mainly affect the slope by which the thickness of the downstream edge of the deposit layer reduces. An increased deposition efficiency increases the amount of particles that deposit at the wall, up to the point where the deposition process becomes limited by the amount of particles that are available for deposition. Finally, we found that the relatively small spatial extent of the deposit layer that is found by Haskett and Tartera can only be matched by the drift-flux deposition model if we assume that the phase separation of asphaltenes occurs over a significantly smaller pressure range than suggested by the simulations by Kurup et al. (2011).

In the rightmost graph of Figure 8.4, the influence of agglomerate break-up, variations in the re-entrainment coefficient ϑ and variations in the rate of asphaltene phase separation (both with respect to the matched set of parameters) the are shown. To investigate the relation between the pressure and the rate at which asphaltenes separate from the oil, we consider how the deposit layer changes if the phase separation of the asphaltenes is assumed to occur at a uniform rate as a function of the pressure inside the phase separation window, instead of following a normal distribution (viz. when most particles appear around the window-centre, which is the default assumption in the model, as given in expression (4.29)).

We find that the break-up of agglomerates only has a small effect on the formation of the deposit layer. For this reason, also no difference between the binary breakage, and the, according to our Eulerian-Lagrangian model results more realistic asymmetric break-up is found. The value of the re-entrainment coefficient ϑ is found to have an important effect on the shape of the deposit layer profile, however.

The value of the coefficient ϑ of the re-entrainment model determines how fast the re-entrainment rate increases with the wall shear stress if the wall shear stress is larger than the yield stress of the deposit layer. For the original value of $\vartheta = 0.43$ that was proposed by Eskin et al., we find that re-entrainment is occurring over a much larger region of the well depth than is needed to arrive at a deposit layer profile with a flat central region as was observed by Haskett and Tartera (1965). This is the reason that the value of ϑ was increased in the matched parameter set. Note that in the simulations for $\vartheta = 0.43$ that are shown in the rightmost graph of Figure 8.4, the value of τ_w^0 was changed such that the complete re-entrainment occurs at the same value of the wall shear stress as in the matched-parameter simulation, in which $\vartheta = 1.29$. The corresponding yield-stress is 18 Pa instead of 300 Pa.

The functional form that is assumed for the amount of asphaltene that separates from the crude oil as a function of the pressure is also found to have a significant effect on the shape of the deposit layer that is formed. When phase separation of asphaltenes is assumed to occur as a uniform function of the pressure inside the phase separation window instead of assuming that it mostly occurs towards the centre of the window, the front-edge slope of the deposit layer is found to be much more shallow. At the
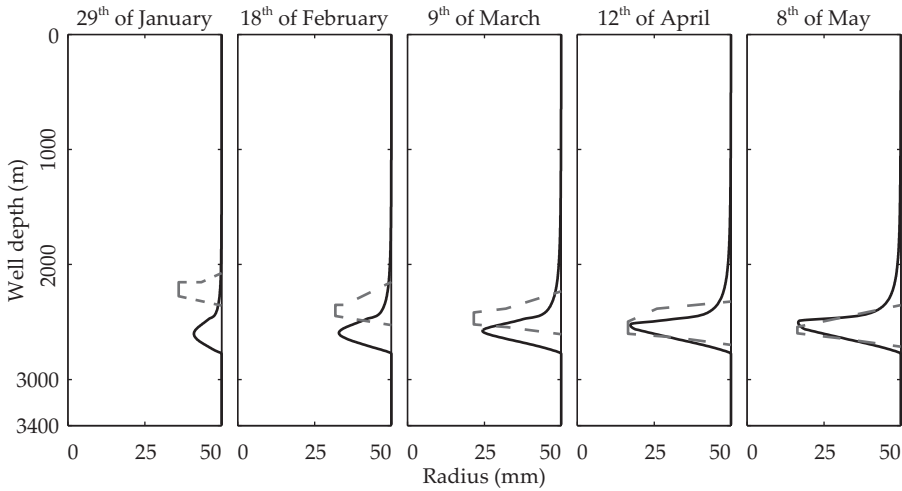
Figure 8.5: Time series of the predicted deposit layer profiles (solid black lines) compared to experimental data reported by Haskett and Tartera (1965) (dashed grey lines).

same time, the strongest diameter decrease occurs higher in the well, and the slope of the back end of the deposit layer is found to remain virtually unchanged.

Figure 8.5 shows the comparison of the matched model results with the experimental data presented by Haskett and Tartera (1965) for four additional time instants prior to the measurement of the final deposition profile. Even though the temporal evolution of the thickness of the deposit layer is quite accurately represented by the one-dimensional drift-flux model, the evolution of the spatial location of the deposit is not. In the actual Hassi-Messaoud field, the deposit layer is found to form at a location higher in the well initially, moving towards greater depth as time proceeds. To get similar results in the one-dimensional drift-flux model, the region where asphaltene phase separation takes place should move downwards in the well as time progresses.

Figure 8.6 shows a contour plot of the pressure as a function of time and of the depth inside the well. Since we find that the lower pressure limit of the phase separation window stays at approximately the same depth inside the well as time proceeds, whereas the upper pressure limit moves upward when the deposit layer is growing in thickness, a shift of the deposit layer downward in the well cannot be expected when the pressures that demark the phase separation window are constant in time.

Field production case

As an additional validation case for the one-dimensional engineering model that is described in Chapter 4, we study production data for an oil well made available to us that have not been reported in the literature. We compare both the pressure
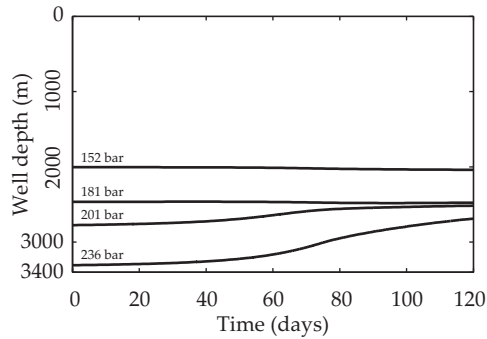
Figure 8.6: Pressure contours as a function of the time and the depth inside the well for the matched Hassi-Messaoud MD4-well simulations.

and hold-up distribution in the well to the results of the OLGA simulations that have been conducted by TNO for this well, and the predicted oil production rate to actual measurements that have been obtained in the field. Asphaltene deposition is a substantial problem in the particular field that is under study, and several campaigns of acid and/or solvent injection have been undertaken to remove the asphaltene deposit layers.

To protect the identity of the well that is studied, and not to reveal its actual geometry and performance, all of the results that are presented in this section use arbitrary or non-dimensional units. For the same reason, some of the parameters of the population balance model, such as the asphaltene concentration, are not specified. These parameters are not changed between the different cases that are presented. For the particular oil that is under study, no data on the pressure window over which asphaltene phase separation occurs are available. We assume that the asphaltene phase separation only occurs inside the wellbore, and only in the region where single-phase flow occurs.

In the OLGA simulations, a fixed heat transfer coefficient between the well and the surrounding soil is assumed. In the drift-flux model, we both consider a case in which the temperature profile as predicted by OLGA is used, as well as a case with uniform temperature throughout the wellbore, which is equal to the mean of the reservoir temperature and the temperature at the top of the well. In both models, the same PVT-table is used to characterise the reservoir fluid, and the Productivity Index inside the reservoir is used as the closure parameter to match the predicted flow rate to the actual production rate that is measured in the field.

Figure 8.7 shows a comparison of the pressure and liquid hold-up between the OLGA and drift-flux simulations. In both models, the wellbore diameter is assumed to be equal to its nominal value, as the well has been cleaned by solvent injection just prior to the production rate measurements that were reproduced in the models. The results in Figure 8.7 show that for both temperature profiles the drift-flux model
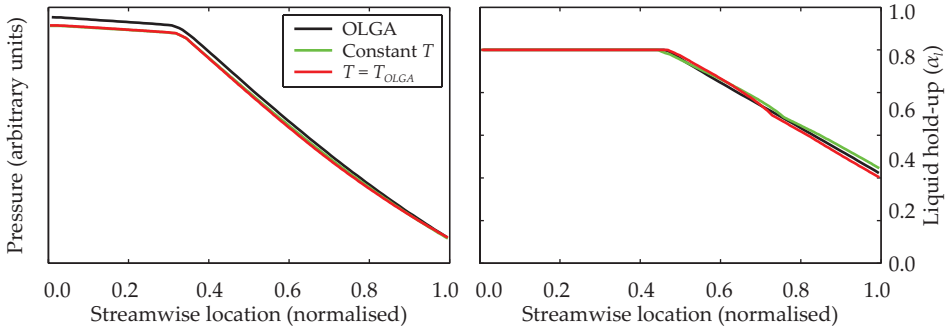
Figure 8.7: Comparison of the pressure and the liquid hold-up as a function of the streamwise coordinate, between OLGA simulations and simulations conducted using our drift-flux model for an undisclosed well.

reproduces the OLGA results with good accuracy. A slight deviation between both models is found in the bottomhole pressure, that is smaller in the drift-flux model when compared to OLGA as a result of a slightly reduced pressure drop over the wellbore.

In all further simulations, we will use the temperature profile predicted by OLGA as an input to the drift-flux model. The matched parameters for the Hassi-Messaoud MD4 well, given in Table 8.1, are used for the population balance and deposition models. The only deviations are (i) $n_x = 250$, (ii) different values for P_{onset} and P_{lower}, and (iii) a choke is present in the system.

Figure 8.8 shows the comparison of the model predictions with the temporal evolution of the actual oil production data that were obtained in the field. Also, the predicted profile of the deposit layer is shown as a function of the depth of the well, for several instants in time. The initial stage of the production decline can be represented accurately by the one-dimensional drift flux model if parameters of the Hassi-Messaoud field are used in the population balance equation, no matter whether re-entrainment is taken into account or not. For long time scales, significant differences in both the production rate and the deposition profile are found upon including re-entrainment in the model. We find that the production data can be well represented for a yield stress of the deposit layer that is equal to 65 Pa.

Evaluation of production scenarios

Now that we have shown that the one-dimensional model can represent the oil production rate as it is observed in the well that is under study with reasonable accuracy, the model can be used as an engineering tool to asses the optimal strategy by which the well can be produced. Optimisation of the control strategy of the well could be aimed at, for instance, maximising the production of crude oil over a
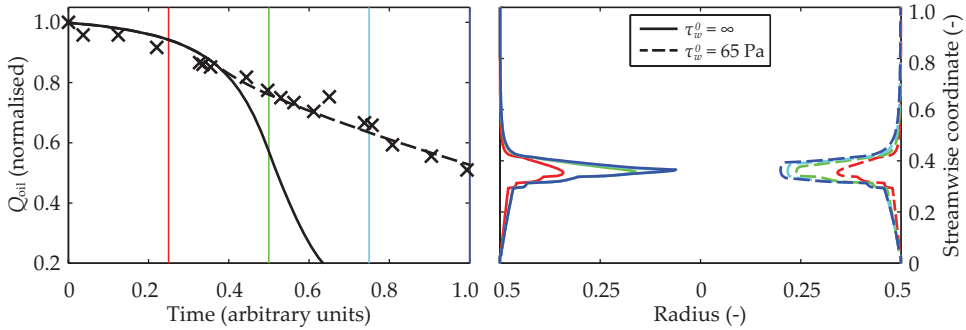
Figure 8.8: Oil production rate, as predicted by the one-dimensional drift-flux model, compared to measured data (crosses) for an undisclosed oil well (left). Predicted diameter profile as a function of time and the depth of the well (right). The colour key for data in the right graph indicates the time snapshots as shown in the left graph.

certain period of time, or at minimising the total cost per produced barrel of oil. For simplicity, we here consider the production strategy to be optimal when it gives the largest possible average production of crude oil per day.

Notwithstanding the injection of chemical asphaltene inhibitors during the production of crude oil, the opening of the choke and the frequency by which asphaltene deposits are removed from the well are the only parameters that can be controlled during the oil production. We consider how the mean flow rate of oil over time changes as a function of the choke opening. Also, we will consider different timings for cleaning the well by the injection of an asphaltene solvent; this means that we will consider such a cleaning procedure to be initiated when the minimum remaining open cross-section area of the wellbore, A_{cs}, has decreased to different levels. We assume that the injection of the solvent requires a shutdown of the production for a few days, and that the well will return to a completely clean state after the solvent injection.

Figure 8.9 shows the mean daily oil production rate, as a function of the choke setting and the minimum open cross-sectional area of the pipe that exists before the well is cleaned using solvents. The maximum achievable production rate from the well is found for a choke opening of 1.0, irrespective of the timing of the clean-up operation. In general, we find that the mean daily oil production rate is largest when the well is cleaned at the moment the cross-sectional area of the wellbore is partly blocked by the deposit layer. If the value of A_{cs} is chosen too large, the well will be cleaned very frequently; this means that the well is cleaned when the instantaneous production rate has not been decreased that much, because the deposit layer is still very thin. In this case, the average production rate decreases because the well is not producing at all for a significant fraction of time, during the clean-up procedures. On the other hand, if the value of A_{cs} is chosen too small, the wellbore will be cleaned much less frequently. Now, however, there is a relatively long period prior to the clean-up procedure in
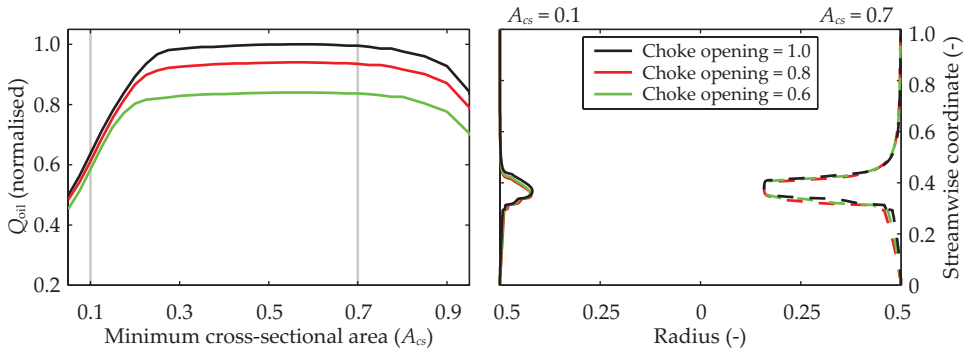
Figure 8.9: Mean average flow rate as a function of the minimum cross-sectional area that remains before the well is cleaned, for different choke settings (left). Diameter profile of the well as a function of the streamwise distance at a minimum open cross-sectional area of 0.1 and 0.7 (right).

which the instantaneous oil production is very small, thereby also decreasing the mean production rate over prolonged periods of time.

Balancing the interests of maximising the oil production rate and minimising the number of interventions, we find that cleaning can best be commenced when about 25% of the cross-sectional area is still open. This opening approximately marks the point where Q_{oil} still has not decreased much from its maximum value, while the number of required cleaning interventions is still relatively small. We find that for obtaining the largest possible average oil production rate, the well should always be operated with the surface choke fully open.

8.3   Improvements in engineering model closure relations

In this section, we will reflect on how the insights in the agglomeration, break-up, deposition and re-entrainment processes that have been obtained using the Eulerian-Lagrangian model can be used to arrive at improved closure relations for the one-dimensional drift-flux model that was described in Chapter 4.

In Chapters 5, 6 and 7, we have considered the following phenomena for which closure relations are required in one-dimensional models: (i) the collision rate of agglomerates, (ii) the fragmentation of agglomerates during break-up events, and (iii) the wall-normal velocity of agglomerates during deposition.

Collision rate. In the one-dimensional drift-flux model, the collision frequency is computed using a superposition of the collision kernels due to Brownian motion and due to turbulent velocity fluctuations. Because Brownian motion is not relevant for the relatively large primary particles that have been considered in the Eulerian-Lagrangian model, only collisions due to turbulent velocity fluctuations and mean fluid shear were taken into account in Chapters 5 and 6. We found that the collision

rate is underestimated by collision kernels (both when considering only the effects of mean shear, only the effects of turbulent velocity fluctuations, or a superposition of both effects). This shows that the «true» collision rate of the agglomerates is larger than predicted by the closure relation that is presently used in the one-dimensional drift-flux model.

Like in many other engineering models for asphaltene deposition, the collision rate predicted by the collision kernel is multiplied by a collision efficiency (ς) that is much smaller than one in the one-dimensional drift-flux model. The value of the collision efficiency is not determined from first principles, but instead it is found by matching model predictions to measurement data. The collision efficiencies that are obtained this way are of the order $\mathcal{O}(10^{-5} - 10^{-3})$. Contrarily, the correction factors for the collision kernel that were derived from the Eulerian-Lagrangian models are of $\mathcal{O}(1)$. The increase in the actual collision rate that would result from collision kernels that are corrected for the discrepancies found in Chapters 5 and 6 would therefore completely be absorbed in decreasing values of the matched collision efficiencies. Protocols to estimate the collision efficiency a priori, remediating the necessity to use it as a matching parameter, are therefore required before the improvements in the collision kernel will translate into better performance of one-dimensional models.

Fragmentation. Because break-up is a complex process, many engineering models in which agglomerate break-up is considered assume that agglomerates always form two fragments of equal mass upon being broken. The same assumption is made in the population balance model for asphaltenes deposition that was proposed by Eskin et al. (2011), which was used as a basis for the dispersed-phase solver in the one-dimensional drift-flux model.

The results of our Eulerian-Lagrangian model simulations show that the formation of two equal fragments is a poor representation of the actual break-up that takes place in the flow. Instead, there is a wide distribution in the fraction of the number of primary particles that ends up in both agglomerate branches. However, the results that have been obtained using our one-dimensional drift-flux model for the Hassi-Messaoud oil field indicate that the deposition of the asphaltenes is rather insensitive to whether break-up is occurring or not. As a result, a more sophisticated representation of the fragmentation of the agglomerates instead of assuming binary breakage will hardly influence the predicted deposition rate. We have verified this by considering how the deposition of asphaltenes changes if instead of binary breakage, it is assumed that agglomerates break in branches that contain ¼ and ¾ of the primary particles of the broken agglomerate (which is the most probable outcome of a break-up event in the Eulerian-Lagrangian model). The deposition rate was hardly affected by this change.

Deposition velocity. Like for the collision rate that is predicted by the collision kernel, the deposition rate predictions that are adopted in engineering models like the one-dimensional drift-flux model that is considered in this work involve the multiplication of the deposition velocity by a deposition efficiency (ϕ) that is much smaller than one. We find that values of $\mathcal{O}(10^{-6}-10^{-4})$ for the latter parameter are required to match the predictions of our drift-flux model to experimental results.

At the same time, the results of our Eulerian-Lagrangian simulations show that the deposition velocity of the agglomerates due to turbulent velocity fluctuations is only underestimated by about a factor of two by the closure relation that is currently applied in the drift-flux model. The improvements that can be derived from the results of the Eulerian-Lagrangian model in terms of the deposition velocity are therefore insignificant as long as the deposition efficiency in engineering models cannot be determined by other means than fitting the model results to experimental data.

8.4   Summary

In this chapter, a critical review is presented of the Eulerian-Lagrangian model with respect to its ability to represent the actual evolution of asphaltene particles as they emerge after phase separation. The hydrodynamic force model, despite the simplifying assumptions that have been made in its derivation, can represent the hydrodynamic force distribution inside the agglomerates with reasonable accuracy when two-way coupling is used. In one-way coupling, the hydrodynamic force on the particles in the direction of the mean flow is found to be significantly overestimated.

Due to its computational complexity, the present implementation of the model is not able to represent the primary particles at a small enough scale to be representative for real asphaltenes. As a result, there is a mismatch between the length scales in the turbulent flow that affect the dynamics of the agglomerate evolution as presented in Chapters 5, 6 and 7 of this thesis with respect the real asphaltene agglomeration as it will occur in the field. This discrepancy can only be remediated if the computational power that can be invested in the simulations is increased by orders of magnitude, through parallelisation of the algorithms of the model.

The actual parallelisation of the model was not pursued in the scope of the current work, but is highly recommended for future research. Apart from the ability to simulate using primary particle with more realistic sizes, it also enables simulating smaller dispersed phase volume fractions. Thereby, it allows the experimental data by Rahmani and co-workers and/or Solaimany-Nazar and Rahimi to be used to validate the model. Validation of the mechanisms that govern deposition and re-entrainment in the Eulerian-Lagrangian model remains challenging, however, because suitable data (of experimental and/or numerical nature) are lacking in the literature. Conducting experiments in a Taylor-Couette flow-cell that is equipped with sensors to monitor the rate of deposition and re-entrainment, as well as the deposit layer characteristics, as explained in this chapter, is therefore advisable.

We have presented results of novel experimental techniques that have been applied to asphaltene samples to estimate the model parameters for the Eulerian-Lagrangian model. In these experiments tensile tests and adhesion tests between asphaltenes and stainless steel surfaces were conducted. The results of the experiments indicate that the range of parameters for the inter-particle and for the particle-wall interaction strengths used in Chapters 5, 6 and 7 are reasonable for the asphaltene sample that was studied in the lab.

The one-dimensional drift-flux model that was proposed in Chapter 4 was validated against asphaltene deposit layer profile measurements reported in the literature by Haskett and Tartera (1965) for the Hassi-Messaoud oil field in Algeria. Also, model predictions were compared to both OLGA simulations and actual production data for an oil field for which no data are reported in the literature. For the Hassi-Messaoud MD4 well, we found that the model can represent the final deposition profile with reasonable accuracy. The temporal evolution of the thickness of the deposit layer is also represented with reasonable accuracy, but the model is unable to capture the temporal shift in the depth within the wellbore where the deposition occurs as reported by Haskett and Tartera.

For the well for which unpublished production data were made available to us, we found that the drift-flux multiphase flow solver can accurately reproduce the results of the OLGA simulations for the pressure and hold-up distribution in the clean state. Also, the model can give a good representation of the decrease in the oil production rate that is observed in the field as asphaltene deposition occurs. By using the model to assess several possible production strategies, we have found that this particular well can best be produced with the choke valve fully opened, while cleaning the well as soon as the minimum open cross-sectional area of the wellbore has decreased to about 25%. In this way the best balance between an as large as possible average daily oil production and a minimum number of cleaning interventions is found.

In Chapters 5, 6 and 7, corrections to the closure relations for the collision rate, fragmentation and deposition velocity were derived. We find that agglomerate break-up does not have a strong influence on the asphaltene deposition rate. Therefore, it is not necessary to consider more sophisticated break-up models than the presently used binary breakage in engineering models for asphaltene deposition, despite the fact we have found that binary breakage is not representative of the actual break-up that is occurring in the Eulerian-Lagrangian simulations.

The magnitude of the corrections to the collision rate and deposition velocity that were derived from the Eulerian-Lagrangian simulation results are minor when compared to the corrections that result from empirical fitting parameters that are present in existing engineering models for asphaltene deposition. In future research, it will be necessary to find means for approximating the values of these empirical closure coefficients *without* fitting the model predictions to measured data. With this additional step, the insights that have been obtained in this work can be used to achieve better predictions in the models that can be applied on a field-relevant scale.

Chapter 9

Conclusions and outlook

Deposition of asphaltenes is a serious problem that may be encountered during the production of crude oil from subsurface reservoirs. Asphaltenes are a fraction of crude oil itself that can, depending on the operating conditions, such as the pressure and temperature, separate from the oil. Eventually they may form deposits at the boundaries of the flow domain, for instance inside the reservoir, in the well tubing or in the pipelines. As the cross-section that is open to the flow decreases, the pressure drop in the system increases and the oil production rate reduces. This production deferment gives a significant loss of revenue of the oil well. Likewise, the intervention costs associated with removing asphaltene deposits are considerable.

Very limited literature on the hydrodynamic aspects of asphaltene deposition is available, and this study is intended to fill that gap. To this end, we have proposed and implemented an Eulerian-Lagrangian model for agglomeration and deposition. In this model transport, break-up and re-entrainment, as induced by a turbulent carrier phase, are also taken into account. All four principal mechanisms of break-up (straining, shearing, bending and twisting) are included in the model, and the complex internal structure of the agglomerates is accounted for and resolved in time. In this respect, our model is the first of its kind. A novel treatment for adhesive wall boundary conditions was proposed, in which the attractive particle-wall interaction is modelled using a damped harmonic oscillator, combined with a time-relaxation to impose wall-parallel boundary conditions for the deposited particles.

Section 9.1 summarises the results and conclusions that follow from our Eulerian-Lagrangian simulations of agglomeration and break-up in absence of deposition and re-entrainment. In Section 9.2, we summarise the conclusions that can be drawn from simulations in which deposition and re-entrainment were taken into account using the Eulerian-Lagrangian model.

We have also contributed to the further development of an one-dimensional engineering model that previously was implemented by TNO for the prediction of asphaltene deposition under actual oil production conditions. The conclusions that result from the simulations using this model will be given in Section 9.3. Alongside

with this, the improvements of the closure relations for this one-dimensional model that can be derived from the insights obtained in Eulerian-Lagrangian simulations are summarised.

In Section 9.4, a critical review of the shortcomings of the models that have been proposed in this work will be given, and we present our outlook for possible future research using the Eulerian-Lagrangian model, as well as on asphaltene deposition in general.

9.1   Eulerian-Lagrangian model: Agglomeration and break-up

Using the Eulerian-Lagrangian model that was proposed in Chapter 3, we studied agglomeration and break-up in a periodic domain, with a constant number of primary particles and thus a constant dispersed-phase volume fraction. Under these circumstances, the competition between agglomeration and break-up leads to a statistical steady-state, in which individual agglomerates undergo collision and break-up events, but the collective properties of the agglomerate population no longer change over time.

Steady-state mean mass of agglomerates. When the forces that the dispersed phase exert onto the continuous carrier phase are neglected (viz. one-way coupling), the mean steady-state mass of the agglomerates is found to increase linearly with the resistance of the inter-particle bonds to straining and shearing. For the torque-induced break-up mechanisms, the scaling exponents are lower than one, at about two-thirds. This is in line with what one would expect based on the fractal dimension of the agglomerates and the fact that the induced torque scales both with the hydrodynamic force and the radius of the agglomerate. Under one-way coupling, the scaling exponents relating the mean steady-state mass of the agglomerates to the strength of the inter-particle bonds are similar for agglomerates that are formed in channel and pipe flows, and are valid for Reynolds numbers in the turbulent flow regime.

At fixed values of the strength of the inter-particle bonds, the mean agglomerate masses are smaller in the pipe than in the channel. This is because the slip velocity of the individual primary particles with respect to the carrier phase has a larger magnitude in the pipe. The increase in the slip velocity itself stems from the fact that the inner layer of the turbulent flow occupies a larger fraction of the cross-section of the flow domain in the pipe than in the channel. The strong streamwise velocity gradients in the wall-normal direction, as well as strong turbulent velocity fluctuations that occur in this region, cause large instantaneous velocity gradients over the agglomerates and thus increase the slip velocity of individual primary particles.

Because we consider agglomerates that, like real asphaltenes, have a very small relative inertia, the mean slip velocity of the agglomerates with respect to the fluid surrounding them is relatively small. The agglomerates thus act as spatial filters of the carrier-phase velocity. When the hydrodynamic forces that are exerted by the fluid onto the dispersed phase are coupled back to the continuous phase itself (two-way coupling), this causes the turbulent velocity fluctuations to be damped.

Consequently, the slip velocity of the individual primary particles with respect to the surrounding fluid reduces. As a result, the hydrodynamic force that is exerted on the particles decreases, and the internal stresses that are induced in the agglomerate also decrease when moving from one-way to two-way coupling. The mean mass of the agglomerates at fixed values of the internal strength under two-way coupling is thus larger than the mean mass that results when one-way coupling is applied.

Fractal dimensions. The fractal dimensions of the agglomerates show an increasing trend for increasing values of the strength of the inter-particle bonds. Their range (1.8–2.3) agrees favourably with the largest values reported in the literature for the fractal dimensions of asphaltene agglomerates. The fractal dimensions of agglomerates that are broken by straining are smaller than those of agglomerates that are broken by bending, twisting, and, in particular, shearing. If the strength of the inter-particle bonds is relatively small, the fractal dimensions of the agglomerates are smaller in the pipe flow than in the channel flow. The fractal dimensions increase more strongly with increasing values of the strength the bonds though, especially when two-way coupling is considered.

Agglomerate shape. We characterised the shape of the agglomerate by the aspect ratio of the length of the agglomerates along their primary axes. The most probable agglomerate shape has proportions of approximately 1.4/1.0/0.7 for the major, intermediate and minor axis, respectively, corresponding to a slightly flattened and elongated sphere-like shape. We find that this most probable agglomerate shape, as well as the shape distribution function, are insensitive to the strength of the inter-particle bonds, the flow geometry, the Reynolds number, and whether one- or two-way coupling is considered.

Collision kernels. Collision kernels that are based on the mean shear rate and the turbulent velocity fluctuations are able to qualitatively capture the collision rate as a function of the mean number of primary particles per agglomerate found in our simulations. However, quantitatively, our Eulerian-Lagrangian model shows a collision rate that is up to a factor of 10 larger than the predictions given by the collision kernels form the literature. The overall collision rate in the pipe is larger than in the channel. Since the mean shear rate and turbulent velocity fluctuations are not too different in both geometries, the predicted collision kernels are similar. Larger correction factors are therefore required in the pipe to match the kernel predictions to the collision rates found in the simulations when compared to the channel.

Break-up of agglomerates. For all break-up mechanisms, the fragmentation yield, measured by the fraction of primary particles that end up in the branches that are formed during break-up events, is asymmetric. Binary breakage, in which agglomerates break into two equal fragments, is found to be a poor representation of the actual break-up process, even though it is frequently used as a break-up mechanism in engineering models. Our results show that agglomerates are most likely to break into parts that contain approximately one quarter and three quarters of the primary particles that originally were contained in the agglomerate that is broken.

169

Effects of agglomerate formation and break-up on the carrier-phase flow. When two-way coupling is considered, the velocity field of the continuous carrier phase is modified by the presence of the dispersed phase. The presence of a dispersed phase that undergoes agglomeration and break-up changes the flow rate to a much larger extent than a non-agglomerating dispersed phase with otherwise identical properties and with the same volume fraction does. For all of the cases that have been considered in this work, an increase in the fluid flow rate is observed.

As the internal strength of the agglomerates increases, the percentage increase in the flow rate initially rises, until it reaches a plateau level and eventually slightly decreases for agglomerates that have a very large strength. This is caused by a balance of two counteracting mechanisms. On the one hand, the apparent viscosity of the fluid increases due to the finite size of the agglomerates (which can be quite large compared to the typical structures that are found in the flow, and increases with increasing strengths of the inter-particle bonds) introduces a long-range coupling in the fluid velocity. On the other hand, the two-way coupled agglomerates reduce the turbulent velocity fluctuations, thereby lowering the eddy viscosity of the continuous carrier phase.

Laminar and transitional flow. The properties of the agglomerates that are formed by the competition between agglomeration and break-up are either insensitive to the Reynolds number of the turbulent flow, or simple mappings have been found that collapse the results for multiple Reynolds numbers onto common scaling relations. We checked whether the scaling relations for the mean agglomerate mass also hold if the flow is not turbulent, but laminar or transitional instead. Our results show that this is not the case: in a laminar flow, the mass of the agglomerates for instance is significantly larger than predicted by the turbulent scaling relations. The inherent irregular motion that is present in turbulence thus is an important feature in determining the character of the agglomerates that are formed, even though the properties of the agglomerates are not too sensitive to the exact magnitude of the Reynolds number when the flow is turbulent.

Take home message for engineering model developers. Our results show that the properties of the agglomerates do not change that much depending on which mechanism is responsible for agglomerate break-up. Exact knowledge on what break-up mechanism is relevant for asphaltenes is therefore not required when constructing a predictive engineering model. The underprediction of the collision rate and the asymmetry in the agglomerate break-up are more substantial in this respect. We will come back to these aspects in Section 9.3. From a pragmatic perspective, the formation and break-up of agglomerates in channel and pipe flow are similar enough to neglect the effect of the geometry in engineering models.

9.2   Eulerian-Lagrangian model: Deposition and re-entrainment

For studying deposition and re-entrainment using the Eulerian-Lagrangian model, in- and outflow boundary conditions were used for the continuous carrier phase as well as for the dispersed phase. Only the initial phase of the deposition process

was considered, as arriving at a steady-state between deposition and re-entrainment would require too much computational time. We studied the deposition and re-entrainment processes, the morphology of the deposit layer, as well as the effects that the formation of the deposit layer has on the pressure drop in the flow domain. The change of these properties was investigated as a function of the internal strength of the agglomerates, the ratio between the internal strength and the adhesion strength to the wall, and the particle-wall interaction range.

Properties of the deposition and re-entrainment processes. We distinguish between agglomerates that are being transported to the wall by the flow for the first time (primary deposition), by the flow after being re-entrained (secondary deposition), or by colliding to an agglomerate that already has deposited at the wall. Similarly, for re-entrainment we distinguish between agglomerates that are removed from the wall either by the flow itself, or because they are part of a deposited agglomerate that is broken from the wall when an inter-particle bond is broken.

During primary deposition, almost only single primary particles and primary particle doublets are transported to the wall. Because the transport of agglomerates to the wall is unaffected by the parameters of the deposition model, we find that both the amount of primary deposition and the properties of the agglomerates that are deposited at the wall this way are unaffected by the strength of the particle-wall interaction potential. On the other hand, re-entrainment of agglomerates, and potential subsequent secondary deposition, are dependent on the tendency of agglomerates to get removed from the wall under the influence of hydrodynamic stresses. Therefore, these processes depend on the adhesion strength between the particles and the wall. For decreasing strengths of the particle-wall interaction potential, the re-entrainment rate increases more strongly than the secondary deposition rate, and thereby the net deposition rate of primary particles decreases.

The wall-normal velocity of the agglomerates during deposition is an important parameter in closing the deposition models that typically are used in one-dimensional engineering models. We find that the deposition velocity predicted by the empirical relation for turbulent velocity fluctuations that is used in the one-dimensional drift-flux model underpredicts the deposition velocity as found in the Eulerian-Lagrangian model by about a factor of two.

Properties of the deposit layer. Our results show that depending on the strength of the adhesive force between the particles and the wall of the flow domain, three different regimes for the agglomerate properties can be defined. For small adhesive strengths, the deposited agglomerates continuously shift over the wall of the flow domain, because the adhesive force is too small to overcome the hydrodynamic stress that is exerted by the continuous carrier phase. As a result, there is little relative motion between the different agglomerates that have deposited at the wall, and the agglomerates do not undergo very strong additional agglomeration after deposition. For intermediate wall-adhesion strengths, small deposited agglomerates remain stationary at the wall for most of the time. Larger agglomerates are still shifting over the wall, however, such that the motion of the deposit layer becomes

intermittent and frequent collisions between deposited agglomerates occur, thereby leading to the formation of large sheet-like structures.

If the particle-wall adhesion strength is increased even further, all of the deposited agglomerates become firmly attached to the wall and further agglomeration after the initial deposition becomes a much less frequently occurring phenomenon. In this latter regime, the internal strength of the agglomerates is found to become an important parameter in determining the morphology of the deposit layer, as this influences how far agglomerate branches can protrude into the flow before they are broken loose from the deposit layer. For increasing Reynolds numbers, we find that the transitions between the aforementioned regimes shift to larger values of the non-dimensional particle-wall adhesion strength.

Effects of agglomerate deposition and re-entrainment on the carrier-phase flow. Since the volume of the primary particles is not explicitly taken into account in the continuous carrier-phase solver, the dimensions of the flow domain do not change when a deposit layer is formed. Still, the interaction that occurs if two-way coupling is considered ensures that deposition does have an influence on the flow of the carrier phase. In the simulations of deposition and re-entrainment, in- and outflow boundary conditions are used for the continuous carrier phase. The flow rate is thus fixed in these simulations, and the formation of a deposit layer increases the pressure gradient. Increases by up to 90% were found for the cases that have been considered in this work.

Take home message for engineering model developers. Even though only the initial stage of the formation process of a deposit layer has been studied using the Eulerian-Lagrangian model, a few interesting observations have been made regarding the deposition and re-entrainment of agglomerates. Our results support the hypothesis by Eskin et al. (2011) that relatively small agglomerates are more likely to deposit at the walls of the flow domain than larger ones. We have also found that both the internal strength of the agglomerates, as well as the adhesion strength between the walls of the flow domain and the dispersed phase are important in determining the properties of the deposit layer. An accurate determination of the values of these adhesion parameters for asphaltenes is therefore important. Tensile tests and asphaltene-steel adhesion strength measurements that have been conducted at TNO seem promising techniques to determine these values for asphaltene samples.

9.3 One-dimensional model: field-scale observations and closure relations

We have also considered a one-dimensional engineering model for predicting asphaltene agglomeration and deposition in field-relevant flow geometries. This model is based on an existing implementation of a population balance model for asphaltene deposition that was proposed in the literature, which was combined with an one-dimensional drift-flux (gas/liquid) multiphase flow solver by TNO prior to this work. We have further extended this model by integrating the effects of deposition and

re-entrainment into the population balance equation that is used to model the agglomeration and break-up of the asphaltenes. Also, the reduction of the wellbore diameter was incorporated into the multiphase flow solver, such that the temporal evolution of the deposit layer and the associated decrease of the oil production can be studied as a function of time.

Hassi-Messaoud field, Algeria. For the Hassi-Messaoud oil field, asphaltene deposit layer profiles have been published in the literature by Haskett and Tartera (1965). We find that the final shape of the deposit layer can be well represented by the one-dimensional drift-flux model, provided that the pressure window in which asphaltene phase separation occurs is narrowed compared to the stability predictions made by Kurup et al. (2011) for the Hassi-Messaoud reservoir fluid. The temporal evolution of the deposit layer profile is captured with reasonable accuracy by the model in terms of diameter reduction, but not in terms of the location where the deposit layer is formed.

Unpublished field production data. For an oil production well for which unpublished production data from the field were made available to us, we showed that the one-dimensional drift-flux model can reproduce the pressure and hold-up profiles as they are found in simulations using the commercial one-dimensional model OLGA with good accuracy. The model can also successfully represent the actual decrease of the production rate that was measured in the field under progressing asphaltene deposition. Subsequent analysis of possible production strategies suggest that the highest possible average oil production rate can be achieved by producing the well with a fully open surface choke, and cleaning the wellbore as soon as about 75% of its cross-sectional area is blocked by the deposit layer.

Improvement of closure relations based on insights obtained using the Eulerian-Lagrangian model. The results that were obtained using the Eulerian-Lagrangian model show that the collision kernel and the empirical sub-model for the deposition velocity as a result of turbulent velocity fluctuations in the continuous carrier phase, which are used as closure relations in the one-dimensional drift-flux model, underpredict the observed collision and deposition rates, respectively. The correction factors that are needed to match the predictions to the actual values observed in the detailed simulations are of the order of 1 to 10.

The collision and deposition models that are applied in the one-dimensional drift-flux model multiply the aforementioned collision kernel and deposition velocity by collision and deposition efficiencies, respectively, that account for the fact that not all collision events lead to successful agglomeration, and not all particle-wall collisions lead to a deposit being formed (viz. «reaction-limited» behaviour). These efficiencies are tuning parameters that are used to match model predictions to measurements or other calibration data. Their typical values are several orders of magnitude lower than one; such small values are reported both in the literature, and are also required in the one-dimensional drift-flux model that was presented in this work. The improvements in the predictions for the collision rate and the deposition velocity that have been derived from the Eulerian-Lagrangian simulation results will therefore result in only

slight changes of the values of the collision and deposition efficiencies that follow from the matching procedure. In future research, it thus is necessary to find means for approximating the values of these closure coefficients *without* fitting the model predictions to measured data. After this additional step, the insights that have been obtained using the Eulerian-Lagrangian model can be used to achieve better predictions in the models that can be applied on a field-relevant scale.

The influence of break-up on the deposition rate was negligible for the cases that have been considered using the one-dimensional drift-flux model, even if a break-up efficiency of one is used. As such, the exact fragmentation of the agglomerates, with asymmetric rather than binary breakage, is not of primary concern in improving the model predictions of the one-dimensional drift-flux model considered in this work.

9.4   Outlook

In this section, we provide a critical assessment of the present shortcomings of the Eulerian-Lagrangian model that has been proposed in this work in relation to its ability to represent the actual evolution of asphaltenes after phase separation. We will give some leads on how these shortcomings may be overcome in future work. We will finish by giving our recommendations on where the focus on future research on asphaltenes should be.

Parameter space. Due to the computational complexity of the Eulerian-Lagrangian model, compromises had to be made with respect to the parameters that were studied in this work. In terms of the Reynolds number of the continuous carrier phase and the strength of the inter-particle bonds as well as the strength of the particle-wall interaction potential, we have been able to do a decent job. By contrast, sacrifices have been made in terms of the size and number of primary particles that have been studied in this work.

In all of the simulations that have been conducted using the Eulerian-Lagrangian model in the present work, an equivalent primary particle radius similar to the diameter of the largest asphaltene *agglomerates* (hundreds of micrometres) that have been reported in the literature has been used. The dimensions of the agglomerates that are formed in our simulations are thus significantly larger than those of real asphaltene agglomerates. As a result, there is a mismatch between the length scales in the turbulent flow that affect the dynamics of the agglomerate evolution in the simulations as presented in Chapters 5, 6 and 7 of this thesis, with respect to the real asphaltene evolution as it will occur in the field.

Code parallelisation. To consider primary particles with a more realistic size, a much larger number of particles needs to be considered. This requires an increase of the computational resources that can only practically be achieved by code parallelisation. Parallelisation of the dispersed phase algorithm (possibly combined with that of the continuous carrier-phase solver) could lead to a significant speed-up of the computations. It would also allow to increase the level of detail by which the agglomerate shape can be represented, while still being able to reach the steady-state

between agglomeration and break-up (and perhaps also between deposition and re-entrainment) within a feasible amount of time. Pursuing parallelisation of the algorithm will therefore be very valuable. Some thoughts on this can be achieved are given in Section 3.13 of this thesis.

Model validation. Experimental data on asphaltene agglomeration and break-up under well-defined flow conditions are reported only sporadically in the literature. The data that are available could potentially be used to validate the agglomeration and break-up components of the Eulerian-Lagrangian model developed in this work. Simulations that match the experimental conditions used in the literature are very computationally intensive, however, and the single-threaded computational time that would be required makes that validation is not practically achievable at present.

The lack of experimental data in the literature in which the deposition (and re-entrainment) of (asphaltene) agglomerates with a complex shape is studied in detail prevents validating the damped harmonic oscillator formulation for the deposition and re-entrainment model that was proposed in the present Eulerian-Lagrangian model. Conducting experiments that address this issue is the only way to enable the model validation. This could for instance be done by adding sensors to measure the properties of the deposit layer and the deposition and re-entrainment rates to a Taylor-Couette flow cell. Asphaltene deposition already previously has been studied in the literature in such a device, but these processes were not yet monitored in detail. Constraints of time and budget have prevented us to do so in the present project, but this is a valuable approach for future research. In Chapter 8, we have summarised our recommendations on how such experiments can be designed.

Rigid or flexible agglomerates? The assumption of absolute rigidity of the agglomerates stems from the fact that some asphaltene deposits are known to have a very brittle character. It is known, however, that other types of asphaltene deposit in tacky, liquid-like state, such that we know that not all asphaltenes produce rigid agglomerates. We came across flexibility of agglomerates as a possible cause for the discrepancies in the Eulerian-Lagrangian model predictions and experimental results that are obtained for asphaltenes or asphaltene model compounds. Investigating how the properties of the agglomeration, break-up, deposition and re-entrainment processes change if the agglomerates are flexible is therefore very appealing. In Section 8.1 we have therefore have outlined what modifications need to be made to the model such that agglomerate flexibility can be taken into account.

The Eulerian-Lagrangian model as a general tool to study agglomeration, break-up, deposition and re-entrainment in turbulent flows. Our Eulerian-Lagrangian model is the first of its kind. The model was used to study the dynamics of a dispersed phase that undergoes agglomeration, break-up, deposition and re-entrainment as it occurs in turbulent flows, while taking into account the internal structure of a large number of agglomerates. This allows the study of the fundamentals of the interactions between agglomerates with complex shapes and turbulence. Pursuing the further development and application of the Eulerian-Lagrangian model is therefore very interesting.

In this work, we have only scratched upon the surface of the wide range of interesting phenomena that can be studied using the model. As an example of fundamental studies that could be conducted in the future, changes in the correlation length of the turbulent flow that are induced by the dispersed phase could be investigated in a systematic way. Preliminary results for this approach have shown that the correlation lengths in general increase, though not isotropically and uniformly as a function of the wall-normal coordinate. By studying different density ratios, the formation of agglomerates in gas flows can be studied as well, which for instance occurs in pollution transport in the atmosphere. With adaptations, the model possibly can also be applied to study agglomeration and deposition phenomena of medical relevancy, such as the formation of thrombosis or atherosclerosis.

Concluding thoughts. Considering the objectives that were laid down in the first chapter of this thesis, an important consideration is whether we can expect that at some moment in the future, the Eulerian-Lagrangian model will be mature enough such that it can serve as a reliable and accurate method to study the formation and deposition of real-life asphaltene agglomerates.

From the practical perspective of oil producers, there is only added value associated with the model once a fairly complete verification and validation of the model with respect to asphaltenes has been achieved. Developing the required lab experiments, however, will take time, thereby limiting the practical applicability of this work to asphaltene deposition in the short term. Moreover, further improvements in the engineering models, that remove the necessity for obtaining the values of closure coefficients using data fitting, are required. With these future improvements, the insights that have been obtained using the Eulerian-Lagrangian model can be used to arrive at an improved predictive power in engineering models.

Despite these remaining challenges, looking at asphaltene deposition from a hydrodynamic perspective, rather than only from a chemical perspective (through experiments in chemical laboratories) is vital for obtaining predictive engineering models that can be used in the field. Only by combining the efforts from both disciplines (viz. multiphase flow and chemical engineering), conducting experiments that are useful for understanding how the flow affects the deposit formation process, and most importantly, sharing research results amongst the various disciplines, significant steps can be made to really understand how asphaltene deposition can best be remediated in the field.

List of most important symbols

Symbol	Unit*	Description	Defined in
f	–	Break-up yield (fragmentation)	Equation (5.8)
n	–	Number of grid cells	Figure 3.1
m	kg	Mass	–
r	m	Radial coordinate	Figure 3.1
t	s	Time	–
u_∇	m/s	Pressure gradient velocity	Equation (3.12)
x	m	Streamwise coordinate	Figure 3.1
y	m	Spanwise coordinate	Figure 3.1
z	m	Wall-normal coordinate	Figure 3.1
D_f	–	Fractal dimension	Equation (5.9)
F_L^N, F_L^S	N	Maximum straining, shearing force	Figure 3.2
F_L^*	–	F_L rescaled according to . . .	Equation (5.1)
H, R	m	Channel height, pipe radius	Figure 3.1
L	m	Length of computational domain	Figure 3.1
K	–	Number of agglomerate size classes	Equation (2.3)
N	#	# of primary particles per agglomerate	–
$\dot{N}_p$	#/s	Primary particle injection rate	Section 7.1
R_g	m	Radius of gyration	Equation (5.10)
R_p	m	Primary particle radius	–
T_L^B, T_L^T	Nm	Maximum bending, twisting torque	Figure 3.2
U	m/s	Streamwise velocity component	Figure 3.1
V	m/s	Spanwise/circumferential velocity	Figure 3.1
W	m/s	Wall-normal velocity component	Figure 3.1
Re_∇	–	Pressure gradient Reynolds number	Equation (3.11)
Re_{bulk}	–	Bulk Reynolds number	Equation (3.13)
$\mathbb{K}$	J	Turbulent kinetic energy	Equation (5.18)

---

*Unless noted otherwise, the results in Chapters 5, 6 and 7 are presented in non-dimensional form, dictated by star-units, as given in equation (3.8). Physical dimensions are denoted here for reference only.

Symbol	Unit	Description	Defined in
r	m	Location relative to centre of mass	Section 3.4
B	–	Body reference frame base vector	Section 3.4
F	N	Force vector	–
I	kgm^2	Moment of inertia tensor	Equation (3.33)
T	Nm	Torque vector	–
U	m/s	Velocity vector: $[U, V, W]^T$	–
X	m	Location vector: $[x, y, z]^T$	–
Ω	rad/s	Angular velocity	–
α	–	Hold-up	Section 4.1
β	–	Break-up efficiency	Equation (2.2)
γ	–	Particle-wall interaction parameter	Equation (3.57)
δ_c	m	Particle-wall interaction range	Equation (3.58)
δ_w	m	Minimum wall-normal coordinate of deposit layer	Section 7.1
ϵ	J/s	Dissipation rate of $\mathbb{K}$	Equation (5.15)
ζ	–	Damping ratio	Equation (3.59)
ϑ	–	Re-entrainment coefficient	Equation (4.41)
μ	Pas	Dynamic viscosity	–
ρ	km/m^3	Density	–
ς	–	Collision efficiency	Equation (2.2)
τ_p	s	Particle relaxation time	Equation (3.41)
τ_w, τ_w^0	N/m^2	Wall shear-stress, deposit yield stress	Equation (4.41)
ϕ	–	Deposition efficiency	Equation (4.41)
Γ	#/m^{3}s	Collision kernel	Equation (2.2)
Θ	m	Thickness of deposit layer	Section 7.1
$\mathcal{A}$	%	% of wall area covered by deposit layer	Section 7.1
$\mathcal{C}$	–	Collision kernel correction factor	Section 5.3
$\mathcal{D}$	#/m^{3}s	Break-up kernel	Equation (2.2)
$\mathcal{N}$	#/m^3	Particle or agglomerate concentration	–
$\mathcal{R}$	–	Reference frame transformation matrix	Equation (3.36)
$\mathcal{T}$	s	Agglomerate lifetime	Equation (5.8)
$\mathcal{W}$	–	Rescaled strength of particle-wall interaction	Equation (7.1)
$|_a$	–	Agglomerate	–
$|_{bu}$	–	Measured at break-up	–
$|_{cm}$	–	Centre of mass	–
$|_{dho}$	–	Damped harmonic oscillator	Equation (3.57)
$|_p$	–	Particle	–
$|_{rns}$	–	Relaxation to no-slip condition	Equation (3.60)
$|_{ss}$	–	Measured in steady-state	–

Bibliography

K. Akbarzadeh, H. Alboudwarej, W. Y. Svrcek, and H. W. Yarranton. A generalized regular solution model for asphaltene precipitation from n-alkane diluted heavy oils and bitumens. *Fluid Phase Equilibria*, 232:159–170, 2005.

K. Akbarzadeh, J. Ratulowski, T. Lindvig, T. Davies, Z. Huo, G. Broze, R. Howe, and K. Lagers. The importance of asphaltene deposition measurements in the design and operation of subsea pipelines. *Presented at the 2009 SPE Annual Technical Conference and Exhibition, New Orleans, USA, 4–7 October 2009*. SPE 124956, 2009.

K. Akbarzadeh, D. Eskin, J. Ratulowski, and S. Taylor. Asphaltene deposition measurement and modeling for flow assurance of tubings and flow lines. *Energy & Fuels*, 26:495–510, 2012.

E. M. Al-Safran and M. Kelkar. Predictions of two-phase critical-flow boundary and mass-flow rate across chokes. *SPE Production & Operations*, 24:249–256, 2009.

S. F. Alkafeef, F. Al-Medhadi, and A. D. Al-Shammari. A simplified method to predict and prevent asphaltene deposition in oilwell tubings: Field case. *SPE Production & Facilities*, 20:126–132, 2005.

C. D. Andereck, S. S. Liu, and H. L. Swinney. Flow regimes in a circular Couette system with independently rotating cylinders. *Journal of Fluid Mechanics*, 164: 155–183, 1986.

G. Barthelmes, S. E. Pratsinis, and H. Buggisch. Particle size distributions and viscosity of suspensions undergoing shear-induced coagulation and fragmentation. *Chemical Engineering Science*, 58:2893–2902, 2003.

E. S. Boek, H. K. Ladva, J. P. Crawshaw, and J. T. Padding. Deposition of colloidal asphaltene in capillary flow: Experiments and mesoscopic simulation. *Energy & Fuels*, 22:805–813, 2008.

E. S. Boek, A. D. Wilson, J. T. Padding, T. F. Headen, and J. P. Crawshaw. Multi-scale simulation and experimental studies of asphaltene aggregation and deposition in capillary flow. *Energy & Fuels*, 24:2361–2368, 2010.

R. B. de Boer, K. Leerlooyer, M. R. P. Eigner, and A. R. D. van Bergen. Screening of crude oils for asphalt precipitation: Theory, practice, and the selection of inhibitors. *SPE Production & Facilities*, 10:55–61, 1995.

B. J. Boersma. *Electromagnetic effects in cylindrical pipe flow*. PhD thesis, Delft University of Technology, 1997. URL: `http://repository.tudelft.nl`.

D. Browarzik, H. Laux, and I. Rahimian. Asphaltene flocculation in crude oil systems. *Fluid Phase Equilibria*, 154:285–300, 1999.

J. S. Buckley. Microscopic investigation of the onset of asphaltene precipitation. *Fuel Science and Technology International*, 14:55–74, 1996.

J. S. Buckley. Asphaltene deposition. *Energy & Fuels*, 26:4086–4090, 2012.

E. Buenrostro-Gonzalez, C. Lira-Galeana, A. Gil-Villegas, and J. Wu. Asphaltene precipitation in crude oils: Theory and experiments. *AIChE Journal*, 50:2552–2570, 2004.

D. Chen and M. Doi. Microstructure and viscosity of aggregating colloids under strong shearing force. *Journal of Colloid and Interface Science*, 212:286–292, 1999.

R. Cimino, S. Correra, A. Del Bianco, and T. P. Lockhart. Solubility and phase behavior of asphaltenes in hydrocarbon media. In E. Y. Sheu and O. C. Mullins, editors, *Asphaltenes: Fundamentals and Applications*, chapter III. Springer, 1995[†].

R. Cimino, S. Correra, P. A. Sacomani, and C. Carniani. Thermodynamic modelling for prediction of asphaltene deposition in live oils. *Presented at the 1987 SPE International Symposium on Oilfield Chemistry, San Antonio, USA, 4–6 February 1987*. SPE 28993, 1995[‡].

G. A. W. de Combe. Breakup of polystyrene particles in turbulent Taylor-Couette flow. Master's Thesis, Delft University of Technology, 2013.

S. Correra and F. Donaggio. OCCAM: onset-constrained colloidal asphaltene model. *Presented at the 2000 SPE International Symposium on Formation Damage, Lafayette, USA, 23–24 February 2000*. SPE 58724, 2000.

J. L. Creek. Freedom of action in the state of aphaltenes: Escape from conventional wisdom. *Energy & Fuels*, 19:1212–1224, 2005.

C. T. Crowe, M. Sommerfeld, and Y. Tsuji. *Multiphase flows with droplets and particles*. CRC Press, 1997.

B. Dubrulle, O. Dauchot, F. Daviaud, P.-Y. Longaretti, D. Richard, and J.-P. Zahn. Stability and turbulent transport in Taylor-Couette flow from analysis of experimental data. *Physics of Fluids*, 17:1–19, 2005.

D. R. Durran. The third-order Adams-Bashfort method: An attractive alternative to leapfrog time differencing. *Monthly Weather Review*, 119:702–720, 1991.

J. G. M. Eggels. *Direct and large eddy simulation of turbulent flow in a cylindrical pipe geometry*. PhD thesis, Delft University of Technology, 1994. URL: `http://repository.tudelft.nl`.

M. Ernst, M. Dietzel, and M. Sommerfeld. A Lattice Boltzmann method for simulating transport and agglomeration of resolved particles. *Acta Mechanica*, 224:2425–2449, 2013.

J. Escobedo and G. A. Mansoori. Heavy-organic particle deposition from petroleum fluid flow in oil wells and pipelines. *Petroleum Science*, 7:502–508, 2010.

D. Eskin, J. Ratulowski, K. Akbarzadeh, and S. Pan. Modelling asphaltene deposition in turbulent pipeline flows. *The Canadian Journal of Chemical Engineering*, 89:421–441, 2011.

D. Eskin, J. Ratulowski, K. Akbarzadeh, and S. Andersen. Modeling of asphaltene deposition in a production tubing. *AIChE Journal*, 58:2936–2948, 2012.

M. Faraji and A. R. Solaimany-Nazar. A study of the dynamic evolution of asphaltene aggregate size distribution using Monte Carlo simulation. *Energy & Fuels*, 24:4952–4960, 2010.

J. C. Flesch, P. T. Spicer, and S. E. Pratsinis. Laminar and turbulent shear-induced flocculation of fractal aggregates. *AIChE Journal*, 45:1114–1124, 1999.

S. K. Friedlander. *Smoke, dust and haze: fundamentals of aerosol dynamics*. Oxford University Press, 2000.

M. Frigo and S. G. Johnson. The design and implementation of FFTW3. *Proceedings of the IEEE*, 93:216–231, 2005.

H. Goldstein, C. Poole, and J. Safko. *Classical Mechanics*. Addison-Wesley, 2002.

H. Groenzig and O. C. Mullins. Molecular size and structure of asphaltenes from various sources. *Energy & Fuels*, 14:677–684, 2000.

A. Guha. Transport and deposition of particles in turbulent and laminar flow. *Annual Review of Fluid Mechanics*, 40:311–341, 2008.

B. A. van Haarlem. *The dynamics of particles and droplets in atmospheric turbulence: A numerical study*. PhD thesis, Delft University of Technology, 2000. URL: `http://repository.tudelft.nl`.

A. Hammami and J. Ratulowski. Precipitation and deposition of asphaltenes in production systems: A flow assurance overview. In O. C. Mullins, E. Y. Sheu, A. Hammami, and A. G. Marshall, editors, *Asphaltenes, Heavy Oils, and Petroleomics*, chapter 23. Springer, 2007.

A. Hammami, C. H. Phelps, T. Monger-McClure, and T. M. Little. Asphaltene precipitation from live oils: An experimental investigation of onset conditions and reversibility. *Energy & Fuels*, 14:14–18, 2000.

M. Han and D. F. Lawler. Interactions of two settling spheres: Settling rates and collision efficiency. *Journal of Hydraulic Engineering*, 117:1269–1289, 1991.

C. E. Haskett and M. Tartera. A practical solution to the problem of asphaltene deposits – Hassi Messaoud field, Algeria. *Journal of Petroleum Technology*, 17:387–391, 1965.

A. Hirschberg, L. N. J. de Jong, B. A. Schipper, and J. G. Meijer. Influence of temperature and pressure on asphaltene flocculation. *Society of Petroleum Engineers Journal*, 24:283–293, 1984.

M. Jamialahmadi, B. Soltani, H. Müller-Steinhagen, and D. Rashtchian. Measurement and prediction of the rate of deposition of flocculated asphaltene particles from oil. *International Journal of Heat and Mass Transfer*, 52:4624–4634, 2009.

N. B. Joshi, O. C. Mullins, A. Jamaluddin, J. Creek, and J. McFadden. Asphaltene precipitation from live crude oil. *Energy & Fuels*, 15:979–986, 2001.

S. Kawanaka, S. J. Park, and G. A. Mansoori. Organic deposition from reservoir fluids: A thermodynamic predictive technique. *SPE Reservoir Engineering*, 6:185–192, 1991.

A. Khoshandam and A. Alamdari. Kinetics of asphaltene precipitation in a heptane–toluene mixture. *Energy & Fuels*, 24:1917–1924, 2010.

G. K. El Khoury, P. Schlatter, A. Noorani, P. F. Fischer, G. Brethouwer, and A. V. Johansson. Direct numerical simulation of turbulent pipe flow at moderately high reynolds numbers. *Flow, Turbulence and Combustion*, 91:475–495, 2013.

A. S. Kurup, F. M. Vargas, J. Wang, J. Buckley, J. L. Creek, J. S. Hariprasad, J. Subramani, and W. G. Chapman. Development and application of an asphaltene deposition tool (ADEPT) for well bores. *Energy & Fuels*, 25:4506–4516, 2011.

K. A. Kusters. *The influence of turbulence on aggregation of small particles in agitated vessels*. PhD thesis, Eindhoven University of Technology, 1991.

K. J. Leontaritis and G. A. Mansoori. Asphaltene flocculation during oil production and processing: A thermodynamic colloidal model. *Presented at the 1987 SPE International Symposium on Oilfield Chemistry, San Antonio, USA, 4–6 February 1987*. SPE 16258, 1987.

Y. Li, J. B. McLaughlin, K. Kontomatis, and L. Portela. Numerical simulation of particle-laden turbulent channel flow. *Physics of Fluids*, 13:2957–2967, 2001.

Z. Liao, J. Zhao, P. Creux, and C. Yang. Discussion on the structural features of asphaltene molecules. *Energy & Fuels*, 23:6272–6274, 2009.

K. Liffman. A direct simulation Monte-Carlo method for cluster coagulation. *Journal of Computational Physics*, 100:116–127, 1992.

E. Lundanes and T. Greibrokk. Separation of fuels, heavy fractions, and crude oils into compound classes: A review. *Journal of High Resolution Chromatography*, 17: 197–202, 1994.

P. Luo and Y. Gu. Effects of asphaltene content on the heavy oil viscosity at different temperatures. *Fuel*, 86:1069–1078, 2007.

J. T. T. Mäkinen. Particle accretion and dissipation simulator: Collisional aggregation of icy particles. *Icarus*, 177:269–279, 2005.

T. Maqbool, A. T. Balgoa, and H. S. Fogler. Revisiting asphaltene precipitation from crude oils: A case of neglected kinetic effects. *Energy & Fuels*, 23:3681–3886, 2009.

T. Maqbool, S. Raha, M. P. Hoepfner, and H. S. Fogler. Modeling the aggregation of asphaltene nanoaggregates in crude oil—precipitant systems. *Energy & Fuels*, 25: 1585–1596, 2011[†].

T. Maqbool, P. Srikiratiwong, and H. S. Fogler. Effects of temperature on the precipitation kinetics of asphaltenes. *Energy & Fuels*, 25:694–700, 2011[‡].

M. T. Mason. *Mechanics of Robotics Manipulation*. The MIT Press, 2001.

P. Meakin and R. Jullien. The effects of restructuring on the geometry of clusters formed by diffusion-limited, ballistic, and reaction-limited cluster–cluster aggregation. *The Journal of Chemical Physics*, 89:246–250, 1988.

R. D. Moser, J. Kim, and N. N. Mansour. DNS of turbulent channel flow up to Re_τ = 590. *Physics of Fluids*, 11:943–945, 1999.

O. C. Mullins. The asphaltenes. *Annual Review of Analytical Chemistry*, 4:393–418, 2011.

A. T. van Nimwegen, K. C. J. Schutte, and L. M. Portela. Direct numerical simulation of turbulent flow in pipes with an arbitrary roughness topography using a combined momentum-mass source immersed boundary method. *Computers & Fluids*, 108: 92–106, 2015.

H. Pan and A. Firoozabadi. Thermodynamic micellization model for asphaltene precipitation from reservoir crudes at high pressures and temperatures. *SPE Production & Facilities*, 15:58–65, 2000.

J. D. Pandya and L. A. Spielman. Floc breakage in agitated suspensions: Effect of agitation rate. *Chemical Engineering Science*, 36:1983–1992, 1983.

N. I. Papadimitriou, G. E. Romanos, G. C. Charalambopoulou, M. E. Kainourgiakis, F. K. Katsaros, and A. K. Stubos. Experimental investigation of asphaltene deposition mechanism during oil flow in core samples. *Journal of Petroleum Science and Engineering*, 57:281–293, 2007.

S. J. Park and G. A. Mansoori. Aggregation and deposition of heavy organics in petroleum crudes. *Energy Sources*, 10:109–125, 1988.

J. S. Paschkewitz, Y. Dubief, C. D. Dimitropoulos, E. S. G. Shafeq, and P. Moin. Numerical simulation of turbulent drag reduction using rigid fibres. *Journal of Fluid Mechanics*, 518:281–317, 2004.

R. P. Perrine, D. C. Richardson, and D. J. Scheeres. A numerical model of cohesion in planetary rings. *Icarus*, 212:719–735, 2011.

G. Porte, H. Zhou, and V. Lazzeri. Reversible description of asphaltene colloidal association and precipitation. *Langmuir*, 19:40–47, 2003.

L. M. Portela and R. V. A. Oliemans. Eulerian–Lagrangian DNS/LES of particle–turbulence interactions in wall-bounded flows. *International Journal for Numerical Methods in Fluids*, 43:1045–1065, 2003.

M. J. B. M. Pourquié. *Large-eddy simulation of a turbulent jet*. PhD thesis, Delft University of Technology, 1994. URL: http://repository.tudelft.nl.

P. K. Ptasinksi, F. T. M. Nieuwstadt, B. H. A. A. van den Brule, and M. A. Hulsen. Experiments in turbulent pipe flow with polymer additives at maximum drag reduction. *Flow, Turbulence and Combustion*, 66:159–182, 2001.

H. Rahimi and A. R. Solaimany Nazar. Asphaltene aggregates fractal restructuring model, a population balance approach. *Energy & Fuels*, 24:1088–1093, 2010.

N. H. G. Rahmani, J. H. Masliyah, and T. Dabros. Characterization of asphaltenes aggregation and fragmentation in a shear field. *AIChE Journal*, 49:1645–1655, 2003.

N. H. G. Rahmani, T. Dabros, and J. H. Masliyah. Evolution of asphaltene floc size distribution in organic solvents under shear. *Chemical Engineering Science*, 59: 685–697, 2004.

N. H. G. Rahmani, T. Dabros, and J. H. Masliyah. Fractal structure of asphaltene aggregates. *Journal of Colloid and Interface Science*, 285:599–608, 2005[†].

N. H. G. Rahmani, T. Dabros, and J. H. Masliyah. Settling properties of asphaltene aggregates. *Energy & Fuels*, 19:1099–1108, 2005[‡].

E. Ramirez-Jaramillo, C. Lira-Galeana, and O. Manero. Modeling asphaltene deposition in production pipelines. *Energy & Fuels*, 20:1184–1196, 2006.

H. Rassamdana, B. Dabir, M. Nematy, M. Farhani, and M. Sahimi. Asphaltene flocculation and deposition: I. The onset of precipitation. *AIChE Journal*, 42:10–22, 1996.

H. Rassamdana, M. Farhani, B. Dabir, M. Mozaffarian, and M. Sahimi. Asphalt flocculation and deposition. V. Phase behavior in miscible and immiscible injections. *Energy & Fuels*, 13:176–187, 1999.

D. C. Richardson. A self-consistent numerical treatment of fractal aggregate dynamics. *Icarus*, 115:320–335, 1995.

P. G. Saffman and J. S. Turner. On the collision of drops in turbulent clouds. *Journal of Fluid Mechanics*, 1:16–30, 1956.

D. Saha, M. Soos, B. Lüthi, M. Holzner, A. Liberzon, M. U. Babler, and W. Kinzel-bach. Experimental characterization of breakage rate of colloidal aggregates in axisymmetric extensional flow. *Langmuir*, 30:14385–14395, 2014.

U. Schumann and R. A. Sweet. Fast fourier transforms for direct solution of Poisson's equation with staggered boundary conditions. *Journal of Computational Physics*, 75: 123–137, 1988.

K. C. J. Schutte. Numerical simulations of flows with spheres using immersed boundary methods. Master's Thesis, Delft University of Technology, 2010.

K. C. J. Schutte, A. T. van Nimwegen, and L. M. Portela. A combined momentum-mass source immersed boundary method for simulation of flow over multiple, non-stationary objects. *Proceedings of the 8th International Conference on Multiphase Flow, Jeju, South Korea, 26–31 May 2013*, 2013[†]. Paper number 726.

K. C. J. Schutte, L. M. Portela, and R. A. W. M. Henkes. A numerical study on the formation and break-up of particle agglomerates. *Proceedings of the 8th International Conference on Multiphase Flow, Jeju, South Korea, 26–31 May 2013*, 2013[‡]. Paper number 731.

K. C. J. Schutte, L. M. Portela, A. Twerda, and R. A. W. M. Henkes. Hydro-dynamic perspective on asphaltene agglomeration and deposition. *Energy & Fuels*, 29:2754–2767, 2015. URL: `http://pubs.acs.org/articlesonrequest/AOR-nEhNZPwe4FVhMkUUXzeA`.

H. Shi, J. A. Holmes, L. J. Durlofsky, K. Aziz, L. R. Diaz, B. Alkaya, and G. Oddie. Drift-flux modeling of two-phase flow in wellbores. *SPE Journal*, 10:24–33, 2005.

E. B. Sirota and M. Y. Lin. Physical behaviour of asphaltenes. *Energy & Fuels*, 21: 2809–2815, 2007.

A. R. Solaimany-Nazar and H. Rahimi. Dynamic determination of asphaltene aggregate size distribution in shear induced organic solvents. *Energy & Fuels*, 22: 3435–3442, 2008.

A. R. Solaimany-Nazar and H. Rahimi. Investigation on agglomeration–fragmentation processes in colloidal asphaltene suspensions. *Energy & Fuels*, 23:967–974, 2009.

J. G. Speight, R. B. Long, and T. D. Trowbridge. Factors influencing the separation of asphaltenes from heavy petroleum feedstocks. *Fuel*, 63:616–620, 1984.

O. P. Strausz, I. Safarik, E. M. Lown, and A. Morales-Izquierdo. A critique of asphaltene fluorescence decay and depolarization-based claims about molecular weight and molecular architecture. *Energy & Fuels*, 22:1156–1166, 2008.

R. Sureshkumar, A. N. Beris, and R. A. Handler. Direct numerical simulation of the turbulent channel flow of a polymer solution. *Physics of Fluids*, 9:743–755, 1997.

R. A. Sweet, L. L. Lindgren, and R. F. Boisvert. VFFTPK: A vectorized package of Fortran subprograms for the fast Fourier transform of multiple real sequences. 1990. URL: `http://www.netlib.org/vfftpack`. Version 2.1.

P. D. Ting. *Thermodynamic stability and phase behavior of asphaltenes in oil and of other highly asymmetric mixtures*. PhD thesis, Rice University, Houston, Texas, 2003.

F. M. Vargas, D. L. Gonzalez, G. J. Hirasaki, and W. G. Chapman. Modeling asphaltene phase behavior in crude oil systems using the perturbed chain form of the statistical associating fluid theory (PC-SAFT) equation of state. *Energy & Fuels*, 23:1140–1146, 2009.

F. M. Vargas, J. L. Creek, and W. G. Chapman. On the development of an asphaltene deposition simulator. *Energy & Fuels*, 24:2294–2299, 2010.

A. I. Victorov and A. Firoozabadi. Thermodynamic micellization model of asphaltene precipitation from petroleum fluids. *AIChE Journal*, 42:1753–1764, 1996.

J. Wang, J. S. Buckley, and J. L. Creek. Asphaltene deposition on metallic surfaces. *Journal of Dispersion Science and Technology*, 25:287–298, 2008.

S. Wang and F. Civan. Modeling formation damage by asphaltene deposition during primary oil recovery. *Journal of Energy Resources Technology*, 127:310–317, 2005.

E. J. P. Woittiez. How turbulence influences droplet coalescence in convective clouds. Master's Thesis, Delft University of Technology, 2007.

H. W. Yarranton and J. H. Masliyah. Molar mass distribution and solubility modeling of asphaltenes. *AIChE Journal*, 42:3533–3543, 1996.

N. Zuber and J. A. Findlay. Average volumetric concentration in two-phase flow systems. *Journal of Heat Transfer*, 87:453–468, 1965.

Acknowledgements

Even though at the start of a PhD project working on the same research topic for four years seems to be a very long time, from experience I can say by the end of it, you come to realise time has passed very quickly. There are many people that helped me along this academic journey and here I would like to acknowledge them for their support.

First of all, I would like to thank my promotor, Ruud Henkes. Ruud, you taught me a lot on how to approach industry-relevant problems with a pragmatic mindset and I am sure this will come in handy throughout the rest of my career. I really appreciate your focus and dedication to make sure that I finished my thesis (almost) on time, last but not least due to the pace in which you reviewed my work. Thanks for giving me the opportunity to conduct this research.

Secondly, I thank my co-promotor, Aris Twerda. Aris, especially towards the end of the project, when I was working on the one-dimensional model, your support became of inestimable value. I also really enjoyed the trips we had together to Milan, Paris and Galveston.

I am also grateful to Luis Portela. Luis, although you did not remain involved as my daily supervisor until the end of this project, your contributions were invaluable. If you would not have suggested me to do a PhD when I was still working on my Master's thesis, I am sure I would not have been on the verge of obtaining my PhD degree right now. I deeply appreciate your dedication in supporting your students, no matter how long scientific discussions take and how late they end at night.

I would like to thank the ISAPP consortium for funding this project. In particular, my thanks go to Sebastiano, Emanuelle, Ernesto, Alberto, Keld, Chiara and Massimo for their suggestions, support and hospitality. Jan-Dirk, Richard, Dries, Anke and Marlijn: thanks for organising all ISAPP gatherings, and for the quick approvals of my publications requests. At TNO, I would like to thank Tom and Andries for cooperating with me on the one-dimensional modelling, and alongside them Garrelt, Jos, Stefan and all the other members of the Heat Transfer and Fluid Dynamics group for making my visits enjoyable. Thanks also go out to Daniel and Frank for supporting Gilles de Combe in setting up the Taylor-Couette experiments. Hartmut, many thanks for conducting the experiments on the asphaltene sample and for the pleasant time we spent in Galveston.

I am also indebted to the Burgerscentrum for hosting the very informative post-graduate courses I attended in Delft, Eindhoven and Enschede. These allowed me to meet and interact with nice fellow PhD candidates, which I collectively thank for their sociability. Together with the Burgers Program for Fluid Dynamics at the University of Maryland, the Burgerscentrum also gave me the opportunity to attend the turbulence research school in College Park, for which I am very grateful.

Also, I would like to thank all members of the scientific and support staff of the Multi-Scale Physics department and the later Transport Phenomena group. Harry, Chris, Rob, Sasa, Jos, Jurriaan, Mark, Dirk and André: I loved the open and approachable atmosphere in our group and really enjoyed sharing coffee breaks and Friday-afternoon drinks with you. Angela, Fiona and, in particular, Anita: your support and help in the secretariat made my work so much easier. Evert, Jaap, Jos, Stefan en Christiaan: ondanks dat ik als numericus natuurlijk niet veel met jullie heb samengewerkt, wil ik jullie graag bedanken voor de gezelligheid bij koffiepauzes, lunches en andere momenten waarop wij samen kwamen. Richard, ook mijn dank aan jou is groot!

Of course, I would also like to thank all my (ISAPP) colleagues; in particular my roommates. Starting in the Leeghwaterstraat: Davide, Mohammed, Milos and Farzad. Joining in your room as a starting PhD student was a very good experience for me. Thanks for all of your advice regarding how to approach a PhD project. In the Waterzaal my roommates were Dries, Annekatrien and Saidah. Dries, even though we never managed to find a good compromise regarding the temperature in the office, I look back to our time together in one room as being very pleasant. It was always very nice and convenient sitting opposite of someone who was always willing to listen and think (or laugh!) along. Thanks as well for proofreading this thesis.

I also thank my other colleagues of the first hour: Reza, Galileu, Duong and Xiaogang. Bernhard, Niels, Rudi, Anton, Michiel, Laurens and Cees: I really enjoyed the great understanding we had amongst each other. Since most of your projects were already completed before mine, a lot of *gezelligheid* was lost in my last year. Luckily, Anand, Ahad, Harish, Saeid, Wenjie, Manas, Sid, Edoardo, Hrushikesh, Chirag and Maulik did a pretty good job in making up for this deficiency. Gerasimos: I take full responsibility for the fact that our mutual Dutch–Greek learning sessions never flourished; still it was fun trying every now and then.

Kevin, I really enjoyed spending time together with you in College Park and Washington D.C. Martin, vielen Dank für die Durchführung der vollständig aufgelösten Simulationen der Strömung durch eine meiner Agglomerate, und auch für die schöne Zeit die wir im Rahmen der ICMF Konferenz in Süd-Korea verbracht haben.

My gratitude also goes out to the students that did their Bachelor or Master thesis project in our group: Your sociability greatly contributed to the enjoyable working environment. In particular, but in no particular order, I would like to thank Jimmy, Wout, Corné, Shaikh, Romboud, Kimberly, Maudy, Niels, Rosanne, Lynn, Kristian, Conrad, Madelon, Gijs, Mathijs, Ruben (B. & Z.), Sinta, Heleen, Jelle, Patrick, Kelbij, Tjeerd, Ruben, Joost, Jeroen, Alexander, Sherwin, Martin, Ivo, Simon, Joep, Isabelle,

Mike, Thijs, Matthijs (Z. & R.), Harm, Jasper, Erik, Laurens, Agnes, Lidia, Zimo, Paul, Jaap, Marenka, Ellen and Ruiz.

Special thanks go out to the students whom I (co-)supervised during my PhD project. Tirsa, I really enjoyed being your supervisor and am still very impressed by the pace by which you acquainted yourself with my coding. Gilles, I am very grateful for the work you have done in obtaining experimental results in the Taylor-Couette flow cell.

Also outside the university I would like to acknowledge a few people.

Derk Jan, thanks a lot for getting in touch again as my PhD project was approaching its end, encouraging me to apply at Tata Steel. Alongside of you I also thank Bas, Jolanda, Jan, Tim, Koert, and all other folks in IJmuiden and Port Talbot for welcoming me so warmly. You have made me feel like I have never been away since my internship five years ago, which is great.

Of course, I also thank my friends, at home and abroad, for their support. In particular, I'd like to mention here Jeroen, José, Giorgos, Fotini, Vivian, Konstantinos and Savvas. Each of you individually knows what that is for.

Last but certainly not least, I thank my family and especially my parents. Without their support and dedication, I would not have been able to reach what I have reached so far in my life.

Koen

List of publications

Journal articles

K. C. J. Schutte, L. M. Portela, A. Twerda, and R. A. W. M. Henkes. Hydrodynamic perspective on asphaltene agglomeration and deposition. *Energy & Fuels*, 29:2754–2767, 2015. URL: `http://pubs.acs.org/articlesonrequest/AOR-nEhNZPwe4FVhMkUUXzeA`.

A. T. van Nimwegen, K. C. J. Schutte, and L. M. Portela. Direct numerical simulation of turbulent flow in pipes with an arbitrary roughness topography using a combined momentum-mass source immersed boundary method. *Computers & Fluids*, 108:92–106, 2015.

Conference articles

K. C. J. Schutte, L. M. Portela, and R. A. W. M. Henkes. A numerical study on the formation and break-up of particle agglomerates. *Proceedings of the 8th International Conference on Multiphase Flow, Jeju, South Korea, 26–31 May 2013*, 2013[‡]. Paper number 731.

K. C. J. Schutte, A. T. van Nimwegen, and L. M. Portela. A combined momentum-mass source immersed boundary method for simulation of flow over multiple, non-stationary objects. *Proceedings of the 8th International Conference on Multiphase Flow, Jeju, South Korea, 26–31 May 2013*, 2013[†]. Paper number 726.

About the author

Koen Schutte was born in Amsterdam on the 20th of January 1987. In 2005 he obtained his Gymnasium diploma at the Hermann Wesselink College in Amstelveen, whereafter he started a study *Technische Natuurkunde* at Delft University of Technology.

After obtaining his Bachelor's degree in 2008, he continued to study Applied Physics at the same university. After an internship at Tata Steel RD&T in IJmuiden and conducting a graduation project at the department of Multi-Scale Physics he obtained his Master degree in 2011 cum laude.

Later that year, he started his PhD research at the same institute. A reorganization in 2012 transferred him to the Transport Phenomena group of the Chemical Engineering department, where he worked on this dissertation until the end of 2015. On the 1st of January 2016, he rejoined Tata Steel Europe as a Process- and Product-technologist in the Centre of Expertise Strip Rolling & Coating.